

AFML-TR-74-73

Part II

Handwritten initials "R" and "FG" in the top right corner.

**MECHANISMS OF ADHESION FAILURE  
BETWEEN POLYMERS AND METALLIC  
SUBSTRATES**

AD A 025256

**Part II. Aluminum 2024-T3 and Titanium  
6A1-4V with HT424 Adhesive**

*ROCKWELL INTERNATIONAL*

OCTOBER 1975

TECHNICAL REPORT AFML-TR-74-73, Part II  
FINAL REPORT FOR PERIOD APRIL 1974 - AUGUST 1975

RECEIVED  
JUN 9 1976  
D.D.C.

Approved for public release; distribution unlimited

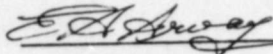
AIR FORCE MATERIALS LABORATORY  
AIR FORCE WRIGHT AERONAUTICAL LABORATORIES  
Air Force Systems Command  
Wright-Patterson Air Force Base, Ohio 45433

NOTICE

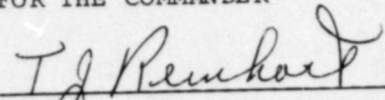
When Government drawings, specifications, or other data are used for any purpose other than in connection with a definitely related Government procurement operation, the United States Government thereby incurs no responsibility nor any obligation whatsoever; and the fact that the government may have formulated, furnished, or in any way supplied the said drawings, specifications, or other data, is not to be regarded by implication or otherwise as in any manner licensing the holder or any other person or corporation, or conveying any rights or permission to manufacture, use, or sell any patented invention that may in any way be related thereto.

This report has been reviewed by the Information Office (IO) and is releasable to the National Technical Information Service (NTIS). At NTIS, it will be available to the general public, including foreign nations.

This final report was submitted January 19, 1976 by Science Center, Rockwell International, 1049 Camino Dos Rios, Thousand Oaks, California 91360 under Contract F33615-72-C-1641, Project 7340, with the Air Force Materials Laboratory, Wright-Patterson Air Force Base, Ohio. E. A. Arvay (AFML/MBC) was the AFML project monitor.

  
E. A. ARVAY  
Project Monitor

FOR THE COMMANDER

  
T. J. REINHART, Chief  
Composites and Fibrous Material Branch  
Non-metallic Materials Division  
Air Force Materials Laboratory

ADDITIONAL TO	DATE STAMP	<input type="checkbox"/>	<input type="checkbox"/>	<input type="checkbox"/>
NTIS	EXT. NO.			
BY	DISTRIBUTION/AVAILABILITY CODES			
	DATE			
	AVAIL. EXT. OR SPECIAL			

*A*

Copies of this report should not be returned unless return is required by security considerations, contractual obligations, or notice on a specific document.

UNCLASSIFIED

SECURITY CLASSIFICATION OF THIS PAGE (When Data Entered)

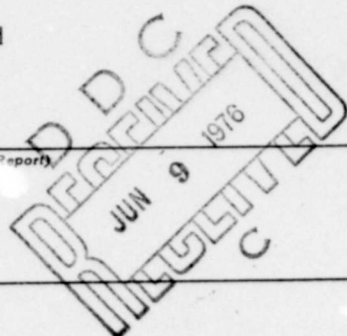
REPORT DOCUMENTATION PAGE		READ INSTRUCTIONS BEFORE COMPLETING FORM
1. REPORT NUMBER AFML-TR-74-73-Part II	2. GOVT ACCESSION NO.	3. RECIPIENT'S CATALOG NUMBER
4. TITLE (and Subtitle) MECHANISMS OF ADHESION FAILURE BETWEEN POLYMERS AND METALLIC SUB- STRATES. Part II. Aluminum 2024-T3 And Titanium 6Al4V With HT424 Adhesive.	5. TYPE OF REPORT & PERIOD COVERED FINAL REPORT 04/01/74 to 07/31/75	
7. AUTHOR(s) Tennyson/Smith	6. PERFORMING ORG. REPORT NUMBER SC534.17FR	8. CONTRACT OR GRANT NUMBER(s) F33615-72-C-1641
9. PERFORMING ORGANIZATION NAME AND ADDRESS Science Center, Rockwell International 1049 Camino Dos Rios Thousand Oaks, Calif. 91360	10. PROGRAM ELEMENT, PROJECT, TASK AREA & WORK UNIT NUMBERS 734202	12. REPORT DATE Oct 1975
11. CONTROLLING OFFICE NAME AND ADDRESS Air Force Materials Laboratory Air Force Systems Command Wright-Patterson Air Force Base, Ohio 45433	13. NUMBER OF PAGES 232	15. SECURITY CLASS. (of this report) Unclassified
14. MONITORING AGENCY NAME & ADDRESS (if different from Controlling Office)	15a. DECLASSIFICATION/DOWNGRADING SCHEDULE	
16. DISTRIBUTION STATEMENT (of this Report) Approved for public release; distribution unlimited		
17. DISTRIBUTION STATEMENT (of the abstract entered in Block 20, if different from Report)		
18. SUPPLEMENTARY NOTES		
19. KEY WORDS (Continue on reverse side if necessary and identify by block number) WETTABILITY, ELLIPSONOMETRY, SURFACE POTENTIAL DIFFERENCE, AUGER ELECTRON SPECTROSCOPY, MICROSCOPY (ELECTRON, SCANNING ELECTRON, OPTICAL), ADHESIVE JOINTS, METAL-POLYMER BONDING, BOND STRENGTH, FAILURE MECHANISMS, MAPPING OF SURFACE CHARACTERISTICS		
20. ABSTRACT (Continue on reverse side if necessary and identify by block number) This report describes the continuation of a study of aluminum 2024-T3 alloy and titanium 6Al-4V alloy adherends, adhesively bonded with epoxy HT424 adhesive. The adherend surface properties, after standard preparation treatments, were characterized with a number of surface tools; Ellipsometry, surface potential difference (SPD), Auger electron spectroscopy (AES), electron, scanning electron and optical microscopy,		

DD FORM 1473 1 JAN 73 EDITION OF 1 NOV 65 IS OBSOLETE

UNCLASSIFIED SECURITY CLASSIFICATION OF THIS PAGE (When Data Entered)

389 949

mt



UNCLASSIFIED

SECURITY CLASSIFICATION OF THIS PAGE(When Data Entered)

contact angle, photo electron emission, and light scattering. A study was made of bond strengths after FPL etching and phosphoric acid anodizing and after aging of these surfaces in water vapor and in water.

By calibrating the above mentioned instruments for hydroxide and organic films of known chemistry, it has been possible to discern the mechanism of aging degradation. The mechanisms of bond failure have been greatly elucidated by a careful study of the data. Suggestions are given to improve bond strength and stability based upon the analysis.



## PREFACE

This report covers the work conducted from 1 June 1974 to 31 August 1975 under the direction of Dr. Tennyson Smith, Manager and Principal Investigator. Those assisting were L. W. Crane, Research Assistant, C. Rhodes, Electron Microscopy and X-ray Diffraction, R. Spurling, Principal Metallographer, J. M. Harris, Auger Spectroscopist and L. F. Bivins, Research Assistant.

This report is a continuation of the study of adhesive bonding of Al 2024-T3 with HT424 adhesive and Ti-6Al4V with HT424 and other adhesives. AFML-TR-74-73 (June 1974) gives the experimental procedures, results and conclusions that emphasize the types and loci of bond failure. This report emphasizes the mechanism of degradation by surface aging in humid atmosphere as well as in liquid water. The reader is referred to AFML-TR-74-73 for details of ellipsometry, surface potential difference (SPD), Auger electron spectroscopy (AES), contact angle, scanning electron and optical microscopy techniques. The photo-electron-emission technique that has been developed since the last report, is described in reference 1. The light scattering technique for measuring surface roughness is described in reference 2, and page 57 of this report.

## SUMMARY

This report describes the continuation of a study of aluminum 2024-T3 alloy and titanium 6Al-4V alloy adherends, which after standard preparation treatments, were characterized with a number of surface tools. Ellipsometry was used to estimate oxide film thickness and optical properties, surface potential difference (SPD) measurements were made to characterize the outer surface dielectric properties, Auger electron spectroscopy (AES) was used to establish chemical analysis of the outer surface and chemical profiles during ion-sputter-back-etching. Topography and morphology were established with electron, scanning electron and optical microscopy. Wettability parameters were established by making contact angle measurements with a series of liquids with differing surface tension. Measurements of photo electron emission and light scattering were made to characterize electron emission and surface roughness properties.

A study was made of surfaces after FPL etching and phosphoric acid anodizing and after aging of these surfaces in water vapor and in water under controlled condition. By calibrating the above mentioned instruments for various hydroxides and organic films of known chemistry, it has been possible to discern the mechanism of aging degradation.

The mechanisms of bond failure have been greatly elucidated by a careful study of the data. Suggestions are given to improve bond strength and stability based upon the analysis.

Bonded joints, using unaged and aged adherends, were fabricated using HT-424, epoxy adhesive with and without glass carrier cloth. Both initial strengths and strengths after aging in various environments were determined.

General conclusions derived from the surface and joint strength studies indicate that although strong bonds are usually associated with surfaces of high energy (clean surfaces) and weak bonds with

surfaces of low energy (contaminated surfaces), we have observed strong bonds can result for surfaces with low energy (e.g. contaminated titanium) and weak bonds can result for surfaces with high energy (e.g. UV irradiated contaminated aluminum). However, all of these results can be explained in terms of the surface properties that we have elucidated. A fresh FPL etched aluminum surface is left with a set of submicroscopic etch pits that have sharp metal ridges. These ridges have very high electrical fields associated with them which render the surface extremely polar. The high energy surface is very strongly attracted to the adhesive primer and makes very strong adhesive bonds. However, the extreme reactivity is also the cause of its own degradation. The high fields associated with the metal ridges are reduced by reaction of the ridges with water molecules or by adsorption of contamination. In either case, the attraction to the primer is greatly reduced. In addition, blunting of the sharp metal ridges by oxidation by water molecules probably transforms the ridges to weak hydroxide. The adhesive which is strongly bonded along the metal ridges for a fresh FPL etch surface is weakly bonded to a weak hydroxide along the ridges and failure may occur in the oxide. It should be noted that failure along ridges would only transfer a small percent of the oxide to the adhesive. We have demonstrated in our previous report (AFML-TR-74-73) that thick hydroxide films are weak. By reducing the electric fields associated with the metal ridges, the organic contamination has destroyed its strong bonding capability even if the outer atom layer is made polar by UV radiation.

The attraction of a phosphate fluoride treated Ti-6Al4V surface for adhesive primer may be somewhat less than that provided by metal ridges on the aluminum but it is sufficient to make strong bonds even in the presence of some contamination. Because of the smoother submicroscopic titanium surface and slightly weaker attraction than freshly etched aluminum, the titanium bond strength can be improved by surface roughening. The roughening probably improves bond strength by increased surface area per unit

projected area, by some submicroscopic high field points and some hook and latch effects.

The weak regions in the Al 2024-T3-HT424 joints are the void volume created by the natural production of water vapor during the cure, and the weak glass carrier. The glass carrier is needed because it provides escape channels for the water vapor and therefore greatly decreases the void volume. It also has an effect with respect to the stress distribution. It is suggested that a carrier be found that acts as a hygroscopic water sink. Even better would be a hygroscopic powder filler to replace the aluminum filler, to reduce void volume and the weak carrier. It is suggested that edges where the glass carrier and extruded adhesive with gas blown channels, be sealed with additional adhesive to prevent access to degrading environments.



TABLE OF CONTENTS

	<u>Page No.</u>
I. Introduction	1
A. Purpose	1
B. Background	2
1. Aluminum	2
2. Titanium	7
C. The Problem	8
D. The Solution to the Problem	9
E. Analytical Procedures	10
II. Experimental Results	12
A. Aluminum	12
1. Relevance of Laboratory Bond Tests	12
1.1 Single Overlap Joints	12
1.1.1 Effect of Glue Line Thickness (GLT)	15
1.2 Double Overlap Joints	18
1.2.1 Effect of Glass Carrier	24
1.2.2 Effect of Primer	28
1.2.3 Effect of Pb and Fe ions	28
1.3 Butt Joints	29
2. The Effect of the Adhesive	29
2.1 Pin Holes	29
2.2 Aluminum Powder Filler	31
2.3 Effect of Adhesive Aging	31
3. The Effect of Controlled Roughness on Surface Properties and Bond Strength	31
4. The Effect of Controlled Hydroxide Films	43
4.1 Idealized Smooth Surfaces	45
4.2 Rough Surfaces	63
4.2.1 Wettability Analysis of Hydroxide Films	68

TABLE OF CONTENTS (cont'd)		Page No.
4.3	Surface Properties of FPL etch Al 2024-T3	68
4.4	Phosphoric Acid Anodized Al 2024-T3	76
4.5	Physical Properties of Al 2024-T3 Surfaces	82
4.6	Chemical Properties of Al 2024-T3 Surfaces	84
5.	The Effect of Controlled Contamination	89
5.1	Contamination with Myristic Acid	90
5.1.1	Smooth Surfaces	90
5.1.2	Rough Surfaces	90
5.1.3	AES Calibration	94
6.	The Effect of UV light on Contamination and Contamination Removal	105
6.1	Effect of UV Radiation	105
6.1.1	Bond Strength	108
7.	The Effect of Different Environments	111
7.1	SET in UHV	111
7.1.1	Bond Degradation for SET in the UHV chamber	124
7.2	SET in Glass Jars	126
7.2.1	Dry Atmospheres	126
7.2.2	Effect of Humidity and Environments	129
7.3	SET in Laboratory Air	136
7.4	SET in Water	149
7.4.1	Surface Properties	149
7.5	Effect of SET on Bond Strength	157
7.6	BET in Water	160
B.	Titanium	164
1.	Surface Treatments and Bond Strength	164
1.1	Comparison of Four Treatments	164
1.1.1	SEM study	164
1.1.2	Effect of Surface Roughness	170
1.1.3	Surface Properties and Bond Strength	175
1.2	Comparison of various Phosphate-Fluoride treatments	177
1.2.1	SEM study	177
1.2.2	Surface Properties and Bond Strength	177
1.2.3	Surface Character Maps	180

TABLE OF CONTENTS (concluded)		Page No.
1.3	Aged Etch Solution	198
2.	Effect of Controlled Contamination on Surface Properties	
3.	Effect of Different Environments	202
3.1	SET in the UHV chamber	202
3.2	SET of Ti-6Al4V in water vapor (glass jars) and in water	204
4.	BET of Ti-6Al4V in water vapor and in water	204
C.	Discussion of Results	211
1.	Aluminum	211
1.1	Answers to Questions	211
1.2	Adhesive Joint Structure and Failure Mechanisms	215
2.	Titanium	222
2.1	Answers to Questions	222
2.2	Adhesive Joint Structure and Failure Mechanisms	224
3.	Conclusicns	224
3.1	Adhesion Mechanisms	224
3.2	Suggesticns for Improvements	229
	APPENDIX A	230
	APPENDIX B	232
	REFERENCES	234

## LIST OF ILLUSTRATIONS

<u>Fig. No.</u>	<u>Page No.</u>
1. Schematic drawing of a double overlap joint.	13
2. Enlarged photographs of 2-3 couple for the resultant single overlap.	14
3. Bond strength <u>vs</u> GLT for Al 2024-T3 - HT424, single overlap joints.	17
4. a) Plot of $\phi_I$ <u>vs</u> GLT, b) Plot of $\sigma_b$ <u>vs</u> GLT for Al 2024-T3 - HT424 from Batch 1.	19
5. Enlarged photographs of a 1-2 couple for a double overlap joint, a) Surface B (Fig. 1), b) Surface A (Fig. 1).	20
6. Plot of average bond strength $\overline{\sigma_b}$ <u>vs</u> average $\overline{\text{GLT}}$ for double overlap joints	23
7. Plot of $\sigma_b$ <u>vs</u> GLT for double overlap joints with HT424F (no glass carrier).	26
8. Photograph of the fracture surfaces of Al 2024-T3 - HT424F (glass free).	27
9. Photographs of adhesive from Batch 3 (left) and Batch 2 (right).	30
10. Photographs of fracture surfaces of Al 2024-T3 - HT435 (no aluminum powder filler).	32
11. SEM micrographs of Al 2024-T3 after electro-polish (top) and 2 minutes FPL etch (bottom).	36
12. SEM micrographs after 13 min FPL etch (top) and 28 min FPL etch (bottom).	37
13. SEM micrographs after 60 min. FPL etch.	38
14. Plot of $\Delta$ , PEE and SPD <u>vs</u> FPL etch time.	40
15. Plot of rms roughness $\sigma$ , $-\delta\psi$ and $\phi_{H_2O}$ <u>vs</u> FPL etch time.	41



LIST OF ILLUSTRATIONS (cont'd)

<u>Fig. No.</u>	<u>Page No.</u>
16. Plot of bond strength <u>vs</u> ellipsometric roughness ( $-\delta\psi$ ). □ HT424 from batch 3 ◆ HT424 from batch 2.	42
17. Plot of bond strength <u>vs</u> $\phi_{H_2O}$ for HT424 from batch 3 (□) and batch 2 (●).	44
18. Plot of weight change <u>vs</u> time for vapor deposited aluminum on gold, during exposure to water.	46
19. SEM micrographs of vapor deposited Al/Au/Cr/Si (top) and Al/Au/Cr/glass (bottom).	47
20. SEM micrographs of vapor deposited Al after exposure to 96°C water (left) and 50°C water (right) for 1/2 hr.	48
21. SEM micrographs of vapor deposited Al after exposure to 96°C water (left) and 50°C water (right) for 1/2 hr.	49
22. SEM micrographs of vapor deposited Al after exposure to 96°C water (left) and 50°C water (right) for 1/2 hr.	50
23. SEM micrographs of vapor deposited Al after exposure to 96°C water (left) for 46.7 hrs and 50°C water (right) for 70 hrs.	51
24. SEM micrographs of vapor deposited Al after exposure to 96°C water (left) for 46.7 hrs and 50°C water (right) for 70 hrs.	52
25. Ellipsometric and SPD parameters as a function of exposure time for vapor deposited Al after phosphoric acid-anodize to 500 Å.	55
26. SEM micrographs of vapor deposited Al after anodizing to 500 Å, then 50°C water exposure for 150 hrs.	56
27. Plot of $\Delta$ <u>vs</u> exposure time for vapor deposited Al (96°C water ●, 50°C water ▽).	57
28. Plot of $\psi$ <u>vs</u> exposure time for vapor deposited Al (96°C ●, 50°C ▽).	59
29. Plot of light intensity I <u>vs</u> $\cos^2\theta$ for 96°C water (top) and 50°C water (bottom).	61

LIST OF ILLUSTRATIONS (cont'd)

<u>Fig. No.</u>	<u>Page No.</u>
30. Plot of $\tan \beta_0$ vs water exposure time.	62
31. SEM micrographs for degreased Al 2024-T3 as received (top), after 50°C water exposure for 21 hrs (bottom).	64
32. SEM micrographs for degreased Al 2024-T3 after 96°C water exposure for 21 hrs.	65
33. SEM micrographs of electropolished, then alkaline cleaned Al 2024-T3 after 96°C water exposure (left) and 50°C water exposure (right).	66
34. Plot of light intensity $I$ vs $\cos^2 \theta$ for Al 2024-T3 alkaline cleaned and vapor degreased samples.	67
35. Wettability envelope for Al 2024-T3 after water exposure.	73
36. SEM micrographs of Al 2024-T3 after the standard FPL etch.	74
37. SEM micrographs of FPL etched Al 2024-T3 after 100°C water exposure for 21 hrs (top) and 50°C water exposure (bottom).	75
38. SEM micrographs of polished (left) and phosphoric-anodized (right) Al 2024-T3.	77
39. SEM micrographs of phosphoric-anodized Al 2024-T3 after electropolish.	78
40. SEM micrographs of phosphoric-anodized Al 2024-T3 after FPL etch.	79
41. SEM micrographs of phosphoric-anodized Al 2024-T3 after FPL etch.	80
42. Plot of $\Delta$ , $\psi$ , SPD and PEE vs number of dips through myristic acid on water, 1588 Å Al/Au/Cr/Glass.	91
43. Plot of $\Delta$ , $\psi$ , SPD and PEE vs number of dips through myristic acid on water, Al 2024-T3.	92
44. Plot of $\phi_{H_2O}$ vs film thickness of myristic acid.	93
45. Plot of $I$ vs film thickness of myristic acid on FPL etched Al 2024-T3.	95
46. Plot of $-\delta\Delta$ , $\delta\psi$ , PEE, $\phi_{H_2O}$ and APPH(C) vs different treated regions of Al 2024-T3 sample.	96

LIST OF ILLUSTRATIONS (cont'd)

<u>Fig. No.</u>	<u>Page No.</u>
47. Plot of $-\delta\Delta$ , $\delta\psi$ , PEE, $\delta(\text{SPD})$ , $\delta\phi_{\text{H}_2\text{O}}$ <u>vs</u> various treated regions of Al 2024-T3.	98
48. Plot of $\Delta$ , $\psi$ , SPD <u>vs</u> number of dips through erucic acid on water. 1588 Å Al/Au/Cr/glass.	101
49. Plot of SPD and $\phi_{\text{H}_2\text{O}}$ <u>vs</u> film thickness of erucic acid on Al/Au/Cr/glass.	102
50. Plot of $-\delta\Delta$ , $\delta\psi$ , PEE and $\delta$ SPD <u>vs</u> number of dips through erucic acid on water, FPL etched Al 2024-T3.	103
51. Change of parameters due to deposition of myristic acid and exposure to UV#1 with plastic cover (left of vertical line). Changes due to exposure to UV#2 (right of vertical line).	107
52. Plot of $\delta\Delta$ , $\delta\psi$ , $\delta$ SPD for SET at 23°C, 95% RH in the UHV system.	113
53. AES before aging in UHV.	116
54. AES after aging 185 hrs in UHV.	117
55. AES after ultra-sonic cleaning in trichlorethylene.	119
56. AES after dipping FPL etched Al 2024-T3 through myristic acid on water.	120
57. AES after dipping three times through myristic acid on water.	121
58. AES of UHV aged sample with PHI cylindrical mirror analyzer.	122
59. Sputter profile of 420 hr UHV aged (97% RH) sample.	123
60. Plot of $\phi_{\text{H}_2\text{O}}$ <u>vs</u> SET at various relative humidities in the UHV chamber.	125
61. Plot of $\phi_{\text{H}_2\text{O}}$ <u>vs</u> SET for samples in glass jars and the UHV chamber at 97% RH.	131
62. Plot of $\phi_{\text{H}_2\text{O}}$ <u>vs</u> SET in glass jars for various relative humidities.	132
63. Plot of SPD <u>vs</u> SET in glass jars for various relative humidities.	133
64. Plot of PEE <u>vs</u> SET in glass jars for various relative humidities.	134
65. Plot of $\Delta$ and $\psi$ <u>vs</u> SET in glass jars for various relative humidities.	135

LIST OF ILLUSTRATIONS (cont'd)

<u>Fig. No.</u>	<u>Page No.</u>
66. AES of sample aged in a glass jar at 58% RH.	137
67. Sputter profile of sample aged in a glass jar at 58% RH.	138
68. AES for the sample aged in a glass jar at 97% RH.	139
69. Sputter profile of the sample aged in a glass jar at 97% RH.	140
70. Plot of $\overline{\phi_{H_2O}}$ vs SET in lab air.	143
71. Plot of $\overline{SPD}$ vs SET in lab air.	144
72. Plot of $\overline{PEE}$ vs SET in lab air.	145
73. Plot of $\overline{\Delta}$ and $\overline{\psi}$ vs SET in lab air.	146
74. AES of lab air aged sample #1.	147
75. AES of lab air aged sample #2.	148
76. Sputter profile of lab air aged sample #1	150
77. Sputter profile of lab air aged sample #2.	151
78. Plot of oxide thickness vs SET for Al 2024-T3 aged in water and water vapor.	155
79. Plot of SPD vs SET for samples aged in water and water vapor.	156
80. Plot of $\sigma_b$ vs BET for adhesive joints in water and water vapor.	162
81. SEM micrographs of degreased Ti-6Al4V	165
82. SEM micrographs of Ti-6Al4V after the phosphate-fluoride treatment (top) and TURCO treatment (bottom).	166
83. SEM micrographs of Ti-6Al4V after the nitric-acid-fluoride treatment (top) and Pasa Jell treatment (bottom).	167
84. SEM micrographs of Ti-6Al4V - HT424 after bond fracture (phosphate-fluoride treatment).	168
85. SEM micrographs of Ti-6Al4V-FM-34B-32 after fracture (phosphate-fluoride treatment).	169
86. SEM micrographs of Ti-6Al4V - HT424 after fracture (nitric acid-fluoride treatment).	171



LIST OF ILLUSTRATIONS (cont'd)

<u>Fig. No.</u>		<u>Page No.</u>
87.	SEM micrographs of Ti-6Al4V - HT424 after fracture (Pasa Jell 107 treatment).	172
88.	SEM micrographs of Ti-6Al4V - HT424 after fracture (TURCO treatment).	173
89.	Plot of light intensity $I$ <u>vs</u> $\cos^2\theta$ for an aluminum mirror and Ti-6Al4V after the nitric acid-fluoride, TURCO and phosphate fluoride treatments.	174
90.	SEM micrographs of phosphate-fluoride treatments as specified at four laboratories.	179
91.	Plot of $\sigma_b$ <u>vs</u> GLT for Ti-6Al4V - HT424.	182
92.	SPD maps for phosphate-fluoride treated Ti-6Al4V.	184
93.	SPD maps for phosphate-fluoride treated Ti-6Al4V.	185
94.	Reflectivity maps for phosphate-fluoride treated Ti-6Al4V.	187
95.	Reflectivity maps for phosphate-fluoride treated Ti-6Al4V.	188
96.	Reflectivity maps for phosphate-fluoride treated Ti-6Al4V.	189
97.	Reflectivity maps for phosphate-fluoride treated Ti-6Al4V.	190
98.	Reflectivity showing macroscopic roughness effect.	192
99.	Computer plots of $\Delta$ and $\psi$ from reflectivity maps (Fig. 94a).	193
100.	Computer plots of $\Delta$ and $\psi$ from reflectivity maps (Fig. 97a).	194
101.	Average values of $\Delta$ and $\psi$ for various map positions of 6 Ti-6Al4V phosphate-fluoride treated samples. <ul style="list-style-type: none"> <li>● corresponds to positions 1,2,3,4</li> <li>▽ corresponds to positions 5,6,7,8.</li> </ul>	196
102.	Plot of $-\delta\Delta$ , $\delta\psi$ , PEE and $\delta(\text{SPD})$ <u>vs</u> number of dips of Ti-6Al-4V through erucic acid on water.	200
103.	Plot of photo current $I$ <u>vs</u> film thickness of erucic acid on Ti-6Al4V.	201
104.	Plot of $\phi_{\text{H}_2\text{O}}$ <u>vs</u> SET for Ti-6Al4V in water and water vapor.	206

LIST OF ILLUSTRATIONS (concluded)

<u>Fig. No.</u>	<u>Page No.</u>
105. Plot of SPD and PEE <u>vs</u> SET for Ti-6Al4V in water and water vapor.	207
106. Plot of $\Delta$ and $\psi$ <u>vs</u> SET for Ti-6Al4V in water and water vapor.	208
107. Plot of $\sigma_b$ <u>vs</u> BET for Ti-6Al4V - HT424 joints in water and water vapor.	210
108. Schematic representation of FPL etched aluminum at three magnifications.	216
109. Schematic representation of an adhesive bond before (top) and after (bottom) cohesive fracture.	218

LIST OF TABLES

<u>TABLE No.</u>		<u>Page No.</u>
1	Single overlap bond strength and $\phi_I$ vs glue line thickness (GLT) for Al 2024-T3 - HT424.	16
2	Effect of GLT on the double overlap bond strength for HT424.	22
3	Effect of GLT on the double overlap bond strength for HT424F without glass carrier.	25
4	Effect of roughness on surface properties.	34
5	Effect of roughness on surface properties and bond strength.	35
6	Wettability analysis.	69
7	Wettability analysis.	70
8	Wettability analysis	71
9	Wettability analysis.	72
10	Physical properties of Al 2024-T3 before and after hydroxide film formation.	82
11	Physical properties of Al 2024-T3 before and after phosphoric acid-anodize and boiling water soak.	83
12	Effect of pre-treatment on anodic films.	85
13	Chemical properties of Al 2024-T3 after various surface treatments.	86 & 87
14	The effect of myristic acid on surface parameters and bond strength.	104
15	Surface parameters after FPL etch and myristic acid treatment.	106
16	Change of surface parameters with exposure to UV lamp #2.	109
17	Effect of myristic acid and UV light on surface parameters and bond strength.	110
18	Aging of FPL etched Al 2024-T3 in a JHV system used as a clean environmental chamber.	114&115

LIST OF TABLES (cont'd)

<u>TABLE No.</u>		<u>Page No.</u>
19	Effect of SET in UHV on bond degradation.	127
20	SET in glass jars with dry O <sub>2</sub> , He and air. Vacuum grease seal.	128
21	Effect of % RH and SET for FPL etched Al 2024-T3, glass jars.	130
22	FPL etch Al 2024-T3, SET in lab air.	141 & 142
23	Effect of 50°C water immersion aging on the surface properties of Al 2024-T3 after the FPL etch.	152
24	Effect of 100°C water immersion aging on the surface properties of Al 2024-T3 after the FPL etch.	153
25	Effect of SET at 100°C, 95% RH on FPL etched Al 2024-T3.	154
26	Effect of SET for various surface preparation and aging of Al 2024-T3.	158
27	Effect of SET in water and water vapor on surface properties and bond strength (Al 2024-T3-HT424, Batch 3, GLT - 0.009").	159
28	BET study of Al 20240T3 - HT424.	161
29	Surface property and bond strength results for various surface treatments of Ti-6Al4V - HT424.	176
30	Ellipsometric results for Ti-6Al4V surfaces that had failed interfacially after various surface treatments and bonding with HT424.	178
31	Surface character and bond strength for Ti-6Al4V - HT424 with various phosphate-fluoride treatments.	181
32	Surface character and bond strengths for various phosphate-fluoride treatments.	183
33	Check of sensitivity and reproducibility of the ellipsometric measurements.	197
34	Effect of solution age on surface character for the phosphate-fluoride treatment of Ti-6Al4V.	199



LIST OF TABLES (concluded)

<u>TABLE NO.</u>		<u>Page No.</u>
35	Effect of SET in the UHV chamber on surface properties of Ti-6Al4V after the phosphate-fluoride treatment.	203
36	Effect of SET at 55°C, 95% RH in glass jars, on surface properties.	205
37	Effect of BET in water vapor and in water for Ti-6Al4V - HT424 (phosphate-fluoride treatment, single overlap joints).	209

## I. INTRODUCTION

### A. The Purpose

The purpose of this research is to identify the physical and chemical characteristics of aluminum and titanium surfaces after standard preparations for adhesive bonding. The relationships discovered between these characteristics and bond strength will help in the design of simpler, less expensive and better processing treatments. A specific objective of our research this period has been to discover the mechanism of degradation (with respect to bond reliability) caused by aging.

Although a few studies have been made to reveal the effect of surface exposure time (SET) and bond exposure time (BET) on bond strength, until very recently little has been known about the chemical and physical changes that cause degradation. The pertinent questions are: what are the characteristics of freshly prepared surfaces that produce strong adhesive bonds and what changes occur to degrade these surfaces with time?

### B. Background

#### 1. Aluminum

In our previous report (AFML-TR-74-73) the following important observations were made with respect to the Al 2024-T3-HT424 system.

a. After surface preparation of Al 2024-T3 with the FPL etch, ellipsometry reveals that the oxide film varies in thickness and structure across the surface. The average

thickness is of the order of 200A with refractive index of  $n \sim 1.8$  close to that for  $\alpha$  alumina ( $n \sim 1.7$ ) but with an effective absorption index much larger ( $k \sim .3$ ) than for  $\alpha$  alumina ( $k \sim 0$ ). The effective absorption index is shown in this report to be related to the surface roughness.

b. Auger spectroscopy and ion-sputter-etching give semi-quantitative chemical profiles of the films formed during surface preparation. Other than the aluminum and oxygen, copper, iron, carbon, nickel and sulfur were detected on the 2024-T3 aluminum after the FPL etch. If chromium was present it was removed by the vacuum system before analysis was begun. Iron segregates to the outer surface of the oxide. Copper segregates into the oxide with a maximum concentration near the central region of the oxide. Nickel segregates to higher concentration in the oxide than in the metal. Silicon is not observed in the FPL etch surface but was markedly noticeable in an area of interfacial fracture. Auger analysis on the adhesive surface that had mated with the FPL etch oxide revealed a large carbon peak as expected but also revealed aluminum, oxygen, nitrogen, copper and traces of iron and magnesium also indicating transfer of oxide to the adhesive and thus failure in the oxide.

c. Microscopy reveals that the FPL etch leaves an aluminum surface with very high density of pit holes with a large spectrum of dimensions. Primer flows into these holes and probably increases adhesion by the hook and latch effect. Failure is observed in the adhesive, in the glass carrier, in the primer and in the primer-metal interface (shown to be in the oxide) for thicker oxide films. Considerable natural porosity is observed in the adhesive.

d. Contact angle measurements provide data for wettability envelopes, which showed that freshly etched 2024-T3 aluminum

alloy is wettable by the HT424 adhesive and primer.

e. Surface aging of 2024-T3 aluminum in humidity chambers causes degradation of the surface (oxide growth and contamination) with associated changes in the ellipsometry, SPD and wettability parameters. The surface degradation results in bond strength degradation. The fraction of the total bond area that fails at the interface ( $\phi_I$ ) increases and the associated bond strength  $\sigma_b$  decreases with Surface Exposure Time (SET).

f. Joint exposure in a humidity chamber causes degradation of the HT424 adhesive and therefore degradation of bonds for 2024-T3 aluminum HT424 joints. The Griffith critical stress analysis from the contact angle and wettability parameters, faithfully predicted that joint exposure in a humidity chamber will cause degradation of the adhesive and interface for the aluminum system but only the adhesive for the titanium system.

g. Surface mapping of 2024-T3 aluminum with respect to ellipsometry and SPD have revealed that these instruments can be used as non destructive testing tools to predict the probable loci of weak bonding prior to the bonding process.

h. It appears that during aging (SET) a structural transformation occurs in the oxide that is produced by the FPI etch. This is reflected in the optical properties. Simultaneous with oxide growth and structural transformation surface contamination can occur with resultant decrease in the polar nature (wettability) of the surface.

Observations from other studies are essentially in general agreement with our conclusions but differ from us and from each

other in some details. Powen<sup>3</sup> comes to the conclusion that the oxide film on FPL etched Al 2024-T3 is 400Å or less and is the hydroxide, boehmite. Weber and Johnston<sup>4</sup> as well as McCarvill and Bell<sup>5</sup> consider the fresh FPL etch oxide film to be  $\gamma$  Al<sub>2</sub>O<sub>3</sub>. The very thin films make it difficult to make conclusive statements as to the hydration state. However, it is generally concluded that aging FPL etched surfaces in humid atmospheres, causes a growth and transformation of the FPL oxide to a hydroxide. For example Pattnaik and Meakin<sup>6</sup>, by sputter time measurements, came to the conclusion that oxide films on FPL etched aluminum are between 100Å and 200Å, in agreement with our sputter time, ellipsometry and photo emission results. They conclude that a layer of amorphous Al<sub>2</sub>O<sub>3</sub> and  $\gamma$ -Al<sub>2</sub>O<sub>3</sub> is formed, but with a thin outer layer of bayerite or boehmite after tap water rinse. Apparently the type of hydroxide and its structural strength depends upon its thickness and conditions of growth. McCarvill and Bell<sup>5</sup> and Powen<sup>3</sup> observed that aging of FPL etched Al 2024-T3 in humid atmosphere, transformed the thin boehmite film to a thicker weak bayerite film which they postulate caused bond degradation. Although Bowen<sup>3</sup>, Bethune<sup>7</sup> and we report that for aged samples, failure is in the oxide, Weber and Johnston<sup>4</sup> establish with ESCA that unaged FPL aluminum surfaces failed in the primer at the primer - metal interface leaving <30Å of primer. It should be noted that our results revealed failure in the oxide for thicker oxides ( ~500Å ) but we have not established this for thinner oxides even after degradation by aging. In this report we conclude that although hydroxide transformations may occur, more subtle processes are also probably involved.

We concluded that the nonuniformity of surface properties caused nonuniformity in bond strength and that the nonuniformity was related to metallurgical nonuniformity rather than surface

preparation. This conclusion is reinforced by the work of Weber and Johnston<sup>4</sup> who discovered that the FPL etch rate was dramatically different on one side of a sample with respect to the other.

Ross et al<sup>8</sup> studied SET aging of Al 2024-T3 and Al 6061-T4 and found that for film adhesives, degradation of FPL surfaces occurred in the first hour then levelled off for 30 day SET. Bond strength actually increases with SET for vapor degreased surfaces. As in our work and that of Minford<sup>9</sup>, Ross et al<sup>8</sup> found bond strengths to decrease for surface preparations in the order FPL, sand or sand blast, vapor decrease.

McCarvill and Bell<sup>5</sup> have studied the effect of time and type of water pretreatment on the bond strength of epoxy - aluminum joints. They conclude that the bond strength of unetched aluminum - epoxy joints induced by tap and distilled water pretreatment at 10°C increased to a maximum, then decreased as a function of immersion time. In distilled water, the maximum bond strength occurs after an immersion time of about 1 hour, after which the bond strength decreases. In the case of tap water pretreatment, the maximum bond strength occurred at about 12 hours of immersion time. The bond strengths at the maxima found for the tap water - pretreated samples were greater than those found at the maxima for the joints pretreated in distilled water. Growth of the hydrated oxide bayerite was proposed as the controlling factor; the bayerite grows more rapidly and less perfectly in distilled water than in tap water.

Although they consider thicker bayerite films to be weak, they believe that thin bayerite films are strong and promote adhesion. The higher bond strength for tap water pretreatment was found to be induced by soluble cations of less than 0.8 Å radius; larger cations had no effect. They postulate that small

soluble cations occupy cationic vacancies in the defect spinel structures of  $\gamma$ - $\text{Al}_2\text{O}_3$  and reduce the negative charge on the surface of the aluminum joints. Joints pretreated in 60°C tap water exhibited higher bond strengths than those pretreated in 60°C distilled water, as the growth of a thick, weak layer of bayerite was inhibited by large anions present in the tap water. Bell and McCarvill<sup>5</sup> also conclude from infrared analysis that no primary chemical bonds are formed between etched or unetched aluminum and an amine - cured epoxy resin, and that roughness slightly increases bond strength.

Vedder and Vermilyea<sup>10</sup> have made a comprehensive study of the reaction of aluminum (and anodized aluminum) with water. They conclude, as do Bernard et al<sup>11</sup> and Hunter et al<sup>12</sup> that the reaction between water and aluminum and water and anodic films on aluminum is essentially the same. The anodic film studied by Vedder and Vermilyea<sup>10</sup> was formed in 1% w/w ammonium borate solution at room temperature at 175 V. According to a review article by Tajima<sup>13</sup> the anodic films formed in ammonium borate are non porous  $\alpha$  alumina. Vedder and Vermilyea<sup>10</sup> conclude that the amorphous natural oxide, or the  $\alpha$  alumina, after anodizing, dissolves in water followed by precipitation of porous aluminum hydroxide (pseudo-boehmite). Pseudo-boehmite is distinguished from crystalline boehmite by its rapid formation and the exhibition of some evidence of crystallinity but a small particle size and a slow rate of crystallization. Vermilyea and Vedder showed that the transformation of amorphous oxide or anodic oxide to pseudo-boehmite is greatly inhibited by phosphate, silicate, arsenate, periodate and tungstate ions, whereas chloride, nitrate, sulfate, bicarbonate and permanganate and acetate ions have little influence and citrate ions accelerates the attack. It may have been this information that prompted Bethune<sup>7</sup> to try phosphoric acid anodize and it is probably the presence of the phosphate ion that protects the anodic film from transformation to a weak porous film of pseudo-boehmite or bayerite.

## 2. Titanium

In our previous report (AFML-TR-74-73) the following important observations were made with respect to the Ti 6Al4V - HT424 system.

a. Standard surface treatments for titanium (as for aluminum) remove the existing surface layer and leave a very rough etched surface covered with a thin ( $\sim 200 \text{ \AA}$ ) oxide film. Examination of a stripped oxide film from Ti 6Al4V with TEM revealed it to be amorphous. However, interference microscopy revealed the stripped film to be considerably thicker ( $\sim 540 \text{ \AA}$ ) than ellipsometric results for unremoved films. There is some question as to whether the stripping process changes the film, since stripping oxide films from FPL etched aluminum produced thick films of completely different character than unremoved films.

b. Auger analysis and profiles of Ti 6Al4V with the phosphate - fluoride treatment revealed, Ti, Al, V, Fe, C, N and O as well as surface contamination P, Ni, S and Cu. If F is present it is masked by one of the Fe peaks. The concentration of O, Cu, Ni, Fe, S and C is larger in the oxide than in the metal. The concentration of Ti, Al and V are lower in the oxide than the metal.

c. Microscopy reveals that Ti-6Al4V - HT424 fails by the various modes as for aluminum but that interfacial failure is at the primer - metaloxide interface rather than in the oxide.

d. Contact angle measurements showed that freshly etched Ti-6Al4V is wettable by the HT424 adhesive and primer.

e. Surface aging of Ti 6Al4V with the phosphate-fluoride treatment does not affect the oxide thickness and negligible



changes in ellipsometry parameters are noted. The fraction of the surface that fails at the interface remains essentially constant with SET as does the bond strength. The wettability parameters do degrade with SET but not sufficient to cause weak bonds.

f. Joint exposure, Bond Exposure Time (BET), in humidity chambers causes degradation of the HT424 as in the aluminum joints.

g. Surface mapping of Ti-6Al4V surfaces was successful in predicting failure loci as for aluminum.

h. Bond strength and surface roughness for Ti-6Al4V decrease in the order phosphate - fluoride, TURCO, nitric acid - fluoride surface treatments. Paul and McGivern, Jr.<sup>14</sup> have also found a direct relation between surface roughness and bond strengths for Ti-6Al4V-FM34. They found a direct relationship between passive film characteristics and bond strength. A dry clean sandblasted surface produced the strongest bonds. Preparation of titanium in acids produced  $TiO_2$  films, in alkaline media  $TiO_2 \cdot H_2O$  films were formed.

### C. The Problem

In view of the above background information, specific questions have arisen. The answers to these questions will considerably expand our understanding of the mechanisms of bond failure and aging degradation and thus fulfill the purpose of this research. The specific questions are:

- a. What relevance have laboratory bond tests to real adhesive joint performance?
- b. What effect has the quality of the adhesive film on bond strength?
- c. What effect does controlled surface roughness have on surface properties and bond strength?

d. Can specific types of hydroxide films and organic molecules be used to calibrate our surface tools in order to understand experimental results for unknown causes of surface degradation?

e. What effect does exposure to ultra violet light have on surface contamination cleaning?

f. What effect does the gas environment have on the aging process? Specifically, will FPL etched Al 2024-T3 degrade with respect to surface energy (increasing contact angles) and bond strength if aged in the absence of organic contamination and/or the absence of water vapor? This question is directly related to the cause of degradation. Is it contamination, hydroxide transformation, some other transformation or a combination of them?

g. Is the effect of aging in liquid water qualitatively similar to aging in humid atmosphere?

h. What are the properties of anodic films formed in phosphoric acid, why do they not degrade as fast as other preparations?

#### D. The Solution to the Problem

To answer the questions posed in C, a better understanding is needed with respect to our surface tools. Each tool, ellipsometry, SPD, PEE, contact angle, AES etc., has generally accepted theoretical and experimental background that can be used for interpretation of experimental measurements. However, it is of importance to make a calibration study of each instrument with known controlled systems that have direct relationship to the unknown systems under study. Therefore, our first study involved preparation of standard Al 2024-T3 and Ti 6Al4V surfaces and then measuring the effect of known films (boehmite, bayerite, organic molecules) on the experimental output of each instrument. This study was carried out in conjunction with our IR&D effort.

To answer the other questions posed in C, carefully planned and executed experiments were performed and these will be described within the text.

#### E. Analytical Procedures

In order to adequately separate the many variables of a bonded joint, an analytical expression for the bond strength  $\sigma_b$ , measured with the Instron tester, can be approximated by the sum of terms for incremental areas  $dA_j$  over the fracture surface,

$$\sigma_b \approx \sum_j \sigma_j dA_j \quad (1a)$$

where  $\sigma_j$  is the average strength in  $dA_j$  at failure.

This approximation becomes increasingly valid as the stress strain curve becomes linear between zero and the point of failure. In most of our work the stress - strain curve was approximately linear to the point of failure so that for our results Eq. 1a is a fair approximation. For total bond area equal to unity  $dA_j/A_T = dA_j = \phi_j$  where  $\phi_j$  is the fractional area of type j. The equation above becomes

$$\sigma_b \approx \sum_j \sigma_j \phi_j \quad (2a)$$

The major regions of the fracture surface are identified as follows:

j	region
m-o	metal-oxide interface
ox	in the oxide
o-p	oxide-primer interface
p	primer
p-a	primer-adhesive interface
g	in glass fiber bundles
v	in void volume
a	in adhesive

If  $\phi_{m-o} + \phi_{ox} + \phi_{o-p} \equiv \phi_I$  and  $\phi_p + \phi_{p-a} + \phi_v + \phi_a \equiv \phi_c$  then Eq. 2 is the same as Eq. 32 of AFML-TR-74-73, where  $\phi_I$  refers to interfacial failure and  $\phi_c$  refers to cohesive failure.

The stress in region  $j$  ( $\sigma_j$ ) can be expressed as the product of a stress intensity factor  $S_j$  which depends upon the mechanical features and a material factor  $M_j$ , which depends upon the physical - chemical properties in region  $j$ . The mechanical features relate to the stress distribution of the test, e.g., the type of test, lap shear, double overlap, butt etc., and the joint structure e.g., the GLT, the glass carrier dimensions, etc.

Failure will commence in the region with the lowest value of  $\sigma_j$  and thus  $\sigma_b$  is a measure of the lowest values of  $\sigma_j$  and will depend upon  $S_j$  as well as  $M_j$  in the region of lowest strength. In order to determine the effect of material properties  $M_j$  on the bond strength other parameters,  $S_j$ , must be held constant. The scatter in  $\sigma_b$  of  $\sim \pm 250$  psi, in our previous report, for identical surface preparations, is shown in this report to be due to variation in  $S_j$  caused by slight differences in GLT in spite of the fact that we attempted to maintain the pressure and temperature in the curing jig at the same values for all experiments. However, most of the changes in  $\sigma_b$  as a function of surface preparation or aging were large enough that averaging of the data revealed the trends. In future work, the GLT should be held constant or the GLT should be measured in each case and  $\sigma_b$  normalized with respect to GLT.

## II EXPERIMENTAL RESULTS

### A. ALUMINUM

#### 1. Relavance of Laboratory Bond Test

It is hoped that laboratory testing of adhesive bonds is directly related to actual performance of real bonded structures. It is therefore pertinent to evaluate various test methods with respect to the similarities and differences between test specimens and real structures. This is very difficult because of the wide variety of conditions that real structures are exposed to. The loading of real structures may be static and only in tension, or only in shear or both, it may be cyclic with high frequency, low frequency, or sporadic, it may be in many different environments, etc.

We have analyzed three types of joints; single overlap, double overlap and butt.

#### 1.1 Single Overlap Joints

In most of our work we have used the single overlap joint. This joint has been the most commonly used in industrial laboratories because it is simple and inexpensive. It has the advantage that both shear and tensile forces are involved as is expected in most real systems. It is of particular advantage in our work because a 1/2" x 1" area is very convenient to prepare and characterize with respect to surface properties. It has the disadvantage that the simplicity in structure increases the complexity of stress analysis.

Figure 1 shows a double overlap joint which becomes a single overlap joint after couple 1-2 fails. When the 2-3 single overlap joint fails, the mating parts are represented in Figure 2. The fractured bond areas in Fig. 2 have all of the features normally observed for a single overlap joint. The top of Fig. 2a and b is the end of the specimen (region D and C1 of Figure 1). Around the bonded area, adhesive flows out during the cure

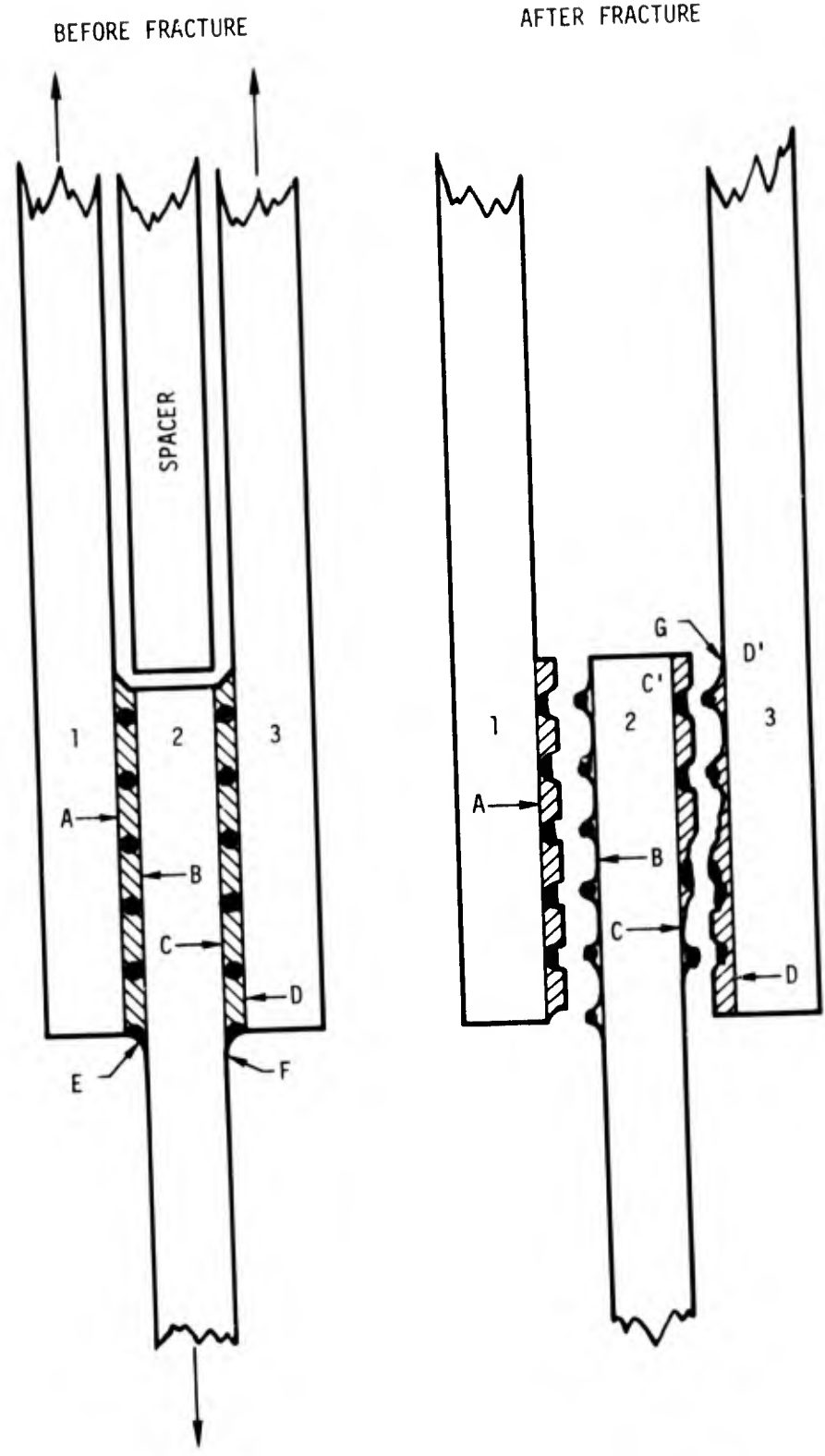
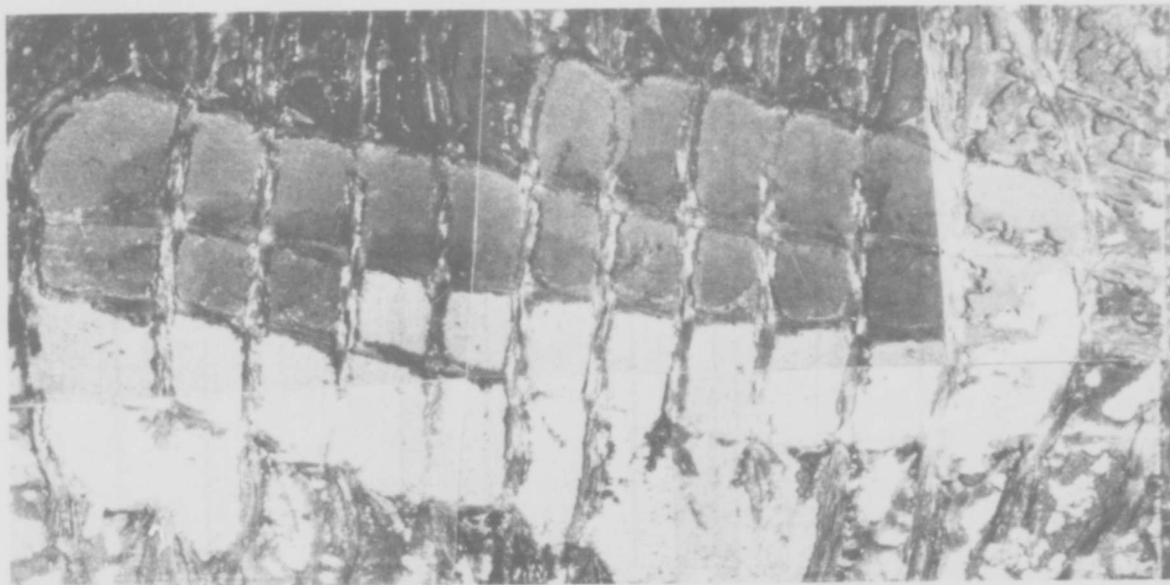
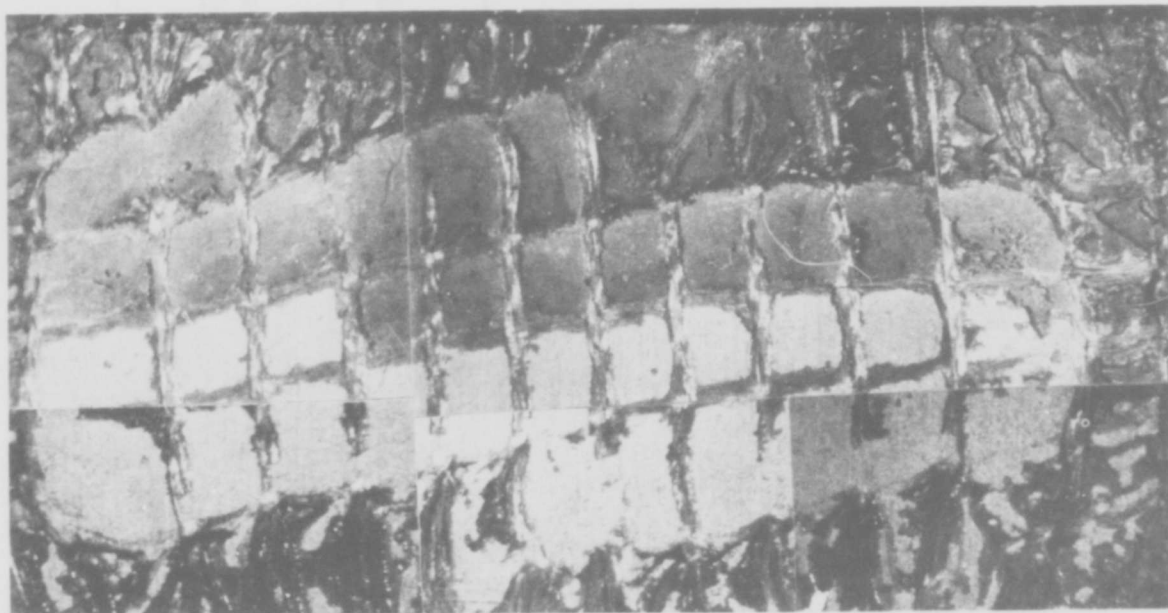


Figure 1. Schematic drawing of a double overlap joint.



a



b

Figure 2 Enlarged photographs of fracture surfaces from the double overlap Al2024-T3-HT424 joint, Couple 2-3 (Fig. 1).

process. The extruded adhesive is full of large pores caused by escaping water vapor formed in the adhesive during the cure. The outer region of the bond area is also full of pores which tunnel into the extruded adhesive and were formed during the escape of water vapor. The inner region of the bond area is divided. The top region, darker in color, is the surface of the adhesive that failed interfacially and the lower half is the surface of the metal that failed interfacially. As pointed out in AFML-TR-74-73 (Fig. 18) the stress distribution is such as to enhance the stress at these regions (C and D1, Fig. 1). Examination of the adhesive between glass fiber bundles in the inner region does not reveal large pores as observed in the outer areas where the gasses could escape. The large pore region in the outer bond area probably simulates regions around rivet holes and along edges of a real structure and are probably somewhat weaker than the inner region. If one is interested in regions away from edges, the single overlap joint may be a poor representation due to the large portion of the bond area near an edge. For this reason, single overlap joints may give low bond strengths as compared to real systems. The porous nature of the outer region will also emphasize access to degrading environments.

#### 1.1.1 Effect of Glue Line Thickness (GLT)

One might expect that the stress distribution is sensitive to the glue line thickness (GLT). Table 1A and Figure 3 show that for a fresh batch of HT424 adhesive (batch 3) the bond strength is directly proportional to and increases with GLT. The bond strength  $\sigma_b$  can be expressed in terms of GLT by the equation

$$\sigma_b \approx 180 \times \text{GLT} + 2210 \text{ (psi)} \quad (1)$$

between GLT ~7 and 10 mils.

At the beginning of the study reported in AFML-TR-74-73 the GLT was expected to be maintained fairly constant by the glass carrier and the significance of the sensitivity to GLT was not



Table 1

SINGLE OVERLAP BOND STRENGTH AND  $\phi_I$  VS GLUE LINE  
THICKNESS (GLT) FOR Al 2024-T3 - HT424

HT 424 from <sup>A</sup>Batch 3

Bond No.	GLT(mils)	$\sigma_b$ (psi)
1	7.0	3470
2	7.2	3500
3	7.9	3630
4	9.5	3900

HT 424 from <sup>B</sup>Batch 1

Bond No.	GLT(mils)	$\phi_I$	$\sigma_b$ (psi)
R12-1	6.5	0.45	3070
2	8	0.10	3260
3	6	0.55	2730
4	8	0.25	3410
5	7	0.15	3340
6	-	0.70	2700
R13-1	7	0.4	3170
2	7.5	0.2	3330
3	8.0	0.15	3300
4	8.0	0.1	3390
5	8.0	0.15	3090
6	7	0.7	2430

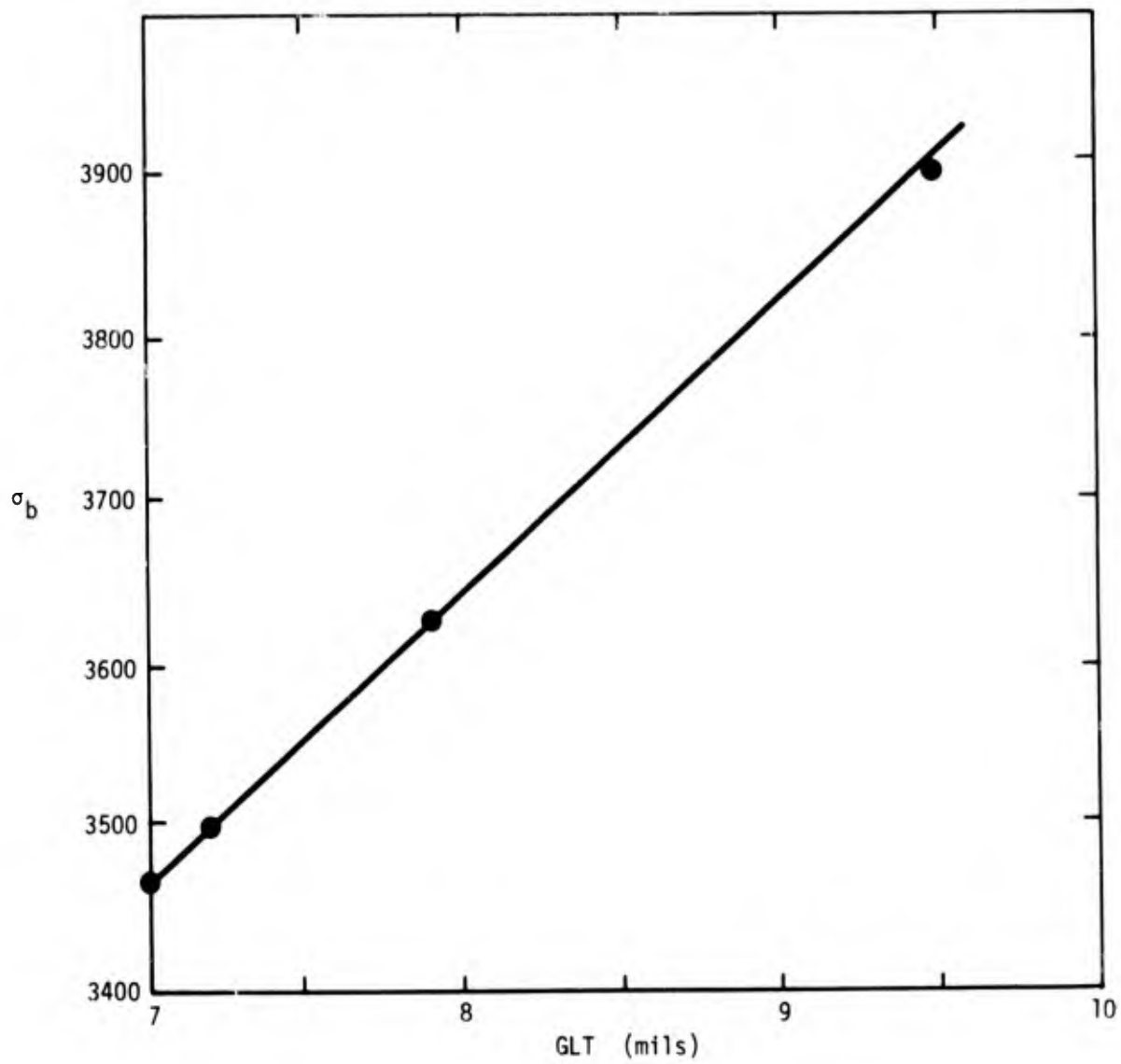


Figure 3. Bond strength vs GLT for Al 2024-T3 - HT424, single overlap joints.

appreciated. After discovering the effect of GLT for batch 3 in the present phase of the study, we measured the GLT for some of the bonds from batch 1 of the earlier study. (Except for a few bonds that have been used for other measurements all of the fractured bonds have been retained.) Table 1 B gives values of  $\sigma_b$  and  $\phi_I$  previously reported in the monthly progress report for October 1, 1972 to October 31, 1972, table 2b, SET = 0 and SET = 2 hours at 54°C and 95% RH. The second column of Table 1 gives the corresponding values of GLT measured in 1975. Although the dashed line through the data in Fig. 4b has the same slope as that in Fig. 3, 180 psi/mil, the intercept at GLT=0 is considerably lower (~0 psi) and the scatter is much greater. The GLT is not the only uncontrolled parameter but is the significant factor that caused the scatter band of about  $\pm 250$  psi in the early work.

Figure 4a demonstrates that the fraction of the bond area that fails at the interface decreases as the GLT increases and approaches zero at GLT  $\approx 9$ . The thicker the adhesive film, the less intensification of stress in regions C and D1 of Figure 1 or the more evenly is the stress distributed. On the other hand, increasing the GLT increases the number of defects in the bond line and therefore the probability of failure in the adhesive at a given stress. It follows that increasing GLT beyond 9 mils will cause  $\sigma_b$  to reach a maximum and perhaps even decrease to the adhesive bulk shear strength. In fact, as will be seen, this occurs for the double overlap bonds if the adhesive has no glass carrier.

## 1.2 Double Overlap Joints

A schematic representation of the double overlap joint is given in Fig. 1. FPL etched Al 2024-T3 was bonded with HT 424 for batch 1. Low power microscope pictures (Figures 2 and 5) of the fracture surfaces reveal a pattern for all bonds. Failure in the reinforced glass matrix is always cohesive, leaving half of the glass on one metal surface and half on the other. Failure

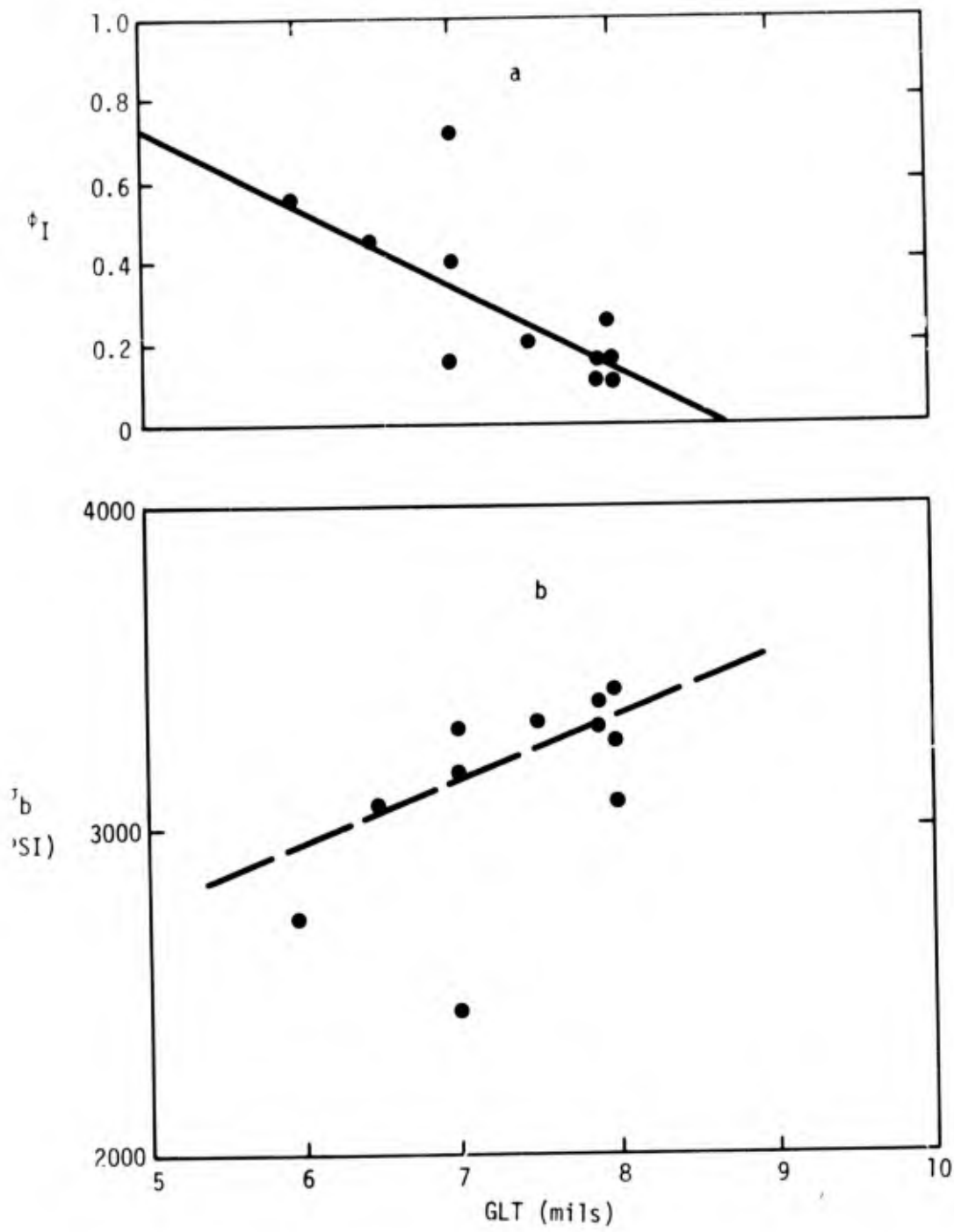
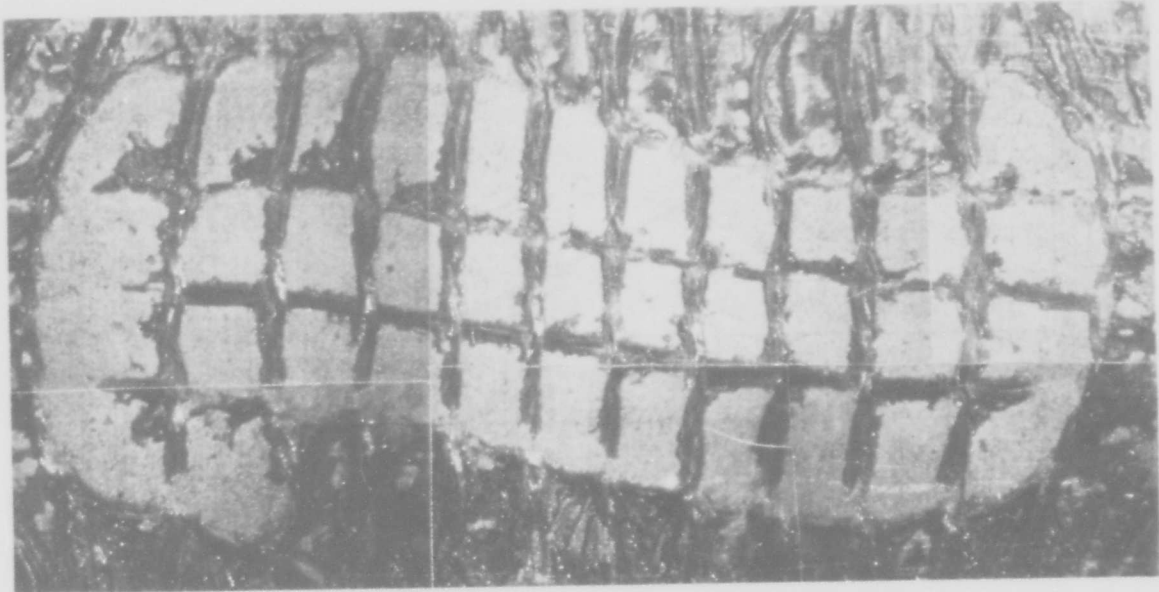
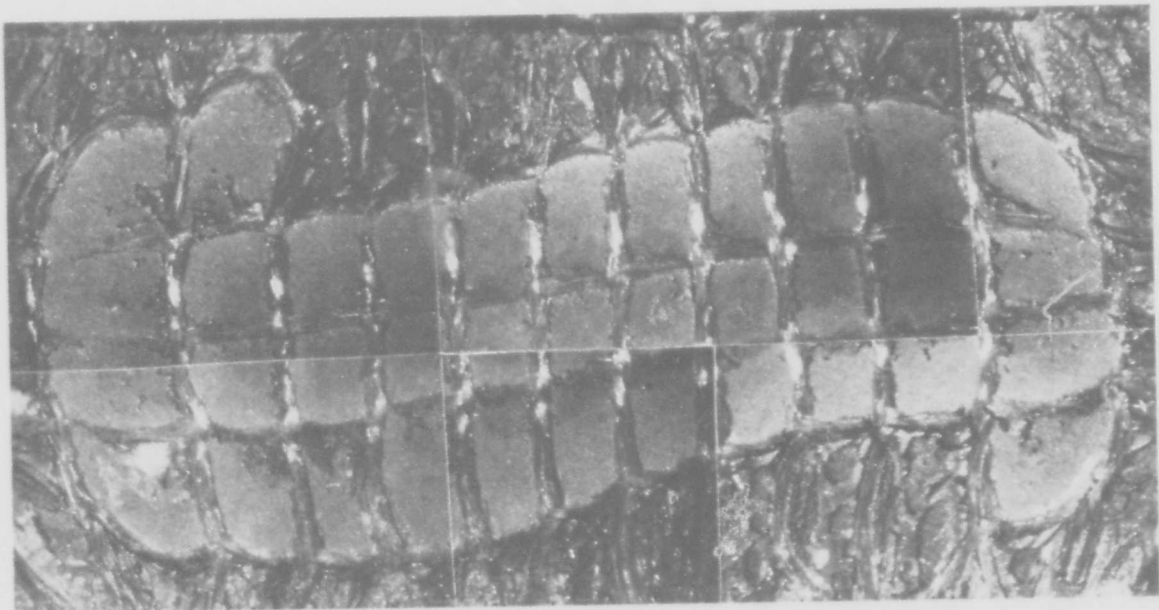


Figure 4. a) Plot of  $\phi_I$  vs GLT,  
 b) Plot of  $\sigma_b$  vs GLT for Al 2024-T3 - HT424 from Batch 1.



D-2 3A2



D-2 3A-1

Figure 5 Enlarged photographs of fracture surfaces from the double overlap Al 2024-T3-HT424 joint, Couple 1-2 (Fig. ).

between one outer plate (surface A Fig. 1) and the center plate (surface B, Fig. 1) is mostly interfacial (except in the glass fibers) at the B surface, leaving the adhesive on the outer plate and half the glass net on the mating side of the center plate. Failure in the regions between the glass net appears to be in the metal oxide. Failure between the other outside plate (surface D, Fig. 1) and the center plate (surface C, Fig. 1) is similar to the normal lap shear couples as in Fig. 2.

Table 2 gives the bond strengths, GLT and  $\phi_I$  values for Al 2024-T3-HT424 with glass carrier. As observed in Fig. 4a  $\phi_I$  is large, averaging  $0.71 \pm 0.09$  for experiment D-1 and  $0.81 \pm 0.04$  for experiment D-2. It is believed that  $\phi_I$  would be unity if it were not for the weak glass carrier and weak porous region at the outer edges. As for the single overlap bonds, stress is concentrated at points E and F in Fig. 1 and failure initiates along the 1-2 or 2-3 bond line depending upon which couple is weakest or which point (E or F) receives the most stress in the Instron tester. Therefore, the measured bond strength is that of the couple that fails first. Because of the stiff nature of the other couple, if failure initiates at point E, the stress is concentrated along surface B. As failure along B is completed, all of the stress is shifted to the 2-3 couple which then can bend as for the normal single overlap joint. Stress is then concentrated at points F and G and failure is promoted along C and D1.

The double overlap bond produces a more constant GLT for a given experimental set. However, the average value of GLT between sets is quite different ranging between 4 and 6 mils for experiments D-1, D-2, D-7 and D-8. A plot of the average bond strengths  $\bar{\sigma}_b$  vs the average GLT is given in Figure 6. From Figure 6 the equation for the double overlap bond strength is

$$\sigma_b \approx 325 \times \text{GLT} + 1725 \text{ (psi)} \quad (2)$$

Table 2

EFFECT OF GLT ON THE DOUBLE OVERLAP BOND STRENGTH  
FOR HT424/Al 2024-T3/FPL ETCH, SET=0.

Exp. Series	Adhesive	Specimen Number							
		1	2	3	4	5	6	Avg.	
D-1	1	$\sigma_b$ (PSI)	3630	3760	3530	3740	3780	3720	3693±76
	No Primer	GLT	6.5	5.5	6	6	6	6	6
	(See sec. 1.2.2)	(mils) $\phi_I$	0.78	0.83	0.69	0.79	0.51	0.67	0.71±.09
D-2	1	$\sigma_b$	3550	3440	3530	3530	3470	3520	3507±34
	Primed	GLT	6	5.5	5	5.5	5.5	5.5	5.5
		$\phi_I$	0.78	0.92	0.83	0.77	0.78	0.81	0.81±0.04
D-7	2	$\sigma_b$	3220	3170	3380	3210	3080	3200	3210±60
	Primed	GLT	4.5	4.5	4.5	5.0	4.0	4.5	4.5
D-8	2	$\sigma_b$	2950	2500	2940				2797±198
	Contaminated PbSO <sub>4</sub> (See sec. 1.2.3)	GLT	3.5	4.0	4.5				4.0

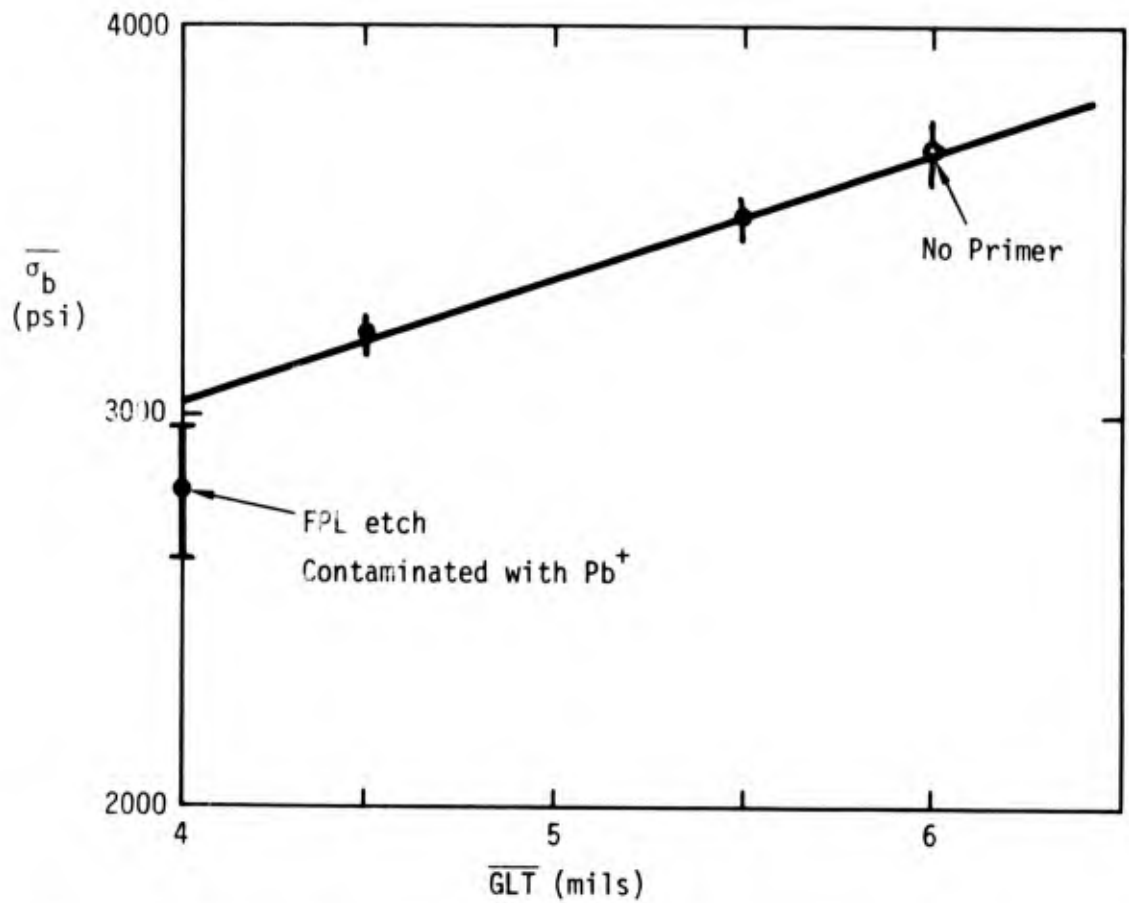


Figure 6. Plot of average bond strength  $\bar{\sigma}_b$  vs average  $\overline{GTL}$  for double overlap joints, HT424/Al 2024-T3. FPL etched and primed ●. FPL etched but not primed ○.



The effect of the GLT is about 1.8 times as large as for single overlap joints. As for the single overlap joints the larger the GLT the smaller the  $\phi_I$ .

### 1.2.1 Effect of Glass Carriers

Table 3 gives bond strengths and GLT for HT424F which is the same as HT424, but without the glass carrier. A plot of  $\sigma_b$  vs GLT is given in Fig. 7. Contrary to bonds with glass carrier, the bond strength decreases with increasing GLT according to the equation

$$\sigma_b \approx -100 \times \text{GLT} + 3150 \text{ (psi)}. \quad (3)$$

The obvious difference between the fractured HT424F adhesive and the HT424 adhesive seen in Fig. 8 is the large void volume ( $\phi_v \sim .6$ ) of the glass free (HT424F) adhesive. The fraction that fails cohesively is  $\phi_c \sim .35$  and the fraction that fails interfacially is  $\phi_I \sim 0.05$ . The line in Fig. 7 extrapolates to  $\sigma_b \sim 3100$  psi at GLT = 0. If the actual shear strength of the adhesive is  $\sigma_s$  then the bond strength  $\sigma_b$  is

$$\sigma_b \approx \phi_c \sigma_s \quad (4)$$

where  $\phi_c \sim 0.35$  and  $\sigma_b \sim 3100$  psi. The approximate shear strength is

$$\sigma_s \approx 8900 \text{ psi}. \quad (5)$$

With the stress concentrated along surface B (Fig. 1) with the double overlap joint, increasing the GLT only increases the probability of failure at a given stress. The water vapor formed during the cure cycle cannot escape whereas for the glass carrier film it can. It is concluded that the glass carrier acts as channels of easy vapor flow out of the bond, as noted by the large porosity in the outer bond regions as in Figs. 2 and 5. By the same token they should act as easy access to degrading environments, such as water vapor. We have not made any aging experiments on the glass free adhesive to check if the lack of the glass inhibits degradation.

Table 3

EFFECT OF GLT ON THE DOUBLE OVERLAP BOND STRENGTH FOR  
 HT424F (WITHOUT GLASS CARRIER)/Al 2024-T3/FPL SPECIMENS SET=0  
 WITH AND WITHOUT CONTAMINANTS IN ETCH

Exp. Series	Adhesive Batch		Specimen Number						Avg. $\sigma_b$
			1	2	3	4	5	6	
D-3	2a	$\sigma_b$ (PSI)	2830	2910	2850	3070	2910	2840	2902±62
		GLT	4.5	5	3	2	1.5	2	
D-4	2a	$\sigma_b$	2530	2160	2640				2443±190
		GLT	8	10	5				7.7
D-5	2a	$\sigma_b$	2570	2400	2460				2477±62
		GLT	4	8.5	7				6.5
D-6	2a	$\sigma_b$	2600	2810	2800				2737±91
		GLT	8	6	6				6.7

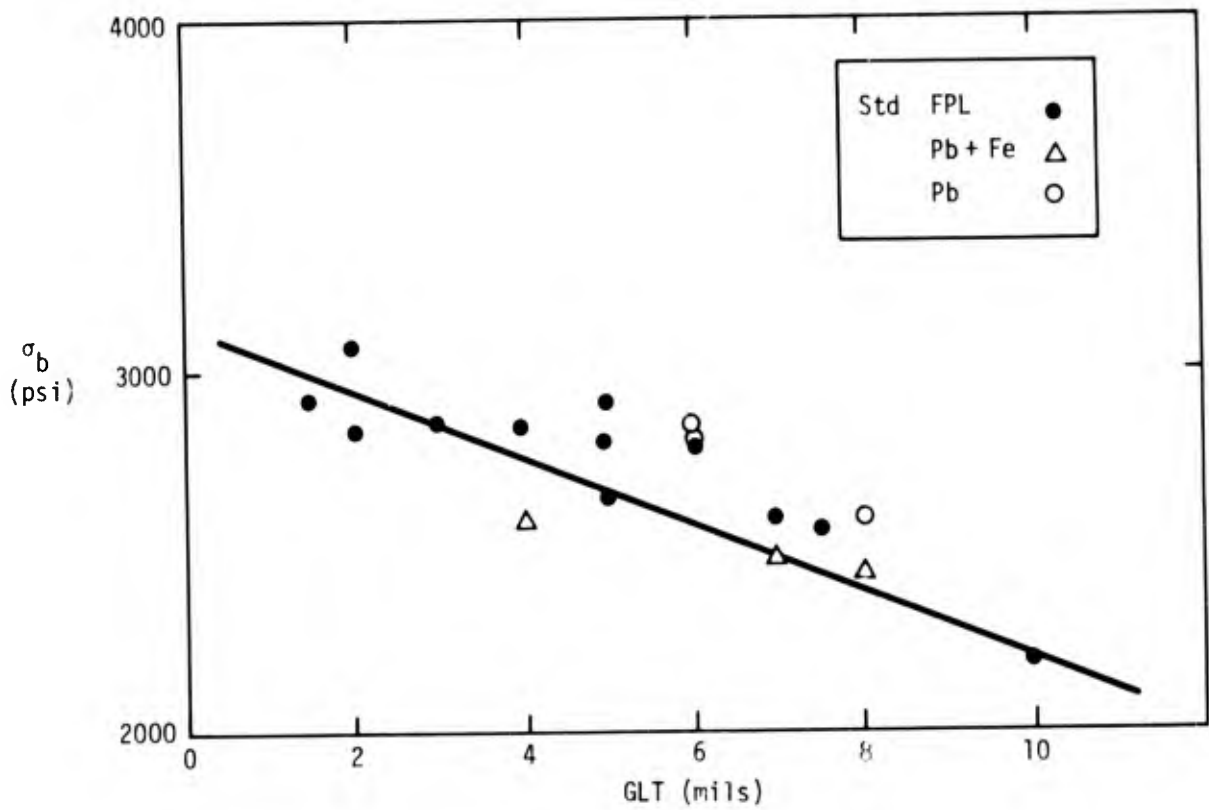


Figure 7. Plot of  $\sigma_b$  vs GLT for double overlap joints with HT424 F (no glass carrier).

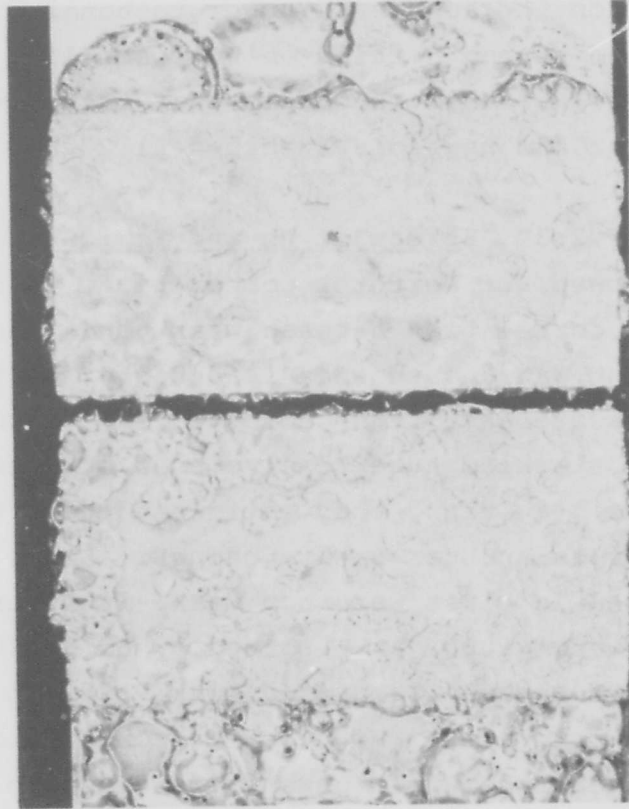


Figure 8 Photograph of fracture surfaces of Al 2024-T3-HT424F with no glass carrier.

### 1.2.2 Effect of Primer

Experiment D-1 in Table 2 was performed without putting HT424 primer on the adherents prior to bonding. Since the resultant bond strength falls on the same line as for those with primer in Fig. 6, it is concluded that the primer had little if any effect for the unaged FPI etched Al 2024-T3.

### 1.2.3 Effect of Pb and Fe ions

E. B. Bowen, of Northrop Corporation, told me that they had discovered a correlation between weak bonds and aged FPL etchant if the etchant was stored in a lead tank. If the etchant was stored in glass beakers, the bonds were of normal strength. In the process of making Auger analysis of samples that had been etched in the lead tank, they estimated the film thickness to be  $\sim 2000\text{\AA}$  (by ions sputter back etching). Since the bonds with samples etched in glass were not weak, it is presumed that the oxide films were  $<2000\text{\AA}$  as reported by us ( $\sim 200\text{\AA}$ ). We etched samples in FPI etchant saturated with  $\text{PbSO}_4$  in order to simulate etchant in a lead tank. However, the oxide films formed in this solution had ellipsometric parameters close to films formed without the  $\text{PbSO}_4$ . Double overlap joints were made with glass carrier free HT424F and with HT424 from Batch 3. During experiment D-5, Table 2, the stirring magnet broke open allowing the iron to contaminate the solution. The experiments were repeated with Pb ion but no Fe ion contamination (D-6, Table 3). The experiment was repeated but with HT424 rather than HT424F (D-8, Table 2). It is apparent that we have not simulated the condition of Bowen's solution from the lead tanks producing thick oxide and weak bonds. However, in Fig. 7, Pb+ contamination gives higher  $\sigma_b$  values than the standard FPL etch and Pb+Fe gave lower values. A more systematic study is needed to establish if these differences are significant.

### 1.3 Butt Joints

Three butt joints were made between the 0.063"x1" ends of six 2 1/2"x1"x.063" Al 2024-T3 samples. After priming the ends of the samples, they were placed in a jig and a film of HT424 adhesive was placed between the primed ends. Curing was done in the jig with a pressure of 50 psi. The bond strengths were 9360 psi, 9472 psi and 9296 psi yielding an average strength of 9376±64 psi. The tensile strength is of the order of the shear strength from double overlap bonds. Examination of the fractured bonds revealed mostly cohesive failure and very little void volume. The disadvantage of these particular butt joints is the small area 0.063 square inches which make surface property measurements more difficult and accentuates edge effects even more than the overlap specimens.

## 2. The Effect of the Adhesive

### 2.1 Pin Holes

Figure 9 shows photographs of a piece of adhesive from Batch 3 (left) and Batch 2 (right). It is obvious that the size of pin holes in the piece from Batch 2 are much larger than from Batch 3. It was thought that the number and size of the pin holes was the cause of lower bond strengths for the larger pin hole samples (Batch 2) and that the samples with larger pin holes might differ in weight from the other. However, it was found that areas from Batch 3 also had larger pin holes and that both batches met the specification of 0.135 #/sq. ft.

To see if areas of adhesive that had pin holes would have weaker bond strength than areas that did not have pin holes, an opacity meter was constructed. Film samples with no pin holes and samples with a large number of pin holes were cut slightly larger than 1"x1/2" and placed in a holder with a 1"x1/2" window. The adhesive was exposed to a small lamp on one side and to a light sensitive diode on the other to obtain a signal proportional to the pin hole area. The adhesive film was then cut from the holder and bonded between Al2024-T3 FPL etched

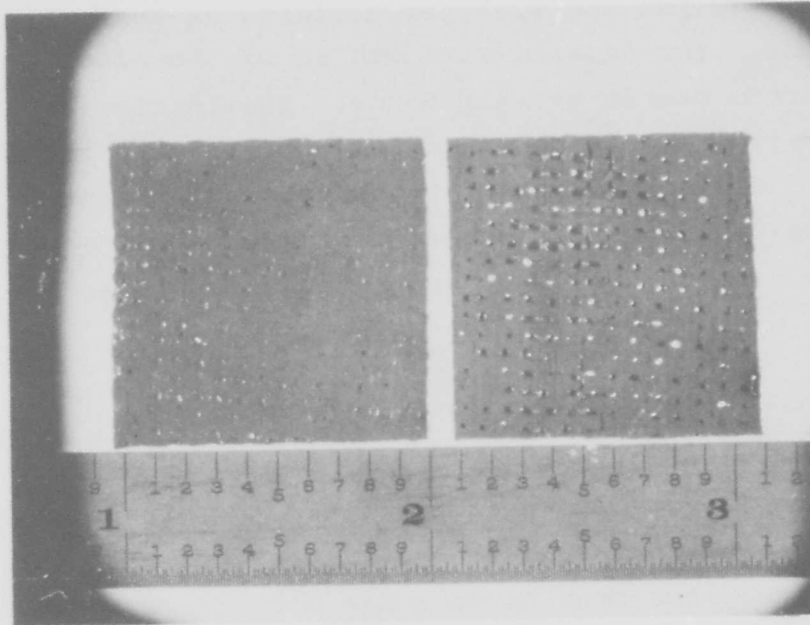


Figure 9 Photograph of HT424 Adhesive Batch 3 (left side),  
Batch 2 (right side).

adherends. No correlation was evident between bond strength and pin hole area.

## 2.2 Aluminum Powder Filler

Experiments were performed with HT435 adhesive which has the same polymer as HT424 but no aluminum powder filler. The glass carrier was a finer mesh with smaller diameter fiber bundles. The weight was 0.05 #/sq. ft., the film was 8 mils thick. With the same cure cycle as for HT424 the GLT proved to be 3 mils with resultant low bond strength. An average bond strength for six bonds was 1655±25 psi. Figure 10 is photographs of the fracture surfaces. Low power microscope examination revealed a large void volume between the glass net, that also reduced the bond strength. Because of these features, the effect of the aluminum powder is undetermined.

## 2.3 Effect of Adhesive Aging

The adhesives were kept under refrigeration and no noticeable change was noted with aging except for Batch 2. The first bonds formed with adhesive from batch 2 had average bond strengths of 3210±60 psi (D-7 Table 2). Six months later, the average bond strength at the same GLT (~7 mils) had dropped to 2840±130 psi at approximately 7 mils GLT. The cause of the adhesive film degradation is not known.

## 3. Effect of Controlled Roughness on Surface Properties and Bond Strength

To see the effect of controlled roughness on surface properties a sample was mechanically polished with 600 grit paper and then electropolished, in 3/2 by vol. MeOH/HNO<sub>3</sub>, for 5 minutes at 20 volts. The sample was then exposed to FPL etch solution for various periods but without the usual preliminary alkaline clean since the alkaline cleaning process produces very rough surfaces. Each time the sample was removed from the FPL etch and





Figure 10 Photographs of fracture surfaces of Al 2024-T3-HT435 with no aluminum powder filler.

rinsed the surface parameters were measured. The results are recorded in Table 4.

Thirty Al 2024-T3 samples were electropolished and exposed to the FPL etch solution for 0, 2, 13, 28 and 60 minutes to produce increasingly rough surfaces. These surfaces were characterized with SEM, ellipsometry, light scattering, SPD, PEE and water contact angle measurements. Two of each preparation were then primed and bonded. To obtain even smoother surfaces than that from electropolishing, six samples were polished with 600 grit, hand polished with "Wenol" metal polish, detergent cleaned and rinsed with distilled water. The average surface properties of these samples and resultant average bond strengths are given in Table 5. The adhesive was HT424 from Batch 2 with average bond line thickness of 8.5 mils. Another set of samples was prepared by first electropolishing and then exposing to FPL etch but these were bonded with HT424 from batch 3, average GLT of 10 mils. The surface parameters and average bond strengths are given in Table 5.

Figures 11, 12 and 13 show SEM pictures that correspond to the first set of samples in Table 5 for 0, 2, 13, 28 and 60 minutes of FPL exposure. The number to the left of the white line at the bottom of the pictures indicates the length of the line in microns. The numbers below this refer to the magnification, accelerating voltage, working distance and picture number. For example the length of the white line in Figure 11, top left is  $10\mu$ , the magnification is X500, the voltage is 20.0 KV, the working distance is 11 mm and the picture number is 002 305. The pictures at the right in Figures 11, 12 and 13 were of the same sample area but of higher magnification. After the electropolish the surface appeared fairly smooth. Increased exposure to FPL etch causes pitting and grain boundary attack until after 60 minutes the entire surface is etched and none of the original flat area can be observed.

From light scattering experiments the smoothest surfaces were the hand polished samples with the rms roughness of  $0.059\mu$  as compared to  $0.11\mu$  after electropolishing and  $0.6\mu$  after 60 minutes of FPL etch. It should be noted that the light scattering measures roughness on a scale much lower than can be observed in the SEM pictures except for the smallest resolvable roughness in Fig. 13c.

Table 4

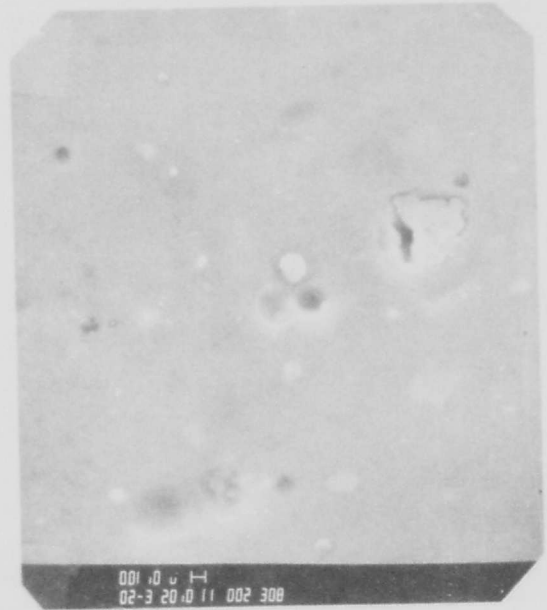
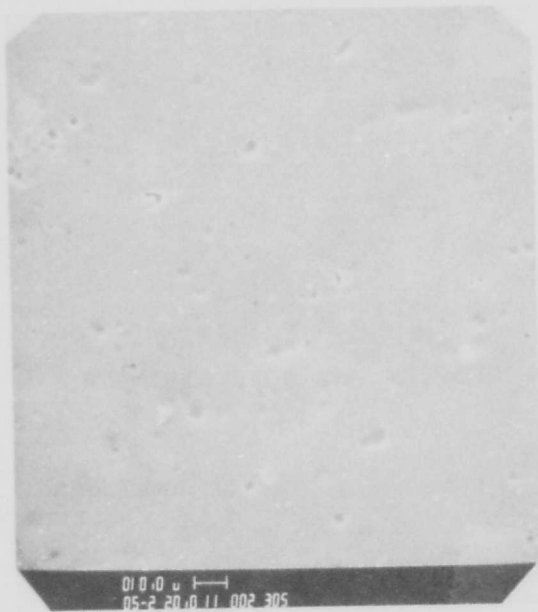
## EFFECT OF ROUGHNESS ON SURFACE PROPERTIES

FPL etch Time	$\Delta$	$\psi$	$-\delta\psi$	SPD	PEE	$\phi_{H_2O}$	Roughness $\sigma$
(min)	(deg)	(deg)	(deg)	(volts)	(amps $\times 10^{-11}$ )	(deg)	( $\mu$ )
0	134.7	40.6	1.2	0.94	27	67	0.111
0.5	118.2	39.8	2.0	0.68	14	11	0.127
1.0	115.4	38.8	3.0	0.48	63	5	0.137
2	111.1	39.0	2.8	0.56	29	4	0.123
4	117.4	38.3	3.5	0.49	57	3	0.140
8	115.3	38.0	3.8	0.48	42	5	0.131
13	117.1	36.9	4.9	0.44	58	1	0.218
18	117.9	36.1	4.7	0.50	76	1	0.224
23	118.5	35.5	5.3	0.37	72	1	0.258
28	123.9	33.7	7.1	0.96	350	1	0.311
33	123.7	33.5	7.3	0.70	140	1	0.328
40	126.7	31.9	9.9	0.90	230	1	0.382

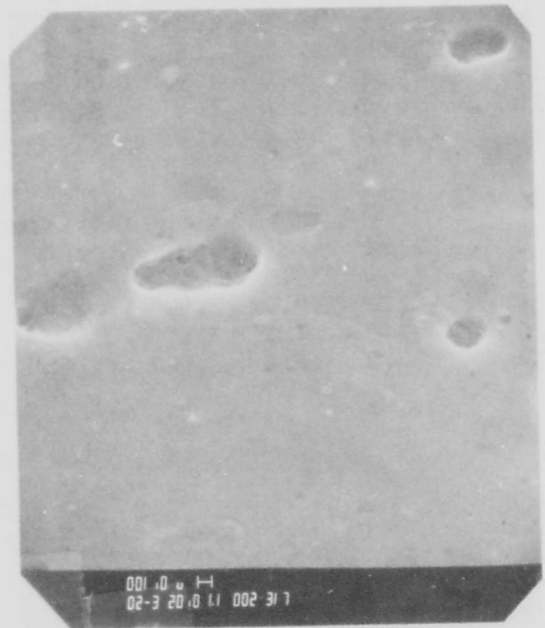
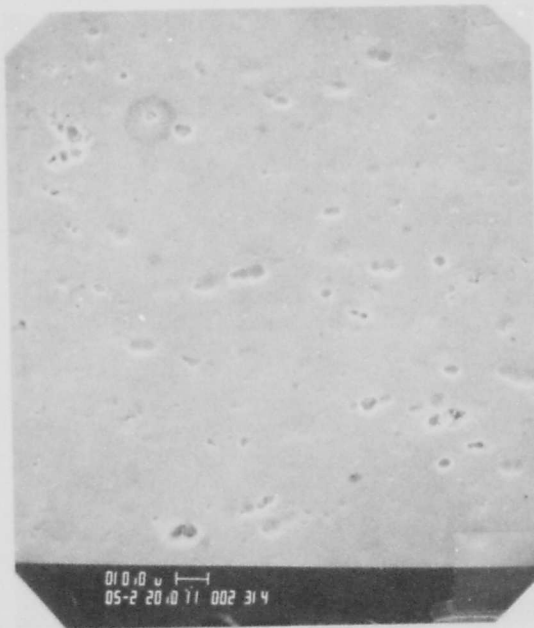
Table 5

## EFFECT OF ROUGHNESS ON SURFACE PROPERTIES AND BOND STRENGTH

FPL etch time (min)	$\Delta$ (deg)	$\psi$ (deg)	$-\delta\psi$ (deg)	SPD (volts)	PEE (amps $\times 10^{-11}$ )	$\phi_{H_2O}$ deg	Roughness $\sigma$ ( $\mu$ )	Bond Strength Psi
HT424 from Batch 2								
0	Mechanical hand Polish					54	0.059	2400 $\pm$ 110
0	136.1	40.8	1.0	1.14	95	25	0.111	2690 $\pm$ 90
2	112.0	39.0	2.8	0.46	50	10	0.159	2867 $\pm$ 80
13	117.1	36.9	4.9	0.49	51	8	0.154	2947 $\pm$ 136
28	120.5	33.4	7.4	0.72	147	6	0.337	2880 $\pm$ 147
60	110.1	34.0	6.8	0.32	2	8	0.570	2810 $\pm$ 107
HT424 from Batch 3								
0	129.2	41.8	0	0.46	0.1	46		3800
5	113.4	38.7	3.1	0.43	5.5	23		3770
10	112.3	38.9	2.9	0.54	5.1	10		3700
20	113.5	37.2	4.6	0.62	34.0	11		3700
30	112.9	36.8	5.0	0.65	30.0	16		3900

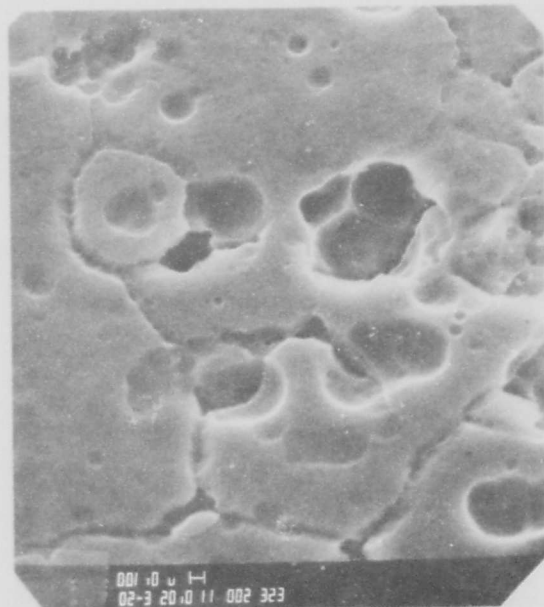
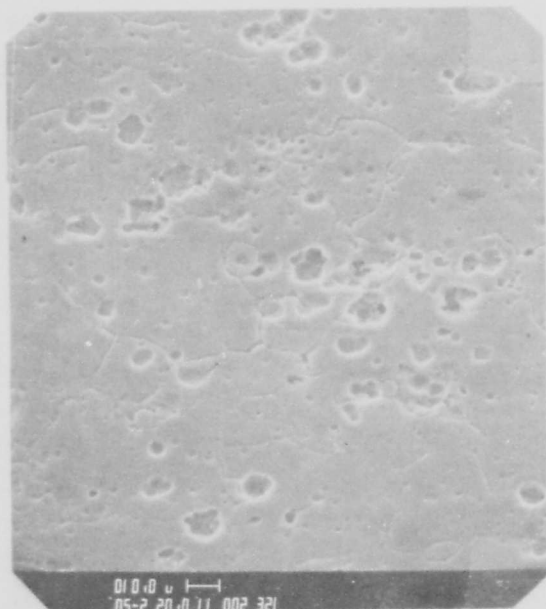


Electropolish

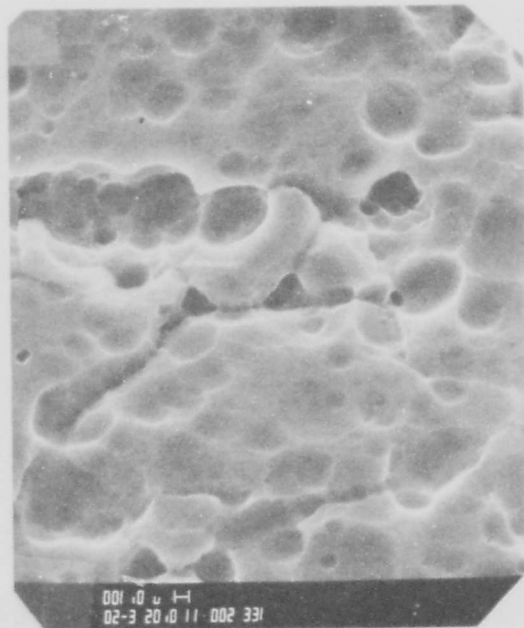
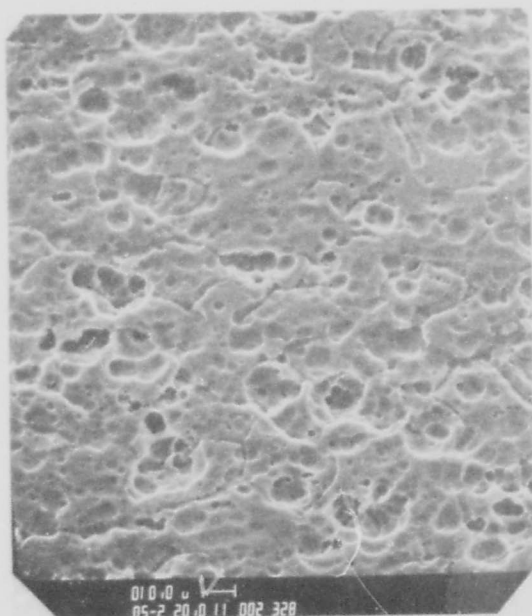


Electropolish + FPL etch 2 min.

Figure 11 SEM pictures of Electropolished Al 2024-T3 (top),  
electropolish + 2 min FPL etch (bottom).

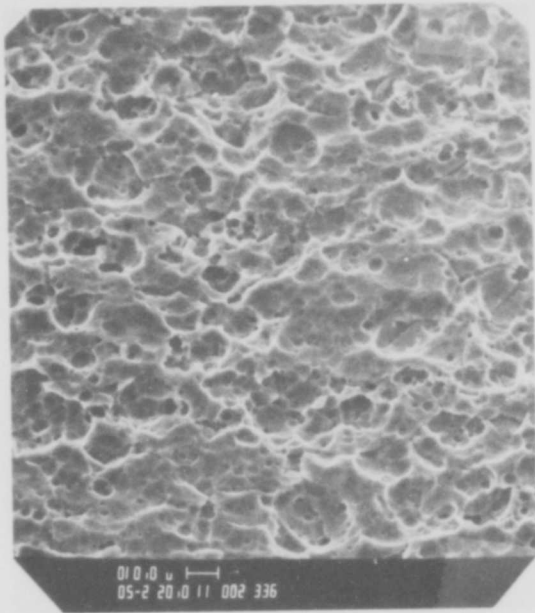


FPL etch 13 min.

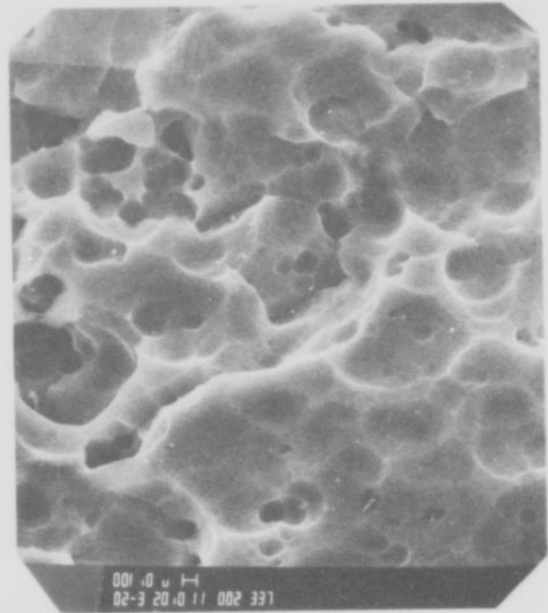


FPL etch 28 min.

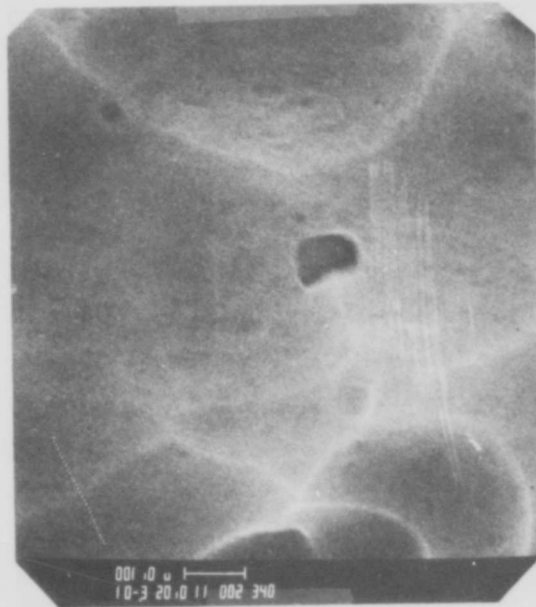
Figure 12 SEM pictures of electropolished Al 2024-T3 + 13 min. FPL etch (top), + 28 min FPL etch (bottom).



a



b



c

Figure 13 SEM pictures of electropolished Al 2024-T3 + 60 min FPL etch.

The ellipsometric parameters  $\Delta$ ,  $\psi$ , the photo emission and the surface potential difference are plotted in Figure 14 vs FPL etch time. The open triangles are for the set of separate samples in Table 5 and the solid points are for the single sample in Table 4. The oxide film thickness at the right ordinate is estimated from the  $\Delta$  values. After the electropolish, the film is about 40 Å thick but immediately increases to about 200 Å after 2 minutes FPL etch. The PEE and SPD follow the same trend as  $\Delta$  or film thickness. As will be seen the attenuation of photo emitted electrons is greater for organic contamination than for oxide (e.g., attenuation index  $\sim 12.6$  Å for myristic acid, as compared to 25 Å for oxide). Consequently the PEE is low at zero FPL etch time even though the film thickness is very low. The FPL etch removes the organic contamination but leaves a thicker oxide film. As the oxide film decreases in thickness with increased etching the PEE increases due to less oxide attenuation. The removal of the organic contamination and formation of a thicker oxide film by the FPL etch increases the work function (decreased SPD). Thinning of the oxide film with FPL etching decreases the work function (increases SPD).

The roughness factor  $\sigma$ , the change in  $\psi$  from the value it would have for a smooth surface,  $\psi'$ , and the water contact angle are plotted in Figure 15 vs FPL etch time. The roughness factor  $\sigma$  is approximately linear with respect to FPL etch time. Except for the first two minutes and at 60 minutes -  $\delta\psi$  is also approximately linear with FPL etch time showing its direct relationship to roughness. However,  $\psi$  is also related to film thickness and reflects the large changes at etch time 0 and 60 minutes. The contact angle drops rapidly as the FPL etch removes the organic contamination and remains near zero between 2 and 60 minutes of FPL etch.

The bond strengths for the samples bonded with HT424 from batch 2 (solid points with mean scatter bars) and from batch 3 (open squares) are plotted vs the roughness factor -  $\delta\psi$  in



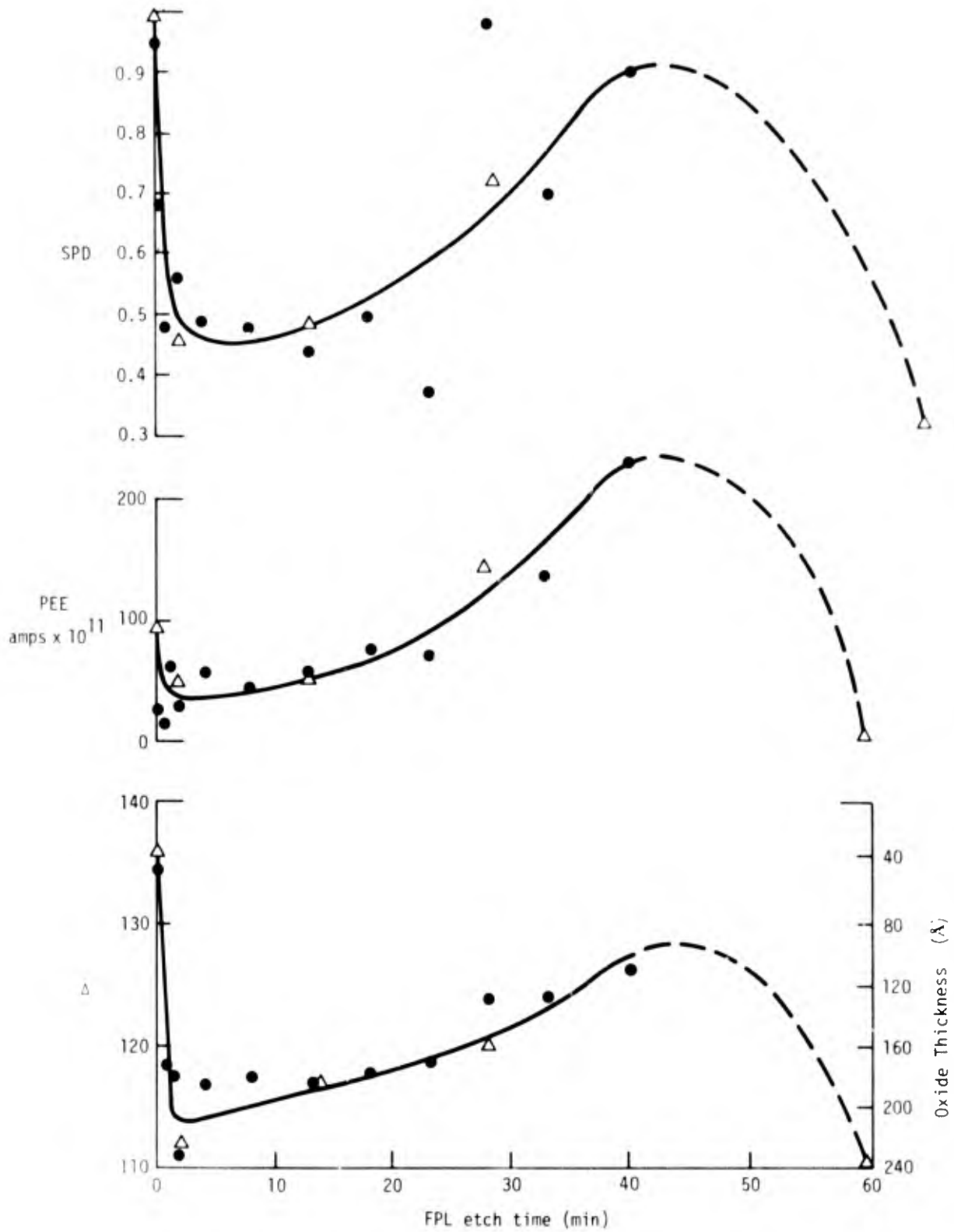


Figure 14. Plot of  $\Delta$ , PEE and SPD vs FPL etch time.

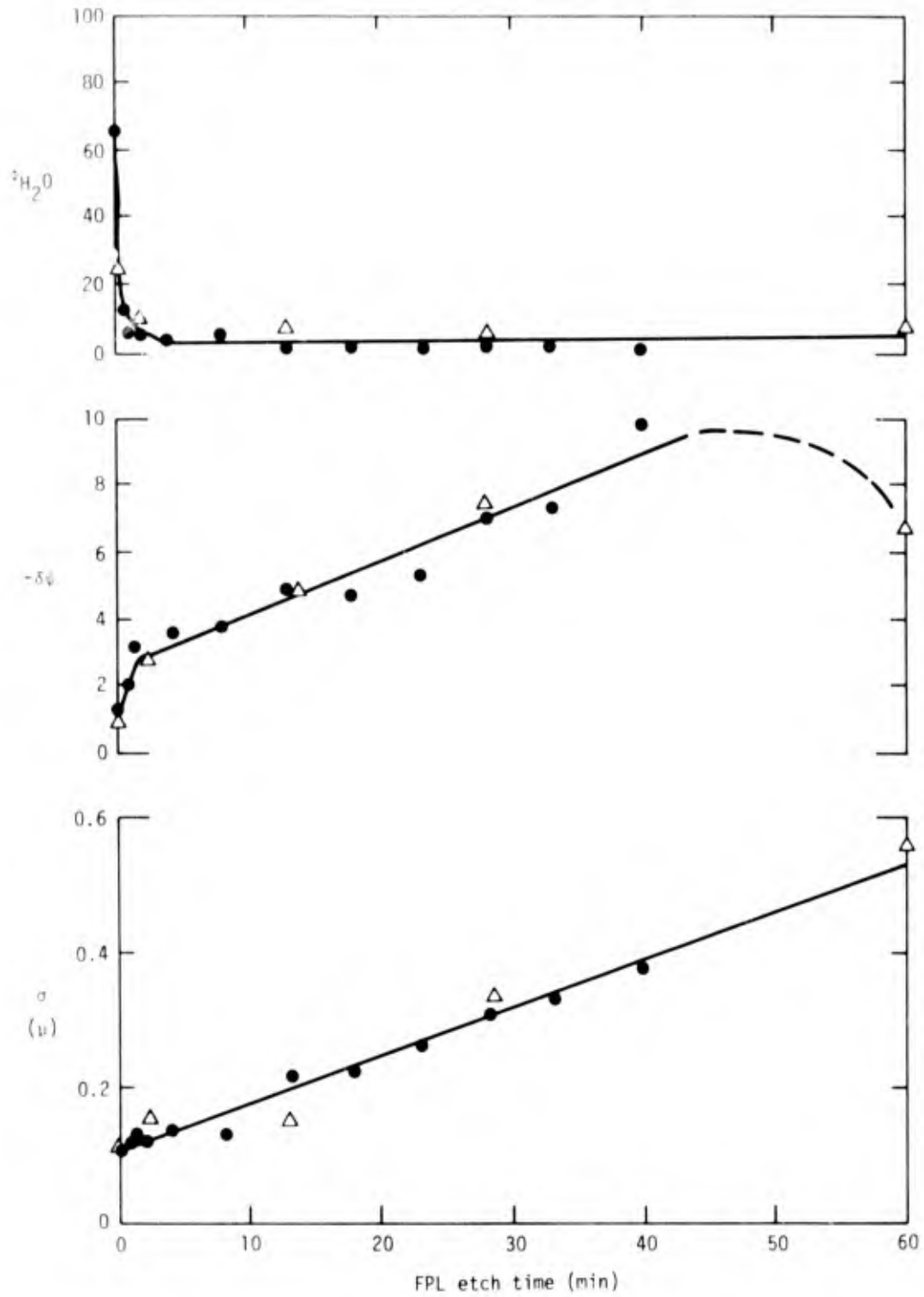


Figure 15. Plot of rms roughness  $\sigma$ ,  $-\delta\psi$  and  $\phi_{\text{H}_2\text{O}}$  vs FPL etch time.

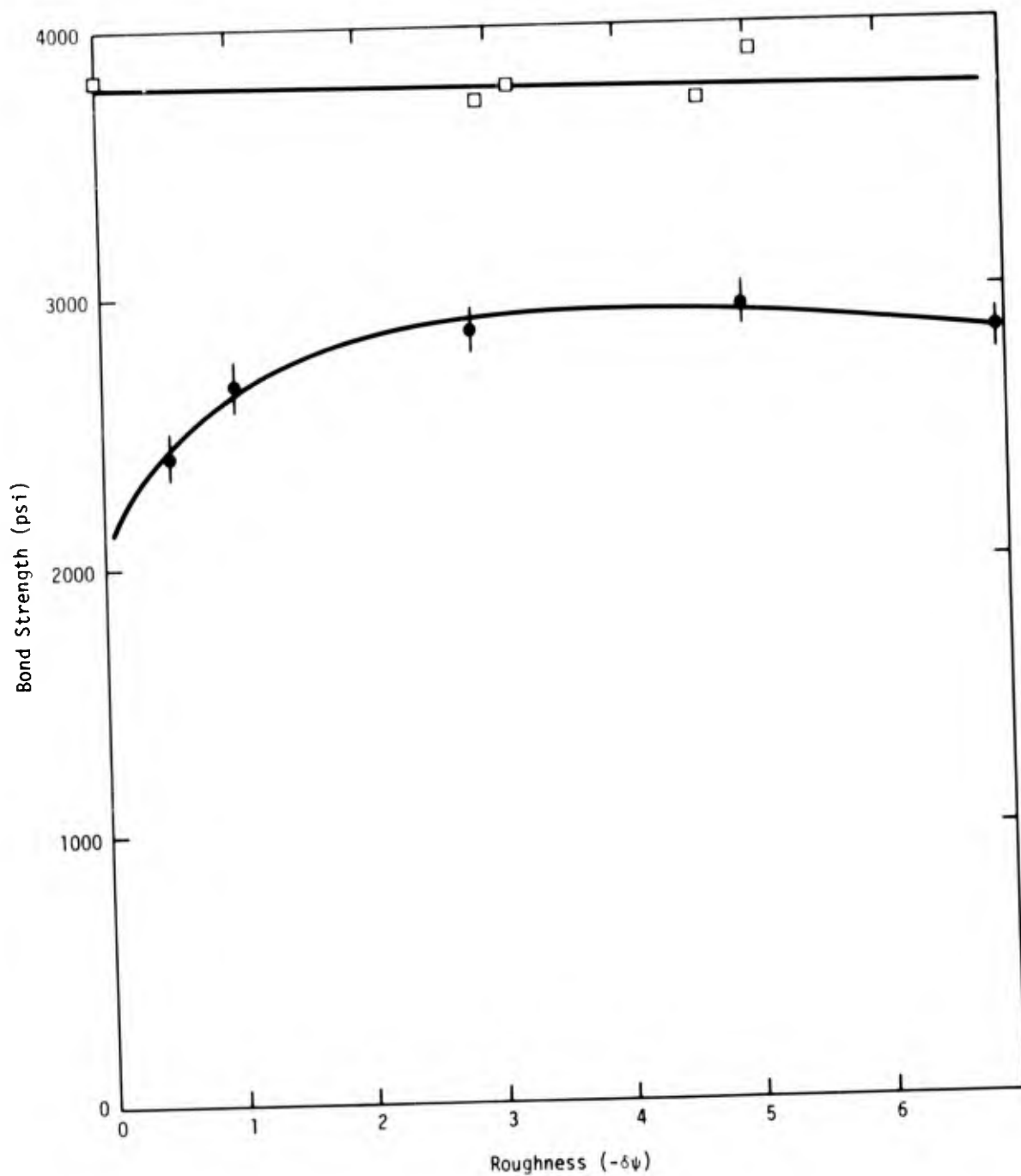


Figure 16. Plot of bond strength vs ellipsometric roughness ( $-\delta\psi$ ).

Figure 16. The adhesive from batch 3, with GLT 8-10 mils gives higher bond strengths, fails primarily cohesively and shows no effect of surface roughness. On the other hand, the adhesive from batch 2 with the thinner bond line thickness (~7 mils) promotes failure at the interface and increases with roughness for smoothest samples. However, there is a direct correlation between bond strength and  $\psi_{H_2O}$  as seen in Fig. 17, indicating that over the range of roughness 0.059 to 0.57 the roughness probably has no effect on bond strength.

We have established that gross roughness has little if any effect on bond strength. More experiments are needed, for which the contact angle is maintained near zero as the surface is roughened, to establish the effect of roughness as the surface approaches a mirror smoothness.

#### 4. The Effect of Controlled Hydroxide Films

In the background section various authors have suggested that aging FPL etched Al 2024-T3 in humid atmospheres causes the transformation of the oxide film from a strong hydrated oxide (boehmite) to a weak bayerite. Also, the anodic film from anodizing in phosphoric acid is strong and does not degrade in humid atmospheres even with the bonds under stress. This is considered to be due to the anodic formation of a strong boehmite film that resists transformation to a weak bayerite. It is known<sup>10</sup> that aluminum, exposed to water below 60°C, forms a layer of bayerite, whereas aluminum exposed to water at 100°C forms a layer of boehmite. We therefore have prepared films that are known to be boehmite and bayerite to answer three questions; a) do either of these films cause degradation with respect to surface energy (i.e., increased contact angles)? This is an important question because aging FPL etched Al2024-T3 does cause a degradation in surface energy and a corresponding degradation in bond strength. b) Are these hydroxide films, formed in water,

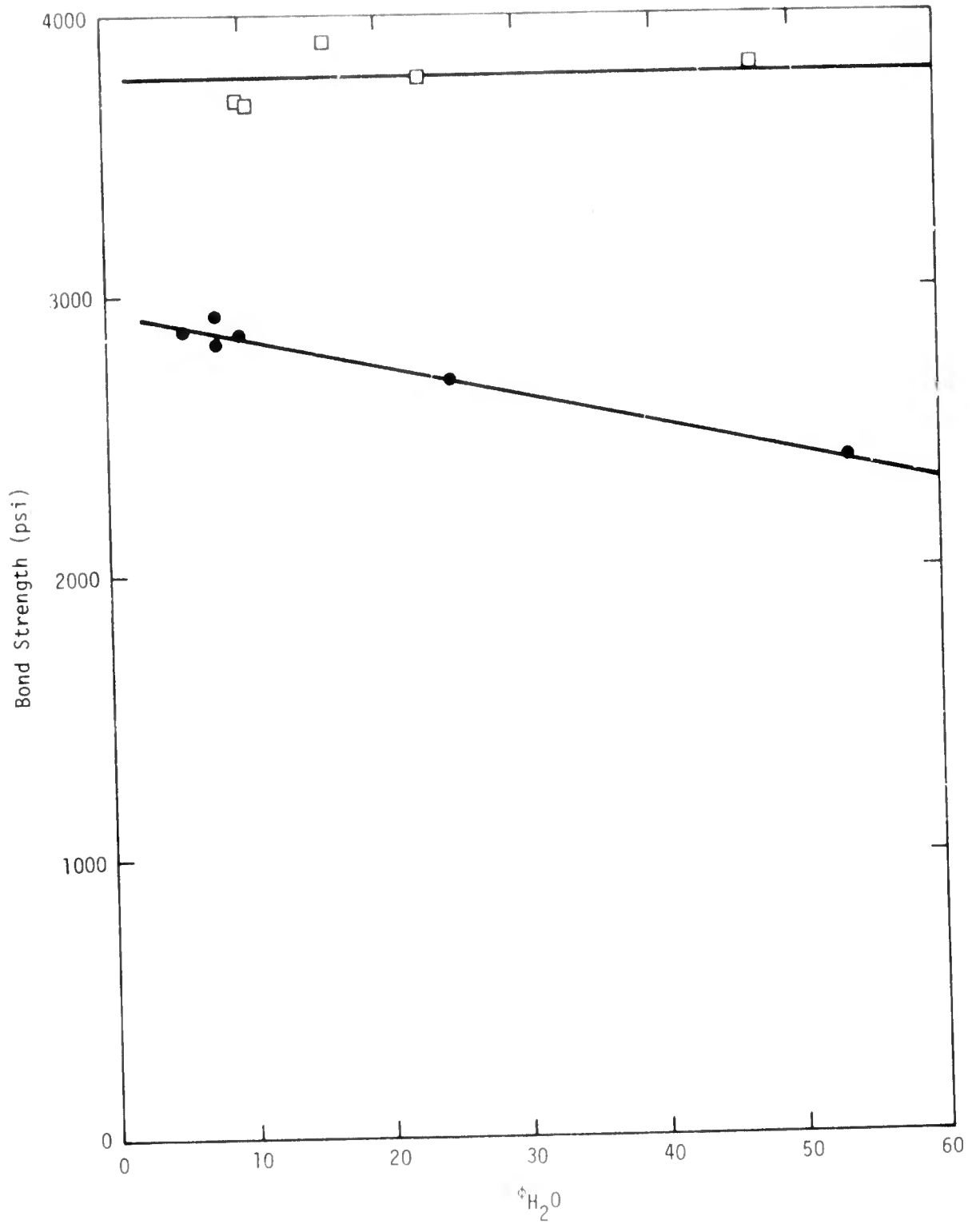


Figure 17. Plot of bond strength vs  $\phi_{H_2O}$  for HT424 from batch 3 (□) and batch 2 (●).

weak with respect to adhesive bonding? c) Can a comparison of the physical and chemical properties of the boehmite and bayerite films help identify the phosphoric acid anodize film.

#### 4.1 Idealized Smooth Samples

In order to prepare boehmite and bayerite films with a minimum of complications, such as roughness and unknown thickness, a 1588 Å layer of aluminum was vapor deposited onto a layer (1000 Å) of gold, onto a layer (200 Å) of chromium on a polished silicon substrate. The polished silicon was used as a very smooth flat surface. The chromium was used to give good adhesion between the silicon and the gold. The gold was used to provide a mirror of inert material for the aluminum. After obtaining initial surface properties by ellipsometry, reflectivity, and SEM, and weight (on a microbalance to  $\pm 2 \mu\text{g}$ ) one sample was placed in 50°C distilled water and the other in 96°C distilled water to produce a layer of bayerite and a layer of boehmite, respectively. At various times the samples were removed, dried, and examined with the surface tools.

Figure 18 shows the weight gain as a function of water exposure time. At the points indicated the gold substrate could be observed. That is, for the 96°C sample (boehmite) between 1.3 and 2.8 hours the film had become transparent, indicating transformation to the oxide. For the 50°C sample (bayerite), the transformation took place between 2.8 hours and 9.4 hours. The calculated weight gain for transformation of 1588 Å of aluminum to boehmite ( $\text{Al}_2\text{O}_3(\text{H}_2\text{O})$ ) is 52.4  $\mu\text{g}/\text{cm}^2$  as compared to 81.0  $\mu\text{g}/\text{cm}^2$  for bayerite. These values are close to the final values at which gold was observed in Fig. 18, i.e. 50  $\mu\text{g}/\text{cm}^2$  (at 96°C) and 80  $\mu\text{g}/\text{cm}^2$  (at 50°C), indicating stoichiometric conversion to boehmite and bayerite.

Scanning electron micrographs of the beginning (Figs. 19 thru 22) and final stages (Fig. 23 and 24) were taken. The top micrographs in Fig. 19 are for the Al/Au/Cr/Si. They appear

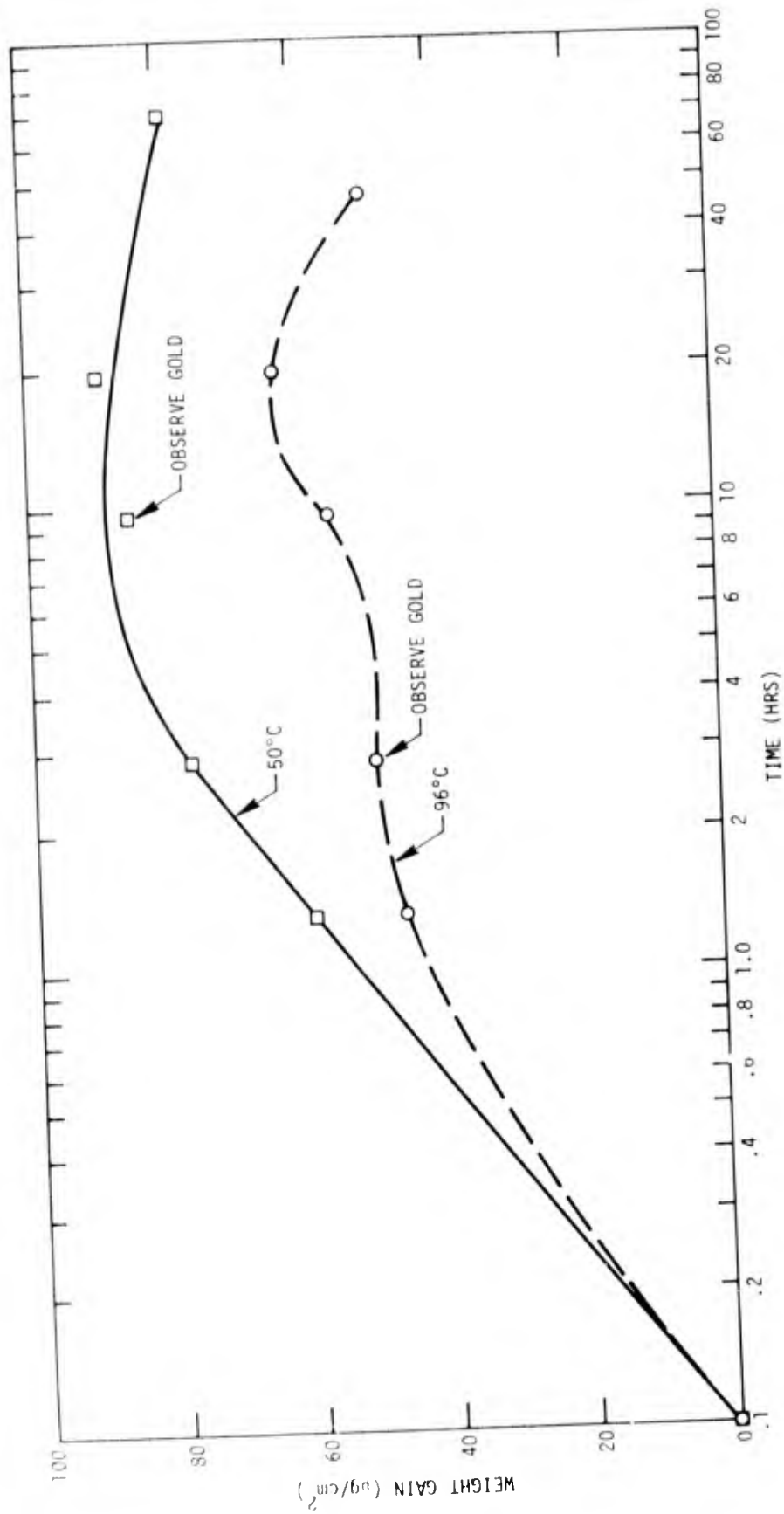
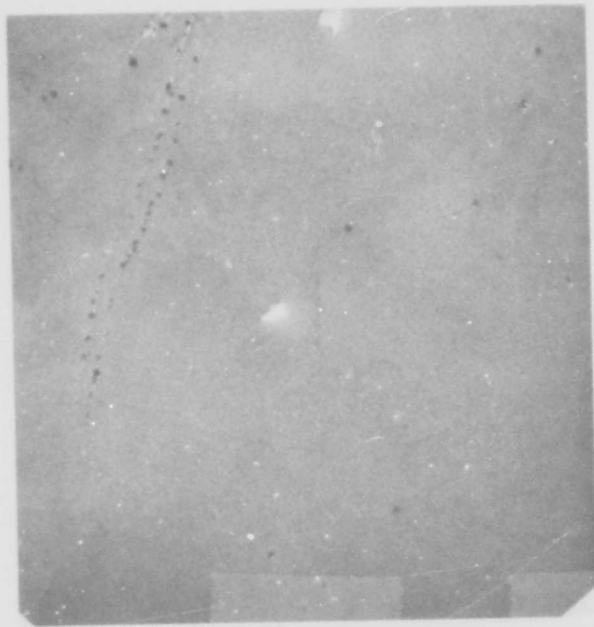


Figure 18. Plot of weight change vs time for vapor deposited aluminum on gold, during exposure to water.



X1000

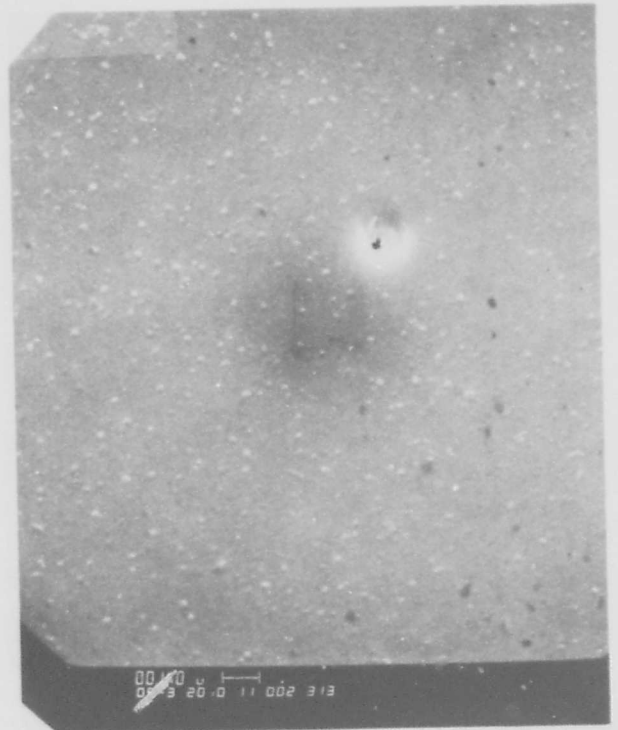


X4000

Vapor deposited (1588 Å) Al/Au/Cr/Si



0 10.0 11 002 318  
03-2 20.0

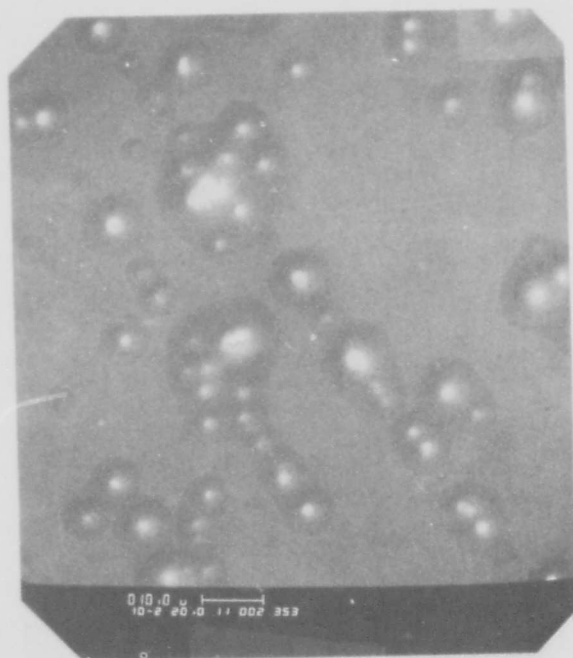
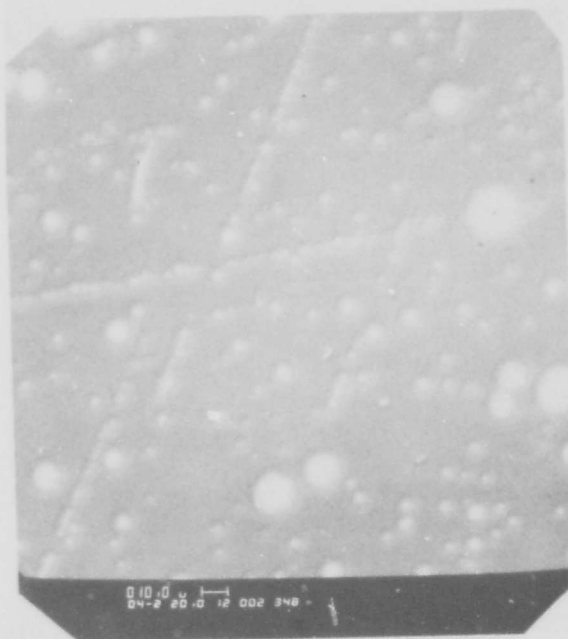


0 10.0 11 002 318  
03-2 20.0

Vapor deposited (3800 Å) Al/Au/Cr/Glass

Figure 19. SEM pictures of vapor deposited Al/Au/Cr/Si (top) and Al/Au/Cr/glass (bottom).

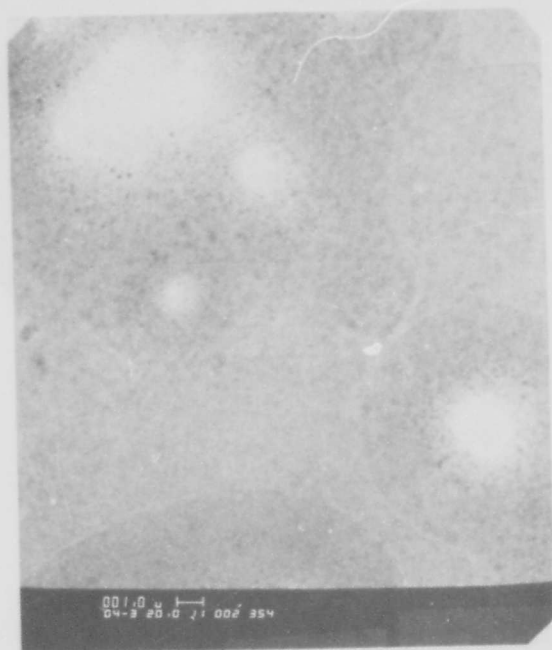
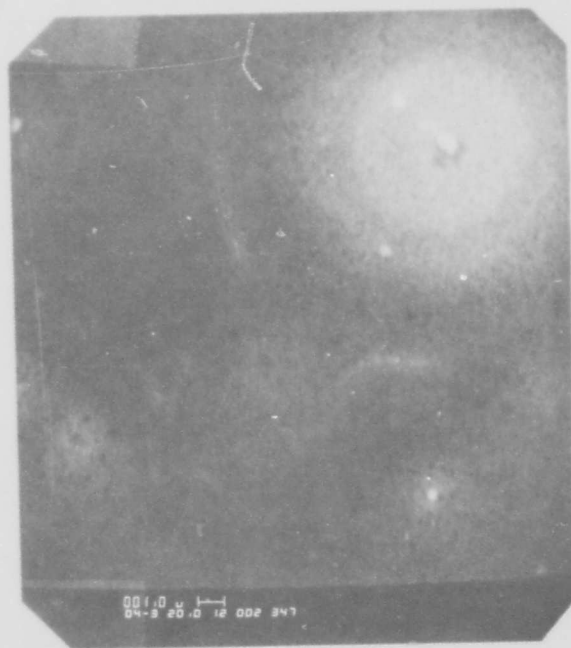
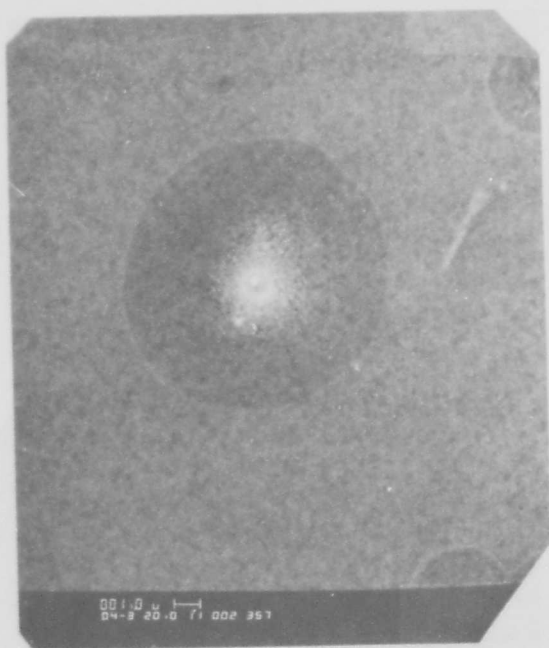




96°C

50°C

Figure 20 SEM pictures of vapor deposited Al after exposure to 96°C water (left) and 50°C water (right) for 1/2 hr.



96°C

50°C

Figure 21 SEM pictures of vapor deposited Al after exposure to 96°C water (left) and 50°C water (right) for 1/2 hr.

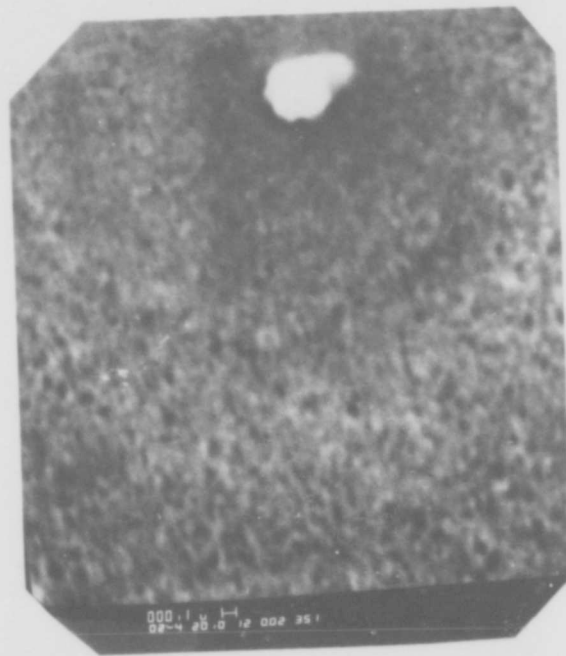
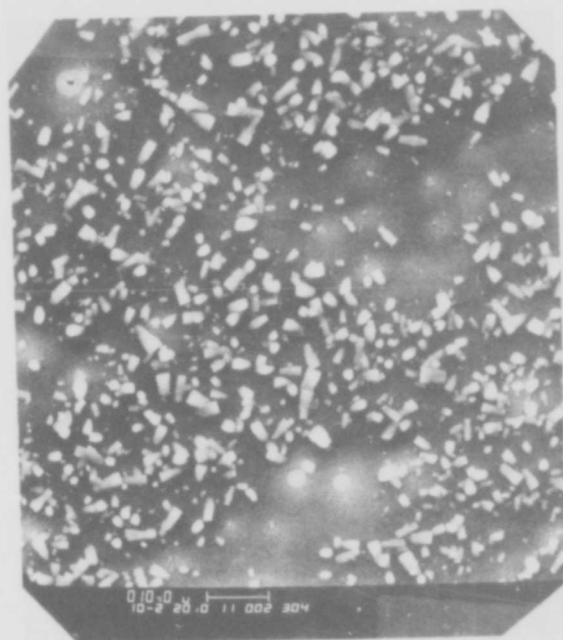
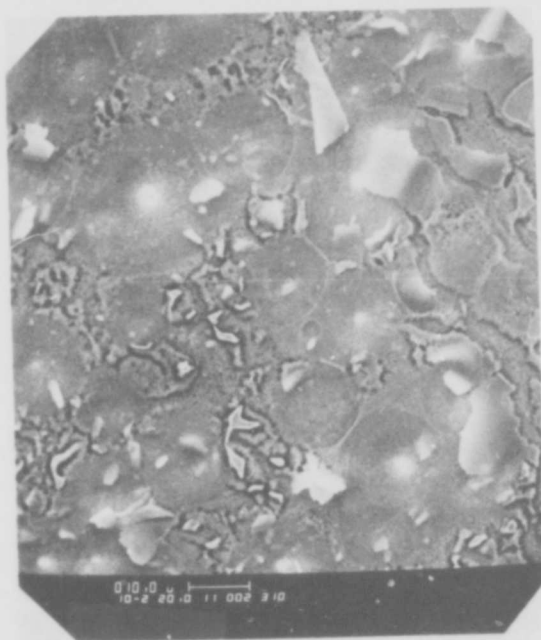
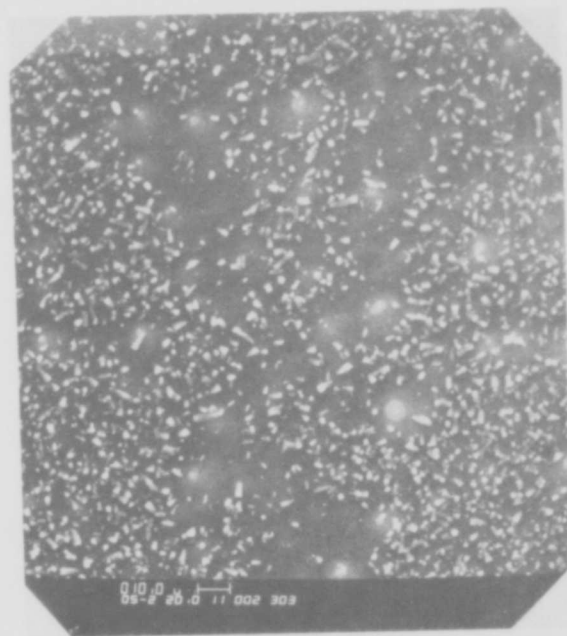
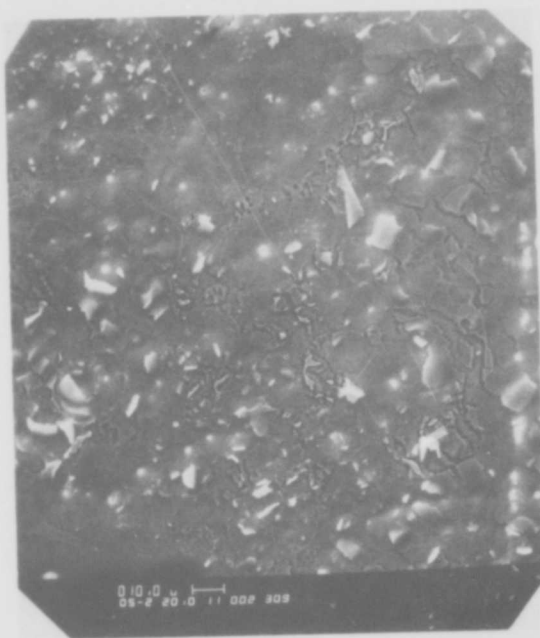


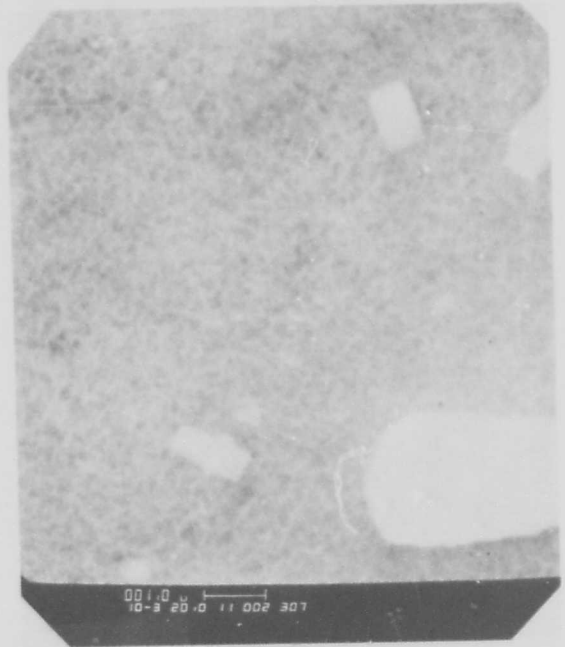
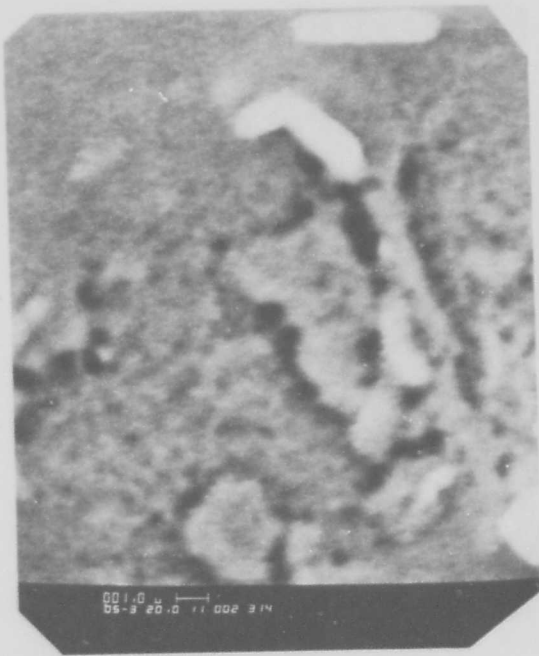
Figure 22 SEM pictures of vapor deposited Al after exposure to 96°C water (left) and 50°C water (right) for 1/2 hr.



100°C water 46.7 hrs.

50°C water 70 hrs.

Figure 23 SEM pictures of vapor deposited Al after exposure to 96°C water (left) for 46.7 hrs and 50°C water (right) for 70 hrs



96°C water 46.7 hrs.

50°C water 70 hrs.

Figure 24 SEM pictures of vapor deposited Al after exposure to 96°C water (left) for 46.7 hrs and 50°C water (right) for 70 hrs.

rather smooth and have small white particles. Each particle is in the center of a circular area of slightly darker shade than the background. These particles are white due to charging in the SEM and therefore are insulating. The white particles are not observed on the vapor deposited aluminum on gold on chromium on glass (bottom of Fig. 19) and must be an artifact of vapor deposition on the silicon. Apparently vapor deposition on Al/Cr/Si substrates leave small particles of aluminum which oxidizes upon exposure to air, then act as nucleation centers upon exposure to water. Figure 20 shows SEM pictures for the 96°C (left side) and 50°C (right side) after 1/2 hour exposure. The shaded circular area around the white particles have expanded and include a white circular area, indicating nucleation and growth starting at the white particles. In some instances the white particles have fallen off the sample leaving a small crater (see Fig. 21). It is obvious that growth of the white areas is faster in the 50°C water than the 96°C water. The white circular area around each particle is insulating and porous. The small dark dots associated with the periphery of the white areas (see Fig. 22) are identified in the microscope as holes. The pores are about 300-500 Å across. Figures 23 and 24 show SEM pictures after exposure to 46.7 hours (96°C) and 70 hours (50°C). The pictures on the left (96°C water) conform to boehmite platelets as observed in refs. 10 and 15. Pictures on the right (50°C) conform to bayerite crystallites. Notice that the circular growth areas observed after 1/2 hour exposure (in Fig. 20) are still observed in Figs. 23 and 24. In the case of the 50°C exposure, the bayerite crystallites are less populated in the circular areas. The SEM pictures and weight change data indicate that the 50°C water produced bayerite and the 96°C water produced boehmite as expected.

To see if phosphoric acid anodic film would inhibit the reaction with water at 50°C a 1588 Å layer of aluminum was anodized in 0.1M  $H_3PO_4$  at 30 volts for 3 minutes and then exposed

to 50°C water for 150 hours. Figure 25 shows the ellipsometric parameters and SPD during the experiment. The lower curve in Fig. 25 is the estimated thickness of the oxide film from the ellipsometric values. The dashed curve at the top of Fig. 25 shows the values  $\psi$  would have had if the aluminum substrate had remained smooth throughout the experiment. The fact that the anodize produced a  $\psi$  value for a smooth substrate indicates that the anodic process does not roughen the aluminum surface beneath the oxide. The large deviation of the experimental values of  $\psi$  (solid curve) from the values for the smooth substrate indicates that the water exposure causes the aluminum surface at the oxide - metal interface to be considerably roughened as shown later from light scattering experiments. The anodic film is 500 Å thick. The vertical dashed line at  $t = 20$  hours in Fig. 25 is the time the gold substrate could be seen through the oxide layer. Beyond 20 hours the experimental values of  $\psi$  approach the theoretical dashed curve as the smooth gold layer is approached. The anodic film caused the SPD to drop 1.5 volts whereas exposure to the water increased it again by about 0.5 volts, during the formation of 1000 Å of oxide in addition to the 500 Å anodic film. Further oxidation to about 3500 Å did not change SPD.

Figure 26 shows SEM pictures after the water soak (of Fig. 25). Particles left during vapor deposition have completely oxidized and some of them have fallen off the gold substrate. Note that the anodic layer has not protected the aluminum from complete oxidation but has inhibited the formation of bayerite crystallites as seen in Fig. 23 (right side). It should also be noted that the films in Fig. 26 have a foamy cellular structure and appear much thicker than 3500 Å. The ellipsometer can only reveal an effective thickness which depends upon the mass of film per  $\text{cm}^2$ . To illustrate this, note Fig. 27, a plot of the ellipsometric phase shift  $\Delta$  as a function of exposure time in the exposure of a 1588 Å aluminum layer to water. The open circles and dashed lines are for the 96°C exposure (boehmite) and the



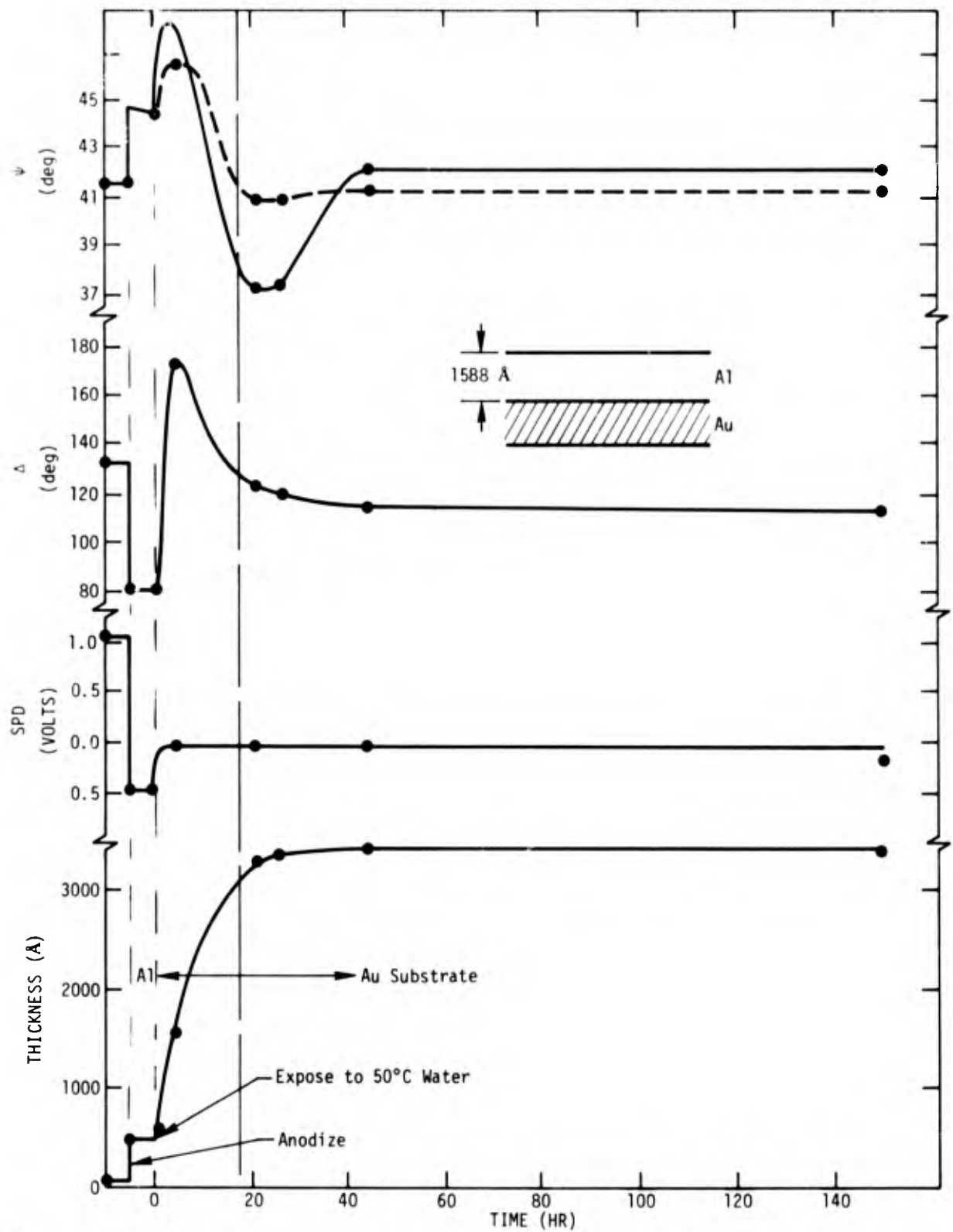


Figure 25. Ellipsometric and SPD parameters as a function of exposure time for vapor deposited Al after phosphoric acid-anodize to 500 Å.



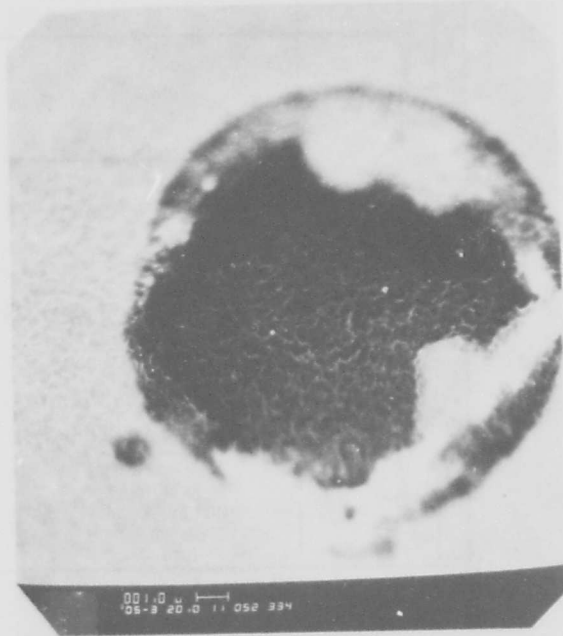
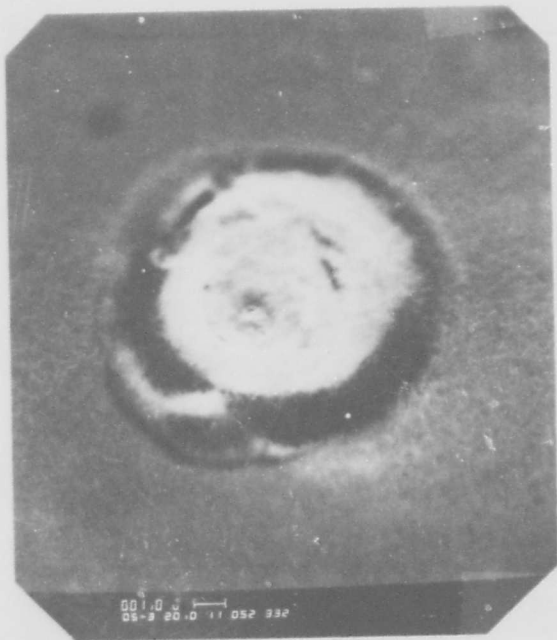
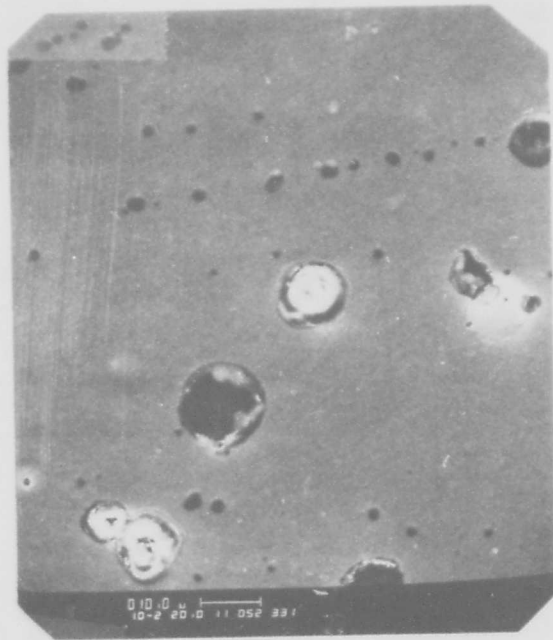
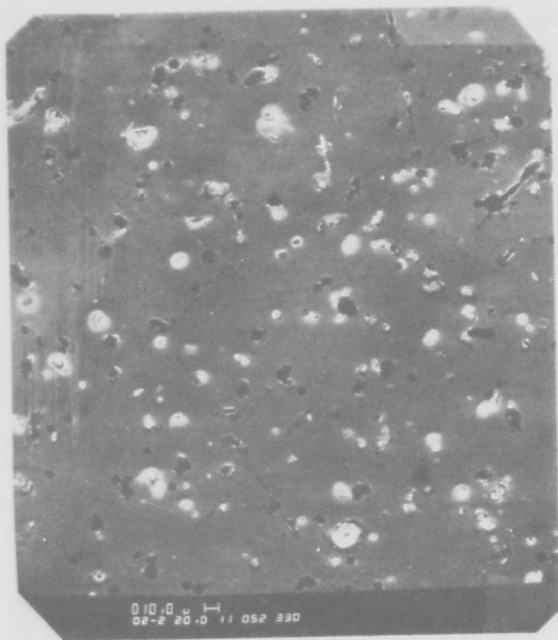


Figure 26 SEM pictures of vapor deposited Al after anodizing to 500 Å then 50°C water exposure for 150 hrs.

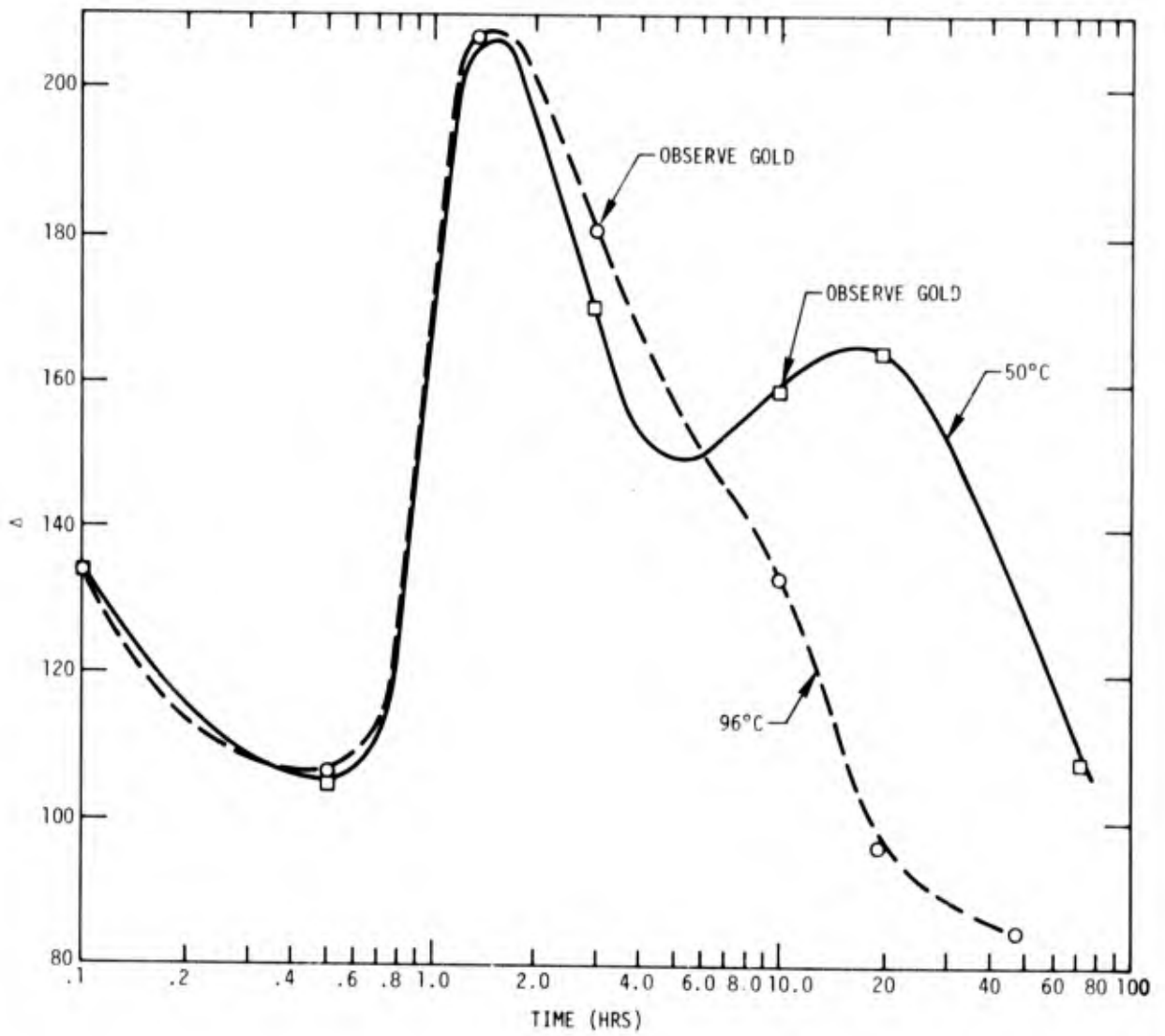


Figure 27. Plot of  $\Delta$  vs exposure time for vapor deposited Al (96°C water o, 50°C water  $\nabla$ ).

open squares and solid lines are for the 50°C exposure (bayerite). The curves have been estimated between experimental data. The fact that the 50°C curve goes through two maxima yields computer calculation of an unambiguous film thickness at 70 hours of approximately 5300 Å, as compared to approximately 2700 Å for the 96°C curve (one maxima). These thicknesses are within experimental error of the equivalent thickness calculated from the weight change (Fig. 16) and theoretical density (i.e. 4900 Å for bayerite, 3166 Å for boehmite). It is noted in Fig. 27 that the two films grow at about the same rate up to 3 hours (about 2900 Å) as long as the effective metal substrate is aluminum. However the  $\psi$  values in Fig. 28 indicate the films are quite different. As pointed out in Fig. 25,  $\psi$  has been shown, in other experiments, to be very sensitive to surface roughness. For a perfectly smooth reflecting surface of aluminum  $\psi$  varies between 41° and 50° for Al<sub>2</sub>O<sub>3</sub> with index of refraction between 1.6 and 1.7. For lower index of refraction it varies between 41 and lower values than 50°. The large deviations beyond these limits in Fig. 28 reveal the effect of surface roughness at the oxide - metal interface.

Another complimentary technique to ellipsometry can be used to establish surface roughness. This reflectivity technique has been developed by Hensler<sup>2</sup> with the scattering theory of Beckmann.<sup>16</sup> The method is nondestructive since the roughness parameters  $\sigma$  and  $T$  are obtained by measuring the intensity of reflected light as a function of angle of incidence. The parameter  $\sigma$  is the rms vertical deviation from a mean surface plane and  $T$  is the auto correlation length, i.e.,  $T$  is the rms length of the asperities. The approximate equation can be expressed

$$I/I_{s0} = e^{-g} + (\pi T^2 \Delta\omega e^{-g/\lambda}) \sum_{m=1}^{\infty} g^m / m! m \quad (6)$$

where the  $I_{s0}$  is the intensity at  $\theta = 90^\circ$  (perfectly flat surface), the first term is for the specular reflected (coherent)

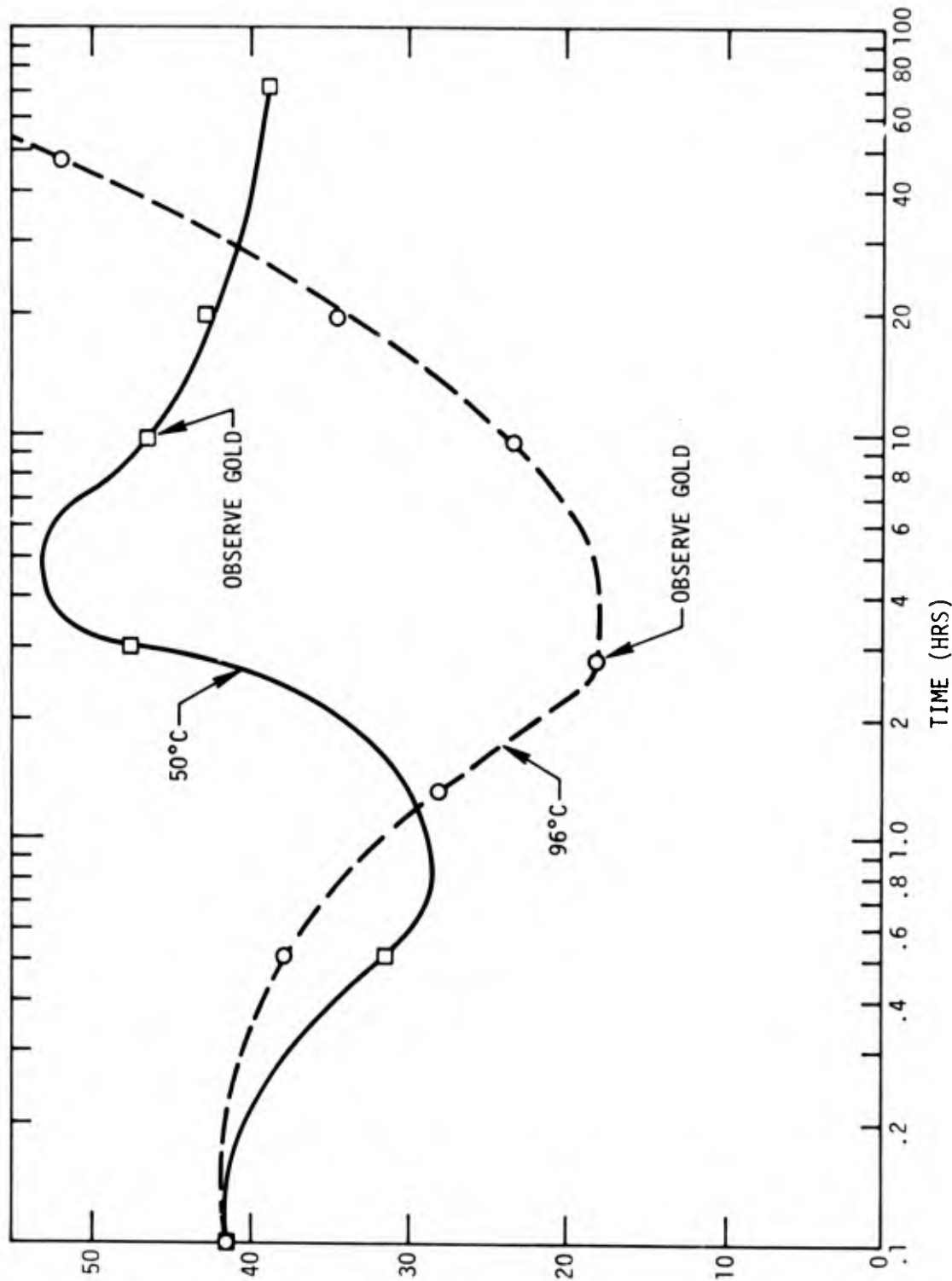


Figure 28. Plot of  $\psi$  vs exposure time for vapor deposited Al (96°C o, 50°C  $\square$ ).

light and the second term is for the diffuse scattered (incoherent) light that is reflected into the specular direction. The parameter  $g$  is related to the roughness parameter  $\sigma$  by

$$g = (4\pi\sigma \cos \theta/\lambda)^2. \quad (7)$$

For large  $\cos^2 \theta$ ,  $e^{-g}$  becomes small and  $T$  can be calculated from Eq. 6 by

$$T \approx ((I/I_{s0}) \lambda^2 g / \pi \Delta\omega)^{\frac{1}{2}} \quad (8)$$

where  $\Delta\omega$  is the solid acceptance angle of the light detector, and  $e^{-g} \sum_{m=1}^{\infty} g^m / m! m$  is approximated as  $1/g$ . Figure 29 shows plots of  $I$  vs  $\cos^2 \theta$  for the 96°C sample (top curves) and 50°C sample (bottom curves). At low values of  $\cos^2 \theta$  Eq. 6 reduces to

$$I/I_{s0} = e^{-g} \quad (9)$$

yielding  $\sigma$  from the slope of the line. At large  $\cos^2 \theta$ ,  $T$  is calculated from Eq. 8. The rms slope of the roughness can be expressed  $\tan \beta_0 = \sqrt{2} \sigma/T$  where  $\beta_0$  is the rms angle with respect to the mean plane. However, the anomalous shapes of the curves, (bottom of Fig. 29) for which  $I$  increases at larger values of  $\cos^2 \theta$ , indicate that the roughness is so gross that shadowing and multiple reflections cannot be neglected. No theory has yet been developed to account for these effects. Therefore, for curves of this type estimates of  $T$  from Eq. 8 and therefore  $\tan \beta_0$  may be in error, but the trends of these parameters and  $\psi$  are good indicators of surface roughening. The rms slope,  $\tan \beta_0$ , for the 96°C sample and the 50°C sample are plotted in Fig. 30, and shows the greatly increased roughness of the 50°C (bayerite) sample after the first hour.

It has been demonstrated in this section that boehmite and bayerite films have been prepared and that their properties can be established with the NDI tools. To establish that these tools can be used for the rough surfaces, generally used for bonding,

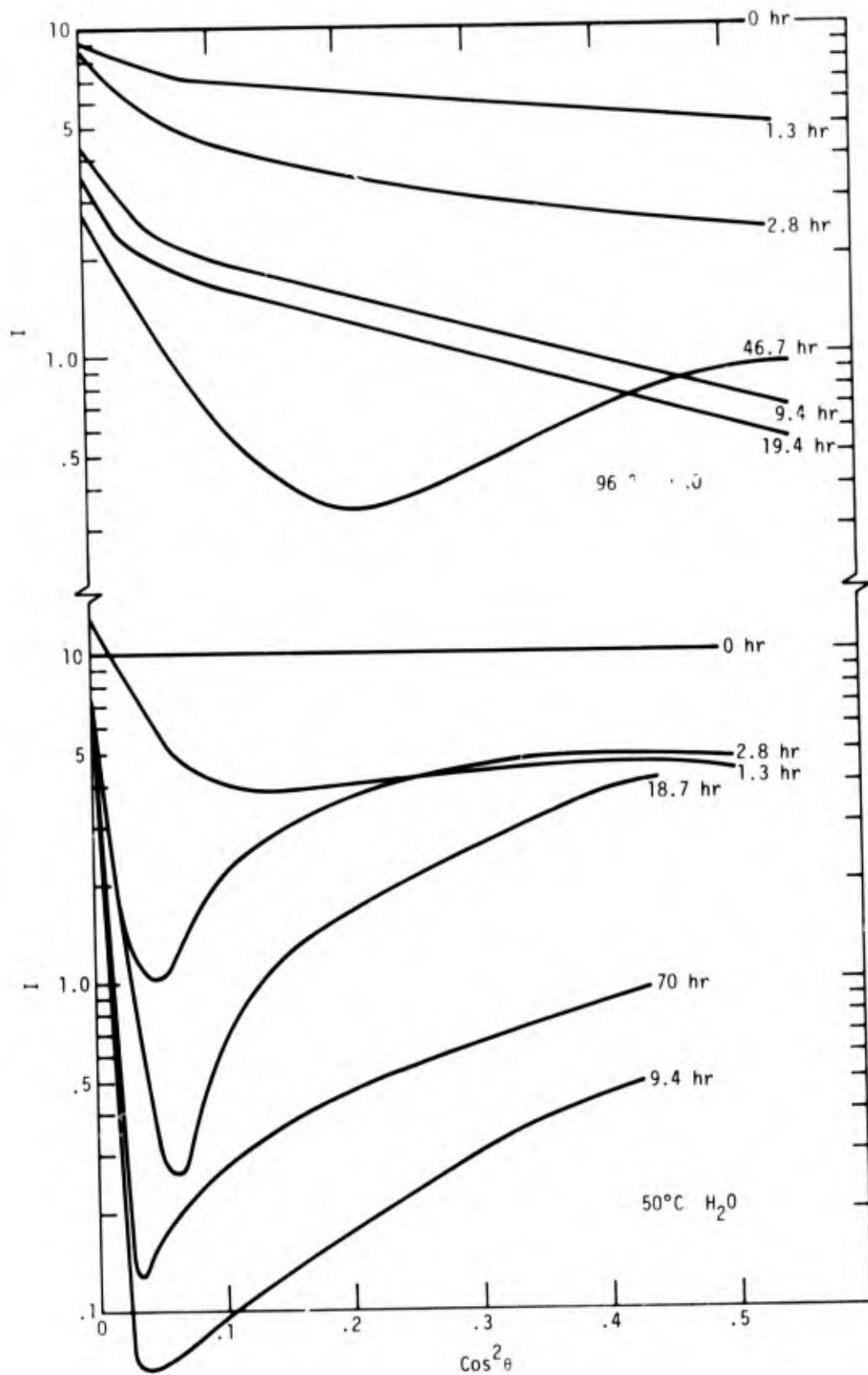


Figure 29. Plot of light intensity  $I$  vs  $\cos^2 \theta$  for 96°C water (top) and 50°C water (bottom).

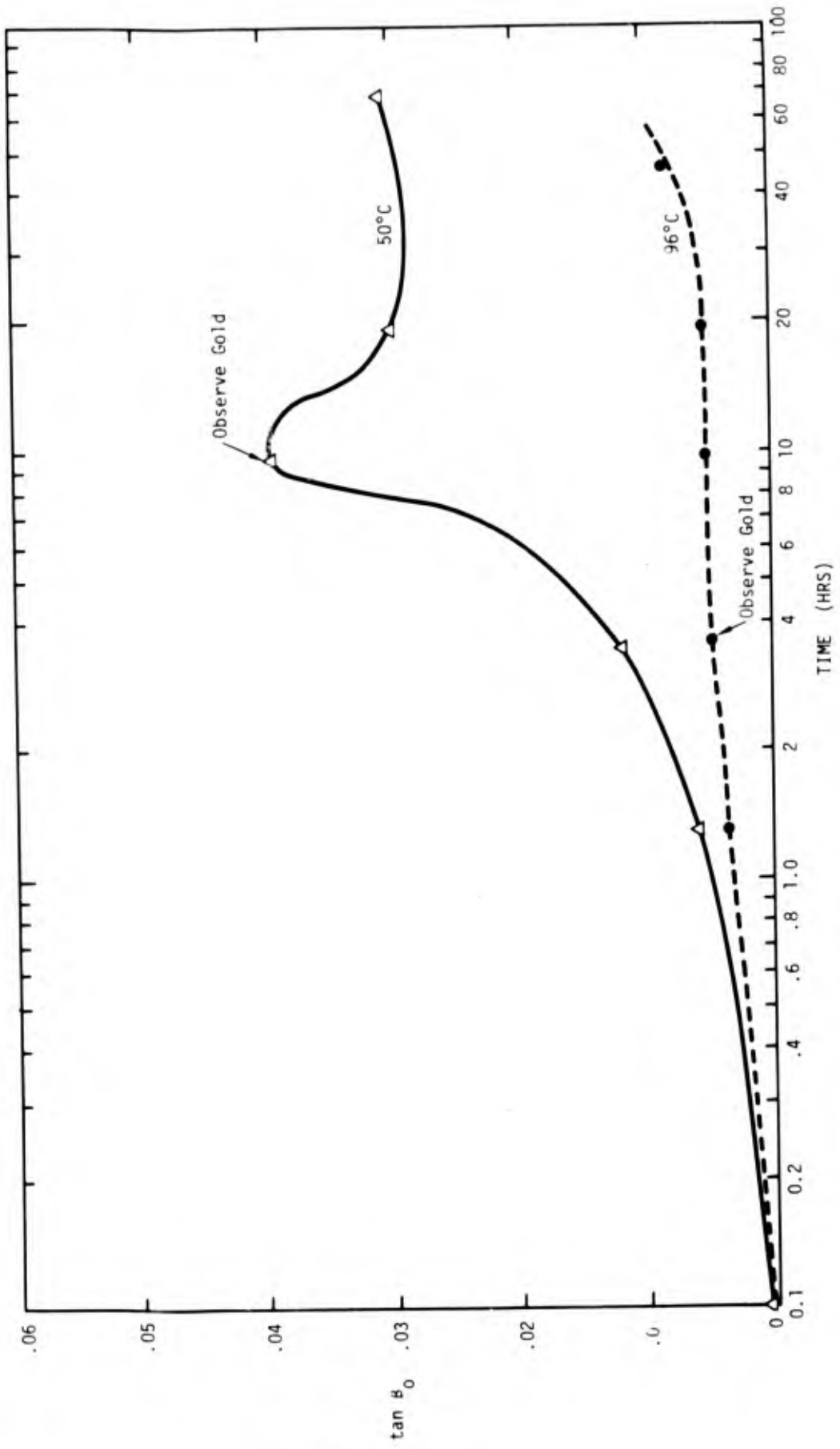


Figure 30. Plot of  $\tan \delta_0$  vs water exposure time.

other experiments were performed on massive aluminum for comparison.

#### 4.2 Rough Surfaces

Two as-received Al 2024-T3 samples were degreased, one was exposed to 96°C water for 21 hours to produce a boehmite film, the other was exposed to 50°C water for 21 hours to produce a bayerite film. The SEM pictures at the top of Fig. 31 are for the samples prior to water exposure. The samples are very rough and the rolling direction is obvious. The pictures at the bottom of Fig. 31 are for the 50°C water exposure for 21 hrs. A fairly thick film has obscured much of the roughness detail but the grooves in the rolling direction are still obvious. Bayerite crystallites are on the surface. The X5000 magnification (bottom right) reveals the foamy structure of the film as was observed for the vapor deposited film with 500 Å anodic layer (Fig. 26). Figure 32 shows the SEM pictures of the boehmite film. The film is highly fractured at about 45° with respect to the roll direction and is flaking off.

Part of the film that protrudes perpendicular to the surface (bottom left, Fig. 32) reveals the film to be  $\sim 1\mu$  thick. The X5000 magnification (bottom right Fig. 32) reveals the pseudo-boehmite observed by Vedder and Vermilyea.<sup>10</sup> SEM pictures for electropolished Al 2024-T3 followed by alkaline cleaning are seen in Fig. 33. The pseudo-boehmite crystallites are observed for the 96°C water exposure but the film is not fractured and flaking. The 50°C exposure produced the same type of surface as for the as-received material but with more bayerite crystalline formation. The SEM pictures reveal that the morphology of the film depends greatly upon the mechanical condition of the aluminum (vapor deposited vs as-rolled vs electro polished and alkaline cleaned).

Figure 34 is an  $I \text{ vs } \cos^2 \theta$  plot for the samples represented in Figures 31, 32 and 33. The degreased sample yields a normal



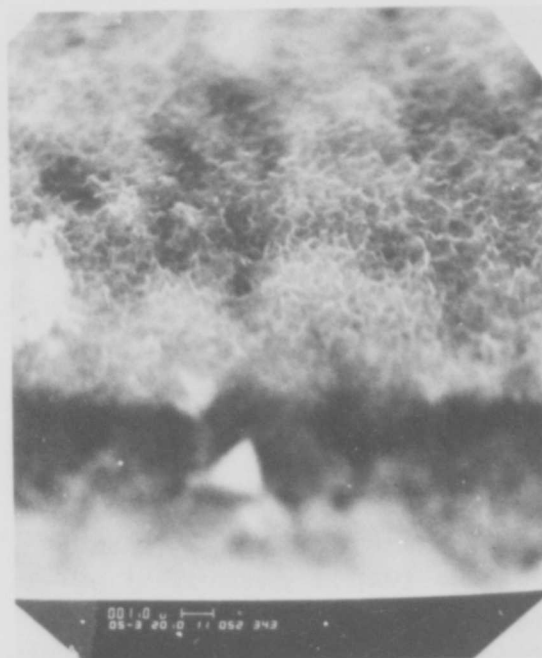
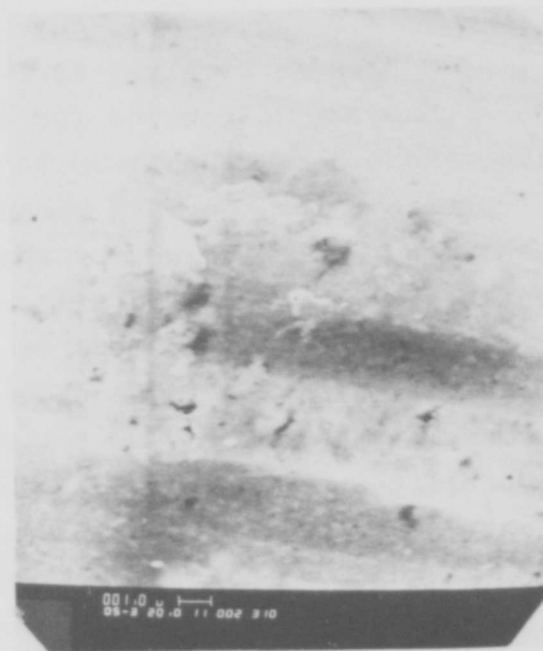
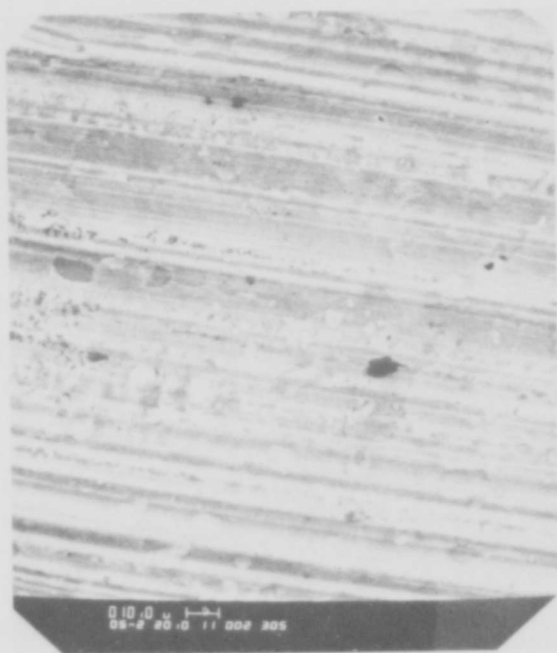


Figure 31 SEM pictures for vapor degreased Al 2024-T3 as received (top) after 50°C water exposure for 21 hrs (bottom).

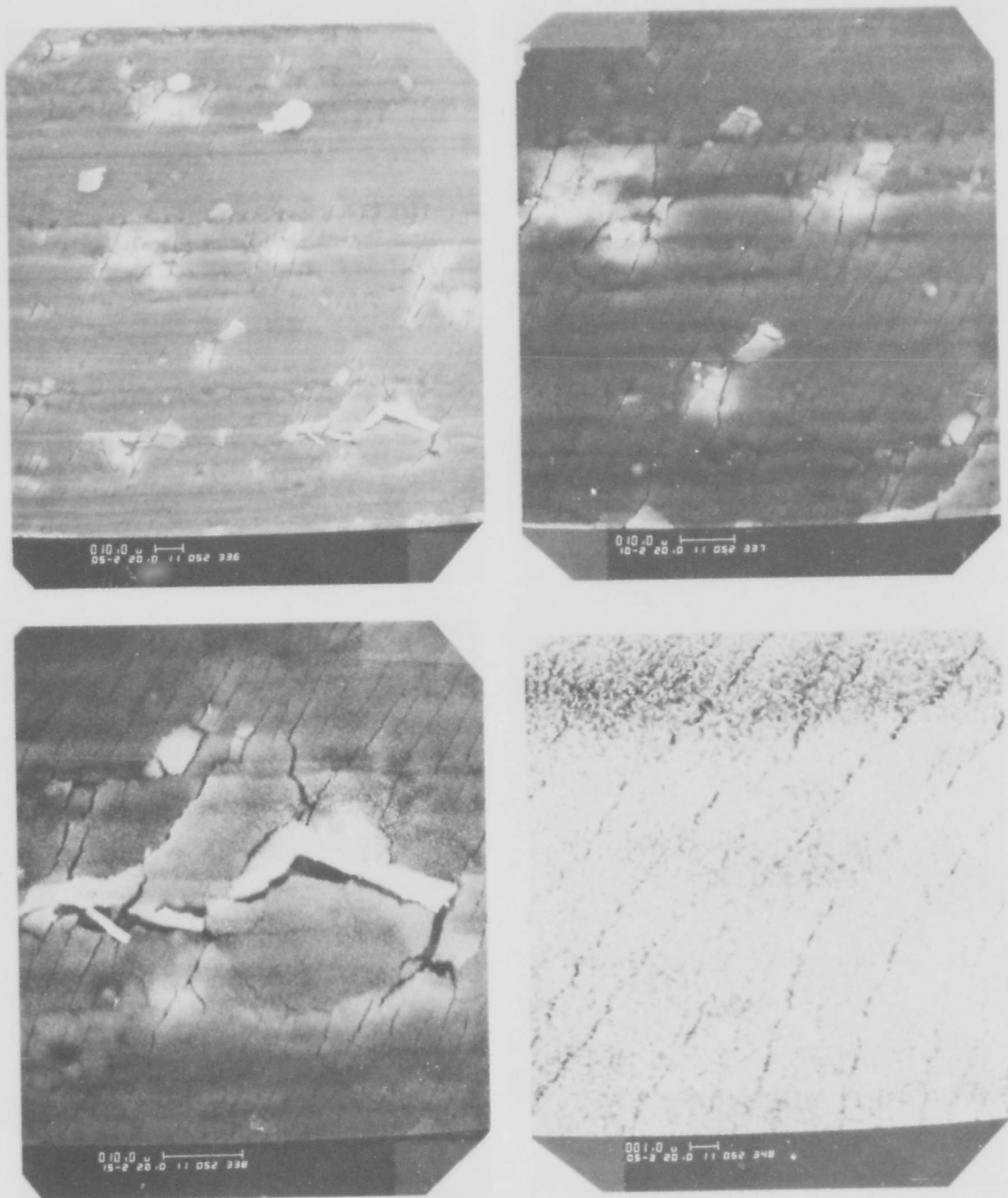


Figure 32 SEM pictures for vapor degraded Al 2024-T3 after 96°C water exposure for 21 hrs.

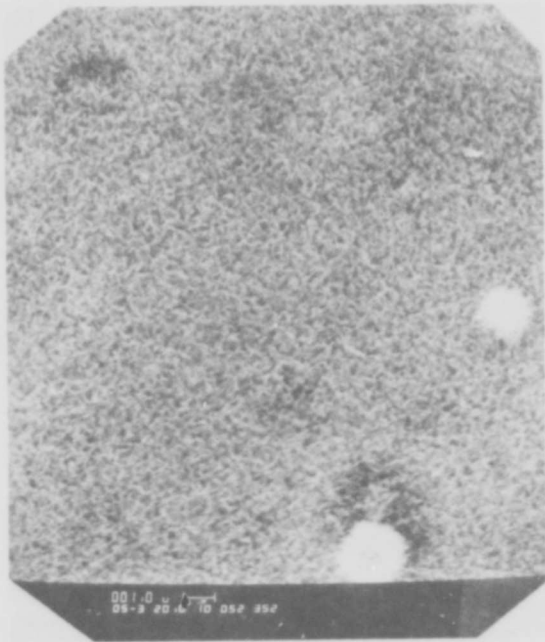
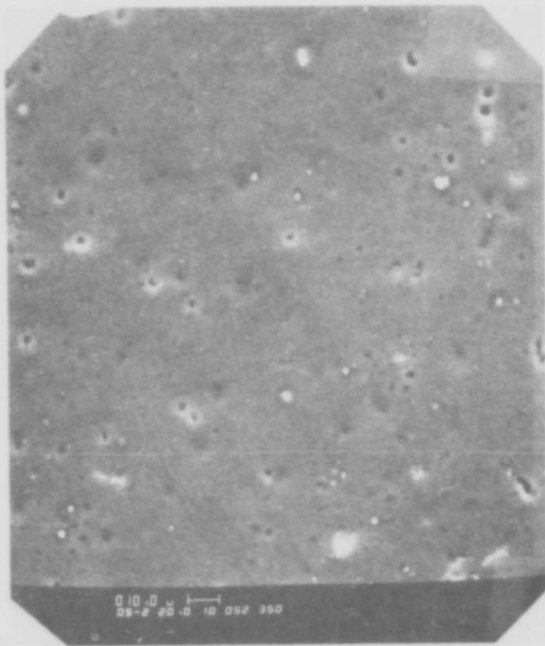


Figure 33 SEM pictures of electropolished then alkaline cleaned Al 2024-T3 after 96°C water exposure (left) and 50°C water exposure (right).

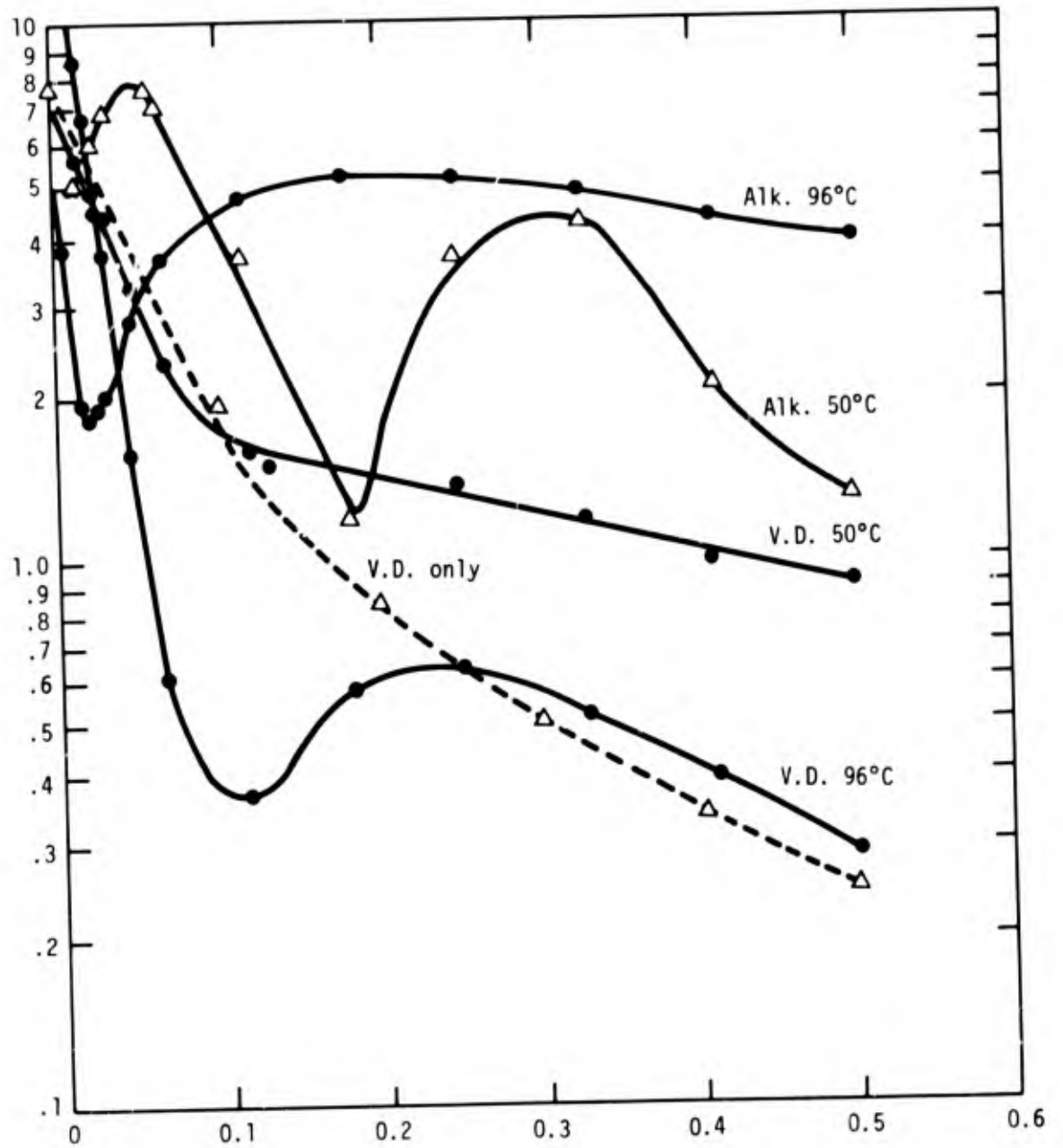


Figure 34. Plot of light intensity  $I$  vs  $\cos^2 \theta$  for Al 2024-T3 alkaline cleaned and vapor degreased samples.

curve, whereas the rest of the curves indicate extreme roughness with shadowing and multiple reflection.

#### 4.2.1 Wettability Analysis of Hydroxide Films

Having established the conditions for the formation of bayerite and boehmite films, two Al 2024-T3 samples were degreased, one was exposed to 50°C water and the other to 96°C water to form bayerite and boehmite surface films, respectively. Two other Al 2024-T3 samples were polished before exposure to the distilled water. A complete wettability study (see AFML-TR-74-73) was performed on each surface. The results are given computer printout of Tables 6 through 9. The wettability envelopes were all like that in Fig. 35. The result indicates that the boehmite and bayerite surfaces are essentially the same with respect to wettability, very low contact angles, and that the increase in contact angles during aging is not due to transformation of one hydroxide form to another. Either hydroxide is wettable by either the uncured or cured HT424 adhesive as indicated by the points that fall well within the envelope.

#### 4.3 Surface Properties of FPL etch Al2024-T3

Figure 36 shows three magnifications of an FPL etched Al 2034-T3 surface. The largest magnification reveals the surface to be covered with very small etch pits between about 300 and 1000 Å in diameter on the floor of much larger etch pits. This appearance does not change after aging in humid atmospheres.

Figure 37 shows SEM pictures of FPL etched Al 2024-T3 after exposure to 50°C distilled water for 21 hours (bottom) and 100°C distilled water (top). It should be noted that for the 100°C water exposure the water completely evaporated prior to 21 hours. In order to estimate the oxide film thickness, samples were bent as in Ref. 3. The pictures at the right of Fig. 37 were taken at the apex of the bend where the oxide was most fractured. The

Table 6

WETTABILITY ANALYSIS

LIQUID	DECREASED AL2024T3 50 DEG. SOAK					W(A)
	GAMMA	GAMMA-D	GAMMA-P	THETA	COS(THETA)	
1 WATER	72.80	21.80	51.00	11.00	.98163	144.26
2 GLYCEROL	64.00	34.00	30.00	10.00	.98481	127.03
3 FORMAMIDE	58.30	32.30	26.00	12.00	.97815	115.33
4 ETHYLEN-G	48.30	29.30	19.00	2.00	.99939	95.57
5 1-BR-NAPH	44.60	44.50	0.00	4.00	.99756	89.09
6 PG-15-200	36.60	26.00	10.60	2.00	.99939	73.18
7 PG-1200	31.30	24.50	6.80	9.00	.98769	62.21

CALCULATED SURFACE PROPERTIES FOR D.G.E. 10.00

DECREASED AL2024T3 50 DEG. SOAK

LIQUID PAIR	GAMMA-D	DEV-D	GAMMA-P	DEV-P	GAMMA-S	DEV	D
1-2	13.26	-9.39	59.60	6.40	72.85	-2.98	-16.07
1-3	6.88	-15.77	70.33	17.13	77.20	1.37	-16.78
1-4	2.76	-19.88	81.25	28.06	84.01	8.18	-18.30
1-5	44.49	21.85	32.94	-20.25	77.43	1.60	-47.69
1-6	1.56	-21.09	86.21	33.02	87.77	11.93	-21.21
1-7	2.16	-20.48	83.53	30.34	85.69	9.85	-23.17
2-3							-1.40
2-4							-4.23
2-5	44.49	21.85	20.21	-32.99	64.70	-11.14	-36.58
2-6	.16	-22.48	124.78	71.59	124.94	49.10	-8.94
2-7							-11.91
3-4	44.49	21.85	15.01	-38.19	59.50	-16.34	-2.83
3-5							-34.05
3-6	.53	-22.01	108.70	55.51	109.33	33.49	-7.50
3-7	44.49	21.85	7.81	-45.39	52.30	-23.54	-10.42
4-5							-29.11
4-6							-4.60
4-7	44.49	21.85	.63	-52.57	45.12	-30.72	-7.46
5-6	44.49	21.85	.54	-52.66	45.03	-30.81	21.74
5-7							17.41
6-7							-2.82

AVERAGE GAMMA D = 22.64 S.D.FROM MEAN = 5.91  
 AVERAGE GAMMA P = 53.10 S.D.FROM MEAN = 11.85  
 AVERAGE GAMMA S = 75.84 S.D.FROM MEAN = 6.55

Table 7

LIQUID	DEGREASED AL2024T3 96 DEG. SOAK				W(A)
	GAMMA	GAMMA-D	GAMMA-P	THETA	
1 WATER	72.80	21.80	51.00	3.00	145.50
2 GLYCEROL	64.00	34.00	30.00	7.00	127.52
3 FORMAMIDE	58.30	32.30	26.00	3.00	116.52
4. ETHYLEN-G	48.30	29.30	19.00	2.00	96.57
5 1-BR-NAPH	44.60	44.60	0.00	3.00	89.14
6 PG-15-200	36.60	26.00	10.60	10.00	72.64
7 PG-1200	31.30	24.50	6.80	12.00	61.92

CALCULATED SURFACE PROPERTIES FOR D.G.E. 10.00

LIQUID PAIR	DEGREASED AL2024T3 96 DEG. SOAK				GAMMA-S	DEV	D
	GAMMA-D	DEV-D	GAMMA-P	DEV-P			
1- 2	12.53	-9.98	61.98	6.89	74.51	-3.29	-16.07
1- 3	7.23	-15.28	71.06	15.77	78.28	.48	-16.78
1- 4	2.29	-20.22	84.59	29.30	86.88	9.08	-18.30
1- 5	44.54	22.03	33.92	-21.37	78.46	.66	-47.69
1- 6	1.13	-21.38	90.11	34.82	91.24	13.44	-21.21
1- 7	1.83	-20.68	86.52	31.24	88.36	10.56	-23.17
2- 3							-1.40
2- 4	44.54	22.03	20.58	-34.71	65.12	-12.68	-4.23
2- 5							-36.58
2- 6	.08	-22.43	128.75	73.46	128.82	51.02	-8.94
2- 7							-11.91
3- 4	44.54	22.03	15.90	-39.39	60.44	-17.36	-2.83
3- 5							-34.05
3- 6	.32	-22.19	116.45	61.16	116.77	38.97	-7.50
3- 7	44.54	22.03	7.78	-47.51	52.32	-25.48	-10.42
4- 5							-29.11
4- 6							-4.60
4- 7	44.54	22.03	.50	-54.79	45.03	-32.77	-7.46
5- 6	44.54	22.03	.63	-54.66	45.17	-32.63	21.74
5- 7							17.41
6- 7							-2.82

AVERAGE GAMMA D = 22.51 S.D. FROM MEAN = 5.96  
 AVERAGE GAMMA P = 55.29 S.D. FROM MEAN = 12.39  
 AVERAGE GAMMA = 77.80 S.D. FROM MEAN = 7.05

Table 8

LIQUID	POLISHED AL2024T3 50 DEG. SOAK							W(A)
	GAMMA	GAMMA-D	GAMMA-P	THETA	COS(THETA)			
1 WATER	72.80	21.80	51.00	10.00	.98481			144.49
2 GLYCEROL	64.00	34.00	30.00	13.00	.97437			126.36
3 FORMAMIDE	58.30	32.30	26.00	5.00	.99619			116.38
4. ETHYLEN-G	48.30	29.30	19.00	1.00	.99985			96.59
5 1-BR-NAPH	44.60	44.60	0.00	1.00	.99985			89.19
6 PG-15-200	36.60	28.00	10.60	8.00	.99027			72.84
7 PG-1200	31.30	24.50	6.80	1.00	.99985			62.60

CALCULATED SURFACE PROPERTIES FOR D.GE. 10.00

LIQUID PAIR	POLISHED AL2024T3 50 DEG. SOAK													
	GAMMA-D	DEV-D	GAMMAP	DEV-P	GAMMA-S	DEV	D	GAMMA-D	DEV-D	GAMMAP	DEV-P	GAMMA-S	DEV	D
1- 2	11.92	-10.74	61.77	8.58	73.69	-2.16	-16.07	44.59	21.93	19.59	-33.60	64.18	-11.67	-4.23
1- 3	7.90	-14.76	68.54	15.35	76.44	.59	-16.78	.31	-22.35	119.65	66.46	119.96	44.12	-11.91
1- 4	2.68	-19.98	81.82	28.64	84.51	8.66	-18.30	44.59	21.93	15.75	-37.43	60.34	-15.50	-2.83
1- 5	44.59	21.93	33.07	-20.12	77.66	1.81	-47.69	.57	-22.10	111.77	58.50	112.34	36.49	-10.42
1- 6	1.38	-21.29	87.42	34.23	88.79	12.94	-21.21	44.59	21.93	7.77	-45.42	52.36	-23.49	-29.11
1- 7	2.30	-20.37	83.28	30.10	85.58	9.73	-23.17							-4.60
2- 3							-1.40							-7.46
2- 4							-4.23							21.74
2- 5							-36.58							17.41
2- 6							-9.94							-30.80
2- 7							-11.67							-2.82
3- 4							-11.91							
3- 5							-2.83							
3- 6							-34.05							
3- 7							-7.50							
4- 5							-10.42							
4- 6							-29.11							
4- 7							-4.60							
5- 6							-7.46							
5- 7							21.74							
6- 7							17.41							

AVERAGE GAMMA D = 22.66 S.D. FROM MEAN = 5.92  
 AVERAGE GAMMA P = 53.19 S.D. FROM MEAN = 11.77  
 AVERAGE GAMMA = 75.85 S.D. FROM MEAN = 5.43



Table 9

LIQUID	POLISHED AL2024T3 96 DEG. SOAK					W(A)
	GAMMA	GAMMA-D	GAMMA-P	THETA	COS (THETA)	
2 GLYCEROL	64.00	34.00	30.00	19.00	.94552	124.51
3 FORMAMIDE	58.30	32.30	26.00	15.00	.96593	114.61
4 ETHYLEN-G	48.30	29.30	19.00	3.00	.99863	96.53
5 1-BR-NAPH	44.60	44.60	0.00	5.00	.99619	89.03
6 PG-15-200	36.60	26.00	10.60	13.00	.97437	72.27
7 PG-1200	31.30	24.50	6.80	8.00	.99027	62.30

CALCULATED SURFACE PROPERTIES FOR D.G.E. 10.00 POLISHED AL2024T3 96 DEG. SOAK

LIQUID PAIR	GAMMA-D	DEV-D	GAMMA-P	DEV-P	GAMMA-S	DEV	D
1- 2	14.75	-8.51	52.97	4.92	67.72	-3.59	-16.07
1- 3	9.90	-13.36	59.78	11.73	69.68	-1.63	-16.78
1- 4	4.77	-18.49	69.90	21.86	74.67	3.37	-18.30
1- 5	44.43	21.17	29.49	-18.55	73.92	2.62	-47.69
1- 6	2.06	-21.20	78.34	30.29	80.40	9.09	-21.21
1- 7	3.00	-20.26	74.93	26.88	77.93	6.63	-23.17
2- 3							-1.40
2- 4	44.43	21.17	18.24	-29.81	62.67	-8.64	-4.23
2- 5							-36.58
2- 6	.48	-22.78	112.96	64.91	113.44	42.13	-8.94
2- 7							-11.91
3- 4	44.43	21.17	14.51	-33.54	58.94	-12.36	-2.83
3- 5	.81	-22.45	104.75	56.70	105.56	34.26	-34.05
3- 6	44.43	21.17	7.82	-40.23	52.25	-19.06	-7.50
3- 7							-10.42
4- 5							-29.11
4- 6							-4.60
4- 7							-7.46
5- 6	44.43	21.17	.43	-47.61	44.86	-26.44	21.74
5- 7	44.43	21.17	.50	-47.55	44.93	-26.37	17.41
6- 7							-2.82

AVERAGE GAMMA D = 23.26 S.D. FROM MEAN = 5.75  
 AVERAGE GAMMA P = 48.05 S.D. FROM MEAN = 10.80  
 AVERAGE GAMMA = 71.31 S.D. FROM MEAN = 5.71

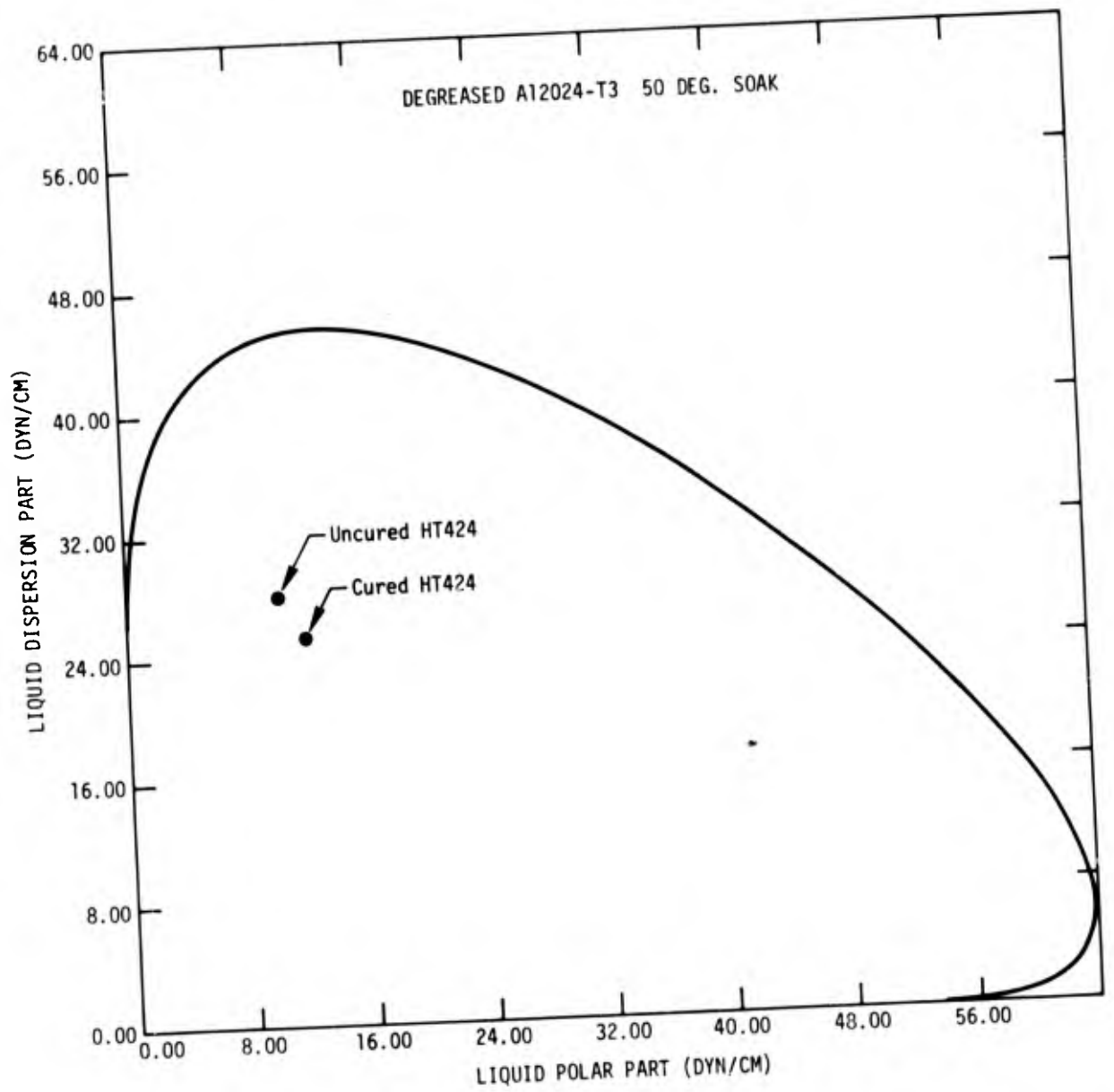


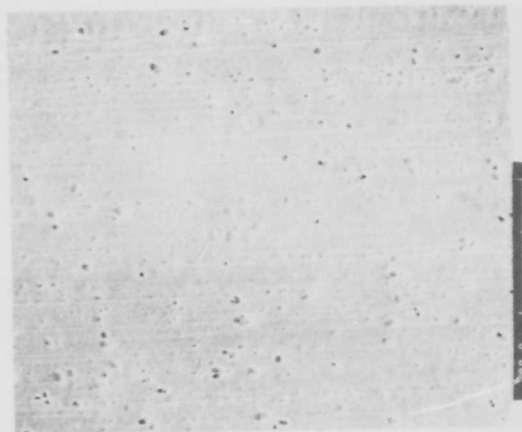
Figure 35. Wettability envelope for Al 2024-T3 after water exposure.



8000X



1600X



240X

Figure 36 FPL etched Al 2024-T3 at various magnifications.

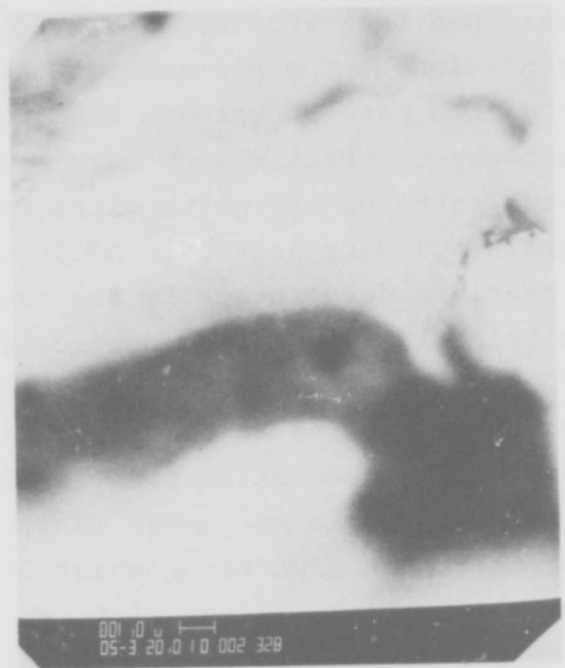
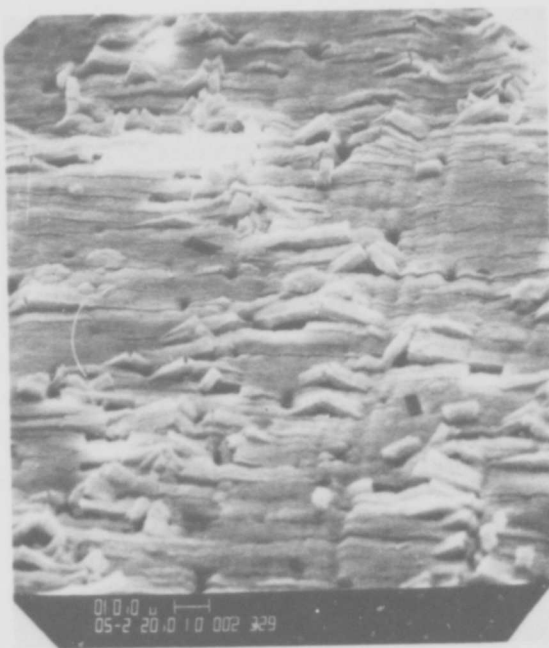
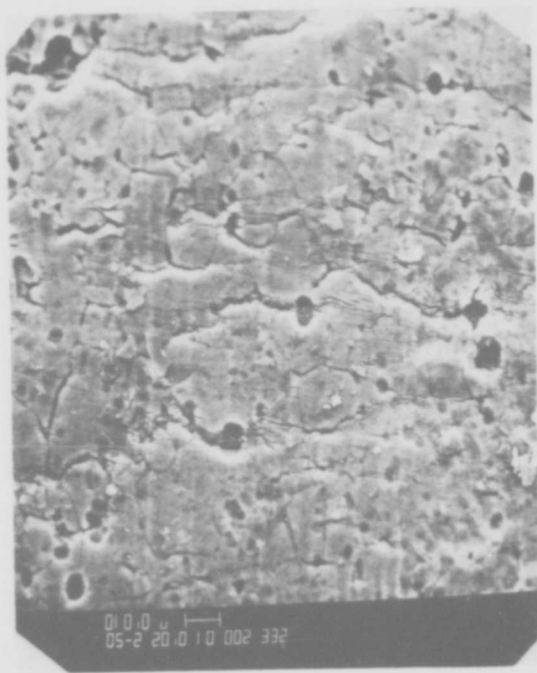


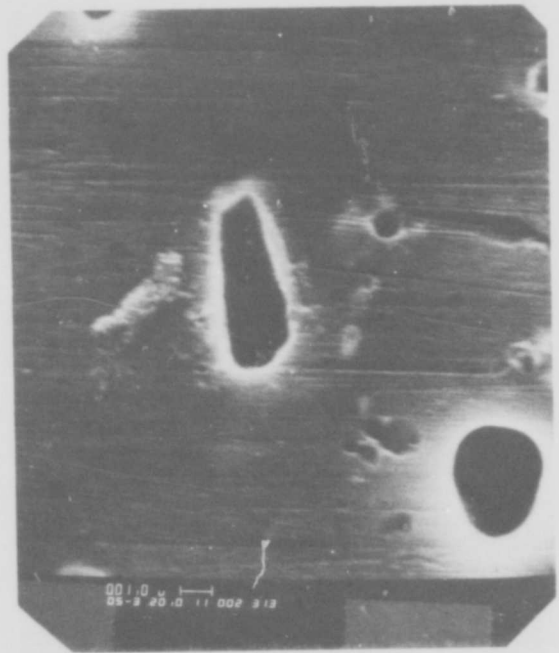
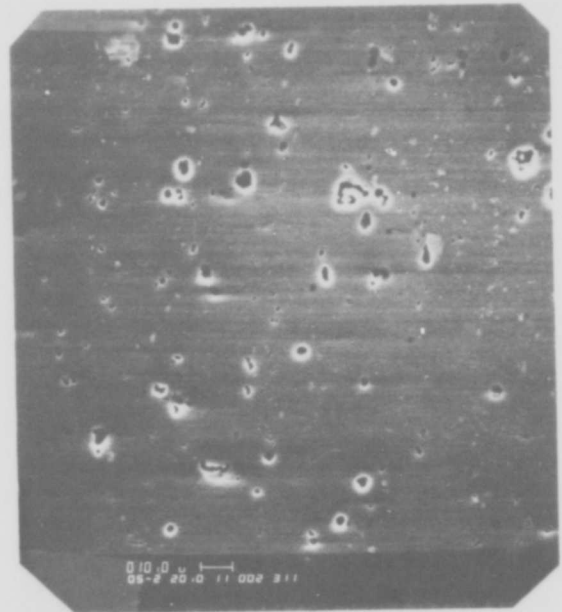
Figure 37 SEM pictures of FPL etched Al 2024-T3 after 21 hrs. at 100°C water (boiled dry) (top), 21 hrs., 50°C water (bottom)

pictures at the left were taken in an area of minimum stress during bending. Estimates of the oxide film thickness is 22000 Å for the 50°C soak and 5000 Å for the 100°C soak. Comparison of the pictures at the left of Fig. 37 with 31, 32 and 33 again illustrates how different the oxide films are for different initial surface preparations.

#### 4.4 Phosphoric Acid Anodized Al2024-T3

Figure 38 shows SEM pictures for polished Al 2024-T3 (left side) and polished plus phosphoric anodize at 10V, 20 min (right side). Figure 39 shows different magnifications of an anodized sample that was previously electropolished. A scratch was placed on the surface in hopes of revealing the edge of the anodic film. The true thickness is distorted but appears to be less than 1 $\mu$ . The film thickness is established to be  $\approx$  2000 Å by ellipsometry.

Figures 40 and 41 show SEM pictures of FPL etched Al 2024-T3 that had been anodized in phosphoric acid under varying conditions. The pictures at the left in Fig. 40 and 41 reveal the etch pattern through the anodic film. In spite of the attempt to prepare each sample with identical etch process, the etch patterns are quite different. Figures 40a and 41a show grain boundary attack in addition to pitting within grains. No grain boundary attack is observed in Fig. 40c and 41c and the pitting in Fig. 41c is considerably more advanced than for Fig. 40c. Estimates of the film thickness from the pictures at the right of Figures 40 and 41, range from 1000 Å to 4000 Å, i.e., small with respect to the pit dimensions. These results indicate the macroscopic roughness is sensitive to the surface pretreatment (FPL etch) which in turn is probably related to metallurgical surface differences from one sample to another. The macroscopic roughness is insensitive to the phosphate - anodize whereas ellipsometric results indicate that microscopic roughness is greatly diminished.



Electropolished

Anodized

Figure 38 SEM pictures of electropolished (left) and phosphoric-anodized (right) Al 2024-T3.

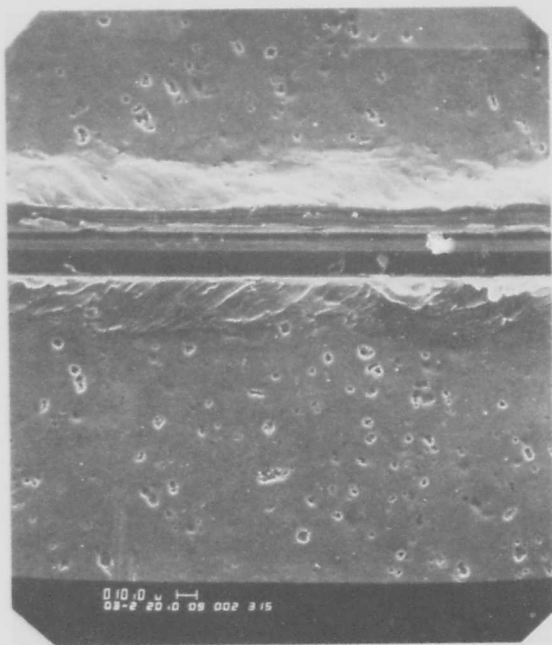
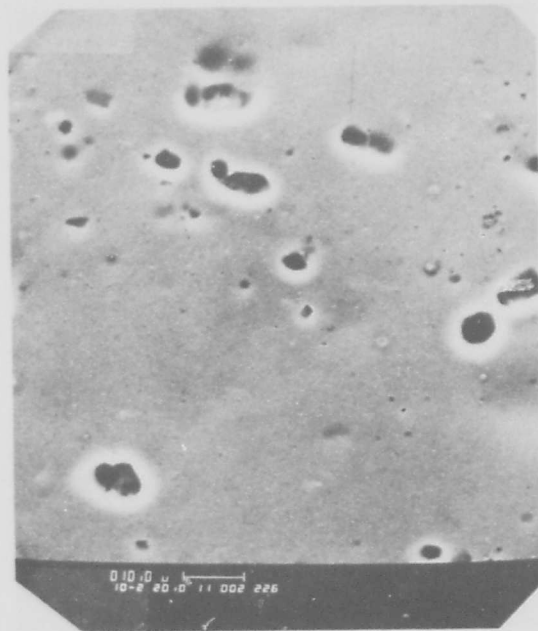
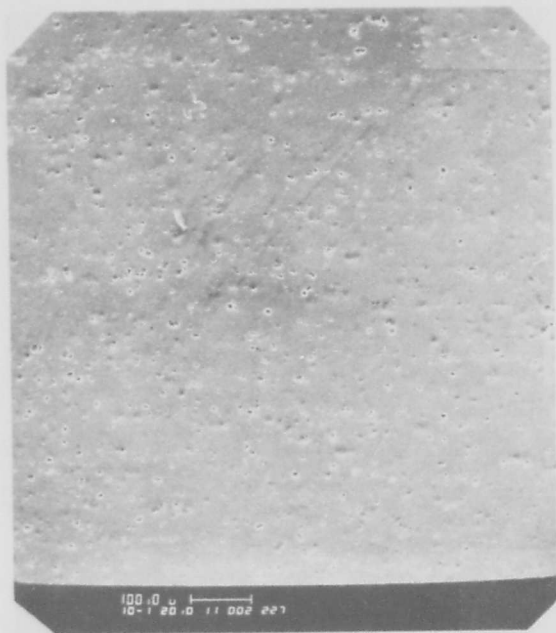
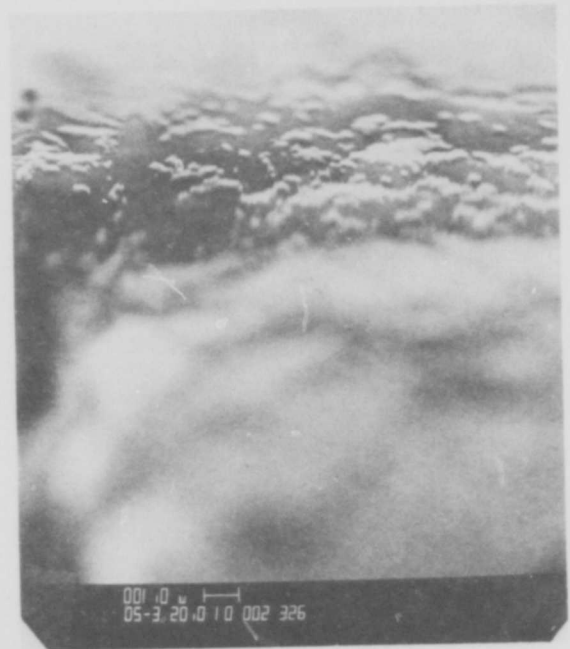
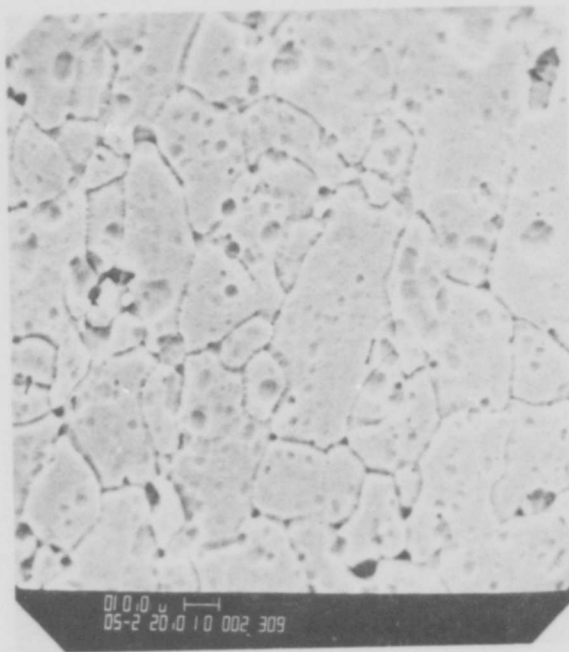
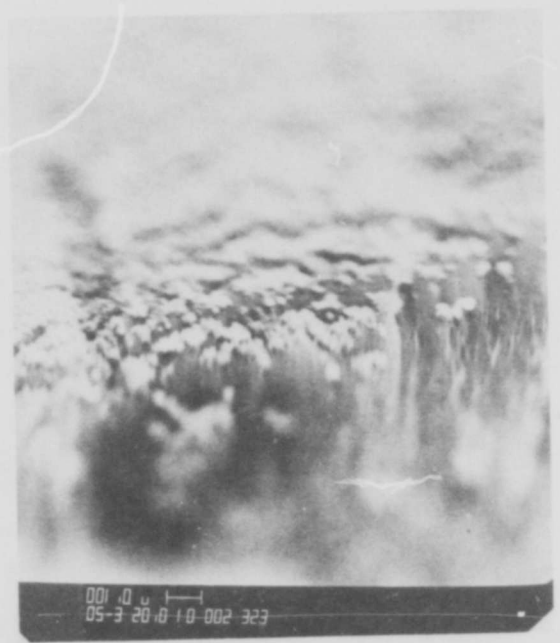
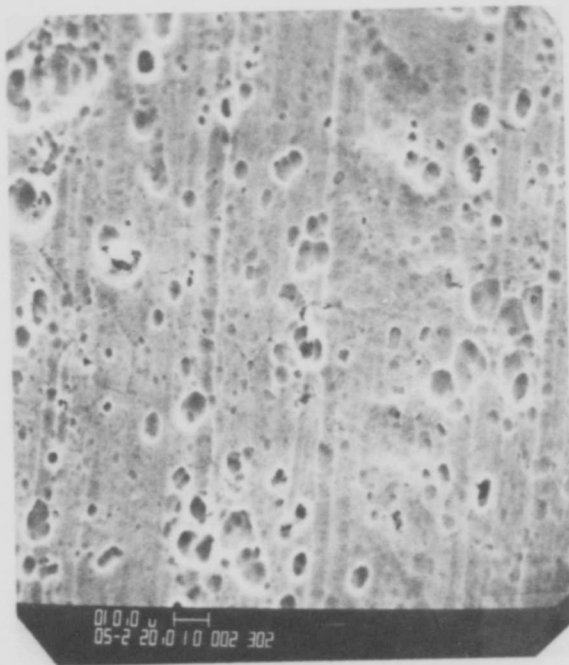


Figure 39 SEM pictures of phosphoric-anodized Al 2024-T3 after electropolished.



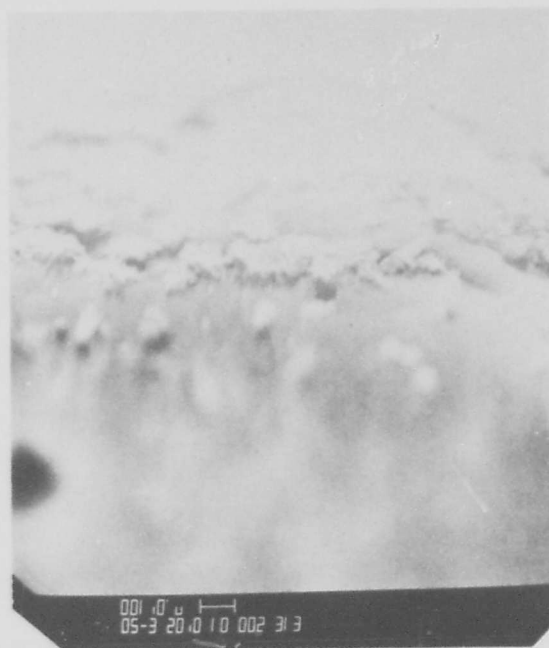
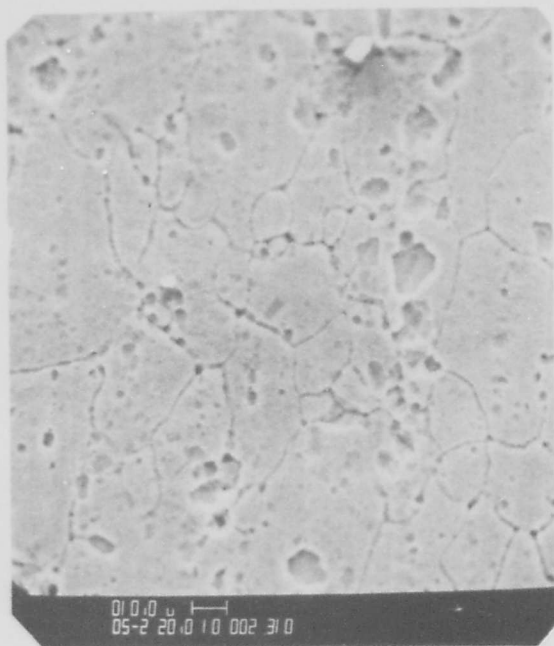
a (P-11, 10%  $H_3PO_4$ , 4V, 22 min) b



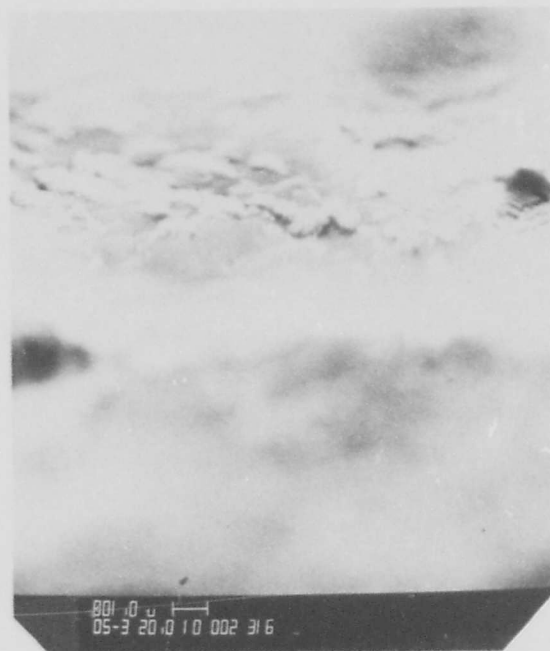
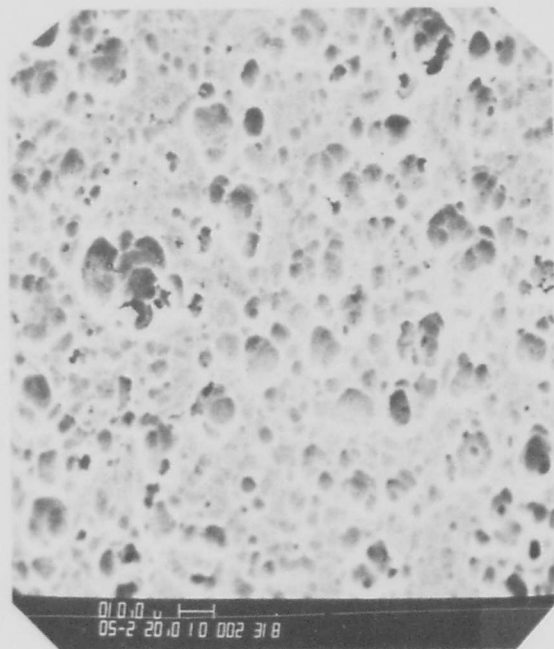
c (P-10, 10%, 10V, 22 min) d

Figure 40 SEM pictures of anodized samples P-11 and P-10. Right side shows bent areas to estimate film thickness.





a (P-12, 10%, 16V, 22 min) b



c (P-20, 15%, 16V, 32 min) d

Figure 41 SEM pictures of anodized samples P-12 and P-20.

#### 4.5 Physical Properties of Al 2024-T3 Surfaces

Table 10 gives a summary of the physical surface properties of Al 2024-T3 before and after exposure to 50°C water and 96°C water. The initial surface treatments were degrease, electropolish and alkaline clean and FPL etch. Because of the cyclic nature of the ellipsometric parameters  $\Delta$  and  $\psi$ , the film thickness cannot be obtained unless  $\Delta$  and  $\psi$  are tracked during film growth. The values of film thickness in Table 10 were obtained by ellipsometry for thin films and by SEM for thick films. Values for SPD group according to the initial surface treatment, = 1 volt for degreased, ~0.4 volts for electropolish and alkaline cleaned and ~0.2 volt for FPL etch. It is surprising that SPD is not greatly affected by the presence of thick hydroxide films. The water contact angle  $\phi_{H_2O}$  is quite low except for samples that were only degreased. Auger spectroscopy has revealed that these samples have a monolayer of hydrocarbon. Apparently the monolayer remains mostly at the oxide - metal interface during hydroxide film formation. The smoothest surface, with respect to the vertical dimension,  $\sigma$ , is obtained with the electropolished pretreatment as might be expected. As received, degreased, alkaline cleaned and FPL etched surfaces have similar values of  $\sigma \sim 0.2\mu$ , about twice as rough as the electropolished samples. Exposure to 50°C and 96°C distilled water has little effect on  $\sigma$ , except in the case of 96°C exposure of degreased and electropolish - alkaline clean, which increases  $\sigma \sim 0.36\mu$ . It should be noted that the roughness measured by light scattering ( $\sigma$ ) and ellipsometry are microscopic in nature ( $\sim 0.1\mu$ ) in contrast to the macroscopic roughness ( $>1\mu$ ) observed by SEM.

Table 11 is a summary of the physical properties of Al 2024-T3 before and after phosphoric acid anodize, boiling water soak and aging in lab air for 720 hours. There is approximately a linear relation between oxide thickness and anodic voltage (i.e.  $\sim 225 \text{ \AA/volt}$ ) for a given anodize time (22 min.). There

TABLE 10

PHYSICAL PROPERTIES OF Al 2024-T3 BEFORE AND AFTER HYDROXIDE FILM FORMATION.

	$\Delta$	$\psi$	Film Thickness $\text{\AA}$	SPD (volts)	$\phi_{\text{H}_2\text{O}}$ (deg)	Roughness $\sigma$ ( $\mu$ )	T ( $\mu$ )	Hydroxide
Degrease	104	34	240	0.95	65	0.20	24	
Degrease + 21 hrs. in 50°C water	122	38		0.91	11	0.20	53	Bayerite
Degrease + 21 hrs. in 90°C water	213	66	10,000	1.46	3	0.36	11	Boehmite
Electropolish	132	40	67	0.76	15	0.11	55	
Electropolish + Alkaline Clean	101	37	280	0.42	-	-	-	
Electropolish + Alk. Clean + 21 hrs. 50°C water	80	41	-	0.40	10	0.20	114	Bayerite
Electropolish + Alk. Clean + 21 hrs. 96°C water	212	48	-	0.41	23	0.36	228	Boehmite
FPL etch	115	38	114	0.20	5	0.20	40	
FF - 21 hr. in air.	104	39	260	0.28	7	0.23	30	
FPL + 21 hr. 50°C water	102	40	22,000 (SEM)	0.07	5	0.21	35	Bayerite
FPL + 21 hrs. 98°C water	110	36	5,000 (SEM)	0.25	5	0.21	34	Boehmite

TABLE 11

PHYSICAL PROPERTIES OF Al 2024-T3 BEFORE AND AFTER  
PHOSPHORIC ACID ANODIZE AND BOILING WATER SOAKS.

Treatment	$\Delta$ (deg)	$\psi$ (deg)	Film Thickness (Å)	SPD (volts)	$\phi_{H_2O}$ (deg)	Roughness		PEE $\times 10^{-11}$ (amps)
						$\sigma$ ( $\mu$ )	T ( $\mu$ )	
V.D.	104	34	260	0.95	67	0.20	24	20
Mechanical and electropolish	132	40	50	0.76	15	0.11	55	27
Phosphoric acid anodize								
Volts								
Time (min)								
30	3	81	45	615	-0.45	5	-	-
10	10	87	45	760	0.0	5	-	-
10	15	231	45	1,984	0.0	5	-	-
10	20	212	42	2,900	-0.11	5	0.15	34
10	10							
boil in water	84	44	600	0.0	5	-	-	-
10	22							
SET to lab air 720 hrs. after	179	40	2,250 (~2,000 SEM)	-0.1	5	-	-	0.1

is also approximately a linear increase in thickness ( $\sim 225 \text{ \AA}$  /min) with time at constant voltage above about 5 volts and 6 minutes. Anodizing has a tendency to smooth the surface on a microscopic scale.

The most interesting features of the phosphate anodize are that the anodic film inhibits film growth for short time exposure to boiling water (e.g. 1 hr. Table 11) and that long surface exposure time (SET 700 hr.) in laboratory air does not degrade the surface with respect to wettability. (i.e. the water contact angle remains  $\sim 5^\circ$ ). It is demonstrated in Table 12 that regardless of the surface pretreatment the anodic film has approximately the same properties. The physical properties of an as received sample, a degreased sample and a contaminated FPL etch sample are given at the top of Table 12. After anodizing all of these samples produced a  $3000 \text{ \AA}$ , wettable film. It is these features that probably account for the excellent bond exposure time (BET) behavior of the phosphate anodize surface preparation. The anodic film provides a high energy surface with wettable character and yet is very inactive with respect to adsorption of organic contamination.

#### 4.6 Chemical Properties of Al 2024-T3 Surfaces

Experiments were performed to see if a relationship exists between the Auger peak to peak heights (APPH) for various elements or the ratio of APPH of one element with respect to another, and the atomic concentrations. Due to the many parameters involved and charging of the oxide layers, no reproducible correlations could be obtained. However, similar experiments with ESCA proved to be more satisfactory.

Table 13 is a summary of the chemical properties, of various films of aluminum oxide, obtained with ESCA. Alumina crystals were used as standards to obtain relative peak heights of a compound with known oxygen to aluminum ratio. The carbon impurity  $1\text{ s } 1/2$  peak was adjusted to 284.3 eV in each case to

Table 12

## EFFECT OF PRETREATMENT ON ANODIC FILM

Pretreatment	(deg)	(deg)	Film Thickness Å	SPD (volts)	PEE (ampx10 <sup>-11</sup> )	ΦH <sub>2</sub> O (deg)
As received	0.6	52.9	-	0.45	0.8	70
MEK degreased	90.0	34.2	190	0.56	0.1	60
FPL etch	113.6	36.8	120	0.37	28.0	40

16V, 22 min., 10% by wt H<sub>3</sub>PO<sub>4</sub> Anodize

As received	108.0	44.3	3,075	-0.15	1.5	7
MEK degreased	115.0	48.4	3,100	-0.23	0.1	6
FPL etch	112.1	44.8	3,090	-0.36	0.9	3

TABLE 13

## CHEMICAL PROPERTIES OF Al 2024-T3 AFTER VARIOUS SURFACE TREATMENTS

Treatment	Element	Photoline	Relative Peakheight	Relative Conc.	Binding Energy	Chemical Shift	Oxide or Hydroxide
Standard Al <sub>2</sub> O <sub>3</sub>	O	251/2	7,500	0.614	530.3		Al <sub>2</sub> O <sub>3</sub> alumina
	Al	151/2	2,273	0.186	118.1		
	C	151/2	2,444	0.200	284.3		
			<u>12,217</u>				
Al2024-T3 21 hrs. 50°C Water	O		18,167	0.821	531.2	0.9	Al <sub>2</sub> O <sub>3</sub> (H <sub>2</sub> O) 2.4
	Al		3,045	0.138	118.4	0.3	
	C		750	0.034	284.3		
	F	151/2	156	0.007			
			<u>22,118</u>				
Anodic 500A 21 hrs. 50°C Water	O		10,500	0.733	531.1	0.8	Al <sub>2</sub> O <sub>3</sub> (H <sub>2</sub> O) 1.6
	Al		2,045	0.143	118.4	0.3	
	C		1,667	0.116	284.3		
	Pb	4f7/2	111	0.008	138.4		
				<u>14,323</u>			
Anodize, 10V, 10min. Table II	O		20,892	0.670	531.0	0.7	Al <sub>2</sub> O <sub>3</sub> (H <sub>2</sub> O) 0.6
	Al		5,342	0.171	119.0	0.9	
	C		4,474	0.143	284.3		
	P	251/2	313	0.010	192.0		
	Si	251/2	128	0.004	154.0		
	Mn	3P1/2,3/2	43	0.001	50.0		
				<u>31,189</u>			
Anodize, 10V, 10min. + boil in water Table II	O		6,000	0.621	531.1	0.8	Al <sub>2</sub> O <sub>3</sub> (H <sub>2</sub> O) Boehmite
	Al		1,364	0.141	118.5	0.4	
	C		1,852	0.192	284.3		
	P		145	0.015	191		
	N	251/2	256	0.026	269.2		

(continued)

Table 13 (cont'd)

Another Al <sub>2</sub> O <sub>3</sub> Standard	O	14,167	0.707	530.8	Al <sub>2</sub> O <sub>3</sub> alumina
	Al	4,318	0.215	118.6	
	C	1,556	0.078	284.3	
		<u>20,041</u>			
Fresh FPL etch	O	13,750	0.751	531.7	Al <sub>2</sub> O <sub>3</sub> (H <sub>2</sub> O) 0.7
	Al	3,864	0.211	119.2	
	C	585	0.037	284.3	
		<u>18,299</u>			
Fresh FPL etch After 3.5 hours in Vacuum	O	11,974	0.706	531.6	Al <sub>2</sub> O <sub>3</sub> 2.7
	Al	4,000	0.236	119.2	
	C	981	0.058	284.3	
FPL etch + age	O	7,708	0.412	531.1	Al <sub>2</sub> O <sub>3</sub> (H <sub>2</sub> O) 0.1
	Al	2,273	0.122	118.4	
	C	8,704	0.466	284.3	
		<u>18,685</u>			



correct for charging. The binding energies are therefore relative to the carbon. The column labelled chem. shift gives the difference in binding energy between the oxygen and aluminum of the oxide films and standard  $\text{Al}_2\text{O}_3$ . The relative peak heights were obtained by multiplying the maximum number of divisions on the recorder paper, for a particular peak, by the number of counts per division and dividing by the number of scans and the cross section for the particular element. The relative concentration was obtained by dividing the relative peak height by the total of all the relative peak heights. This procedure is incorrect but gives a first order approximation for the relative concentration of the impurities. For example, the ratio of the relative concentrations for O and Al in the standard  $\text{Al}_2\text{O}_3$  should be 1.5 as compared to 3.3 from Table 13. Therefore, the formulas at the right of Table 13 are derived from the ratio of the relative concentration of O to Al multiplied by the correction factor  $1.5/3/3 = 0.45$ . It should be noted that this correction factor is the same for both  $\text{Al}_2\text{O}_3$  standards in Table 13 in spite of the fact that the first standard has three times as much carbon contamination. The last column in Table 13 gives the hydrate that corresponds to the oxygen to aluminum ratio. The  $50^\circ\text{C}$  exposure to distilled water yields a pseudo bayerite ( $\text{Al}_2\text{O}_3(\text{H}_2\text{O})_{1.6-2.4}$ ) rather than bayerite ( $\text{Al}_2\text{O}_3(\text{H}_2\text{O})_3$ ). The foamy structured film seen in Figures 20, 21, 22 (beneath the bayerite crystals in 23 and 24), 26, 31, 33 and 37 is pseudo-bayerite. The phosphoric acid anodic film formed at 10 volts for 10 min. is pseudo boehmite ( $\text{Al}_2\text{O}_3(\text{H}_2\text{O})_{0.6}$ ) which transforms to boehmite ( $\text{Al}_2\text{O}_3(\text{H}_2\text{O})$ ) upon boiling in water. The FPL etched Al 2024-T3 yields oxide with formula  $\text{Al}_2\text{O}_3(\text{H}_2\text{O})_{0.3}$ , somewhat less hydrated than boehmite. After 3.5 hours in the vacuum system the formula is reduced to  $\text{Al}_2\text{O}_{2.7}$  indicating a dehydration by the vacuum. More work is needed to determine

what effect the vacuum may have had in lowering the estimated hydration for the other films. There is a definite chemical shift for Al (~0.4 ev) and oxygen (~0.9 ev) upon hydration of  $\text{Al}_2\text{O}_3$  but within experimental error it is the same for boehmite or bayerite.

##### 5. The Effect of Controlled Contamination

It is well known that organic contamination from laboratory or factory atmosphere can degrade a surface with respect to bond strength, yet little is known about what the organic contamination is, how much is present or how much is needed to appreciably degrade the bond. In order to calibrate our instruments and learn more of the effect of organic contamination on bond strength, we have prepared samples with contamination of known molecules.

Controlled contamination is accomplished by placing a crystal of an organic carboxylic acid on the surface of clean water. If the chain length of the molecule is not too long, molecules spread quickly over the water surface to form a monolayer at equilibrium surface pressure. Dipping the metal sample through the monolayer transfers part of the film to the metal. As the molecules are removed by dipping, they are replenished to the water surface from the crystal. We have used two fatty acids, myristic acid and erucic acid. Myristic acid has a saturated hydrocarbon chain  $\text{CH}_3(\text{CH}_2)_{13}\text{COOH}$  and is 23 Å long with a diameter of 4.2 Å. Erucic acid has a double bond with both hydrogen atoms on the same side of the double bond  $\text{cis-CH}_3(\text{CH}_2)_7\text{CH}=\text{CH}(\text{CH}_2)_{11}\text{COOH}$  and is 30 Å long with an effective diameter of 6.28 Å. Films were deposited on vapor deposited (1588 Å) aluminum mirrors that were extremely smooth and upon FPL etch 2024-T3 aluminum which is very rough, in order to establish the effect of roughness.

## 5.1 Contamination with Myristic Acid

### 5.1.1 Smooth Surfaces

Figure 42 is a plot of  $\Delta$ ,  $\psi$ , SPD and PEE (left ordinate) and water contact angle  $\phi_{H_2O}$  (right ordinate) vs the number of dips of the aluminum mirror through a myristic acid monolayer on water. The data between 0 and 1 dip is for dipping the sample in clean water prior to spreading the myristic acid. Values of  $\psi$  and  $\Delta$  indicate the mirror had about 60 Å of oxide that grew to about 90 Å upon exposure to water. The additional oxide caused SPD to drop 0.2 volts and the PEE to drop from  $240 \times 10^{-11}$  amps to  $200 \times 10^{-11}$  amps. Dipping the mirror through myristic acid monolayers on water decreased  $\Delta$  and PEE and increased SPD as the film was transferred. The first dip deposited a layer with average film thickness of 11 Å. This film increased the contact angle from 20° to 89°. Although the film increased to about 24 Å by the third dip,  $\phi_{H_2O}$  remained essentially constant after the first dip. Myristic acid was not transferred to the mirror after 3 dips although SPD decreased, indicating some molecular reorientation. Note that for the very smooth mirror  $\psi$  has the correct theoretical value and does not change appreciably. The theoretical increase in  $\psi$  for 24 Å of film of refractive index 1.5 is 0.06°.

### 5.1.2 Rough Surfaces

Figure 43 is a plot of  $\Delta$ ,  $\psi$ , SPD, PEE and  $\phi_{H_2O}$  vs number of dips of the rough FPL etched Al2024-T3 through myristic acid on water. In this case, between 0 and 1 dip, approximately 0.4 monolayers was deposited on the water surface in a hexane solution. The oxide on the etched sample was 105 Å and the roughness parameter  $\sigma \sim 0.2$ . The 0.4 monolayers of myristic acid increased  $\phi_{H_2O}$  from 3° to 50° and 1 dip increased it to 104°. The initial 105 Å of oxide has dropped the SPD to ~0.44 volts close to that for vapor deposited aluminum after water exposure, although the PEE is dropped to  $90 \times 10^{-11}$  amps as compared to

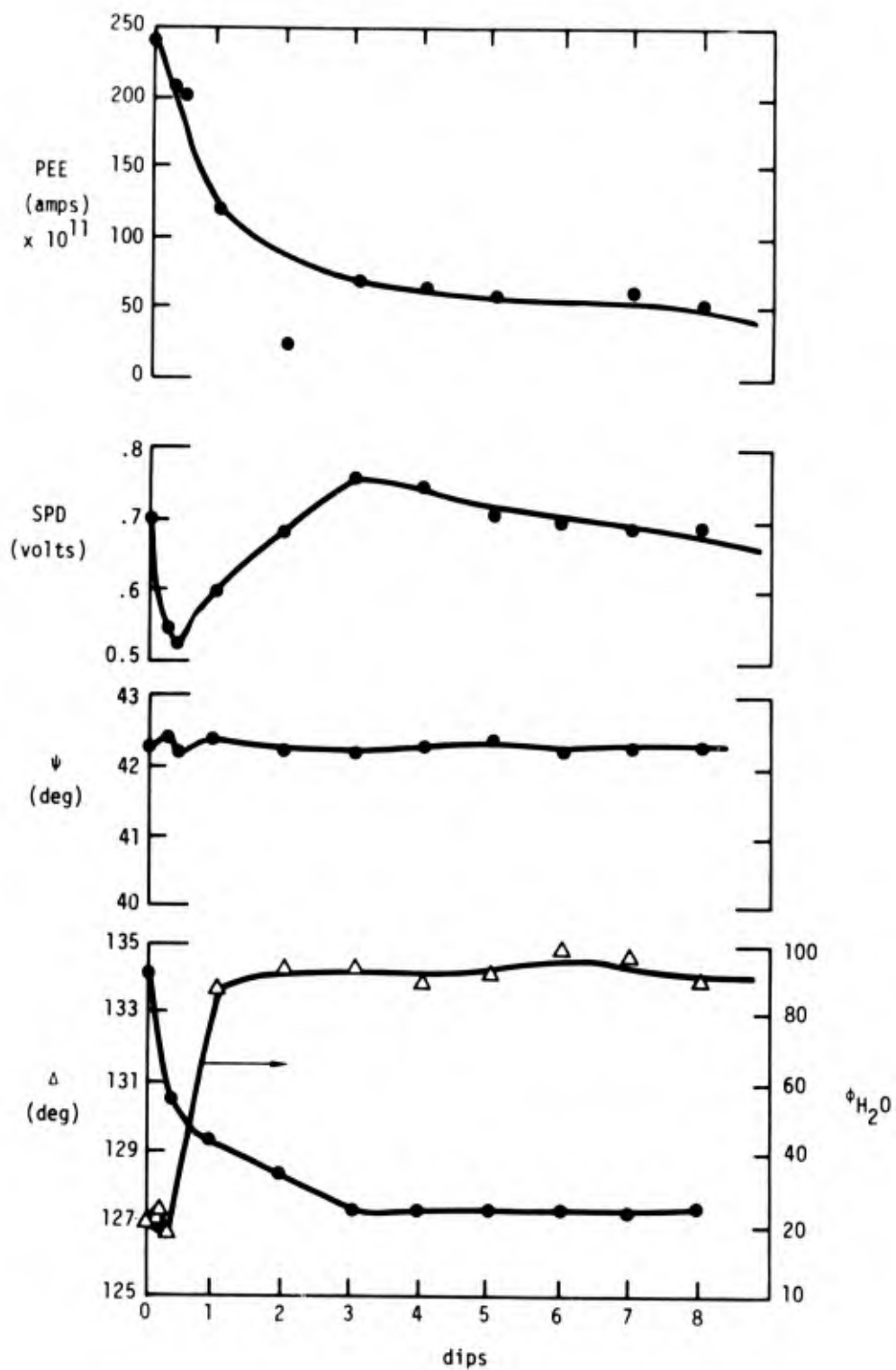


Figure 42. Plot of  $\Delta$ ,  $\psi$ , SPD and PEE vs number of dips through myristic acid on water, 1588 Å Al/Au/Cr/Glass.

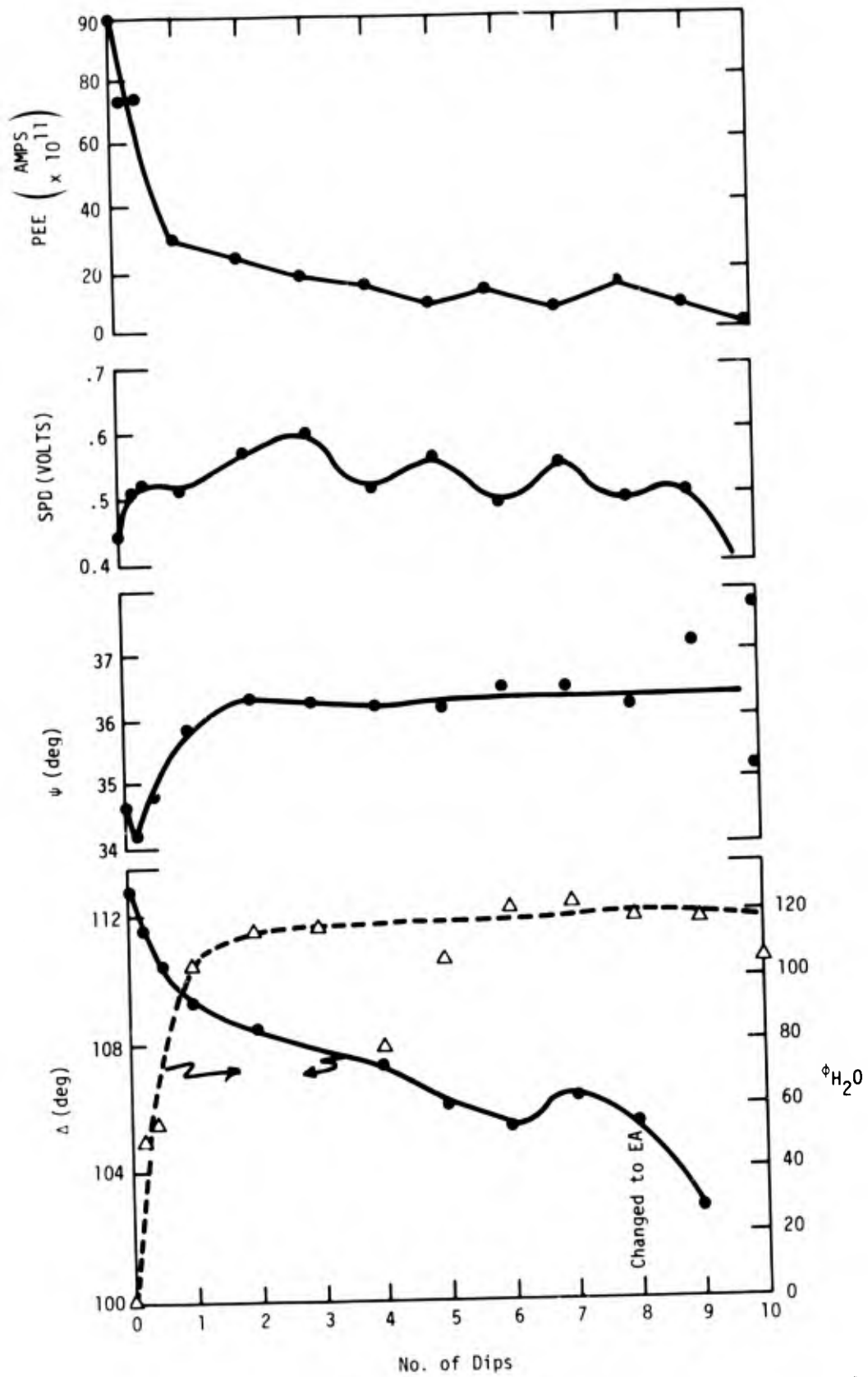


Figure 43. Plot of  $\Delta$ ,  $\psi$ , SPD and PEE vs number of dips through myristic acid on water, Al 2024-T3.

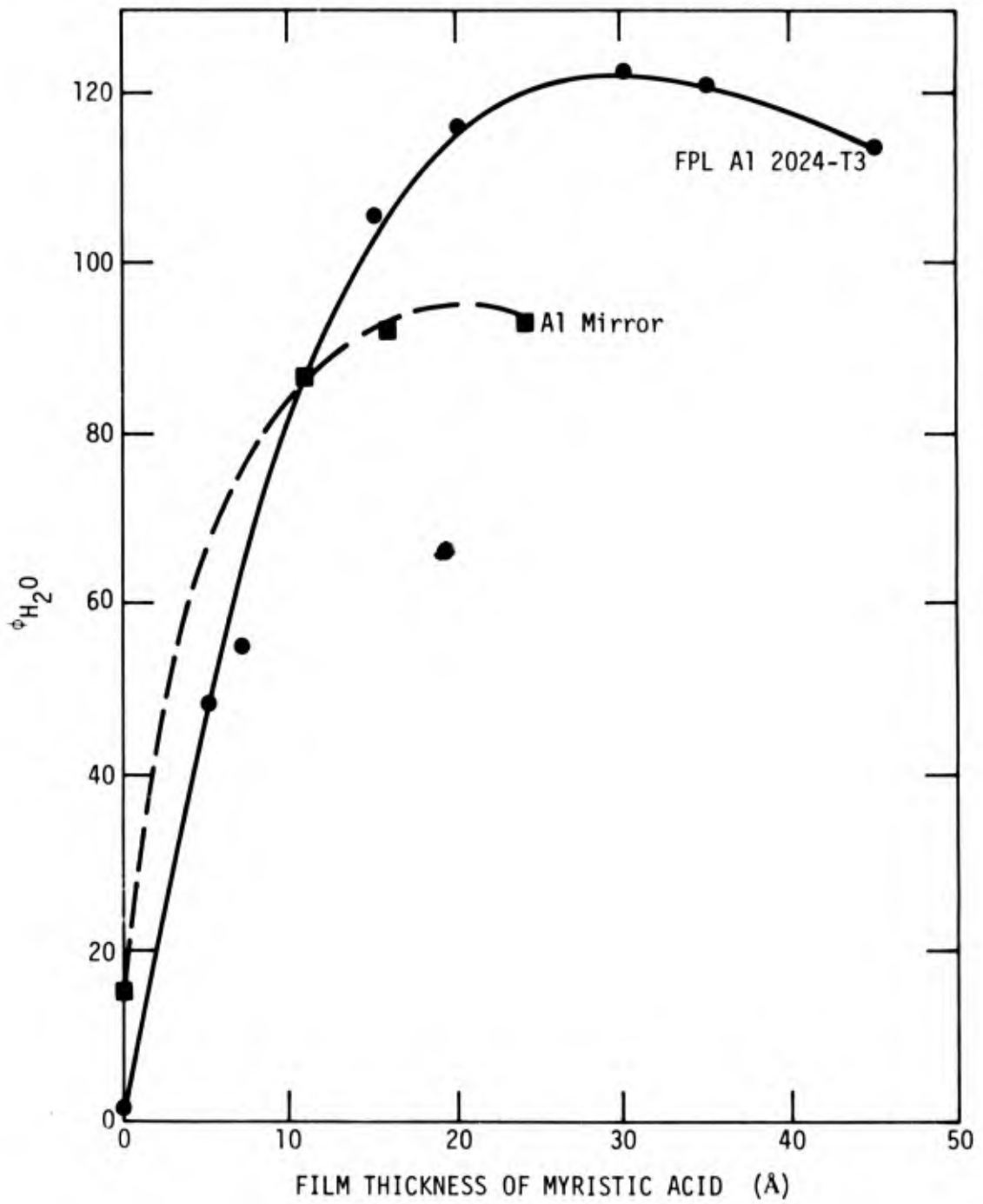


Figure 44. Plot of  $\phi_{H_2O}$  vs film thickness of myristic acid.

$200 \times 10^{-11}$  amps for the mirror. The rough sample causes film pickup through 9 dips (continually decreasing  $\Delta$ ) and causes SPD to alternate between a higher and lower value for odd and even dips. This is probably due to changes in dipole orientation from one dip to the next. The effect of extreme roughness is two fold, the initial value of  $\psi$  is far below the theoretical value for a smooth surface and the increase in  $\psi$  with myristic acid is far greater than theoretical for a smooth surface for the first two dips. Both of these trends are predicted by the theory of Ohlidal and Lukes<sup>17</sup> for correction of ellipsometric data for roughness. Figure 44 is a plot of the water contact angle vs myristic acid film thickness for the smooth and rough surfaces. In each case the contact angle reaches approximately the maximum value for one monolayer (if it's chains are erect) of myristic acid ( $\sim 23\text{\AA}$ ). Figure 45 is a semi log plot of the photo emission current  $I$  vs myristic acid film thickness. The current can be expressed by the equation

$$I = 52 \times 10^{-11} e^{-d/12.6} \text{ (amps) .}$$

The attenuate length of  $12.6\text{\AA}$  is about half that for oxide indicating the higher attenuation power of the organic acid.

### 5.1.3 AES Calibration

To calibrate Auger spectroscopy a 4"x1"x0.063" sample was FPL etched then dipped into clean water to a depth of two inches. The sample was withdrawn 1/2 inch to provide an area exposed to water. At this point 0.5 cc of a solution of myristic acid - in hexane was deposited on the water surface. The solution contained just enough myristic acid to place 0.1 monolayers on the water surface. The sample was withdrawn 1/2 inch more and more solution was deposited to provide 0.5 monolayers. The sample was withdrawn 1/2 inch and enough solution added to provide a monolayer on the water. Each of the areas were labelled as follows 0 - FPL etch, 1 - FPL etch, 2 - FPL + dip in

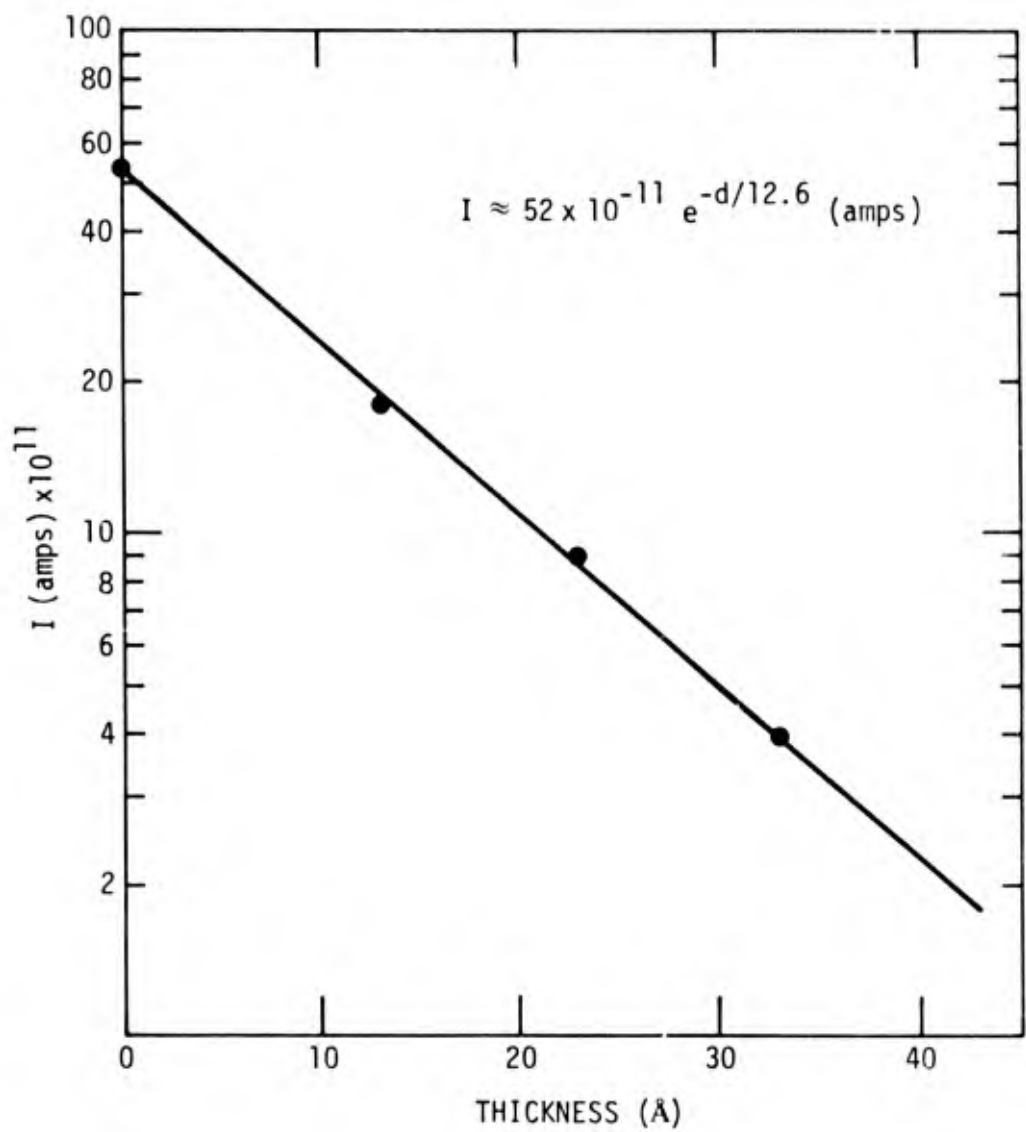


Figure 45. Plot of  $I$  vs film thickness of myristic acid on FPL etched Al 2024-T3.



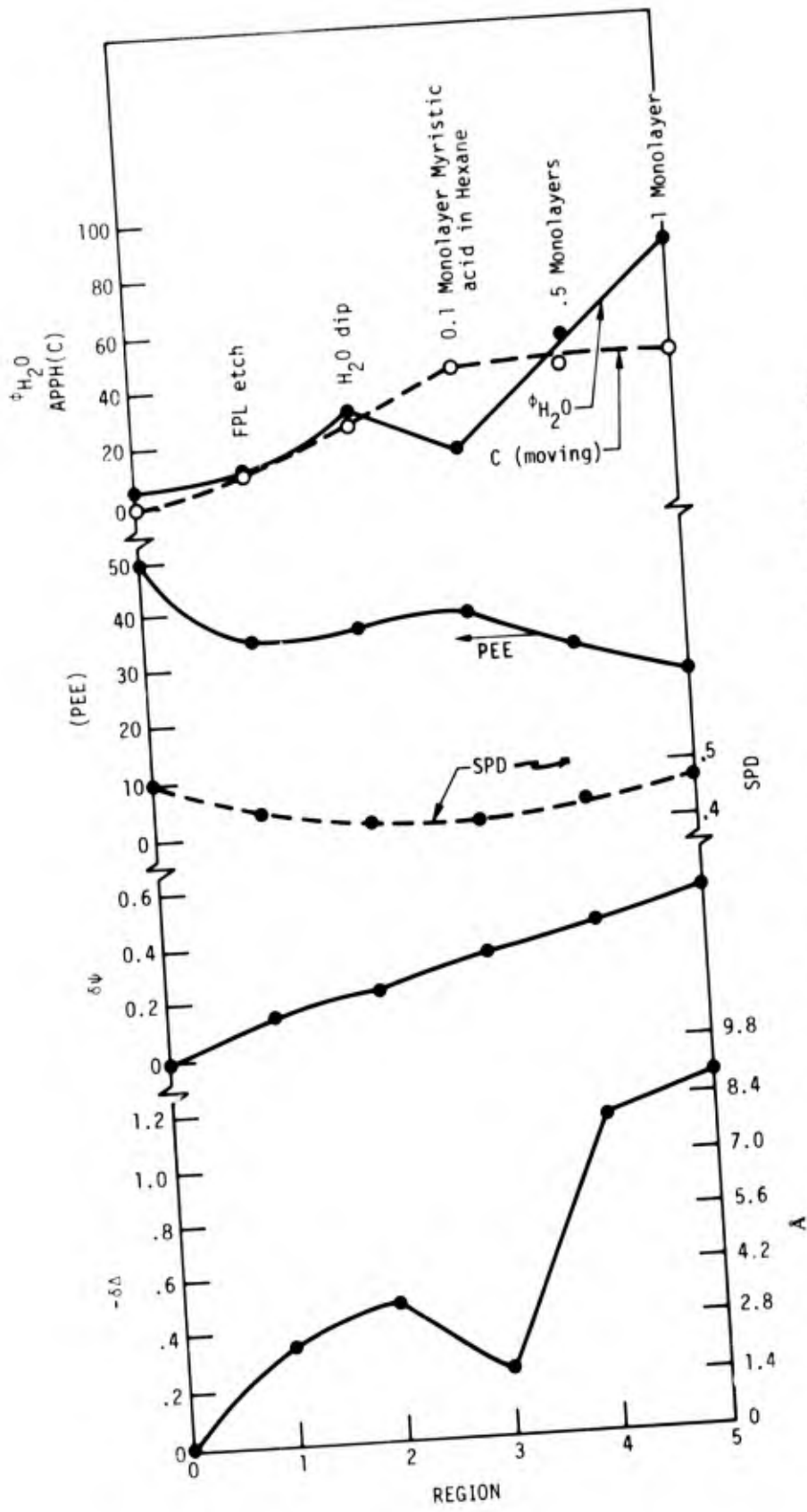


Figure 46. Plot of  $-\delta\Delta$ ,  $\delta\psi$ , PEE,  $\phi_{H_2O}$  and APPH(C) vs different treated regions of Al 2024-T3 sample.

water, 3 - FPL + hexane with 0.1 monolayer, 4 - FPL etch + 0.5 monolayers, 5 - FPL etch + 1 monolayer. Measurements of  $\Delta$ ,  $\psi$ , SPD, PEE and  $\phi_{H_2O}$  were made in each area. The sample was then placed in the UHV system for AES in each area. It was discovered that exposure to the electron beam removed the myristic acid and the carbon peak would quickly decrease and disappear during AES. It was therefore necessary to measure the carbon peak while the sample was moving with respect to the electron beam. The Auger peak to peak heights (APPH) for carbon are therefore low with respect to actual carbon presence prior to AES.

The effect of each treatment step in areas 0 through 5 is shown in Fig. 46. The changes in all of the parameters indicate that region 2 had picked up some contamination from the water dip and that the contamination had migrated into region 1. Deposition of the hexane solution prior to withdrawing through region 3 removed most of the contamination rather than deposit 0.1 monolayers on the water. The unknown contamination on the (so called) clean water surface is swept up into the hexane and redeposited as a particle at the point the hexane completes its evaporation. The particle of contamination does not spread rapidly on the water surface; so that  $\delta\Delta$  and  $\phi_{H_2O}$  indicate removal of contamination in region 3 with respect to region 2. The addition of 0.5 and 1 monolayers to the water surface is reflected in all of the parameters except APPH(C). Apparently the electron beam is removing the organic material too fast for the thicker films.

To check the effect of contamination from the water surface an FPL etched sample was 1- dried for 1.5 hours after FPL etch, 2- rinsed 1 sec. in flowing distilled water, 3- dipped for 1 minute in water, etc. as seen in Figure 47. Step 8 was to place 2cc of hexane on the water surface, 9-hexane solution with 0.1 monolayer, 10- .5 monolayers and, 11- 1 monolayer. Figure 47 shows the changes in the parameters. In this case, dipping in water changed the water contact angle only slightly from about 18° but did add about 28 Å

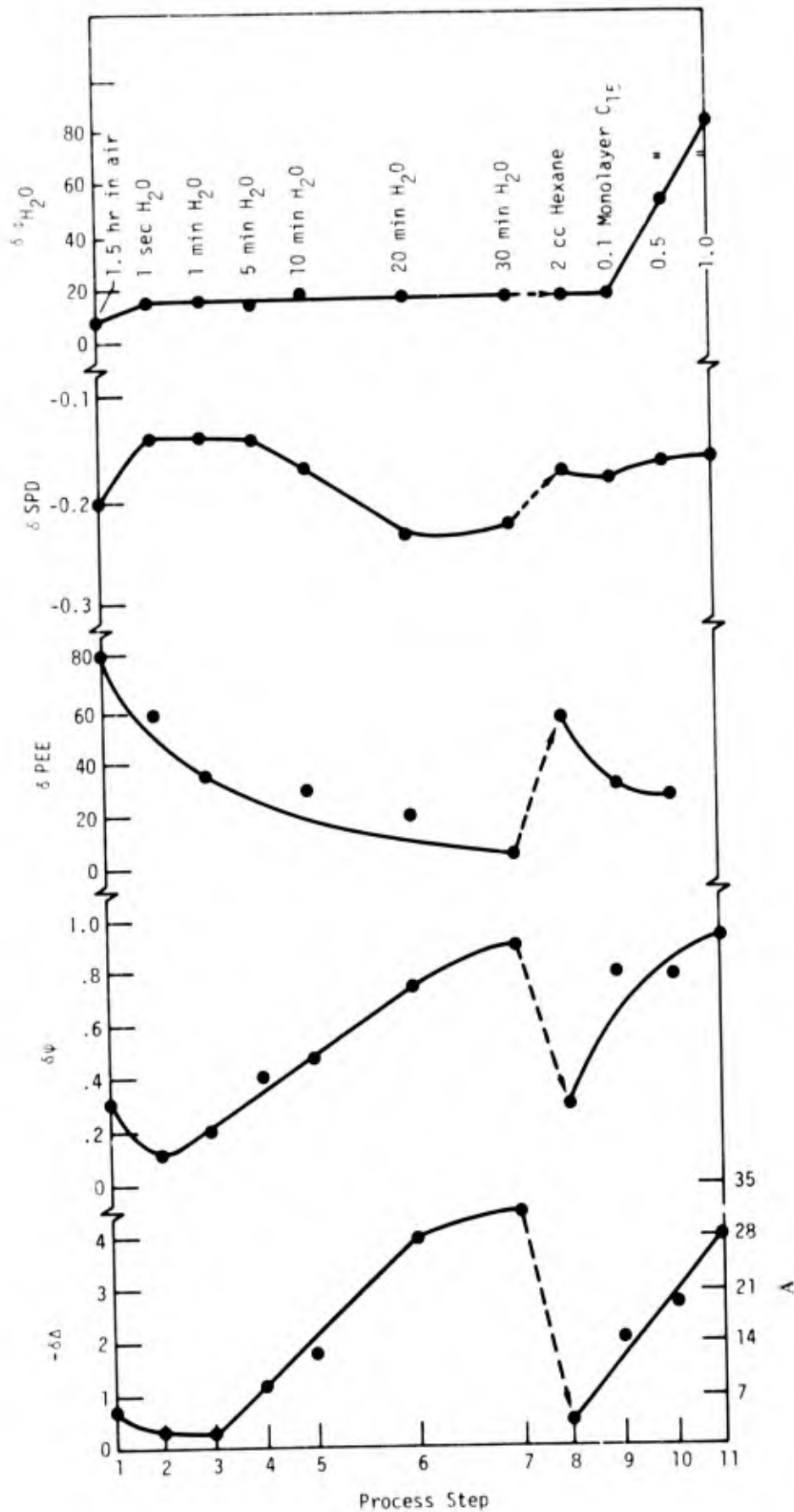


Figure 47. Plot of  $-\delta\Delta$ ,  $\delta\psi$ , PEE,  $\delta(SPD)$ ,  $\delta\phi_{H_2O}$  vs various treated regions of Al 2024-T3.

of contamination. The fact that the contamination was removed by hexane is indicative of its organic nature. The fact that  $\phi_{H_2O}$  changed little is indicative of the polar nature of the unknown contamination. Deposition of myristic acid is reflected in all the parameters and the contact angle increases dramatically due to the non polar nature of the hydrocarbon chain. These results show that regardless of the precautions taken to clean glassware minute amounts of contamination collect on the surface and contaminate metal surfaces as it is removed from the bath. However, this is probably not a problem when rinsing in flowing water.

### 5.2 Contamination with Erucic Acid (EA)

Figure 48 shows  $\Delta$ ,  $\psi$ , SPD and  $\phi_{H_2O}$  for erucic acid deposition on a vapor deposited aluminum mirror. Although myristic acid increased  $\phi_{H_2O}$  to  $90^\circ$  in 1 dip, 8 dips are required for erucic acid. This is probably due to the polarizable nature of the double bond in erucic acid. At 8 dips  $\Delta$  and  $\psi$  correspond to about  $160 \text{ \AA}$  of erucic acid. Again  $\psi$  has the right values for a smooth surface. The sample was left over night between the 17th and 18th dip which increased SPD, decreased  $\phi_{H_2O}$  but had little effect on  $\Delta$  and  $\psi$ . The water surface was cleaned and a new particle of erucic acid was introduced between the 18th and 19th dip. Deposition from the new crystal dramatically increased the change in  $\psi$  per dip and decreased  $\phi_{H_2O}$  in the next 10 dips. Both  $\Delta$  and  $\psi$  show a cyclic nature with a  $10$  dip period. Although myristic acid increased SPD, erucic acid decreased SPD by about 0.5 volts in the first 20 dips, which remained approximately constant thereafter. Figure 49 is a plot of  $\phi_{H_2O}$  and SPD vs erucic acid film thickness. Figure 50 is a plot of PEE and the changes in  $\Delta$ ,  $\psi$  and SPD vs. the number of dips of the rough FFL etched Al2024-T3 through erucic acid monolayers on water. Three identical experiments were performed to check the reproducibility. Although  $\Delta$ ,  $\psi$ , and PEE are fairly reproducible,

SPD is not. The dashed curve below the  $\psi$  data is the theoretical curve for a smooth surface.

### 5.3 Effect of Controlled Contamination on Bond Strength

The effect of  $\sim 3 \text{ \AA}$  of unknown contamination and  $\sim 4 \text{ \AA}$  of myristic acid on surface parameters and bond strength is seen in Table 14. The unknown contamination does not change the water contact angle but the myristic acid increases it by  $36^\circ$ . The unknown contamination decreased SPD by 0.14 volts whereas the myristic acid increases the SPD by 0.05 volts again. Both types of contamination attenuate electrons decreasing PEE. Approximately  $7 \text{ \AA}$  of contamination lowers the bond strength by 300 psi as found previously for another system.

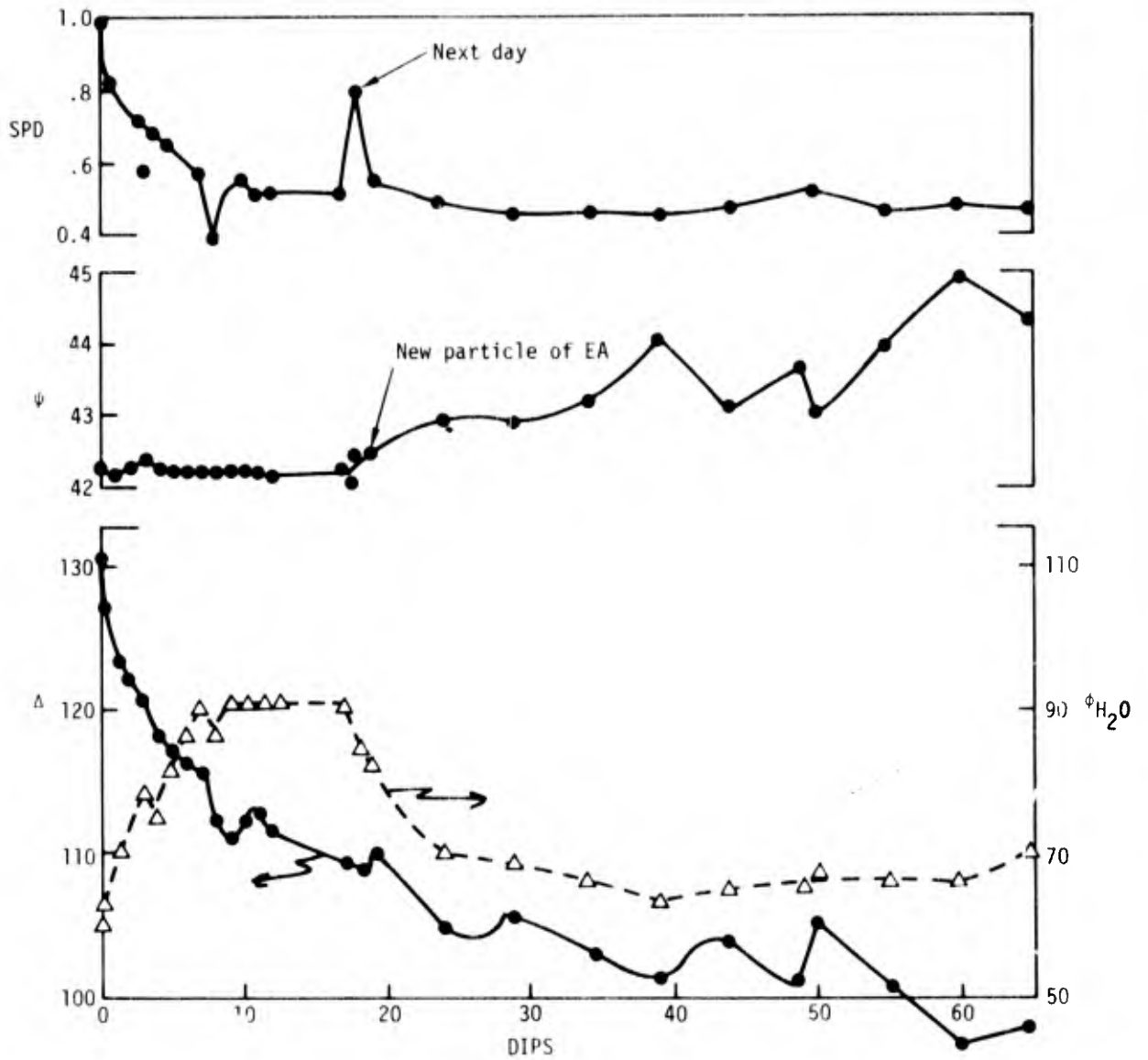


Figure 48. Plot of  $\Delta$ ,  $\psi$ , SPD vs number of dips through erucic acid on water. 1588 Å Al/Au/Cr/glass.

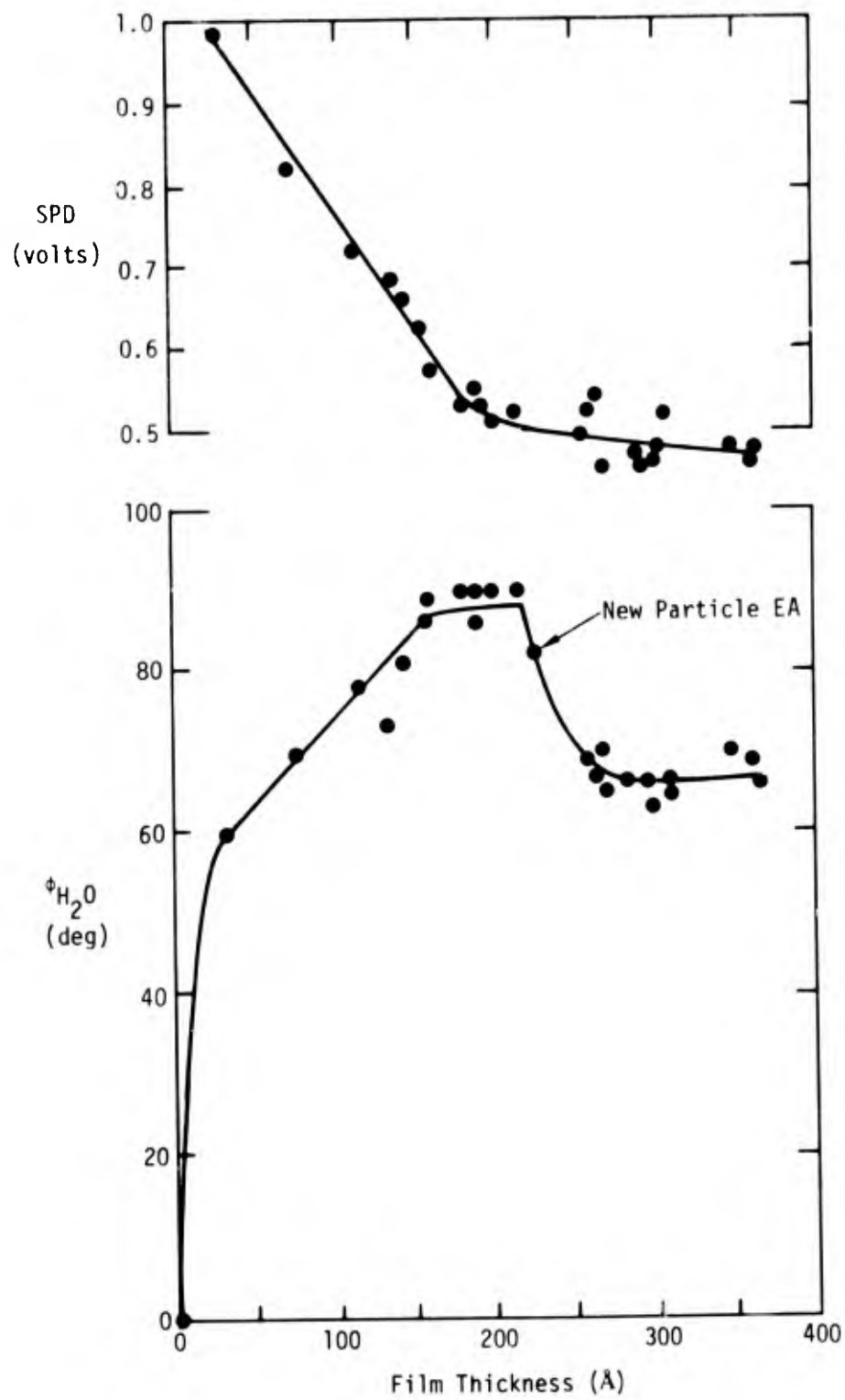


Figure 49. Plot of SPD and  $\phi_{H_2O}$  vs film thickness of erucic acid on Al/Au/Cr/glass.

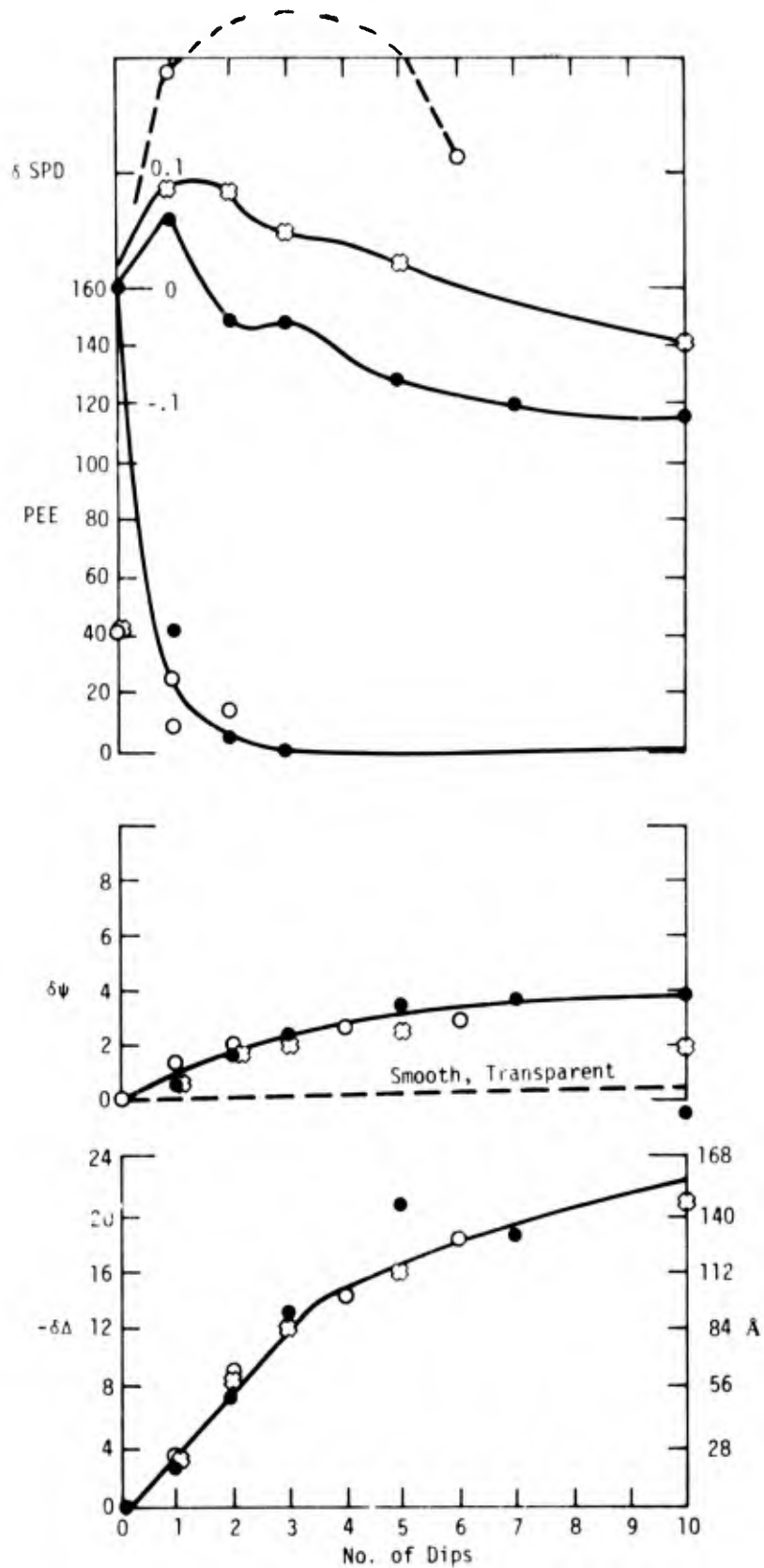


Figure 50. Plot of  $-\delta\lambda$ ,  $\delta\psi$ , PEE and  $\delta$  SPD vs number of dip through erucic on water, FPL etched Al 2024-T3.



Table 14

THE EFFECT OF MYRISTIC ACID ON SURFACE  
PARAMETERS AND BOND STRENGTH

	Contact Angle	$\Delta$ (deg)	$\psi$ (deg)	Thickness $\text{\AA}$	SPD (volts)	PEE $\text{amps} \times 10^{-11}$	$\sigma_b$
FPL	5.5	105.6	38.57	170	0.63	44.5	2917±82
+ Water Dip	5.5	105.0	38.50	173	0.49	29.0	
Effect of Water Dip	0	-0.6	.07	3	-.14	-15.5	-
Monolayer Myristic Acid	41	104.3	38.75	180	0.54	23.7	2593±69
Effect of Mono- layer	36	-0.7	+0.2	4.0	+0.05	-5.3	-324

## 6. The Effect of UV Light on Contamination and Contaminant Removal

It has been discovered on our IR&D project that exposure to UV light (2500 Å), during our photo-electron-emission measurement, changes the surface properties, in particular reducing the contact angle for water. The idea of using UV light to clean a contaminated surface immediately presented itself. To check this effect, an FPL etched Al 2024-T3 sample (0.064"x1"x4") was divided into six regions about 3/8"x1". The regions were labeled 1 to 6 from the top down and the sample was dipped vertically into clean distilled water to the bottom of region 1. After removing the sample to the bottom of region 2 a monolayer of myristic acid was formed on the water surface by placing a crystal of acid on the water. The sample was slowly removed to deposit a monolayer of myristic acid on the regions 3 through 6. Table 15 gives the surface parameters after this treatment.

For this sample the surface parameters were very reproducible from region to region. The effect of a few minutes aging prior to dipping in water was to decrease the SPD by 0.14 volts and decrease PEE by about  $15 \times 10^{-11}$  amps. These changes only slightly affected  $\Delta$ ,  $\psi$  and the contact angle for water. A monolayer of myristic acid increased the film thickness by  $\sim 5$  Å (molecules lying flat) which increased SPD by 0.05 volts and decreased PEE by another  $5 \times 10^{-11}$  amps. The dramatic effect of the monolayer was to increase the contact angle from 5 to 41 degrees. It has been shown previously that the presence of a monolayer can decrease the bond strength of the Al2024-T3 - HT424 system by  $\sim 300$  psi.

### 6.1 Effect of UV Radiation

The data for region 6 in Table 15 are used to determine the surface parameter changes which are plotted as treatment 1, 2 and 3 at the left of Fig. 51. Step 1 was the standard FPL etch, step 2 was deposition of a monolayer of myristic acid and step 3 was

Table 15

## SURFACE PARAMETERS AFTER FPL ETCH AND MYRISTIC ACID TREATMENT

	<u>AFTER FPL ETCH</u>					
	1	2	3	4	5	6
Contact Angle (deg)	5	6	6	5	6	5
SPD (Volts)	0.60	0.61	0.61	0.61	0.64	0.69
PEE (amps x10 <sup>-11</sup> )	44	44	38	44	46	51
Δ (deg)	105.4	105.1	105.6	105.3	105.8	106.4
ψ (deg)	38.5	38.5	38.6	38.6	38.6	38.6

	<u>Treatments (Myristic Acid)</u>					
	none	water	myristic	myristic	myristic	myristic
Contact Angle (deg)	6	5	57	42	30	35
SPD (volts)	0.55	0.49	0.51	0.53	0.55	0.59
PEE (amps x10 <sup>-11</sup> )	30	29	26	24	19	26
Δ (deg)	105.0	105.0	104.5	104.0	104.2	104.7
ψ (deg)	38.8	38.5	38.7	38.8	38.8	38.7

	<u>Aged 15.5 hrs in Air and Exposure to UV #1</u>					
	5	5	6	16	---	930 (15.5 hrs)
Minutes Exposure to UV (1)	5	5	6	16	---	930 (15.5 hrs)
Contact Angle	14	14	14	106	---	124
SPD (Volts)	0.51	0.54	0.54	0.63	---	0.75
PEE (ampsx10 <sup>-11</sup> )	23	21	20	16	---	4.8
Δ (deg)	104.0	104.2	104.0	103.1	---	100.0
ψ (deg)	39	38.7	38.8	39.1	---	39.9

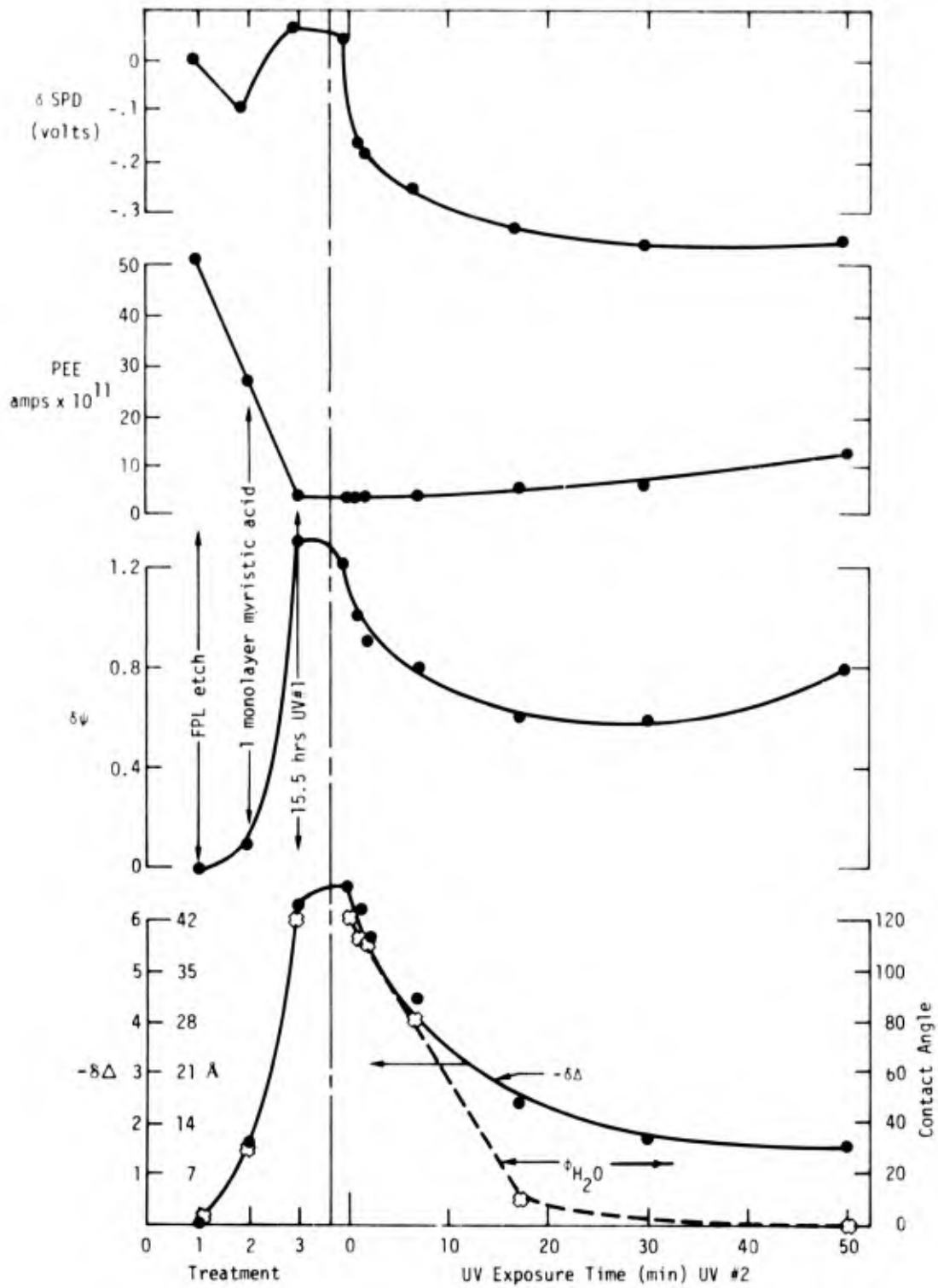


Figure 51. Change of parameters due to deposition of myristic acid and exposure to UV#1 with plastic cover (left of vertical line). Changes due to exposure to UV#2 (right of vertical line).

exposure of the surface to a UV Pen Ray (#1) lamp that was covered with a plastic cover. Steps 2 and 3 caused about a 42 Å increase in film thickness with almost directly proportional change in the water contact angle and decrease in PEE, whereas step 2 decreased SPD and step 3 increased SPD. Exposure of region 6 to the UV lamp used for measuring PEE (Pen Ray, #2) caused the changes in Table 16 and at the right of Fig. 51. In 50 minutes the contact angle returned to  $\sim 5^\circ$ . Changes of  $\Delta$  reveal that about 30 Å of film was removed. However, since  $\psi$ , PEE and SPD did not return to values expected for 30 Å removal, the remaining 12 Å of film or the approximately 200 Å of underlying oxide had been changed.

#### 6.1.1 Bond Strength

Six Al2024-T3 samples were FPI etched, dipped through a myristic acid layer on water and exposed to UV lamp #2 for 30 minutes. The samples were then bonded with HT424 and fractured. Table 17 gives the surface parameters after each step and the resultant bond strength. One dip through myristic acid deposited about 7 Å and increased the contact angle to  $67^\circ$ . The change in PEE corresponds to deposition of about 5 Å of myristic acid, using the attenuation index of 12.5 Å (Fig. 45). Thirty minutes of UV exposure increased the film thickness by about 14 Å more and caused the SPD to drop by about 0.7 volts. The bond strength dropped by about 500 psi due to the contamination in spite of the fact that the contact angle dropped to  $2^\circ$ . In this experiment, the UV exposure made the contamination polar but did not remove it and demonstrates that a wettable surface is not always a strong bonding surface.

The deposition of contamination by exposure to UV light is thought to be due to complicated reactions involving the formation of ozone and combined interactions of airborne contamination, ozone and UV light. The reason for the removal of part of this contamination layer and change of the remaining

TABLE 16

## CHANGE OF SURFACE PARAMETERS WITH EXPOSURE TO UV LAMP #2

Minutes Exposure to UV (2)	0	1	2	7	17	30	50
Contact Angle	124	113	111	85	14	8	5
SPD	0.73	0.52	0.50	0.46	0.35	0.32	0.33
PEE	3.6	3.5	4.0	3.9	5.5	5.6	12
$\Delta$	99.7	100.2	100.8	101.9	104.0	104.7	104.9
$\psi$	39.8	39.6	39.5	39.4	39.2	39.2	39.4

Table 17

EFFECT OF MYRISTIC ACID AND UV LIGHT ON  
SURFACE PARAMETERS AND BOND STRENGTH

Treatment	$\Delta$ (deg)	$\psi$ (deg)	Change in Film Å	SPD (volts)	PEE amps $\times 10^{-11}$	$\phi_{H_2O}$ (deg)	$\sigma_b$ (psi)
FPL Etch	108.3	37.1		0.72	160	3	2917 $\pm$ 82
1 dip, Myristic acid	107.2	37.4	7	0.70	110	67	
30 Min. UV	105.5	39.2	14	-0.04	19	2	2400 $\pm$ 109

layer to a very wettable state is not understood but indicates that both deposition and removal of contamination can occur. Research should be done to discover those parameters that control these processes in order to use the UV technique for surface cleaning under ambient conditions.

## 7. The Effect of Different Environments

### 7.1 SET in UHV

We have performed aging experiments in a UHV system with the purpose of learning whether carbon contamination is necessary for contact angle degradation and bond strength degradation. The UHV system was baked out at about  $10^{-7}$  torr (250°C) for a week to remove any carbonaceous material that might out-gas from the steel and glass (window) walls. When the system was opened, clean dry nitrogen was flowing at all times to prevent contamination during sample loading. Eighteen Al 2024-T3 samples were given the standard FPL etch and placed in the UHV system while still wet from the final rinse. One of the samples was mounted for ellipsometry, SPI and Auger spectroscopy and the rest were mounted vertically in a slotted Al holder that had also had the FPL etch.

After evacuation to perform Auger spectroscopy the system was brought back to atmospheric pressure with air that had been dried and cleaned by passing through a liquid nitrogen trap. A side arm was attached to the UHV system that contained a saturated solution of  $K_2SO_4$  to provide 97% RH in the system. The ellipsometry and SPD was monitored during aging and Auger was performed after aging for 185 hours. The samples were removed one at a time for SPD, ellipsometry, PEE and contact angle measurements as quickly as possible (less than 10 minutes) in the standard laboratory equipment as a check on the UHV results. The



other 12 samples were removed and immediately primed and bonded with HT424 adhesive.

Figure 52 shows the changes that occurred during SET at 23°C, 97% RH in the clean UHV system. The average change in  $\Delta$  and  $\psi$  (essentially complete in the first 10 hrs) is about  $-0.9^\circ$  and  $+0.5^\circ$ , respectively. Evacuation caused  $\Delta$  and  $\psi$  to return to the values just prior to exposure to  $H_2O$  vapor. If it is assumed that water vapor is physically adsorbed and desorbed, the changes in  $\Delta$  corresponds to approximately 4.5 Å or one monolayer of water. However, the corresponding change of  $\psi$  should have been  $+0.04^\circ$  rather than  $+0.5^\circ$ , indicating some other physical change has also occurred. As for previous SET experiments (in glass jars) SPD decreases then increases.

Table 18 shows the ellipsometric, SPD, PEE and contact angle ( $\phi_{H_2O}$ ) history of the samples in the UHV system. Estimated film thickness and the change in film thickness is given in Table 18 assuming the film to be aluminum oxide with index of refraction 1.6. Approximately 22 Å are removed (probably  $H_2O$ ) from 15 minutes after the last rinse in water to evacuation for 19 hrs. Exposure to air that had passed through a liquid nitrogen trap added 15 Å and exposure to 97% RH for 185 hours added another 5 Å. Evacuation removed about 6 Å again. It is postulated that long drying in high vacuum removes about 15 Å of tightly bound water and about 5 Å of physically bond water. A change of about 0.6 volts SPD is associated with the water removal. Exposure to water vapor then decreases SPD by about 0.1 to 0.2 volts, as water is physically adsorbed, followed by gradual increase by .1 to .2 volts with time, but without obvious film thickness change (Fig. 52). A dramatic change in PEE (decrease by factor of 5) and contact angle for water  $\phi_{H_2O}$  (3 to  $94^\circ$ ) is associated with the aging process.

Figure 53 shows an Auger electron spectrogram (AES) for the sample after 35 minutes of evacuation in the UHV system. No carbon is observed. Figure 54 is an AES after 185 hours of SET

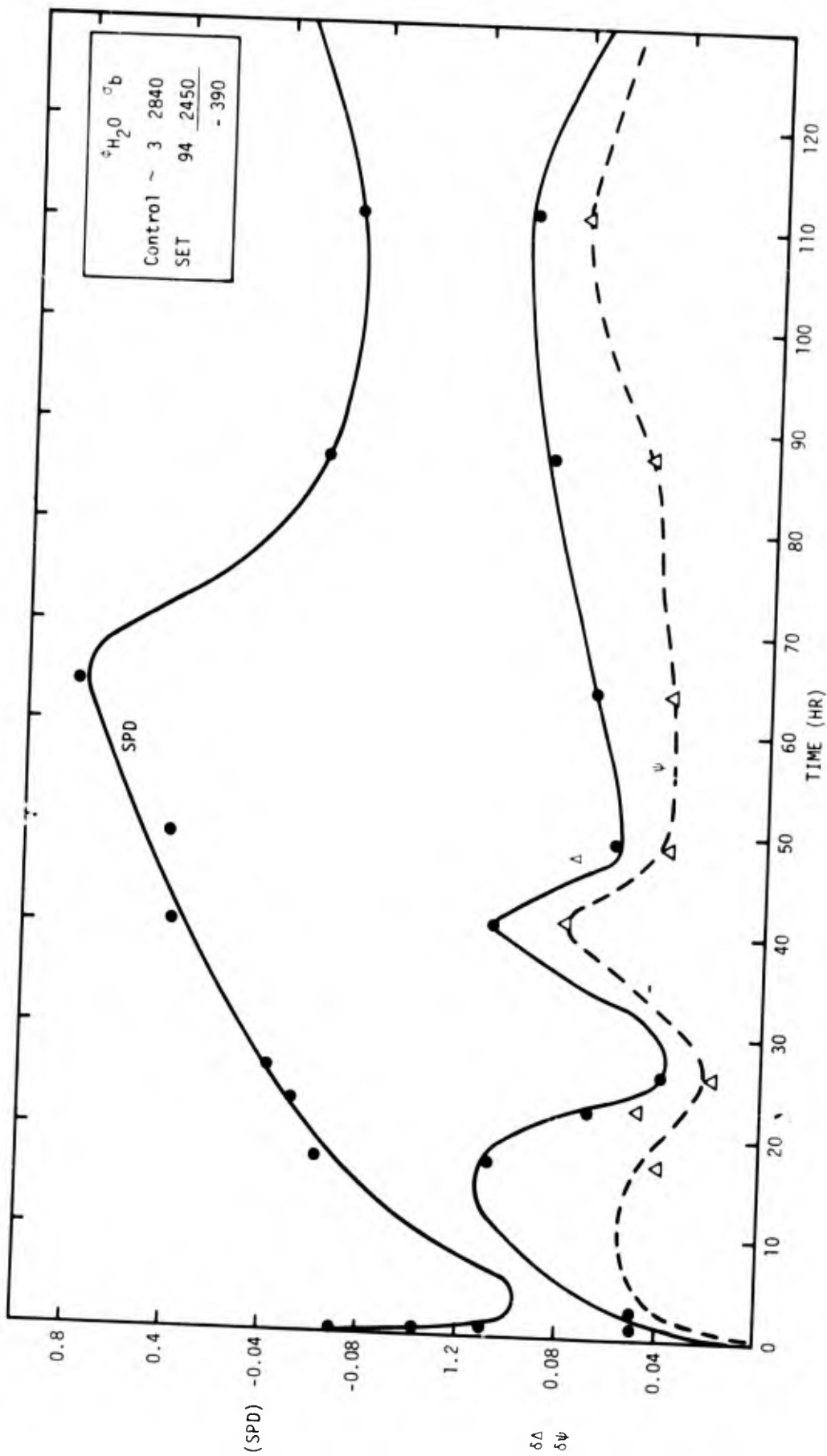


Figure 52. Plot of  $\delta \Delta$ ,  $\delta \psi$ ,  $\delta \text{SPD}$  for SET at 23°C, 95% RH in the UHV system.

Table 18

AGING OF FPL ETCHED Al 2024-T3 IN A UHV SYSTEM  
USED AS A CLEAN ENVIRONMENTAL CHAMBER

History	$\Delta^{\dagger}$ degree	$\psi$ degree	SPD* volts	PEE $\times 10^{11}$ amps	$\phi_{H_2O}$ degree	Estimated Film Thickness Å	Change of Thickness Å
In UHV 15 min. after FPL etch	62.8	37.5	-1.07	(52)	3	270	0
Evacuate to 100 $\mu$	63.3	37.6	-0.68			265	-5
19 hrs at $6 \times 10^{-8}$ torr	65.0	37.1	-0.45			248	-22
Let in clean dry air	63.0	37.7	-0.41			263	-7
Add $K_2SO_4$ Solution							
2.3 hrs. later	62.5	37.9	-0.59			273	-3
185 hrs later	62.0	38.3	-0.39			278	-8
Evacuate to $10^{-6}$ torr	64.2	37.6	-0.61			256	-14
Removed Auger Sample					94		
Removed 3 samples							
Measurements in air 1	107.1 <sup>†</sup>	38.6	0.69	5.5	>90	260	
at 70° angle of incidence 2	109.5	37.7	0.91	11	>90	236	

(cont)

Table 18 (cont)

3	110.1	37.2	0.80	8	>90	230
	~110.5±2.5	37.6±0.3	1.0	52	3	230

Fresh FPL etch

- \* Measured with vibrating electrode in UHV.
- + Measured with radioactive electrode in air, angle of incidence 70°.
- #  $\lambda = 6328 \text{ \AA}$ , Angle of incidence 79.2°.

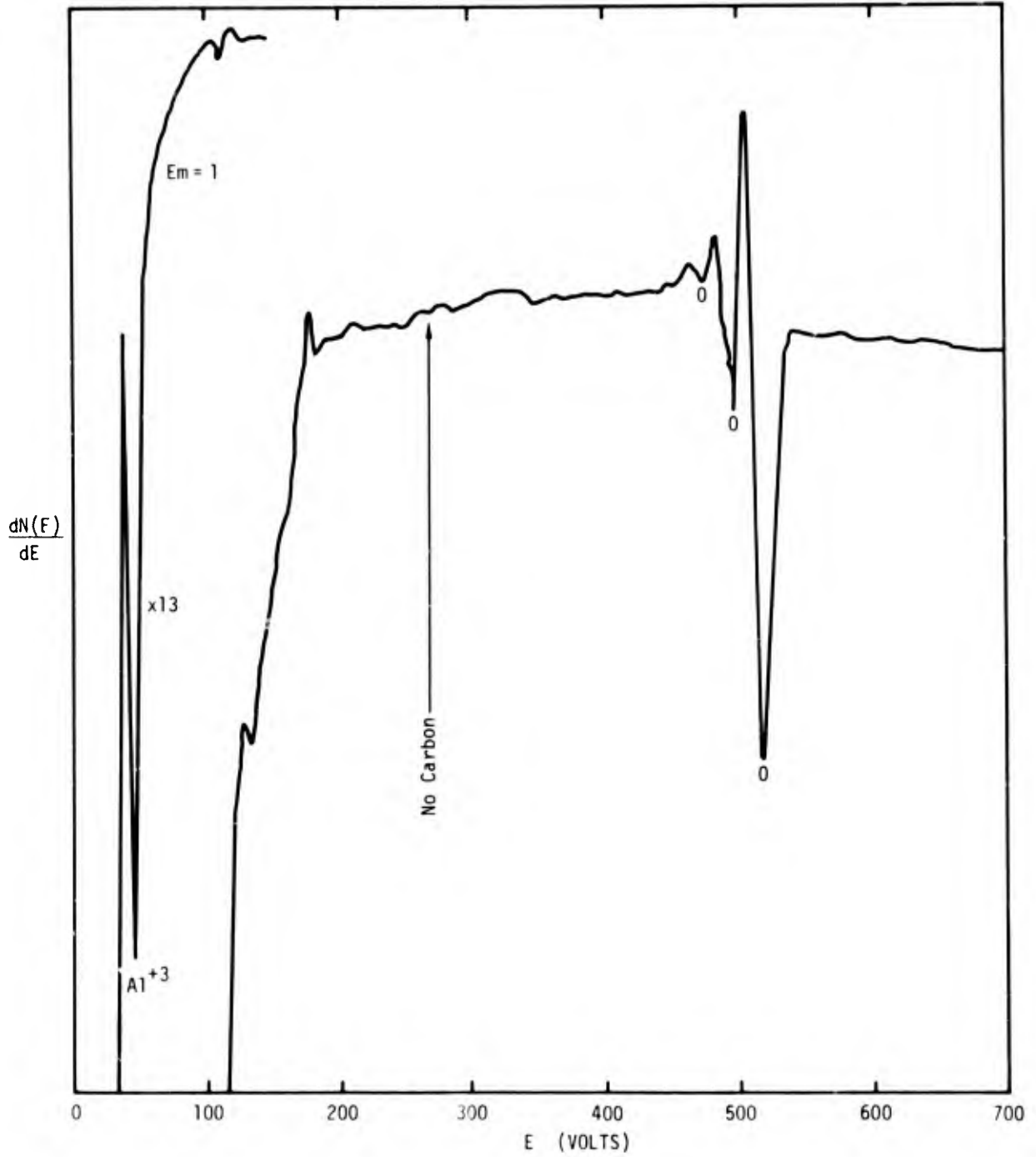


Figure 53. AES before aging in UHV.

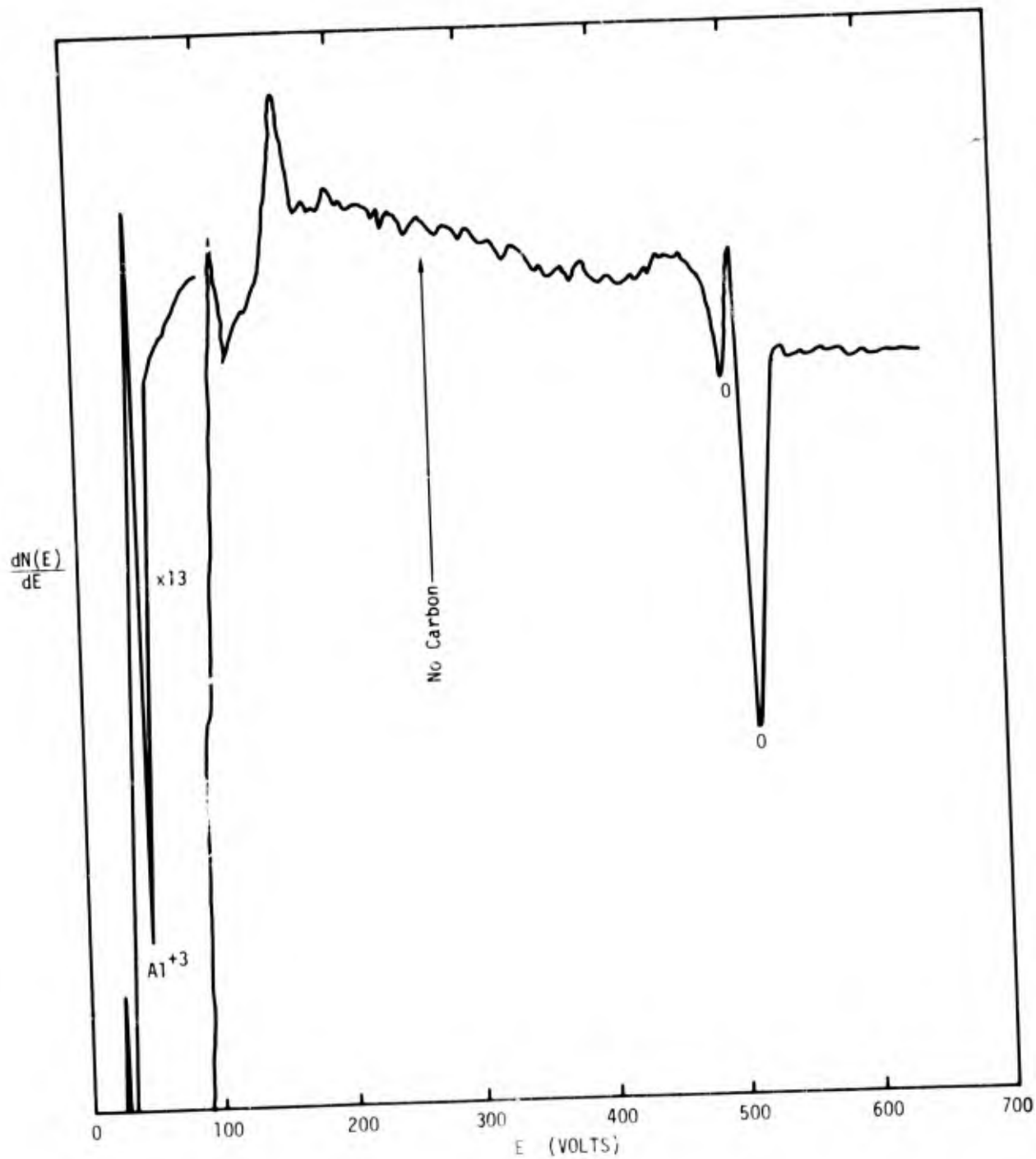


Figure 54. AES after aging 185 hrs. in UHV.

at 23°C, 97% RH. No carbon is observed. After the AES measurement the sample was removed and the contact angle was measured within 10 minutes ( $\phi_{H_2O} = 94^\circ$ ). To be sure that carbon contamination did not occur upon removal of the sample from the UHV to lab air, the sample was replaced and another AES performed. The spectrum was essentially identical to Fig. 54. To be sure that the water used for the contact angle measurement did not contaminate the sample another sample was given the FPL etch and the contact angle measured. The sample was completely wettable ( $\phi_{H_2O} \sim 3^\circ$ ) indicating no contamination from the water.

To demonstrate the sensitivity to carbon, Figure 55 shows the AES for a sample that was ultra-sonically cleaned in trichlorethylene (TCE). Not more than a monolayer of TCE is expected to be left after evacuation in the UHV. The carbon and chlorine are obvious. Figures 56 and 57 are AES for FPL etched samples that has been dipped in water with a monolayer of myristic acid on the surface.

The AES measurements of Figs. 53 through 57 were made with a retarding grid spectrometer. Figure 58 is a spectrogram, of an FPL etched sample after 420 hrs. at 97% RH in an UHV chamber, with a PHI cylindrical mirror analyzer, AES. The lower curves in Fig. 58 have been expanded by a factor of ten with respect to the upper curve. There are very small impurity peaks for S, Cl, C and N as well as the Cu alloy constituent. Figure 59 is an Ar ion sputter profile of the film on the 420 hr. SET, UHV sample. Although the profile is very similar to that for a fresh FPL etch sample, the contact angle is  $100^\circ$ .

As pointed out in section 6 the electron beam removes carbonaceous material and in some cases carbon was not detected unless the sample was moving with respect to the electron beam. To double check that no carbon contamination occurs in the UHV system, samples were checked for carbon with ESCA. After 192 hours in the UHV system with 97% RH, the contact angle had increased from  $10^\circ$  to  $80^\circ$  whereas the carbon peak was the same as

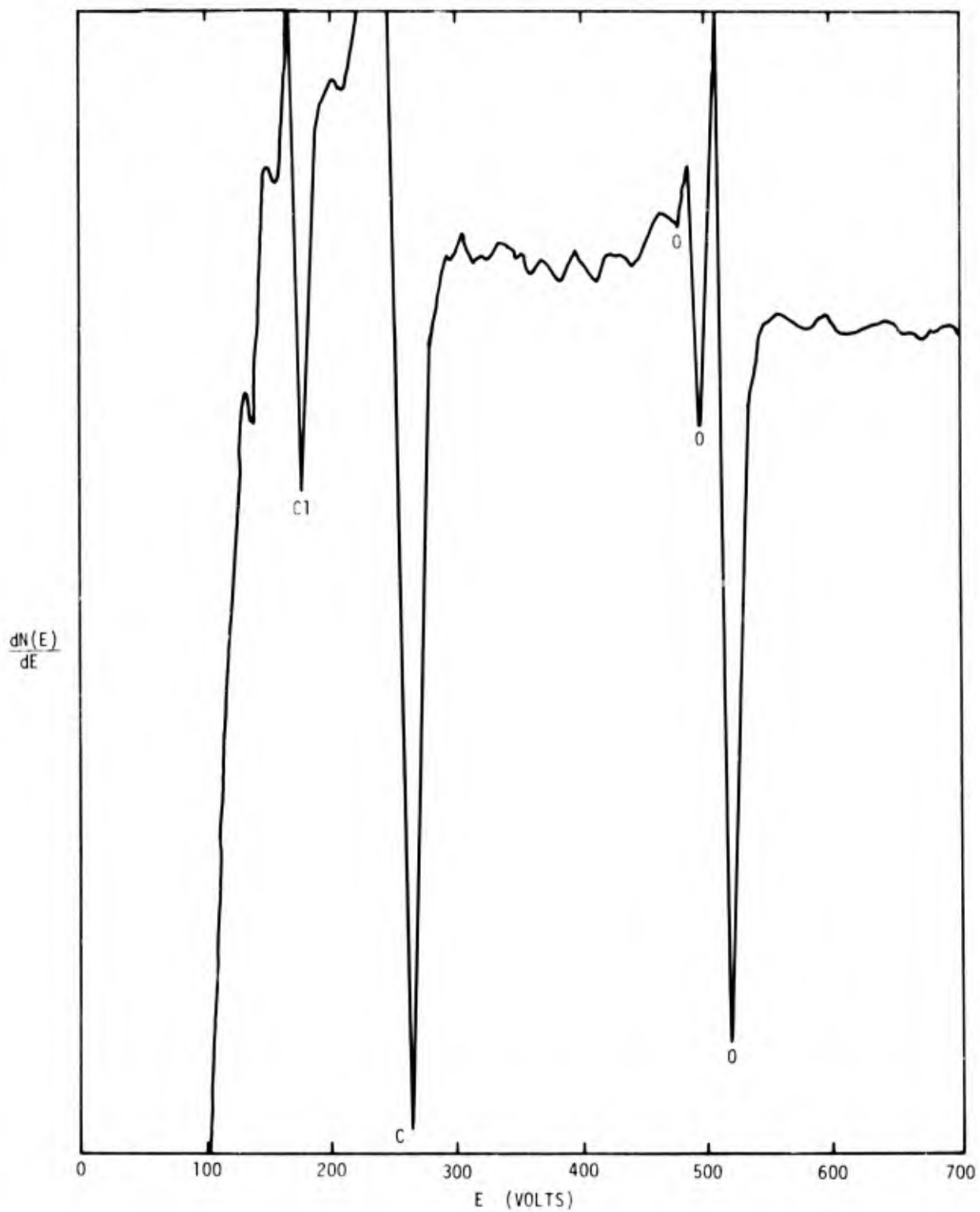


Figure 55. AES after ultra-sonic cleaning in trichlorethylene.



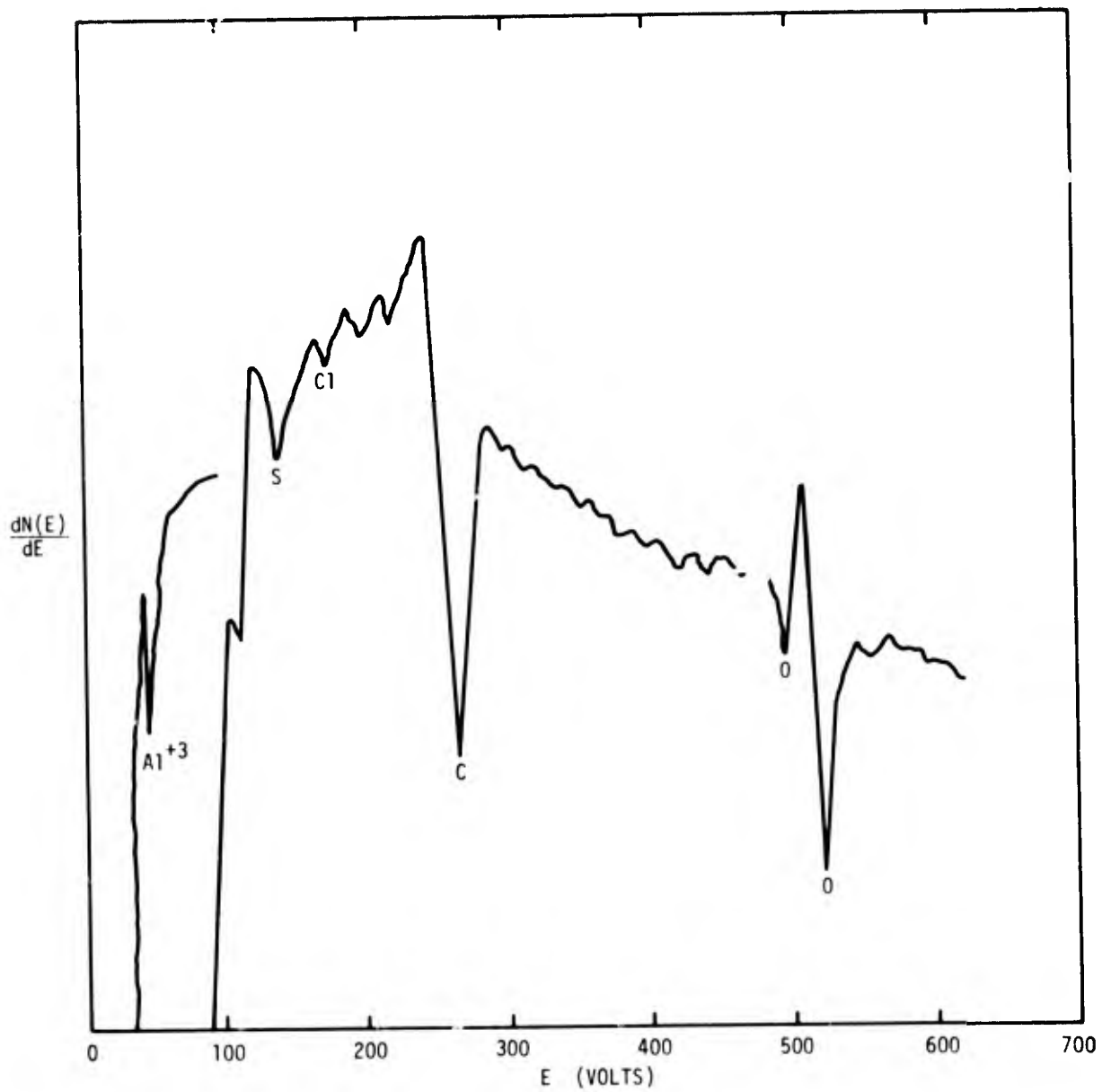


Figure 56. AES after dipping FPL etched Al 2024-T3 through myristic acid on water.

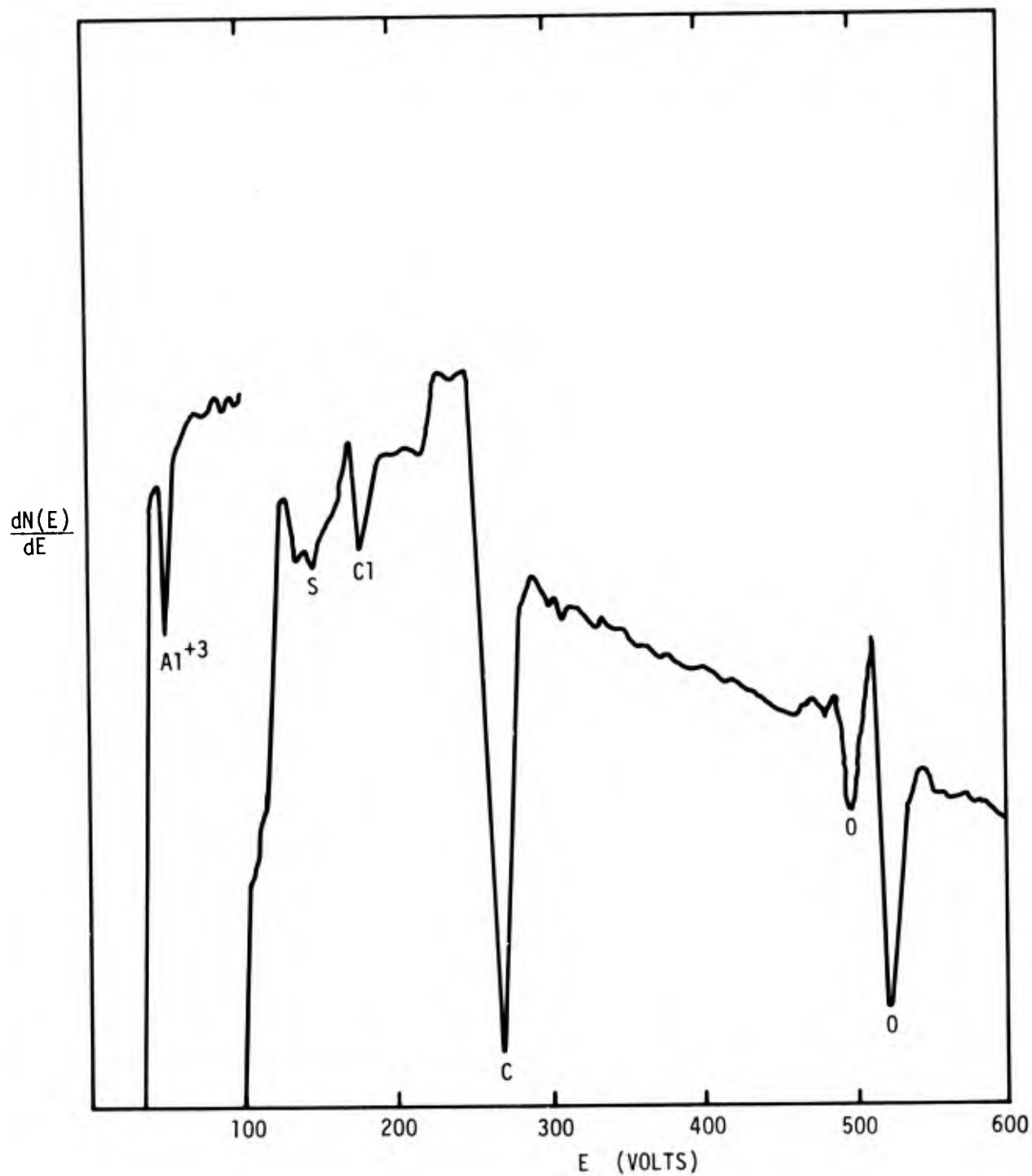


Figure 57. AES after dipping three times through myristic acid on water.

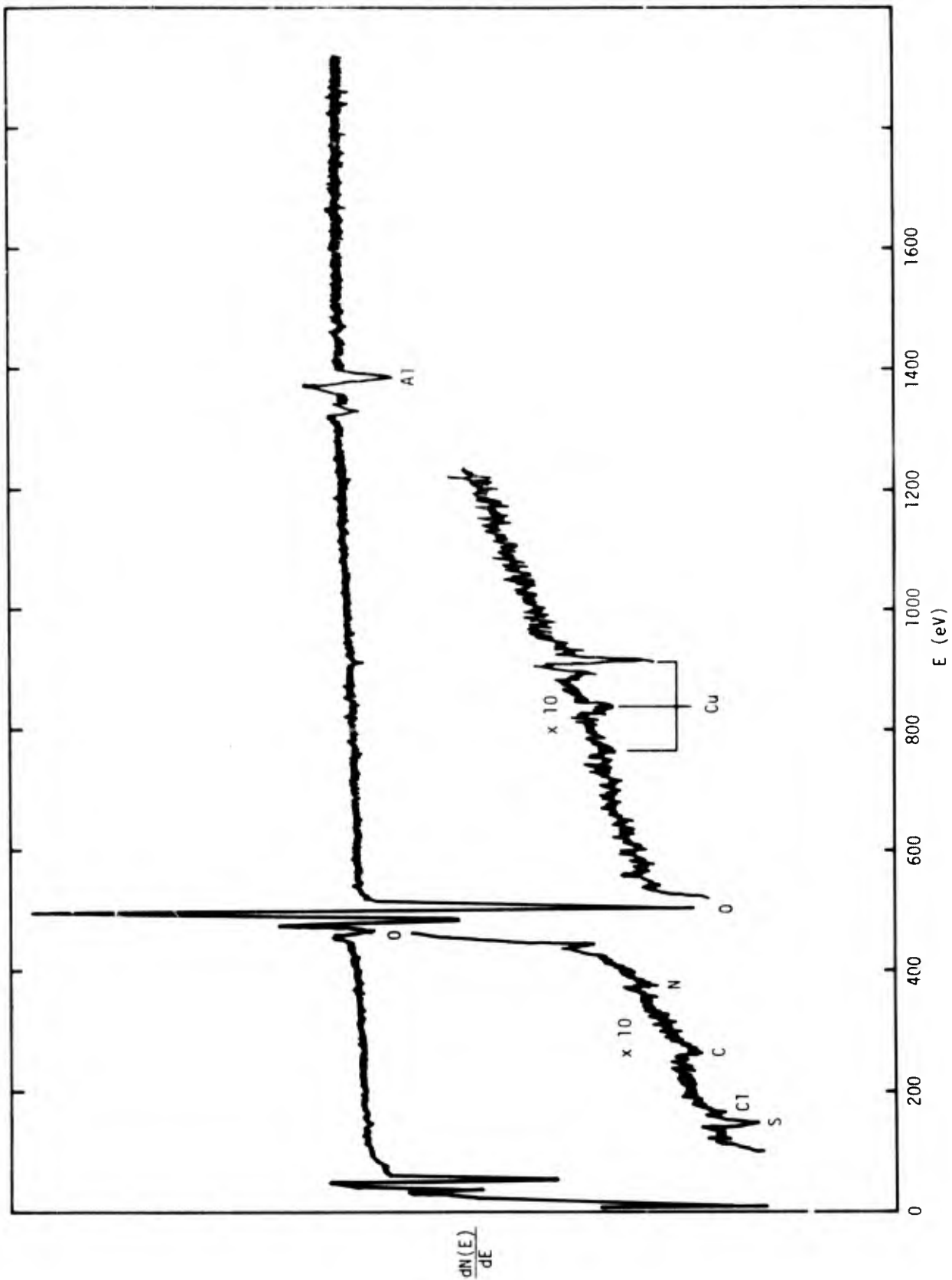


Figure 58. AES of UHV aged sample with PHI cylindrical mirror analyzer.

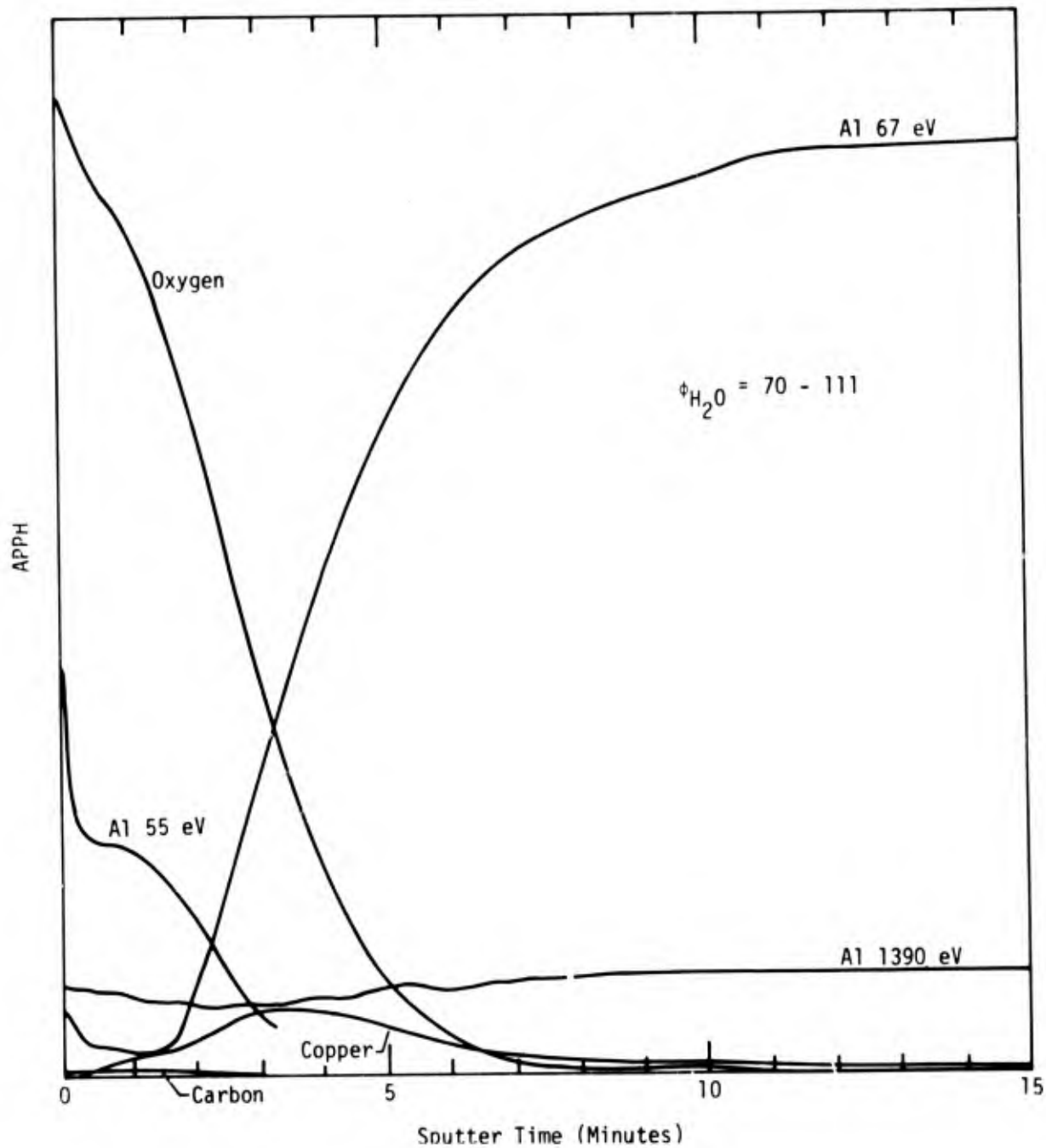


Figure 59. Sputter profile of 420 hr UHV aged (97% RH) sample.

for a completely wettable fresh FPL sample, i.e. with carbon peak ten times less than a non wettable aged sample. These results are considered to confirm that surface degradation of FPL etched Al 2024-T3 samples, with respect to surface energy (contact angles) can occur in the absence of carbon contamination. In order to establish the effect of SET on contact angle, in the absence of organic contamination, a stainless steel tube was passed through the sample holder flange of the UHV system. Water could be forced through this tube to perform contact angle measurements by visual observation through the UHV window. The tube extending to the outside of the chamber had a valve that would be closed during evacuation.

Contact angles proved to be approximately the same whether measured in the chamber or after removal from the chamber. Figure 60 shows the water contact angle as a function of SET for measurements made within the chamber. The contact angle increases approximately linearly with SET up to 20 hours regardless of the relative humidity or atmosphere. After 20 hours the 54% RH curve deviates from the 97% RH curve. Since we have demonstrated that degradation can occur in the absence of organic contamination, experiments were performed to see if surface energy degradation would occur in the absence of water vapor. A sample was placed in the UHV system and exposed to clean dry nitrogen for 116 hours, another was exposed to clean dry oxygen for 20 hours and another to clean dry air for 6 hours. None of these samples showed any change in water contact angle, indicating that if no organic contamination is present, water vapor must be present for degradation to occur in the UHV environmental chamber.

#### 7.1.1 Bond Degradation for SET in the UHV Chamber

It has been demonstrated in the previous paragraphs that if water vapor is present FPL etched Al2024-T3 will degrade with SET

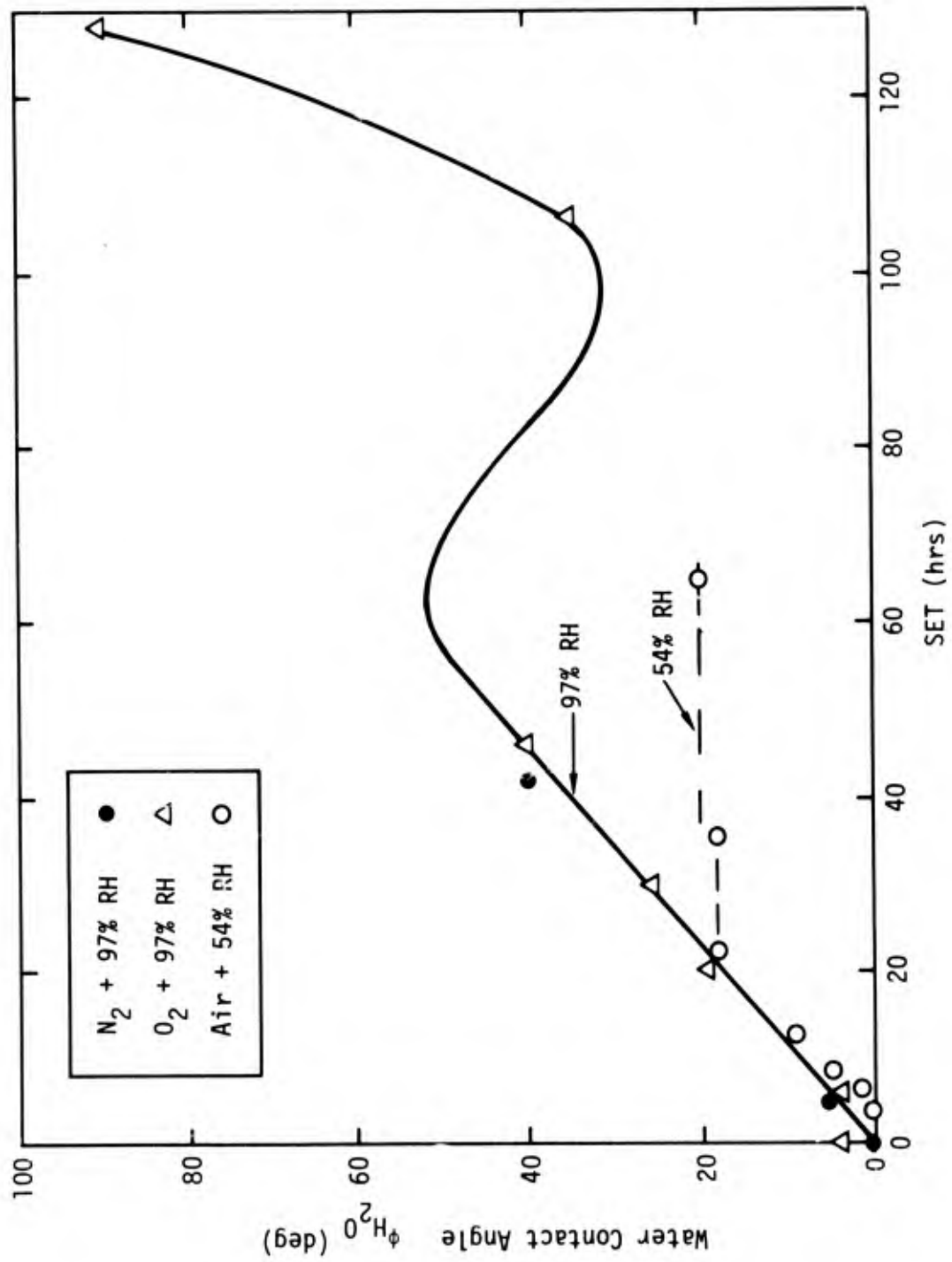


Figure 60. Plot of  $\phi_{H_2O}$  vs SET at various relative humidities in the UHV chamber.

in the absence of organic contamination. To demonstrate the effect of this degradation on bond strengths, six single overlap bonds were made with samples of SET = 185 hours at 23°C, 97% RH in the UHV system and six bonds were made from freshly FPL etched samples for a control. Table 19 gives the bond strengths, indicating that aged samples with no carbon contamination, but a large contact angle, have degraded in bond strength by 390 psi as compared to the control set, with low contact angle.

## 7.2 SET in Glass Jars

Experiments were performed with glass (dessicator) jars for the environmental chamber. The jars were cleaned with FPL etch solution, rinsed with distilled water and dried.

### 7.2.1 Dry Atmospheres

Experiments were performed in clean dry jars to see if degradation would occur in the absence of water vapor. Three jars were evacuated and then brought to atmospheric pressure one with oxygen, one with nitrogen and one with air. To dry the gases, the nitrogen was passed through a liquid nitrogen trap, and the oxygen and air was passed through an acetone and dry ice trap. The jar lids were sealed with silicone high vacuum grease. Table 20 gives the surface parameters before and after exposure to the gasses for 23 hours. Aging in the dry jars caused a dramatic increase in the water contact angle from 3° to 110°. Each surface was contaminated with Si, presumably from the high vacuum grease. Jar number 2 had been rinsed with a hydrofluoric acid solution in previous experiments and the glass had a frosted appearance caused by the HF etch. Samples from this jar consistently revealed F contamination. The ellipsometer results correspond to about 8 Å of contamination. The side of the samples that was exposed to the electron and ion sputter beam

TABLE 19

## EFFECT OF SET IN UHV ON BOND DEGRADATION

Sample	Control, $\phi_{H_2O} = 3$		Aged $\phi_{H_2O} = 94^\circ$	
	$\sigma_b$ (psi)	Sample	$\sigma_b$ (psi)	Sample
1	2800	1	2400	
2	3000	2	2500	
3	2980	3	2600	
4	2900	4	2440	
5	2870	5	2610	
6	<u>2490</u>	6	<u>2150</u>	
	2840 $\pm$ 130		2450 $\pm$ 120	



Table 20

SET IN GLASS JARS WITH DRY O<sub>2</sub>, He AND AIR.  
VACUUM GREASE SEAL.

No.	History	$\Delta$ (deg)	$\psi$ (deg)	SPD volts	PEE ampsx10 <sup>-11</sup>	$\phi_{H_2O}$ (deg)	APPH Contamination			
							C	Si	F	Al
1	Fresh FPL	117.3	35.8	0.43	80	3				
2		117.1	36.2	0.34	83	3				
3		117.3	36.4	0.24	80	3				
	SET in									
1	Air	115.0	36.9	0.16	-	108	0	11	0	2
2	O <sub>2</sub>	115.8	36.7	0.34	61	100	7	6	4	0
3	He	115.8	37.3	0.30	80	113	1	7	0	1

during Auger spectroscopy measurements had a contact angle of about 10 - 20° as compared to ~ 100° on the other side.

These results indicate that in the glass jars surface energy degradation is caused by surface contamination and that different types of contamination are present depending on the jar history.

### 7.2.2 Effect of Humidity and Environment

Four FPL etched samples were placed in 4 jars and maintained at 0, 35, 58 and 97% RH in clean air as a function of time. The results are recorded in Table 21. Figure 61 compares the water contact angle values as a function of SET for 97% RH in a glass jar with that in the UHV chamber. The APPH for carbon was 55 for the glass jar sample as compared to 0.03 for the UHV sample, at the end of the experiment. Although both environments cause a large increase in  $\phi_{H_2O}$  the changes in the UHV chamber are much slower.

Figures 62, 63, 64 and 65 compare the  $\phi_{H_2O}$ , SPD, PEE and  $\Delta$  and  $\psi$  curves respectively vs SET for various relative humidity values in the glass jars. In each case the 0% and 58% RH samples follow the same trends whereas the 35% and 97% RH samples follow the same trend. The contact angle and SPD curves undulate widely with SET whereas the PEE and  $\Delta$  and  $\psi$  curves change approximately logarithmically with respect to time, after a short initiation period (~2 hours). The change in  $\Delta$  and  $\psi$  corresponds to a growth of about 35Å of film in 92 hours, regardless of the relative humidity. The change in PEE had the same trends as for  $\Delta$  and  $\psi$  indicating that the photo emitted electron attenuation is caused by the film growth. The 0% RH curve is peculiar in that a large change in  $\Delta$ ,  $\psi$  and PEE occurs between 1.7 and 4.1 hours. The similarities between the  $\phi_{H_2O}$  and SPD curves for the 35% and 97% RH samples indicate surface degradation processes of the same nature whereas the large deviations of the 0% and 58% curves from each other and from the 35 and 97% curves, indicates the processes are different.

Table 21

EFFECT OF % RH AND SET, FOR FPL AL 2024-T3, GLASS JARS

Sample	SET TIME		$\Delta$	$\psi$	SPD	PEE	
	(hrs)	%RH				$\times 10^{-11}$	$\phi_{H_2O}$
11	Fresh		116.6	34.3	0.46	110	3
12	FPL		114.4	33.6	0.46	120	3
13			115.4	32.4	0.53	175	4
14			116.8	33.8	0.54	170	3
11	1.7	95	116.4	34.7	0.41	95	26
12		58	113.5	33.7	0.20	59	60
13		35	115.6	32.4	0.50	140	3
14		0	116.3	34.1	0.12	120	9
11	2.5	95	115.0	34.6	0.51	100	13
12		58	112.6	33.7	0.30	50	58
13		35	115.0	32.3	0.63	160	21
14		0	115.4	35.2	0.10	26?	39?
	4.1	95	115.6	34.7	0.03	87	20
		58	113.0	33.8	0.64	48	50
		35	114.6	32.8	0.28	160	30
		0	111.4	34.3	0.46	19	50
11	21	95	114.2	35.3	0.4	58	111
12		58	110.2	35.6	0.45	18	37
13		35	113.6	33.3	0.56	100	103
14		0	109.6	35.1	0.04	12	29
11	44	95	113.6	35.2	0.39	44	98
12		58	111.0	35.3	0.36	25	37
13		35	111.6	33.5	0.49	71	107
14		0	110.2	35.6	0.03	9	29
11	95		111.0	36.15	0.36	15	76
12	58	92	98.8	36.8	0.77	19	19
13	35		112.5	33.7	0.36	35	33
14	0		109.5	36.0	0.033	4	50

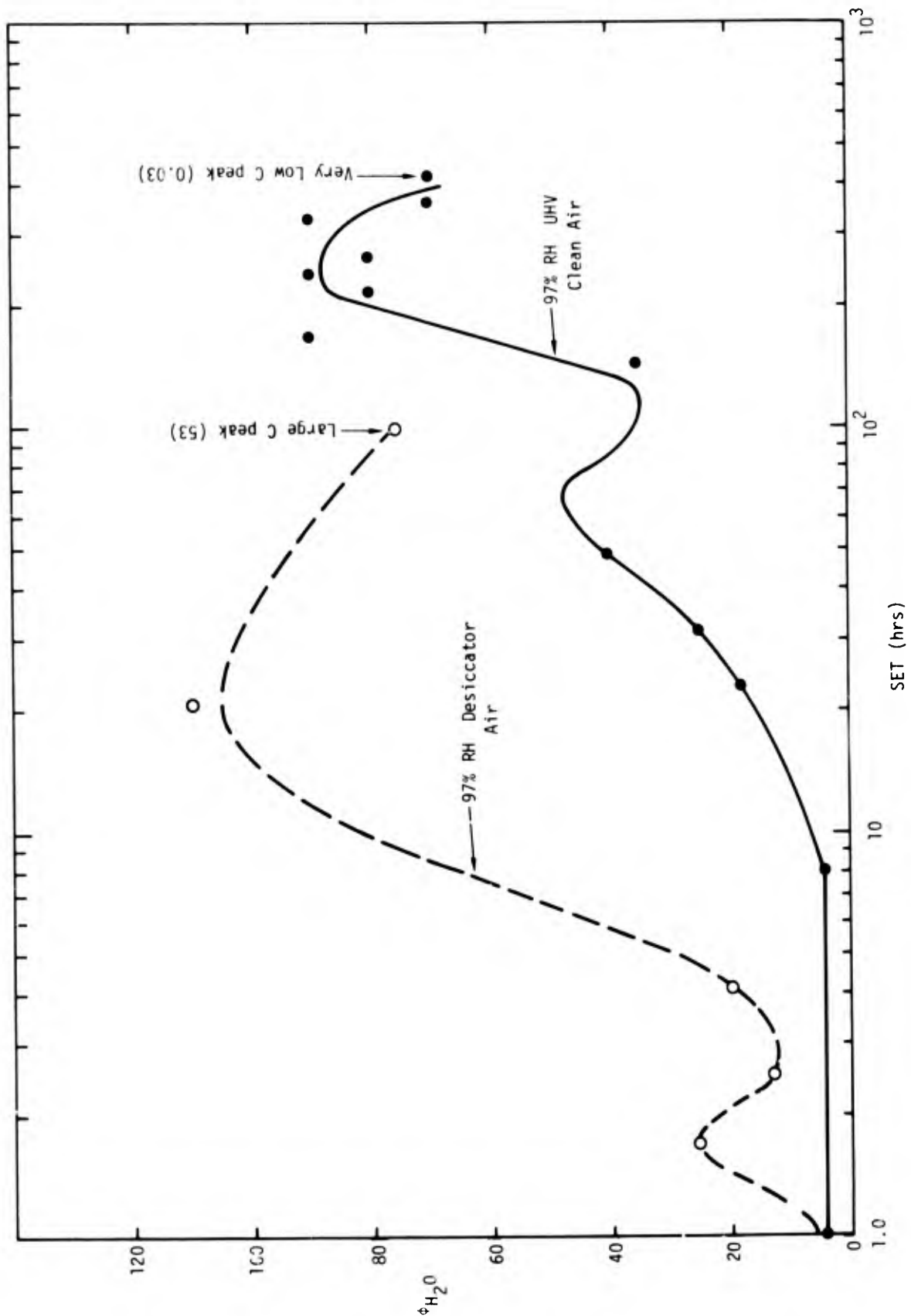


Figure 61. Plot of  $\phi_{H_2O}$  vs SET for samples in glass jars and the UHV chamber at 97% RH.

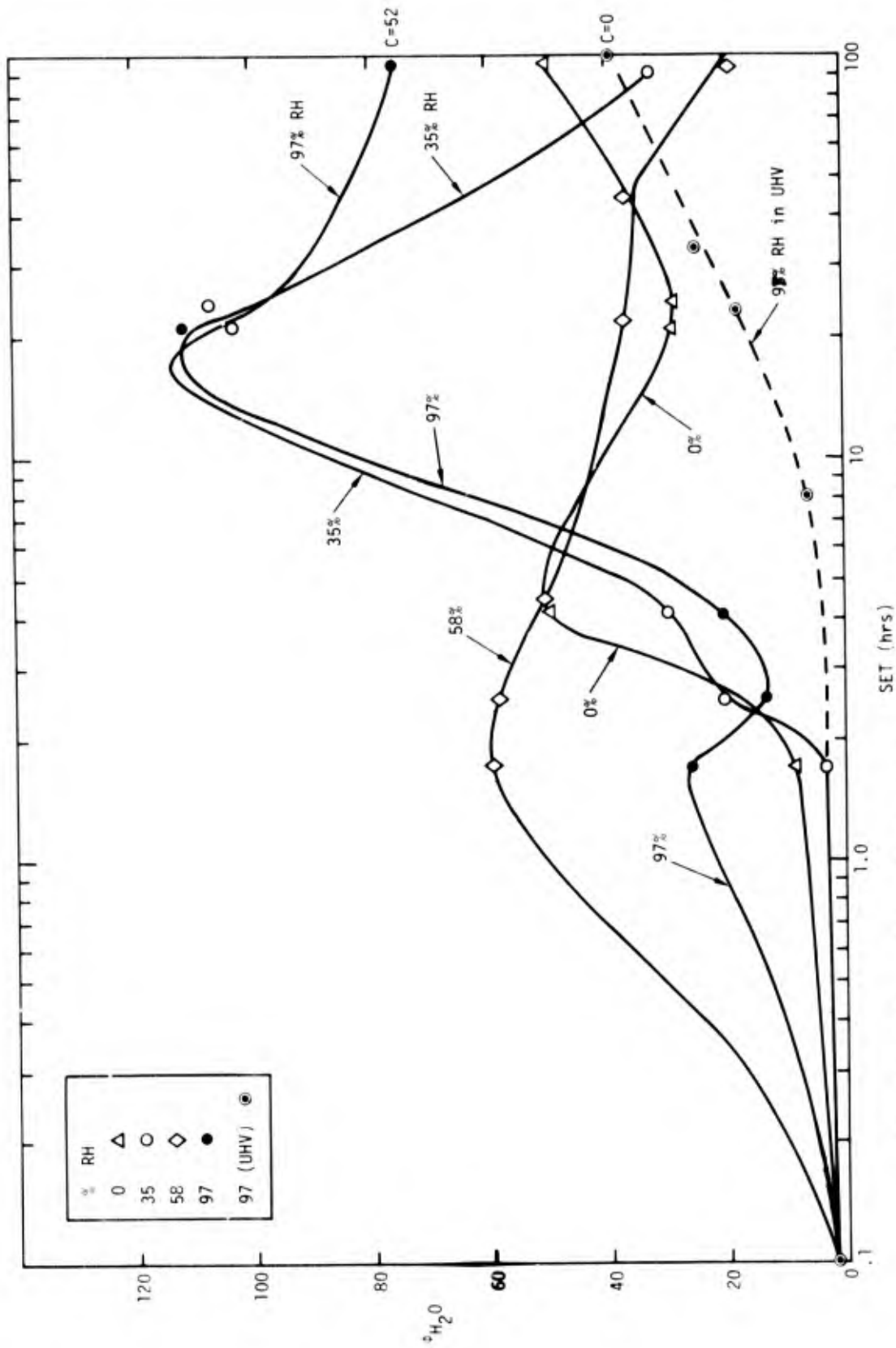


Figure 62. Plot of  $\phi_{H_2O}$  vs SET in glass jars for various relative humidities.

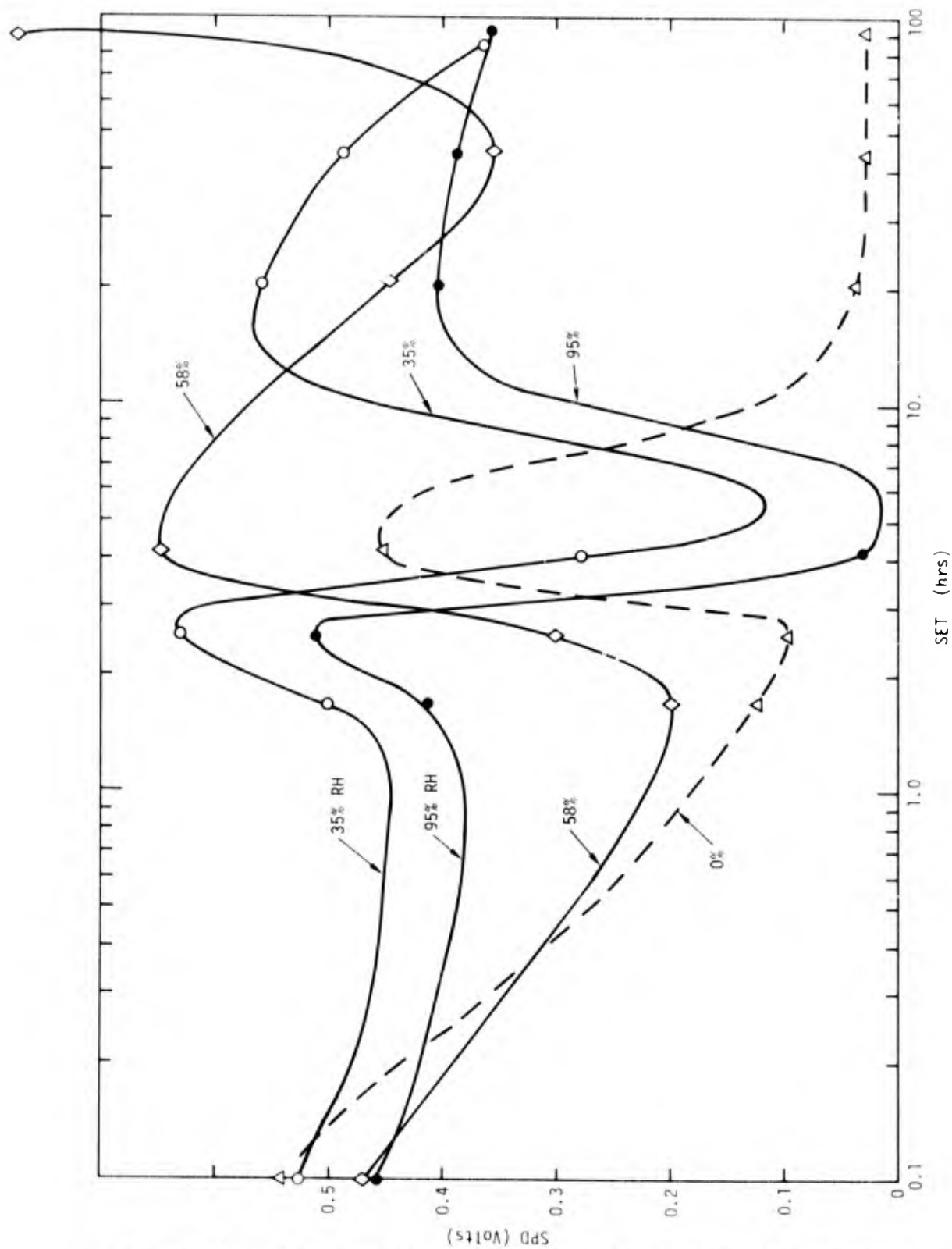


Figure 63. Plot of SPD vs SET in glass jars for various relative humidities.

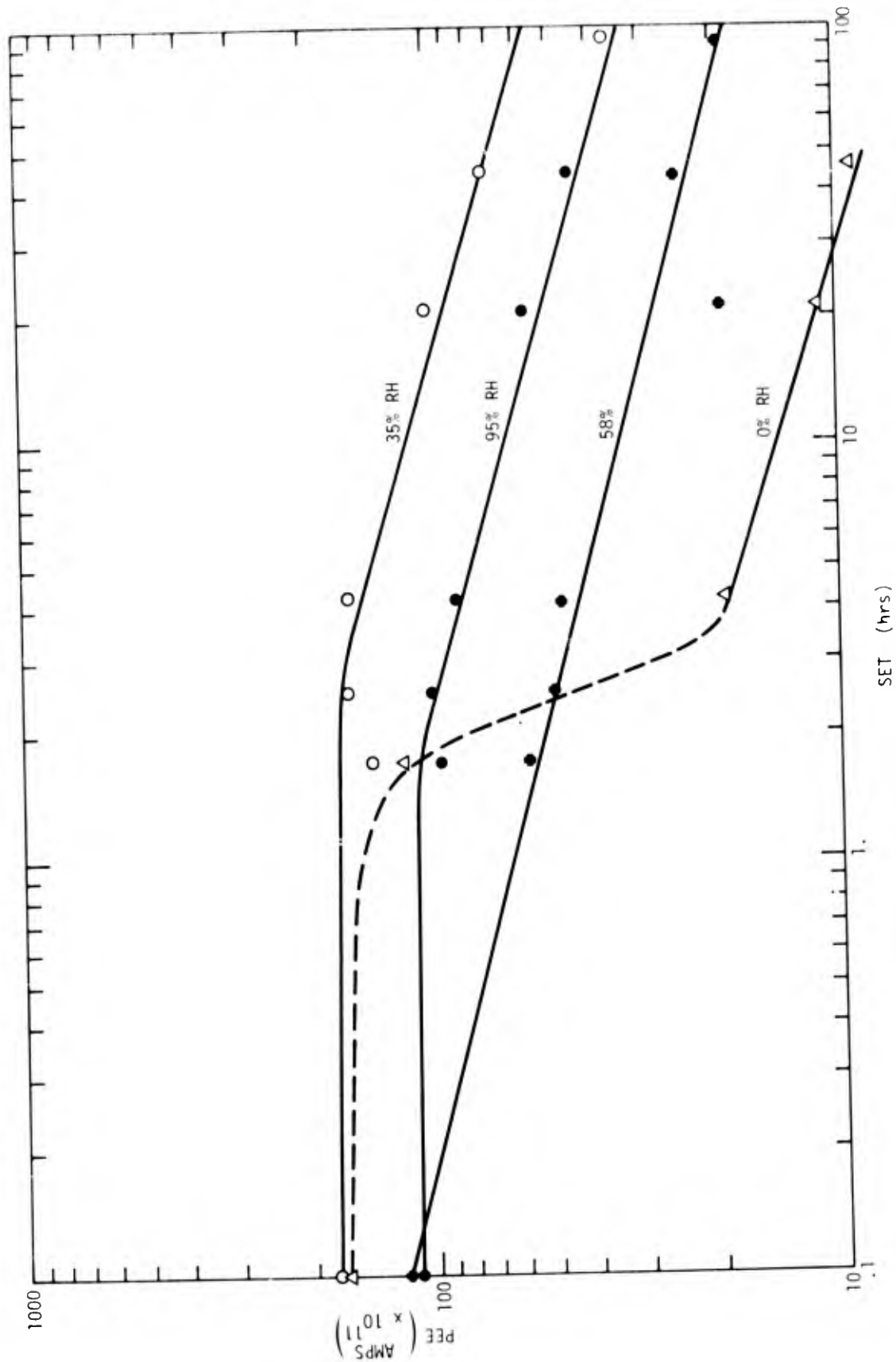


Figure 64. Plot of PEE vs SET in glass jars for various relative humidities.

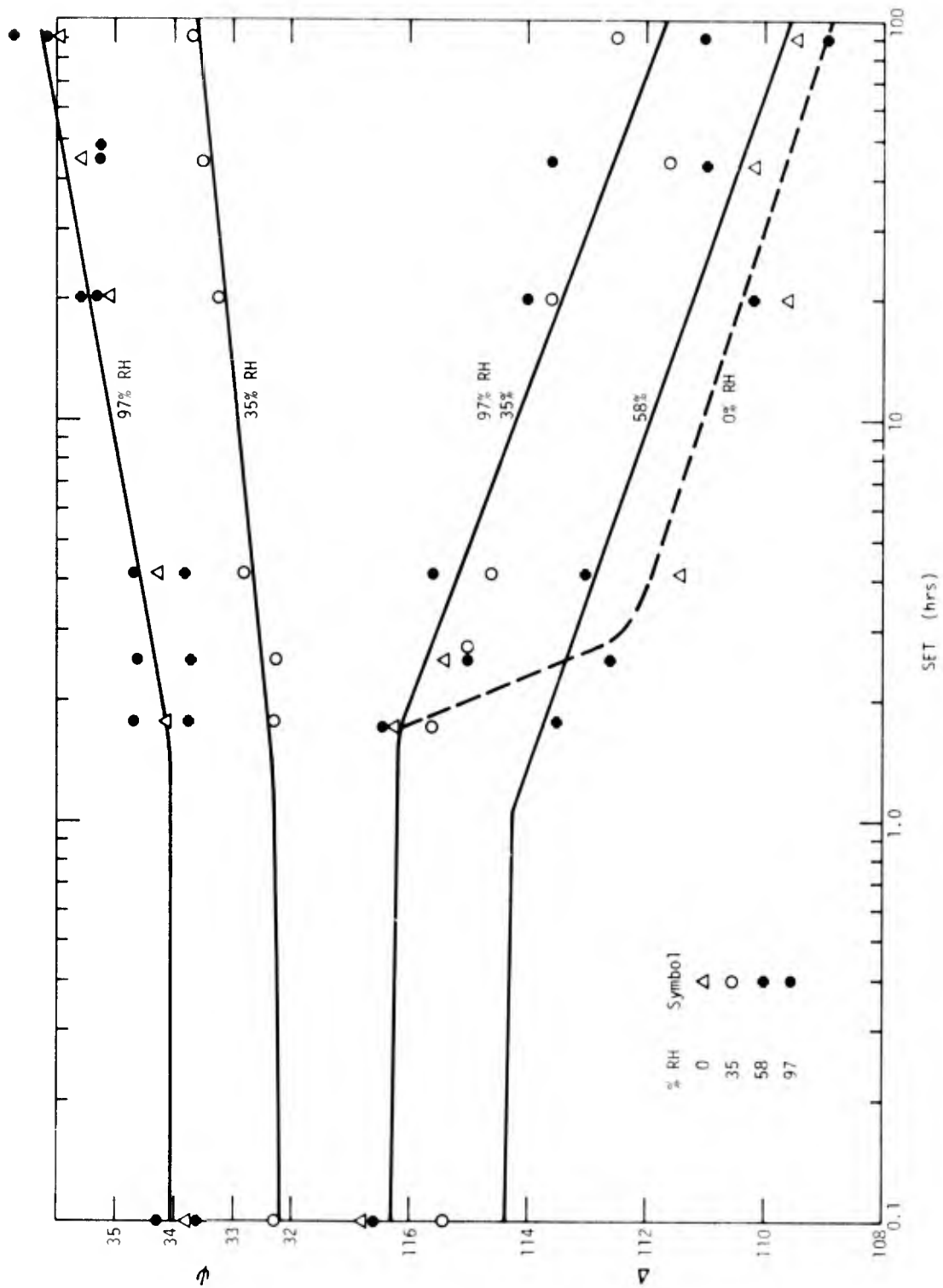


Figure 65. Plot of  $\Delta$  and  $\psi$  vs SET in glass jars for various relative humidities.



A clue as to the cause of the difference is seen in the AES in Figures 66 and 67 for the 58% RH sample and Figures 68 and 69 for the 97% RH sample. The 58% sample had been in the HF frosted glass jar #2 and shows a large F peak as well as Si, S, Cl, C and N impurities. The profile in Fig. 67 reveals the contamination to be in the outer portion of the oxide film. The increase in the APPH for oxygen and Al (55 eV) in the first two minutes of sputtering is due to the removal of the F and C contamination. Figures 68 and 69 show that a carbide rather than oxide film is formed on the 97% RH sample during SET. It takes 120 minutes of sputtering to remove this layer as compared to 10 minutes for the oxide layer in Figure 67.

### 7.3 SET in Laboratory Air

Six Al 2024-T3 samples were FPL etched then placed on a clean white paper on a laboratory bench without covers. The surface parameters were measured at different time intervals and the results are tabulated in Table 22. The average values for the six samples are plotted in Figures 70 to 73. Measurements were made on the top side of the sample except in one case at 16.3 hours for which the bottom (side adjacent to lab bench) was also measured to see if dust fall out was of importance. The fact that the bottom had a larger contact angle (open circle Fig. 68) than the top would indicate that fall out is not of as great importance as the gas environment. The contact angle curve and SPD curve is different from the glass jar and UHV chamber experiments. The ellipsometric and PEE parameters indicate the addition of approximately 20 Å of material to the 115 Å initial oxide layer. Figures 74 and 75 are Auger spectrograms for samples 1 and 2 of Table 22. The APPH for carbon is 8 and the contact angle was 89° for sample 1 as compared to an APPH(C) of 2.5 and contact angle of 23 for sample 2. This is taken to indicate that the contact angle degradation is due to hydrocarbon contamination in lab air. There are small sulfur peaks in Fig.

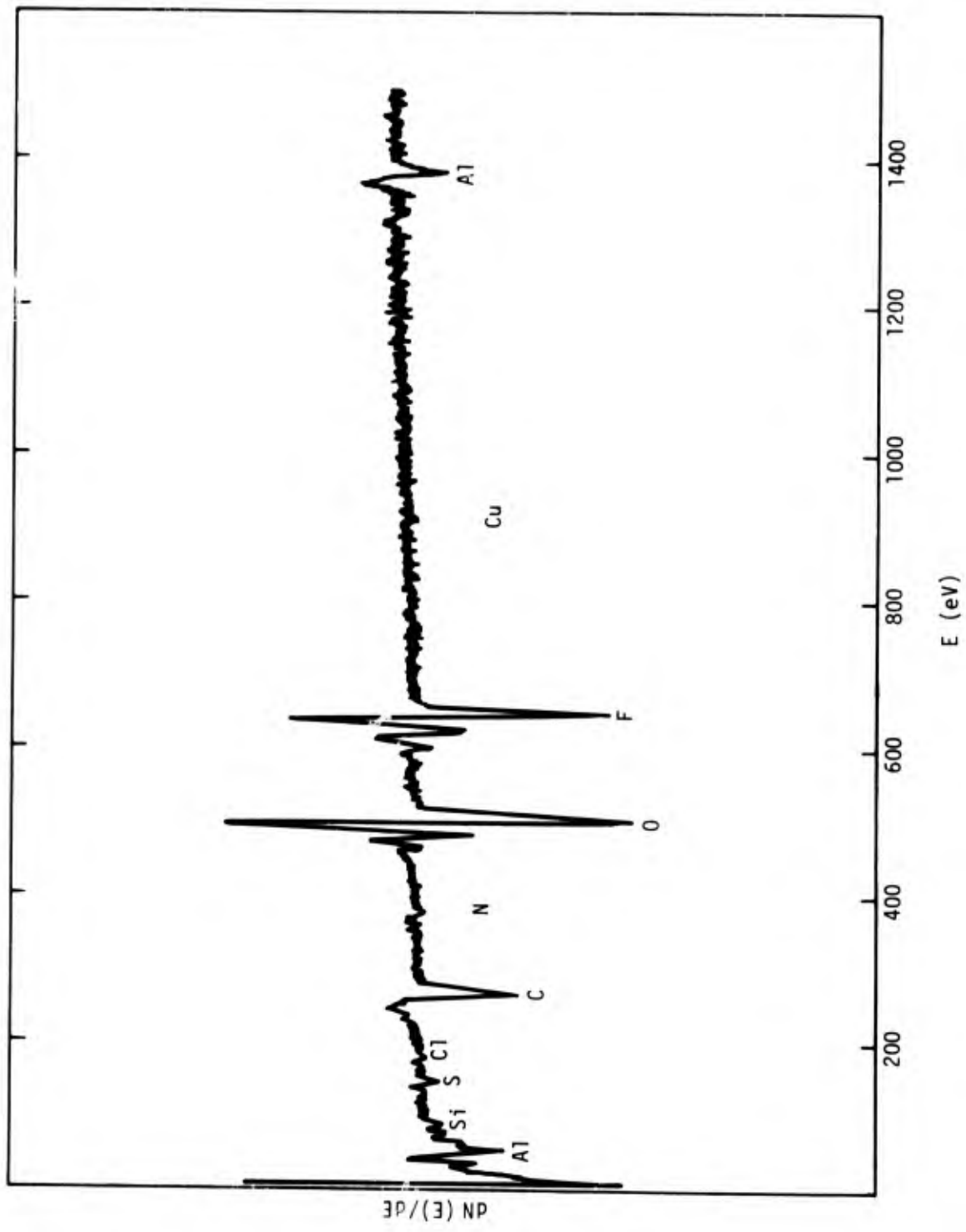


Figure 66. AES of sample aged in a glass jar at 58% RH.

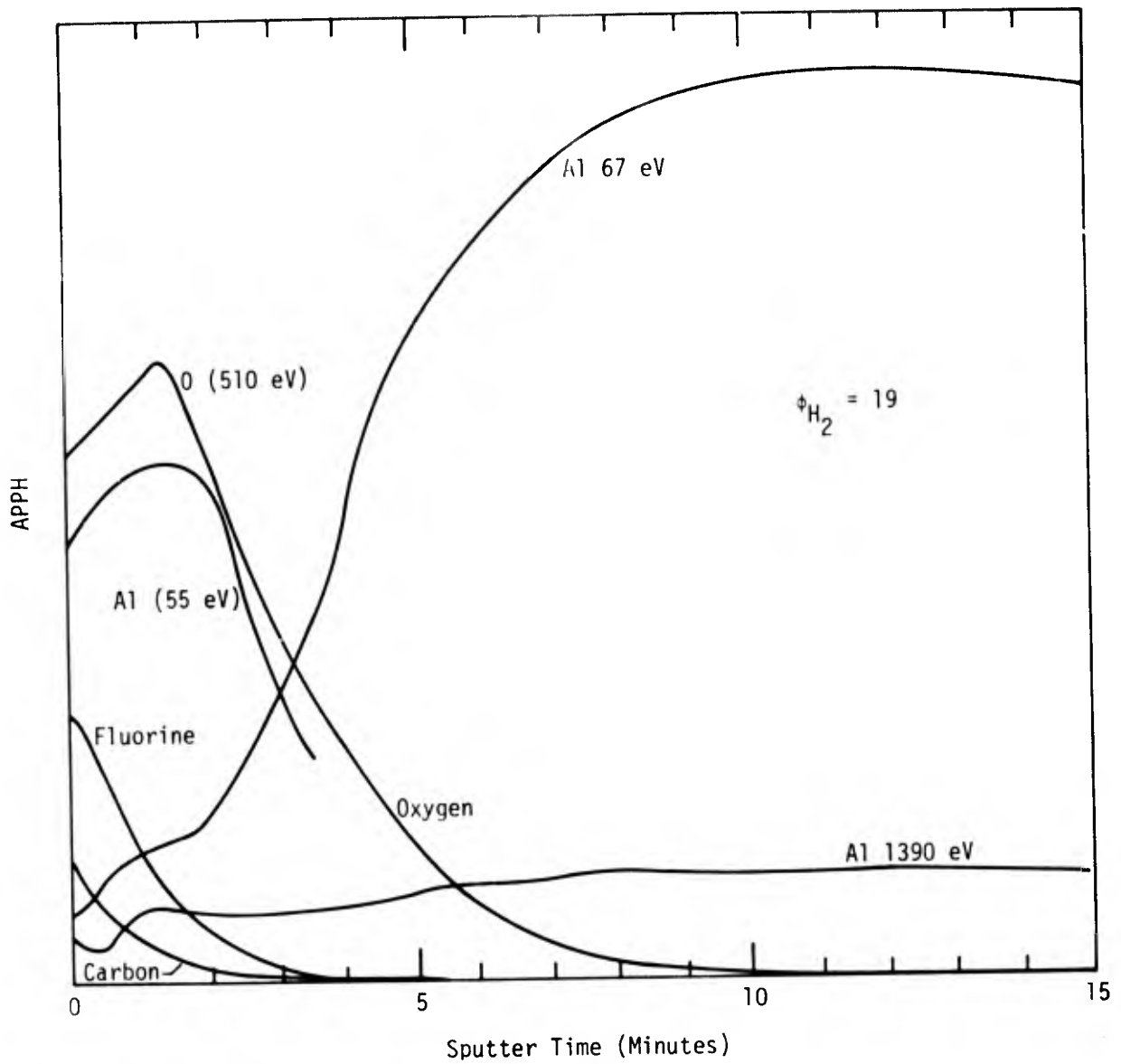


Figure 67. Sputter profile of sample aged in a glass jar at 58% RH.

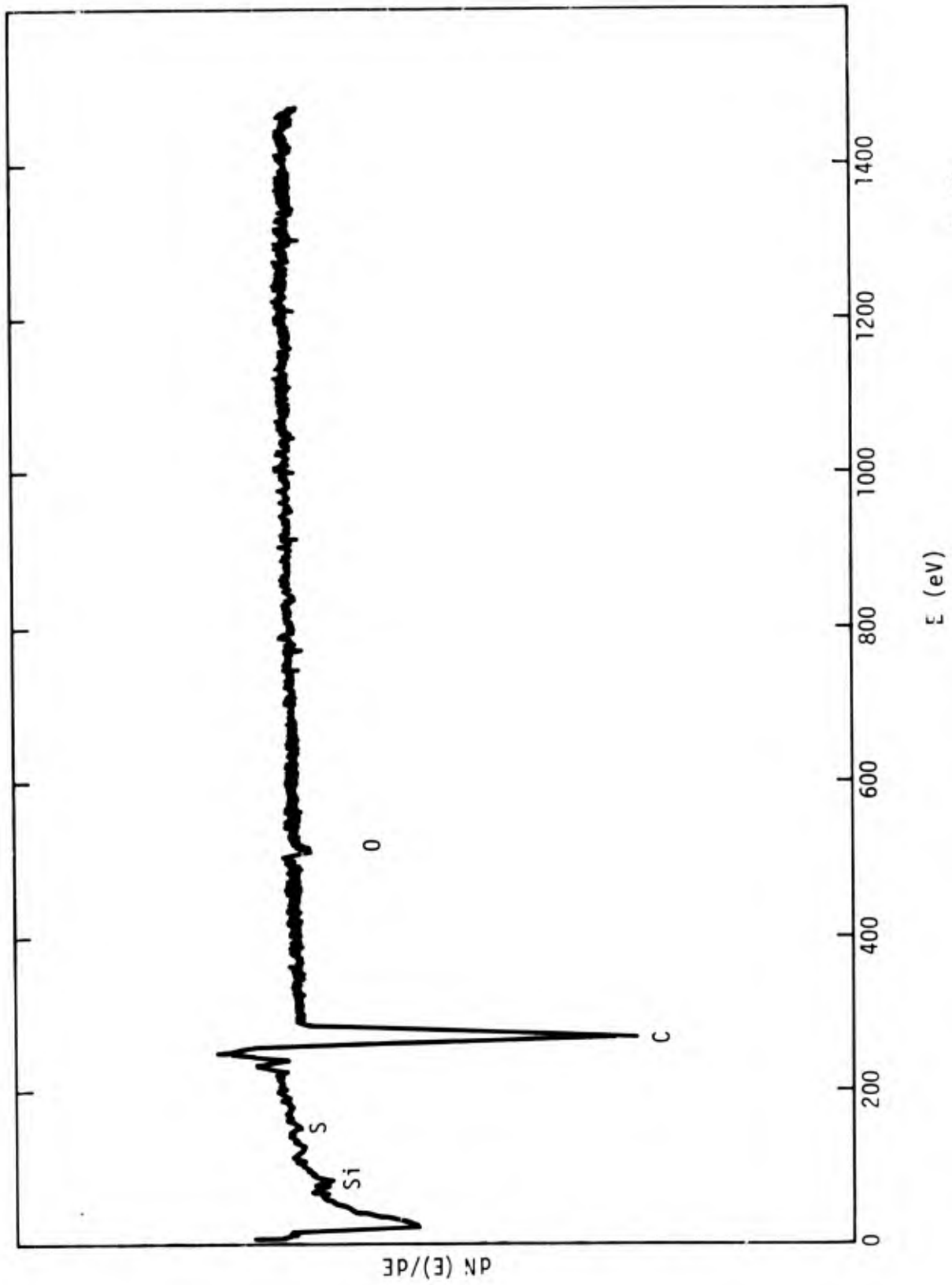


Figure 68. AES for the sample aged in a glass jar at 97% RH.

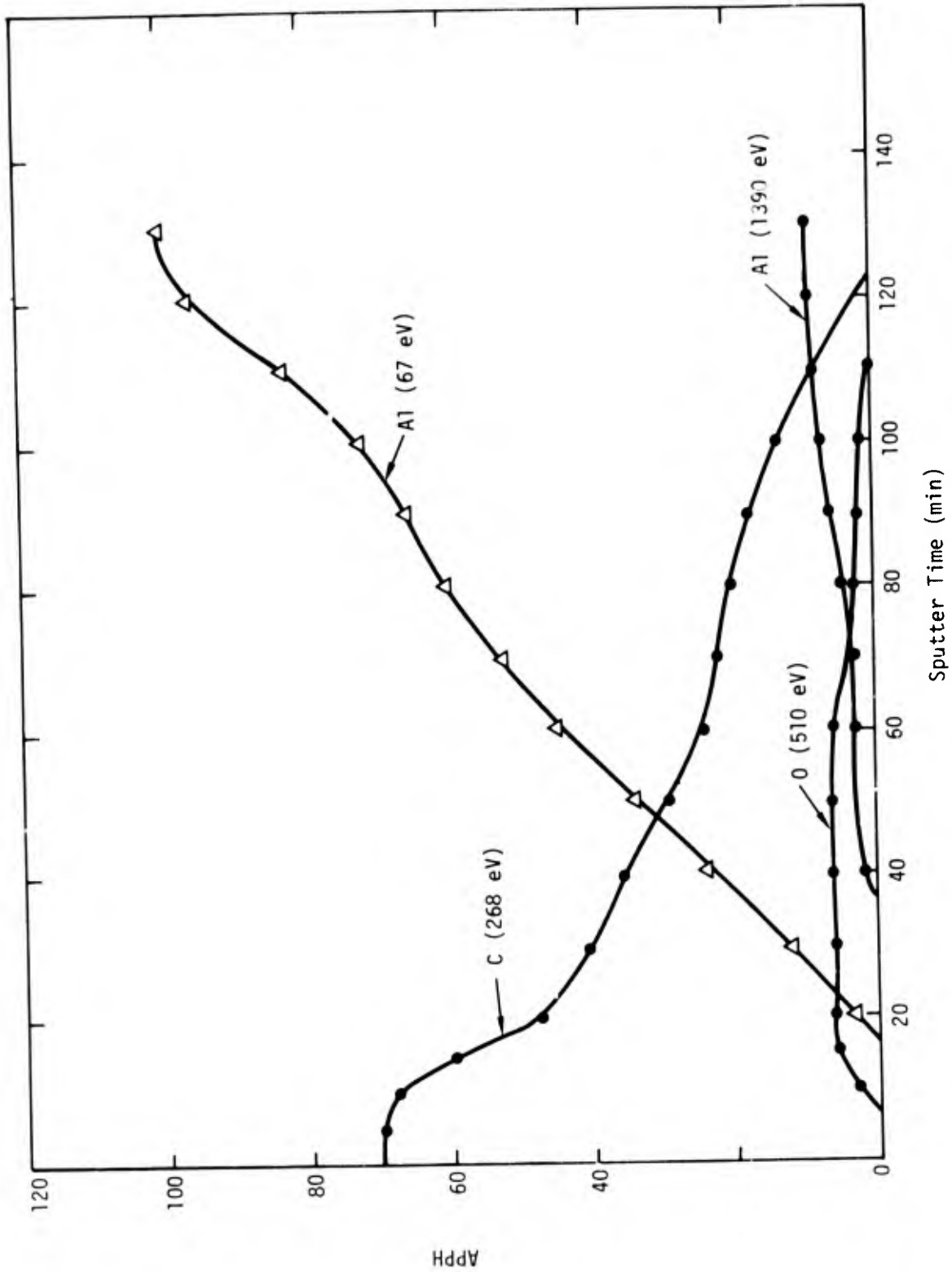


Figure 69. Sputter profile of the sample aged in a glass jar at 97% RH.

Table 22

FPL ETCH A1 2024-T3  
SET IN LAB AIR

Sample Time	$\Delta$	$\psi$	SPD	FEE <sup>-11</sup> x10	$\phi_{H_2O}$	
1	0	111.2	33.48	0.38	80	3
2		110.0	35.05	0.49	84	3
3		112.6	33.6	0.44	72	3
4		110.4	33.8	.48	49	6
5		108.4	34.2	0.46	120	5
6	0.3	109.6	34.8	0.51	47	15
		<u>110±1</u>	<u>34.1±5</u>	<u>0.46±.2</u>	<u>75±10</u>	<u>6±2</u>
1	1.3					6
2						8
3						7
4						14
5						8
6						18
						<u>10</u>
Front of Samples						
1	16.3	109.6	34.6	0.72	3.8	24
2		107.4	34.7	0.70	2.5	19
3		109.8	33.7	0.71	3.0	9
4		109.2	34.8	0.73	1.5	19
5		111.2	33.8	0.57	4.9	18
6		109.0	34.4	0.71	3.0	24
		<u>109±1</u>	<u>34.3</u>	<u>0.69</u>	<u>3.1?</u>	<u>19</u>
Back of Samples						
1	16.3	109.0	33.9	0.60	4.5	70
2		107.2	35.0	0.69	2.1	33
3		108.8	35.0	0.67	1.0	66
4		105.8	35.4	0.71	1.0	68
5		107.2	35.1	0.59	2.2	38
6		108.6	34.3	0.64	6.0	39
		<u>107.7</u>	<u>34.8</u>	<u>0.65</u>	<u>2.8?</u>	<u>52</u>

Table 22 (cont'd)

	24					
1		109.0	34.7	0.40	26	47
2		107.2	34.8	0.43	28	52
3		109.2	33.7	0.56	30	18
4		107.6	35.1	0.73	21	38
5		103.2	35.5	0.68	25	28
6		101.4	36.2	0.65	24	10
		<u>106.</u>	<u>35.0</u>	<u>0.57</u>	<u>25.7</u>	<u>32</u>
	87					
1		108.5	34.6	0.65	14	120
2		108.5	35.2	0.71	21	120
3		108.5	34.8	0.73	11	117
4		107.2	35.2	0.83	14	85
5		108.8	34.6	0.74	14	114
6		105.8	35.1	0.78	16	102
		<u>107.9</u>	<u>34.9</u>	<u>0.74</u>	<u>15</u>	<u>109.7</u>
	111					
1		108.4	35.1	0.74	11	53
2		107.8	34.8	0.73	14	22
3		109.2	34.7	0.72	14	5
4		106.8	35.0	0.80	13	73
5		109.2	34.9	0.70	11	12
6		106.0	35.4	0.82	13	76
		<u>107.9</u>	<u>35.0</u>	<u>0.75</u>	<u>12.7</u>	<u>40</u>
	135					
1		106.6	34.4	0.66	11	92
2		107.6	35.3	0.70	14	15
3		107.2	35.3	0.09	12	85
4		105.4	35.5	0.72	11	54
5		107.6	34.4	0.65	8	13
6		107.6	35.1	0.75	15	64
		<u>107.0</u>	<u>35.0</u>	<u>0.69</u>	<u>11.8</u>	<u>54</u>
	159					
1		107.2	34.6	0.68	10	89
2		107.8	35.2	0.68	13	23
3		106.6	35.4	0.66	11	77
4		107.4	34.8	0.73	7	69
5		108.0	34.6	0.64	13	35
6		104.2	35.6	0.77	20	59
		<u>107.0</u>	<u>35.0</u>	<u>0.69</u>	<u>12.3</u>	<u>58</u>

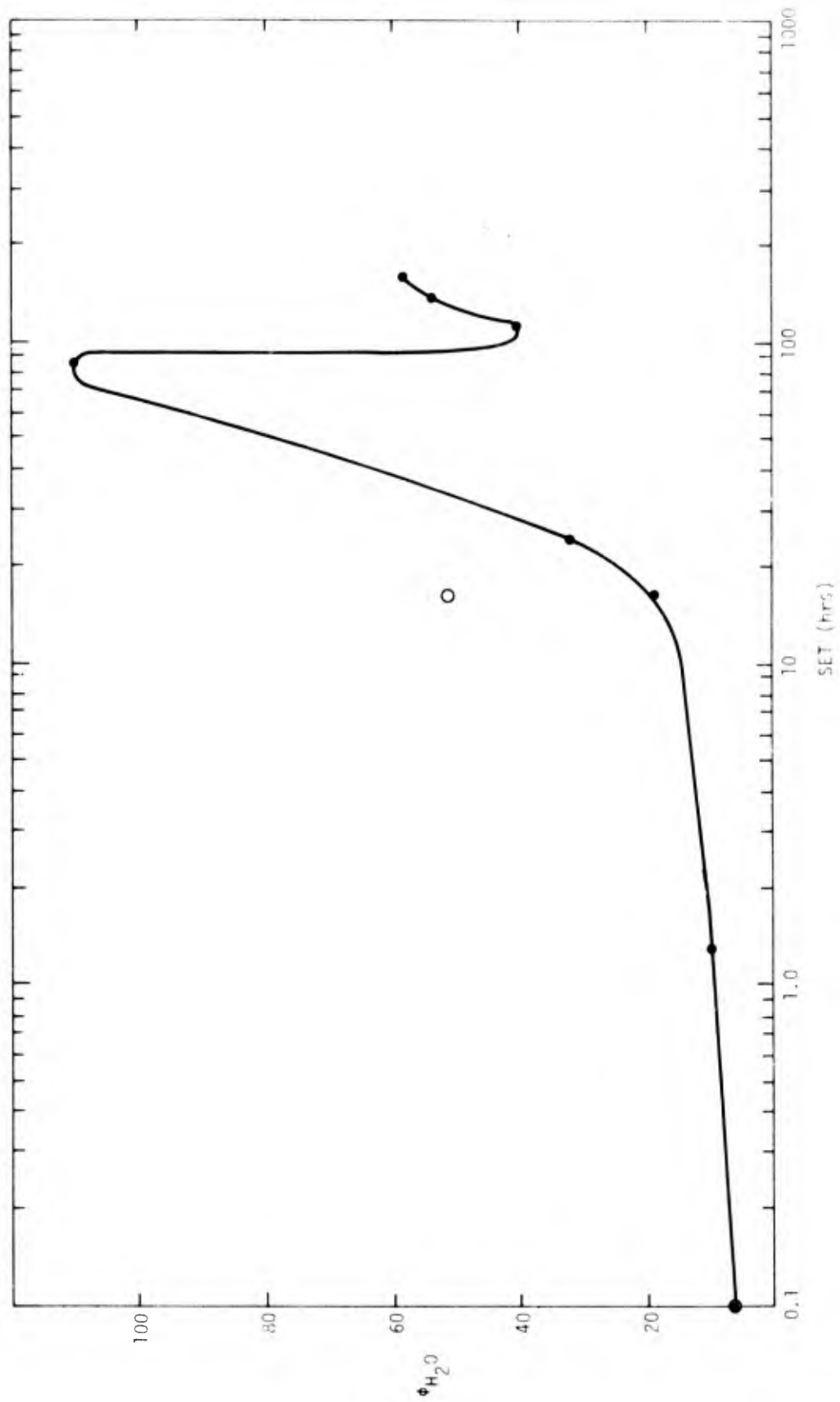


Figure 70. Plot of  $\overline{\phi}_{H_2O}$  vs SET in lab air.



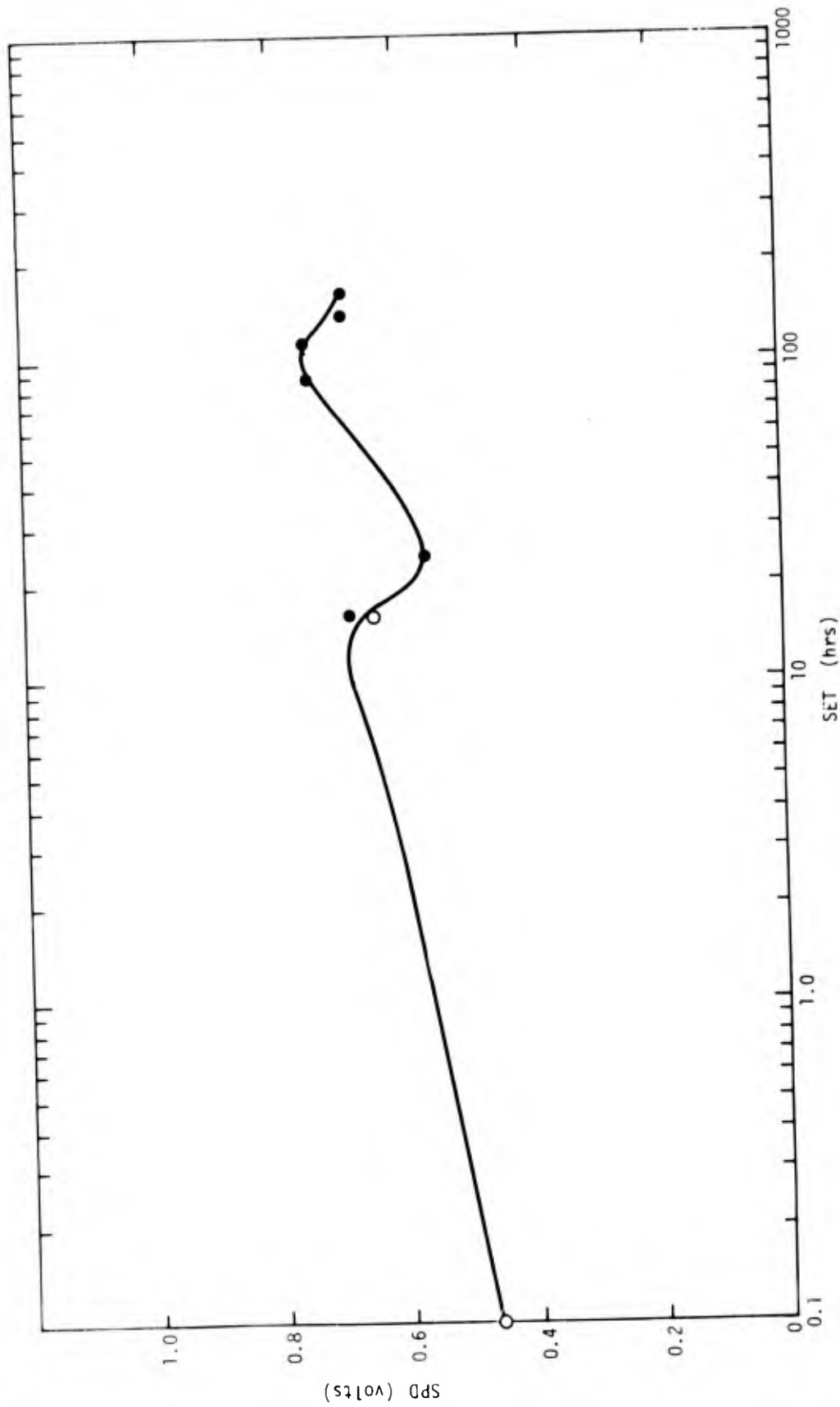
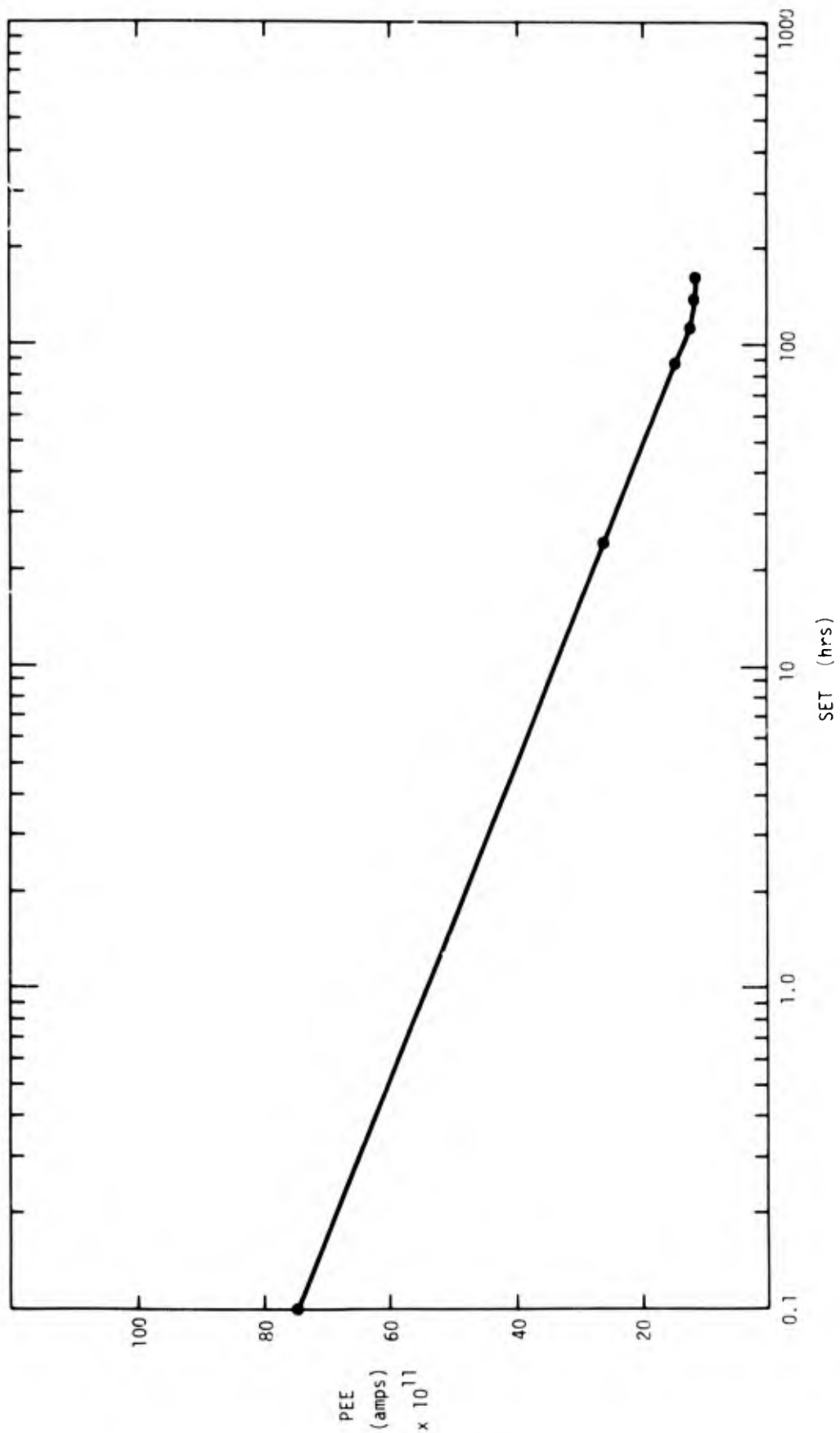


Figure 71. Plot of  $\overline{SPD}$  vs SET in lab air.



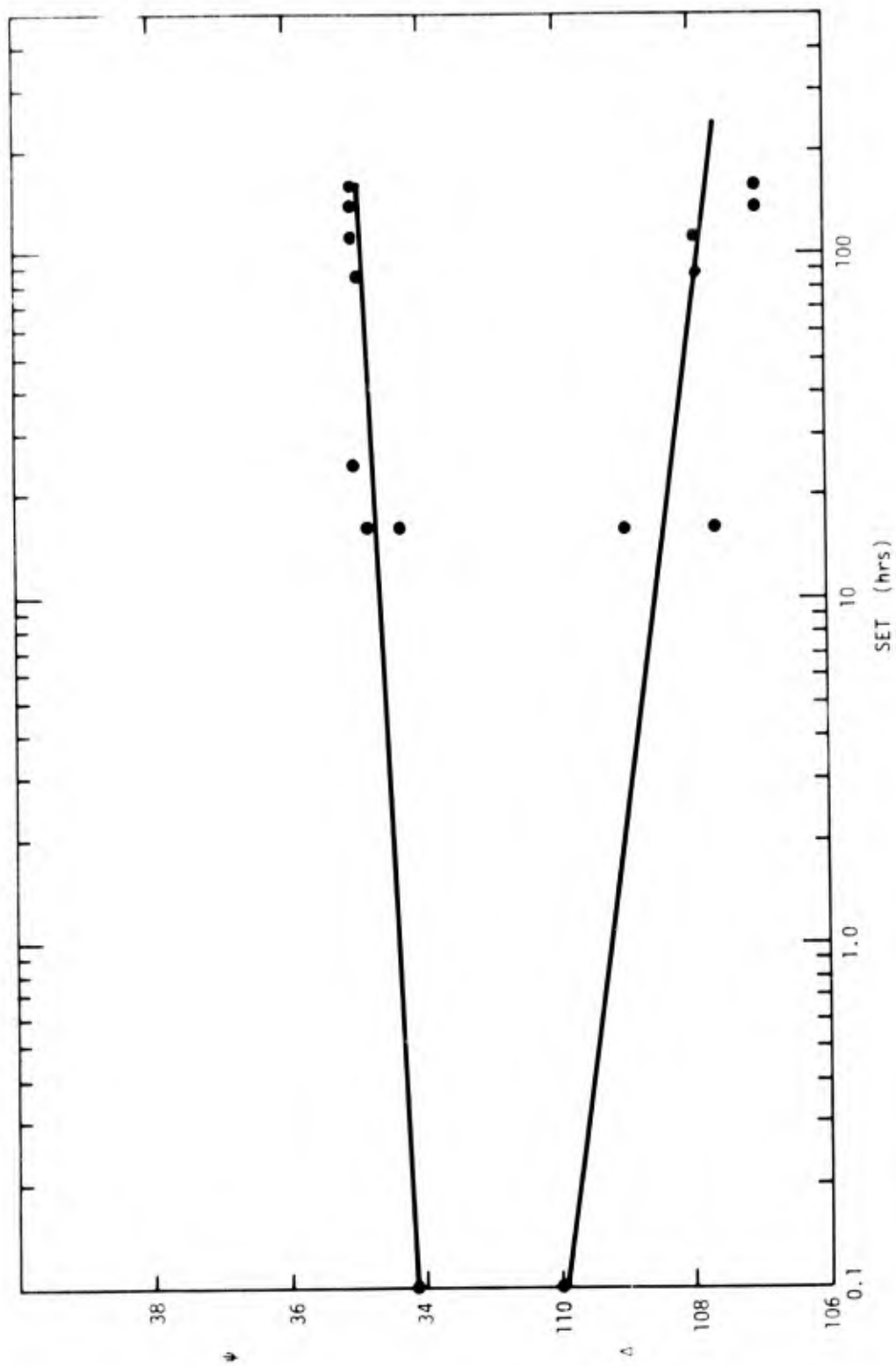


Figure 73. Plot of  $\Delta$  and  $\Psi$  vs SET in lab air.

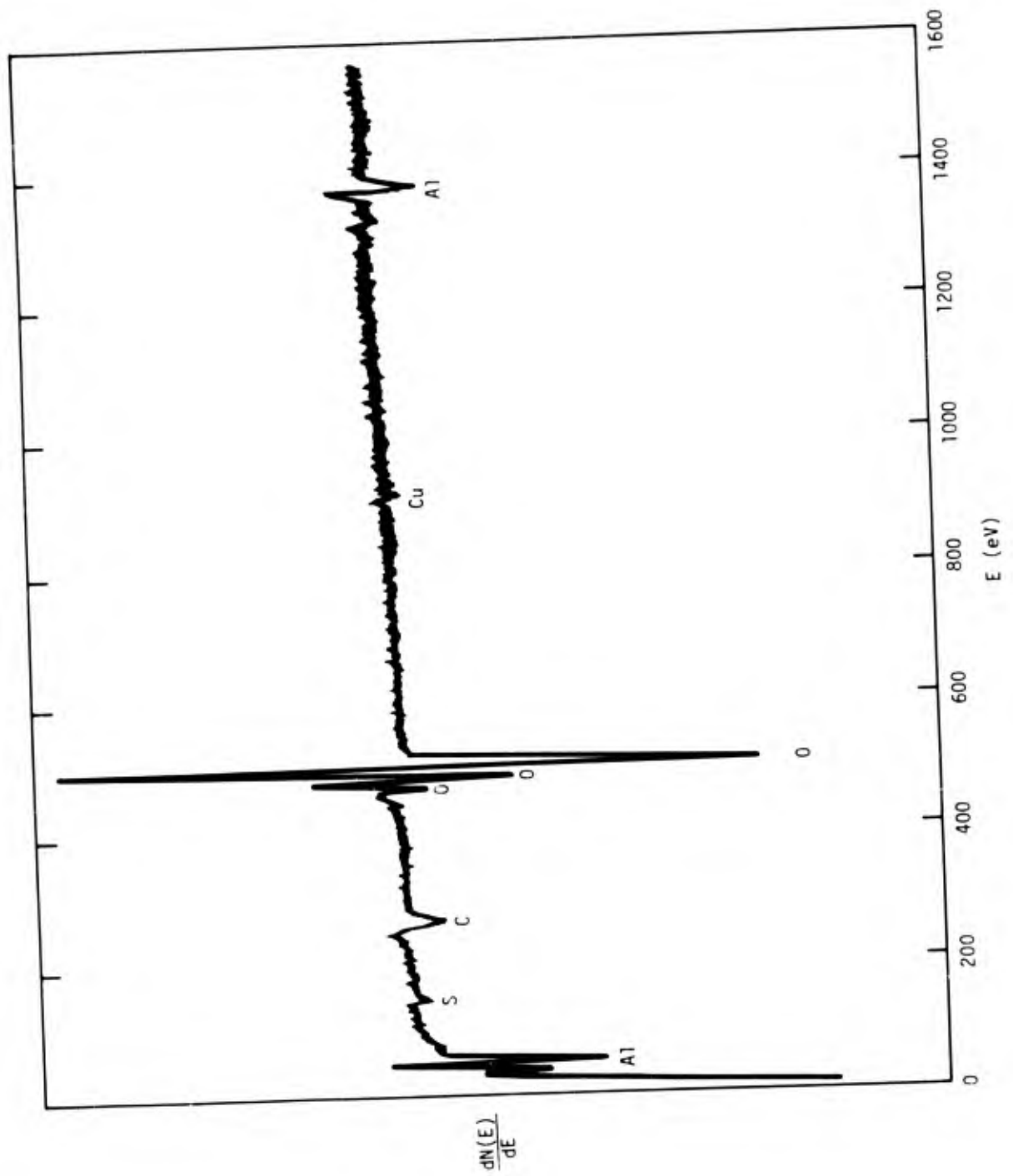


Figure 74. AES of lab air aged sample #1.

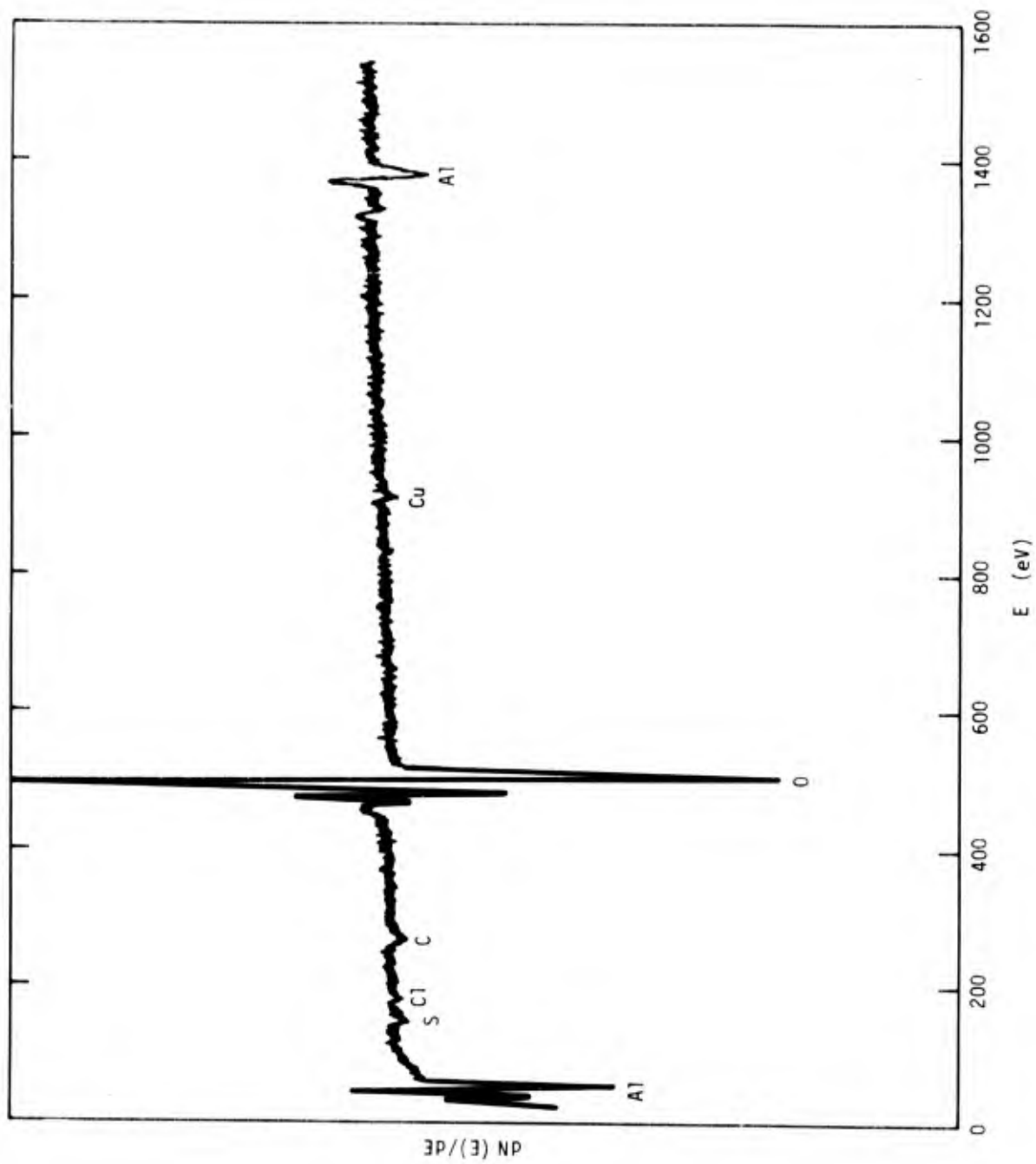


Figure 75. AES of lab air aged sample #2.

74 and 75 as well as the carbon peaks. Figures 76 and 77 show the sputter profiles for samples 1 and 2 respectively. The increase in APPH for oxygen in the first minutes (Fig. 76) is also indicative of carbon contamination since the underlying oxygen increases as the C is removed.

#### 7.4 SET in Water

##### 7.4.1 Surface Properties

Tables 23 and 24 give ellipsometric, SPD and PEE results as a function of immersion time for water immersion at 50°C and 100°C after FPL etch: It is possible to estimate the oxide thickness during the 3.3 hours because  $\Delta$  and  $\psi$  are tracked closely enough through their cycles to know the chromatic order. Since  $\Delta$  and  $\psi$  were not tracked between 3 and 19 hours, it is not possible to estimate film thickness at 19 hours. Attenuation of photo emitted electrons (PEE) to below our sensitivity occurs in about 0.16 hours (300-400 Å). A plot of film thickness and SPD are given in Figures 78 and 79 respectively. The bayerite film grows to about 2600 Å in the first hour at 50°C, then slows to a steady increase of about 1000 Å/hr. The boehmite film grows to about 2600 Å in the first 3 min. at 100°C, then slows down. The SPD decreases from 0.92 volts to 0.33 volts in 3 hours but increased to 0.6 in 19 hours. A corresponding curve is obtained in 100°C water but in a much shorter time.

Table 25 shows ellipsometric, SPD and PEE results for aging at 100°C in watervapor (95% RH). The SPD and film thickness results are also given in Figures 78 and 79 for comparison with the water immersion results. In watervapor at 100°C the film reaches 2600 Å much less rapidly than for 100°C water and more rapidly than in liquid water at 50°C but proceeds at a much slower rate thereafter than in liquid water at 50° or 100°C. The SPD decreases, increases and decreases again. For comparison, Figure 35 of the AFML-TR-74-73 June 1974 shows that at 50°C in

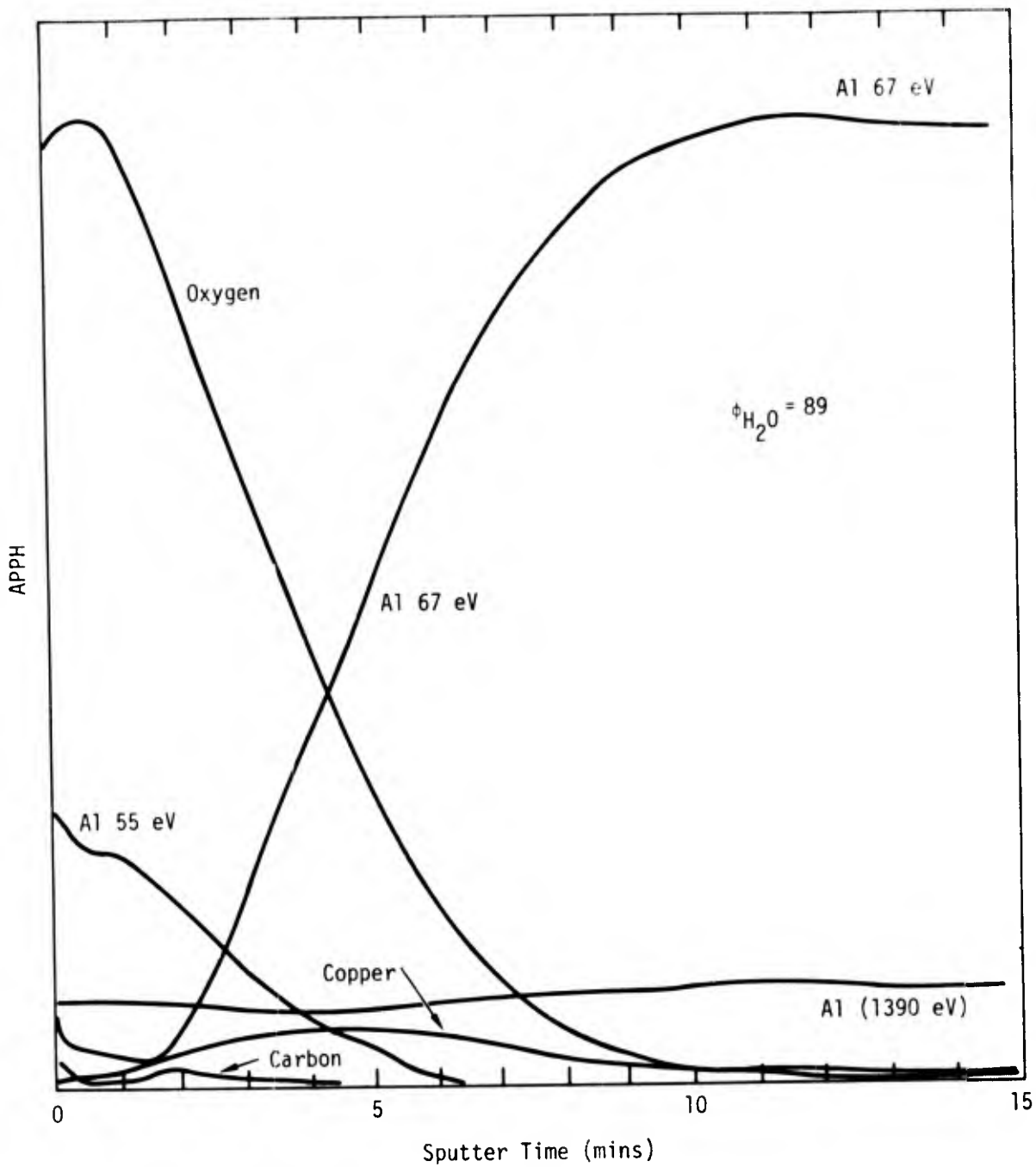


Figure 76. Sputter profile of lab air aged sample #1.

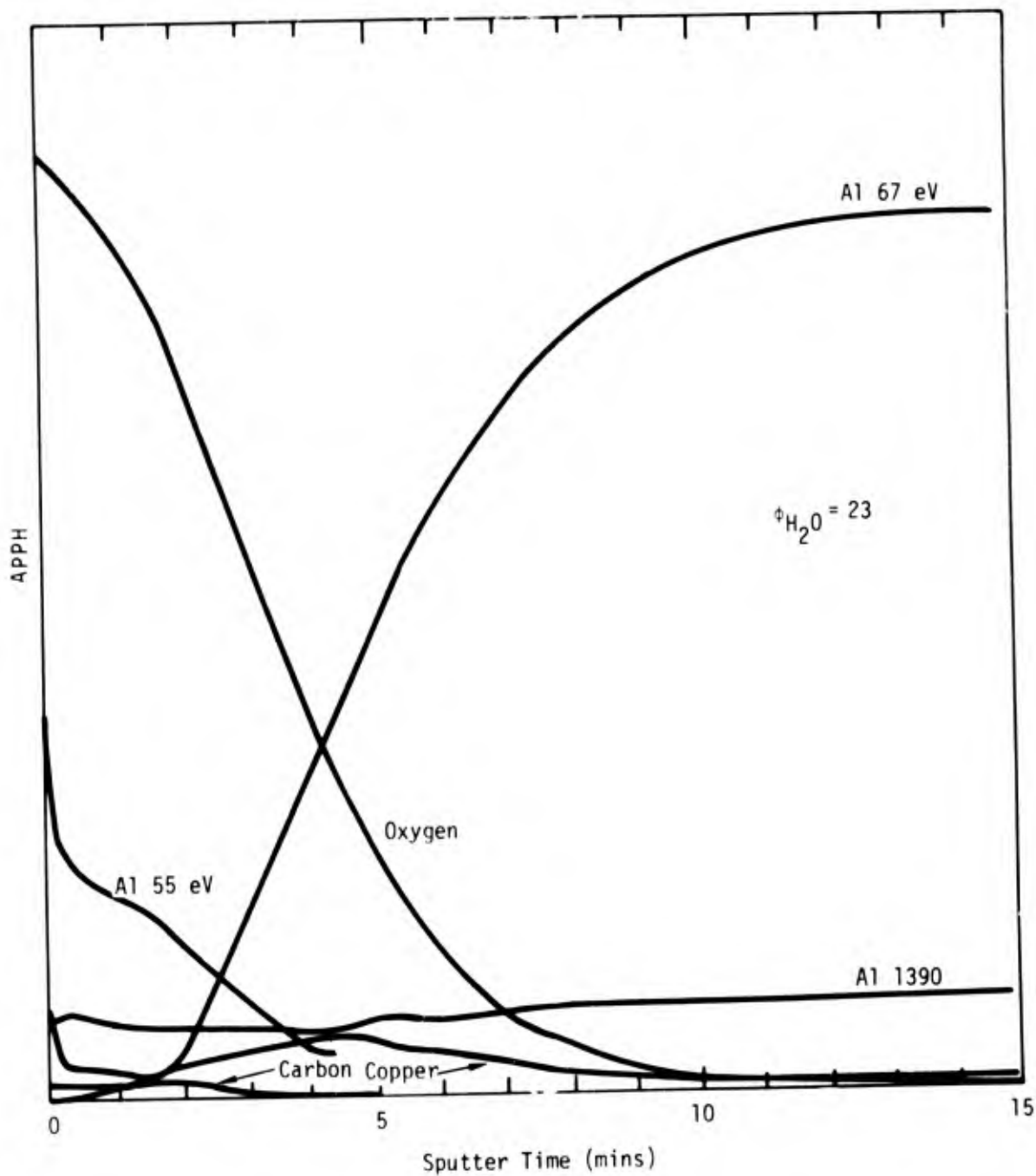


Figure 77. Sputter profile of lab air aged sample #2.



TABLE 23

EFFECT OF 50°C WATER IMMERSION AGING ON THE SURFACE  
 PROPERTIES OF Al 2024-T3 AFTER THE FPL ETCH

Immersion Time (hrs)	$\Delta$ (deg)	$\psi$ (deg)	$\psi'$ (deg)	Oxide Thickness (Å)	SPD (volts)	PEE $\times 10^{-11}$ (amps)
0	112.8	35.7	42.4	210	0.92	110
0.08	107.3	36.8	42.7	260	0.67	22
0.16	93.5	38.9	43.1	410	0.55	0
0.25	87.1	40.4	43.6	500	0.48	
0.42	-154.1	47.7	48.7	1175	0.58	
0.58	183.2	22.6	41.5	2200	0.45	
0.83	110.7	26.8	42.6	2700	0.41	
1.16	91.3	35.1	43.4	2900	0.36	
1.66	95.1	52.0	46.2	3300	0.40	
2.17	189.7	59.0	49.8	3550	0.40	
2.67	-144.3	37.2	41.9	4450	0.33	
3.33	-148.9	27.5	41.7	4500	0.33	
19.0	37.9	39.8			0.62	

TABLE 24

EFFECT OF 100°C WATER IMMERSION AGING ON THE SURFACE  
PROPERTIES OF Al 2024-T3 AFTER THE FPL ETCH.

Immersion Time	$\Delta$	$\psi$	$\psi'$	Oxide Thickness	SPD	PEE
(hrs)	(deg)	(deg)	(deg)	(Å)	(volts)	$\times 10^{-11}$ (amps)
0	108.2	38.1	42.6	250	0.66	41
.017	167.5	33.1	41.4	2300	0.43	0
.033	127.2	35.0	42.1	2550	0.36	
.050	113.1	37.1	42.4	2650	0.28	
.083	101.8	40.1	42.9	2750	0.37	
.17	96.9	44.2	43.0	2820	0.37	
.33	106.6	48.1	47.0	3350	0.47	
.66	181.7	55.4	50.0	3570	0.44	
2.00	-134.1	35.8	42.0	4400	0.52	

TABLE 25

EFFECT OF SET AT 100°C 95% RH ON FPL ETCHED Al 2024-T3

SET (hrs)	$\Delta$ (deg)	$\psi$ (deg)	$\psi'$ (deg)	Oxide Thickness (Å)	SPD (volts)	PEE $\times 10^{-11}$ (amps)
0	110.6	37.4	42.6	200	0.75	68
0.17	181.5	47.3	49.9	1100	0.53	0
0.33	184.5	34.1	41.4	2200	0.66	
1.0	128.0	34.0	41.9	2500	0.80	
2.0	111.4	37.4	42.4	2650	0.48	
3.5	103.2	39.9	42.8	2750	0.53	
21.5	107.2	47.7	47.0	3350	0.42	

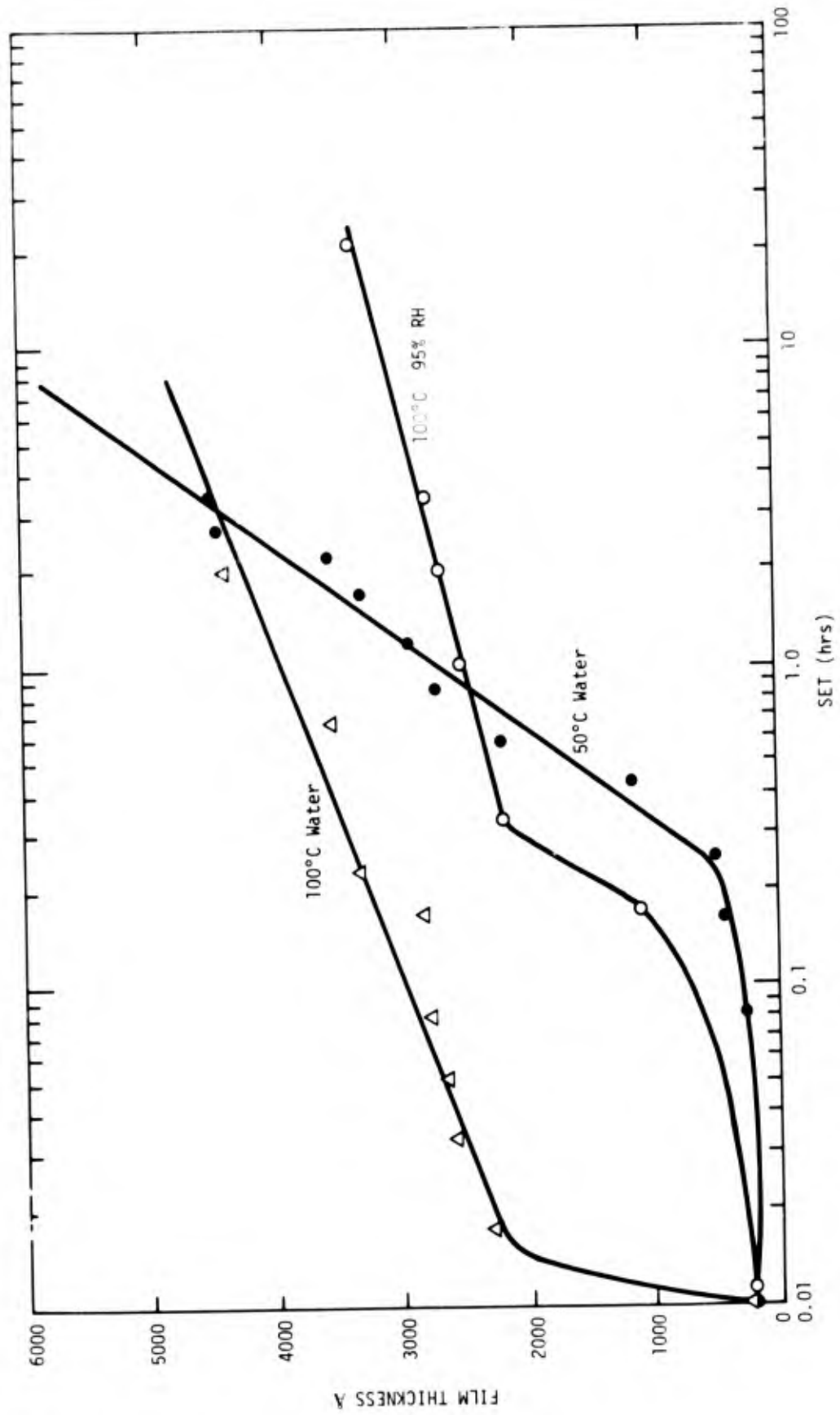


Figure 78. Plot of oxide thickness vs SET for Al 2024-T3 aged in water and water vapor.

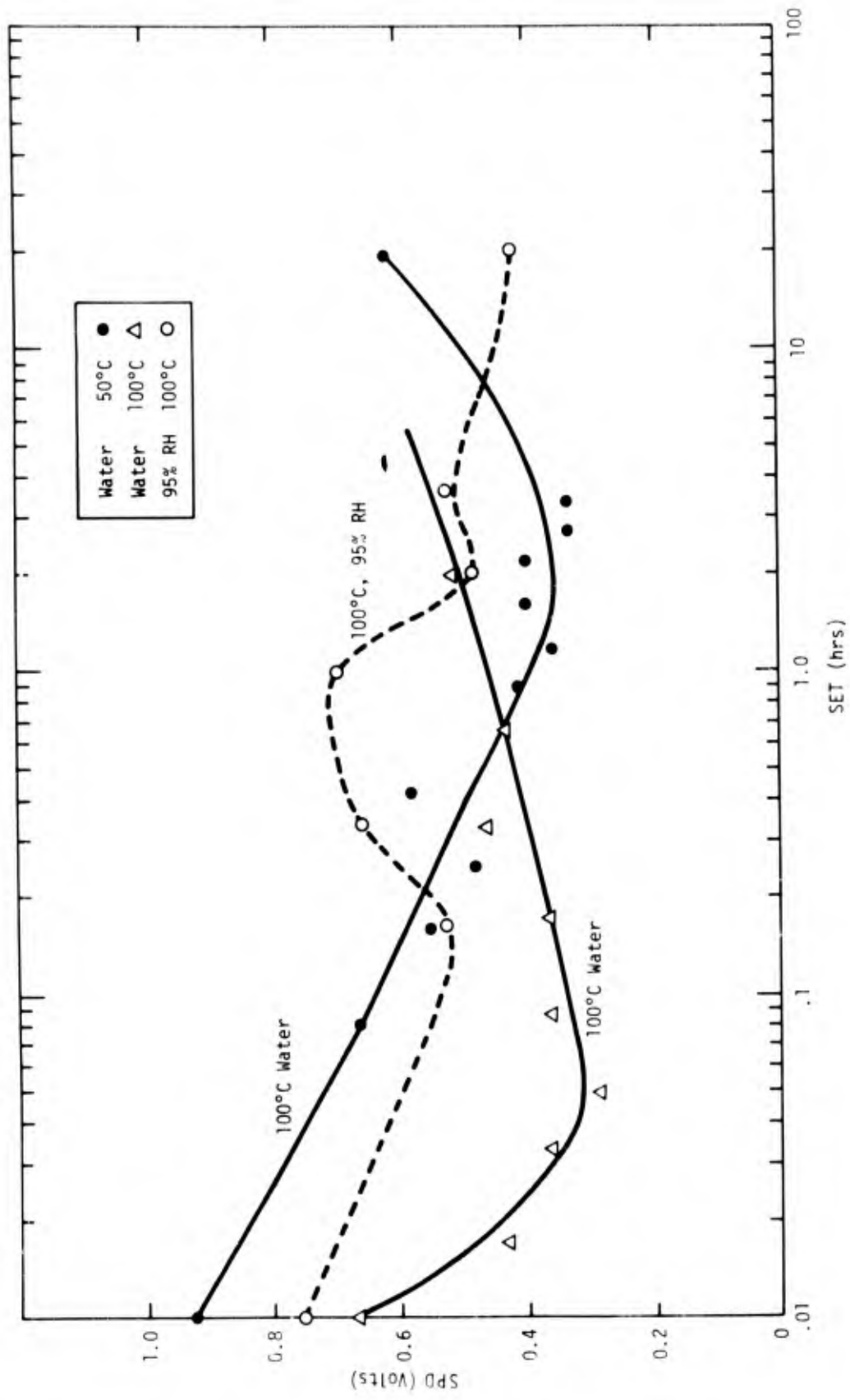


Figure 79. Plot of SPD vs SET for samples aged in water and water vapor.

watervapor (95% RH) the film only grew about 30 Å in 100 hours although the SPD decreased then increased as usual. Figure 65 of this report shows that the film grew about 35 Å in 100 hours at room temperature.

The values of  $\psi$  in Tables 24 and 25 are the theoretical values that would correspond to the  $\psi$  values if the samples were smooth. The rough FPL etch surfaces cause  $\psi$  to cycle with much larger variations than for a smooth surface. We have previously shown a direct correlation between surface roughness and  $\psi$

### 7.5 Effect of SET on Bond Strength

Table 26 shows the effect of SET in water at 50°C, in water at 100°C and in water vapor at 100°C, 95% RH, on the bond strength for HT424 from batch 2. The reported bond strengths are the average of six bonds in each case. In spite of the thick oxide films (to 4400 Å) after SET (bayerite for 50°C immersion and boehmite for 100°C immersion) the bond strengths are close to the control fresh FPL samples.

Table 27 shows the surface properties and bond strengths for similar treatments but with HT424 from batch 3. In this case, the bond strength is very sensitive to the surface treatment. Each of the treated Al2024-T3 samples in Table 27 was bonded with an FPL etched sample. Except for the phosphoric acid anodic sample which failed almost entirely by cohesive fracture ( $\phi_c \sim 1$ ), interfacial failure always occurred at the SET treated surface rather than the fresh FPL etched surface. Except for the as-received degreased sample the samples were FPL etched prior to SET. The film thickness values for thick films in Table 27 are estimated from Figure 78; the fractured area that failed cohesively was estimated visually.

The contact angle of the degreased sample was 80°. Such a sample gave a bond strength of ~ 2400 psi in previous work (AFML-TR-74-73). Exposure to water at 99°C for 5 minutes increased the hydroxide thickness to ~ 2800 Å and lowered the

TABLE 26

EFFECT OF SET FOR VARIOUS SURFACE PREPARATION AND AGING OF Al 2024-T3

SET	Conditions	$\Delta$	$\psi$	Oxide Thickness	SPD	Contact Angle	Bond Strength
(hrs)		(deg)	(deg)	(Å)	volts	(deg)	( $\sigma_b$ ) (psi)
0	FPL etch	110.6	37.4	200	0.75	3	2740±130
0	Phosphate anodize	189.0	46.5	3570	0.08	11	2600±132
0.3	50°C water	-154	47.7	1175	0.58	18	2600±152
2	50°C water	189.7	59.0	3550	0.40	18	2600± 67
2	100°C water	-134.1	35.8	4400	0.52	18	2613±156
2	100°C, 95% RH	111.4	37.4	2650	0.48		2670±100

Table 27

EFFECT OF SET IN WATER AND WATER VAPOR ON SURFACE PROPERTIES  
AND BOND STRENGTH (Al 2024-T3 - HT424, BATCH 3, GTL = 0.009")

Surface Treatment	$\Delta$ (deg)	$\psi$ (deg)	Film Thickness (Å)	SPD (volts)	PEE (amps $\times 10^{-11}$ )	$\phi_{H_2O}$ (deg)	$\phi_c$	$\sigma_b$ (psi)
Acetone degrease	85.4	33.4	200	0.61	7.0	80		
5 min., 100°C, water	157.8	41.0	2800	0.20	0.7	20		
10 "	152.2	39.7	3000	0.12	0.7	6	0.9	420
FPL etch	110.4	37.2	100	0.50	64	8		
10 hrs., Lab air	108.6	37.7	114	0.25	15	50		
2 hrs., 50°C, water			3700	-0.05	0	20	0.1	1300
FPL etch	106.8	36.2	128	0.21	35	3		
2 hrs., 100°C, water			4200	0.004	8	2	0.11	1830
FPL etch	106.0	36.4	135	0.20	29	4		
1 min., 100°C, water			2300	0.37	0.7	1	0.7	3000
FPL etch	109.2	35.8	114	0.44	64	4		
2 hrs., 100°C, 95%RH			2600	0.08	2.7	110	0.9	3560
FPL etch	170.2	35.6	2000	0.38	0.4	14	0.95	3900
Phosphate anodize 10V, 20 min.								



contact angle to  $20^\circ$ . Another exposure for 5 minutes increased the film to about  $3000 \text{ \AA}$  and lowered the contact angle to  $6^\circ$ . Consequently the weak bond strength of 420 psi is probably not due to contamination but to the weak oxide. The failure was essentially all interfacial at the water treated surface. Measurement of  $\Delta$  and  $\psi$  and the increase in SPD and PEE of the fracture surface correspond to an oxide film about  $900 \text{ \AA}$ , indicating failure was indeed in the oxide. The strongest bond from a water treated sample was for 1 minute in  $100^\circ$  water. Even though the boehmite film is  $\sim 2300 \text{ \AA}$ ,  $\sigma_b = 3000$  psi. The thicker ( $\sim 4200 \text{ \AA}$ ) boehmite film (2 hours,  $100^\circ\text{C}$  water) failed mostly at the interface with  $\sigma_b = 1830$  psi. This can be compared with the  $3700 \text{ \AA}$  bayerite film with  $\sigma_b = 1300$  psi. The  $2600 \text{ \AA}$  film formed in  $100^\circ\text{C}$ , 95% RH failed mostly cohesively with  $\sigma_b = 3560$  psi as compared to 3700 psi for the  $\sim 2000 \text{ \AA}$  anodic film. The 340 psi decrease for the water vapor aged sample, as compared to the anodic film sample may be attributed to contamination which caused the large contact angle ( $\phi_{\text{H}_2\text{O}} \sim 110$ ). The 340 psi decrease is of the order caused by a monolayer of myristic acid. As observed earlier, there is a direct correlation between  $\phi_c$  (and therefore  $\phi_I$ ) and bond strength in Table 27, the greater the fraction that failed interfacially the lower the strength.

#### 7.6 BET in Water

Table 28 contains the results for Al 2024-T3 - HT424 BET measurements at  $100^\circ\text{C}$ , 95% RH for the vapor phase and  $50^\circ\text{C}$  and  $100^\circ\text{C}$  for the liquid water phase. These results are graphed in Figure 80. In  $100^\circ\text{C}$  95% RH water vapor bond exposure, the bond strength dropped to about 2300 psi in about 200 hours as compared to about 2500 psi for  $54^\circ\text{C}$  and 95% RH (AFML-TR-74-73 Fig. 50). A similar rapid degradation occurred in  $100^\circ$  water but to about 1800 psi. Bond degradation in  $50^\circ$  water was much slower but decreased to about the same value as for  $100^\circ\text{C}$  water at 1,000 hours ( $\sim 1750$  psi). As mentioned earlier, it is believed that

TABLE 28

## BET STUDY OF Al 2024-T3 - HT424

Time (hr)	100°C, water- Vapor, 95% RH		50°C water		100°C water	
	$\sigma_b$ (psi)	$\pm$ (psi)	$\sigma_b$ (psi)	$\pm$ (psi)	$\sigma_b$ (psi)	$\pm$ (psi)
0	2750	130	2750	130	2750	130
1	2793	116	2847	64	2257	78
23	2480	73	2663	151	2020	100
68	2370	127	2377	29	1810	53
339	2430	60	2070	67	1890	113
1007	2163	209	1743	138	1690	53
0.3					2240	191

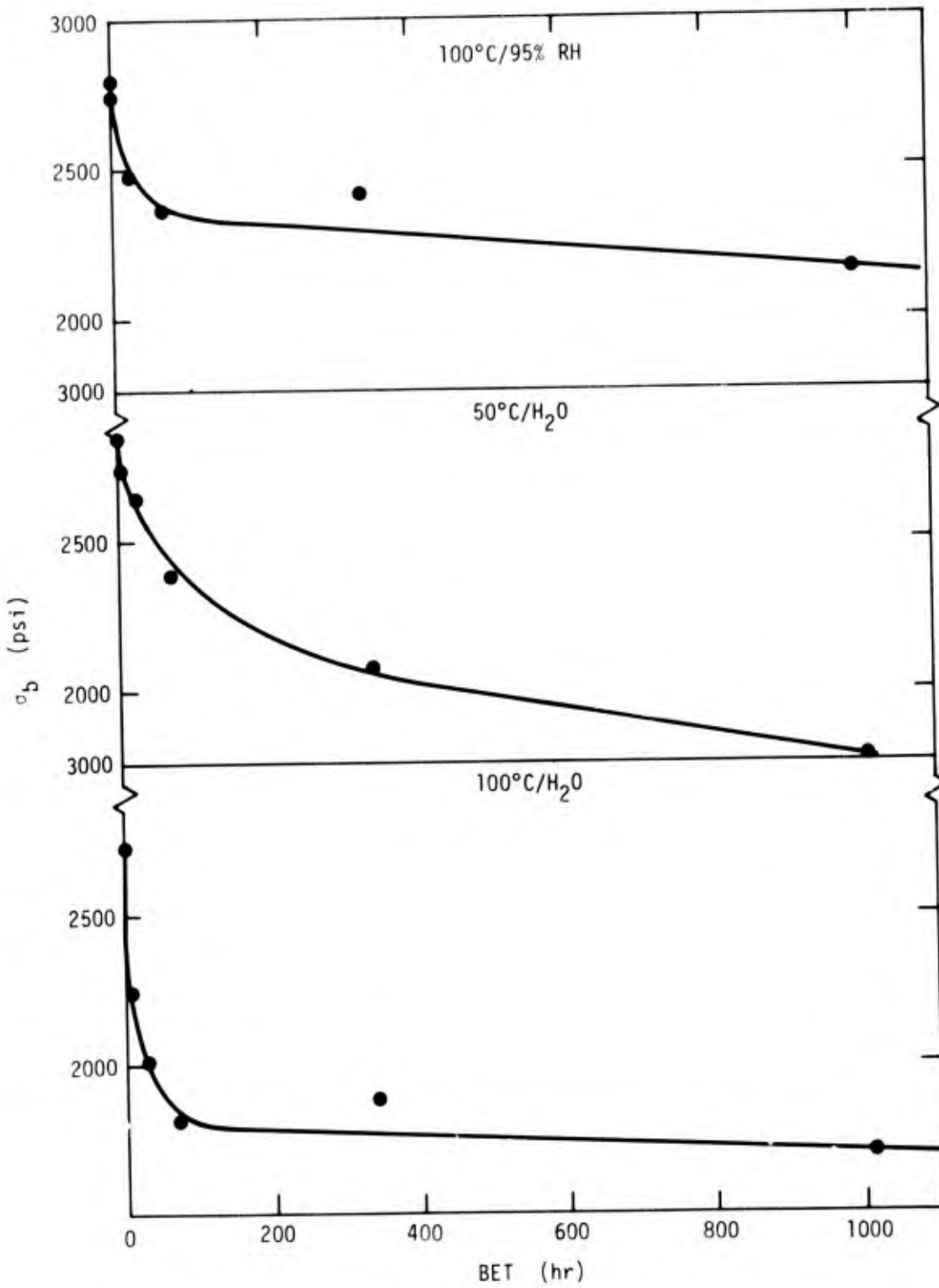


Figure 80. Plot of  $\sigma_b$  vs BET for adhesive joints in water and water vapor.

water and water vapor gains access to the interior of the bond along glass fiber channels and weakens the adhesive.

### 1. Surface Treatments and Bond Strength

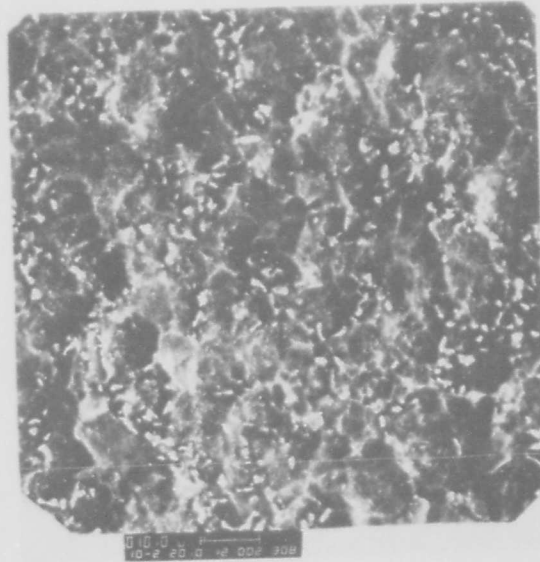
A number of surface treatments have been developed for Ti-6Al4V adhesive bonding. Four of these are phosphate-fluoride, TURCO, PASA JELL, and nitric acid-fluoride. Each of these processes is slightly different in different laboratories. Appendix A gives the detailed steps for each of these processes as used in our laboratory. Appendix B gives details of the phosphate - fluoride process as used in two other laboratories. Some of the surface character and bond strength results were reported in AFML-TR-74-73. In this report, we extend this investigation to discover the effect various modifications to these surface treatments has on surface properties and resultant bond strength.

#### 1.1 Comparison of the Four Treatments

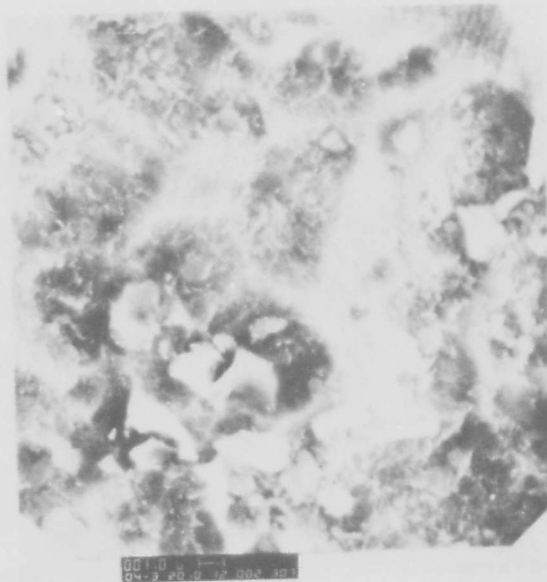
##### 1.1.1 SEM study

Figure 81 shows SEM pictures of a degreased Ti-6Al4V sample for comparison with the SEM pictures for the various surface treatments shown in Figures 82 and 83. The degreased as-received sample is as rough as any of the other surface treatments but appears to have more loose particles.

Figures 84 and 85 show SEM pictures of Ti-6Al4V-HT424 fracture surfaces and Ti-6Al4V-FM34B-32 (new batch) respectively. The surface treatment was phosphate-fluoride. Figure 84a shows a low magnification picture of the adhesive surface (at the left) the glass carrier, the metal interface (center) and some cohesive fracture. Figure 84b is a higher magnification of the metal interface region of Fig. 84a. A good deal of cohesive fracture is observed in this region. A much larger magnification of the metal surface in Fig. 84c is replicated by the adhesive in Fig. 84d. Figure 85a is an SEM picture for fractured Ti-6Al4B-FM34B-32 showing adhesive, cohesive and glass carrier

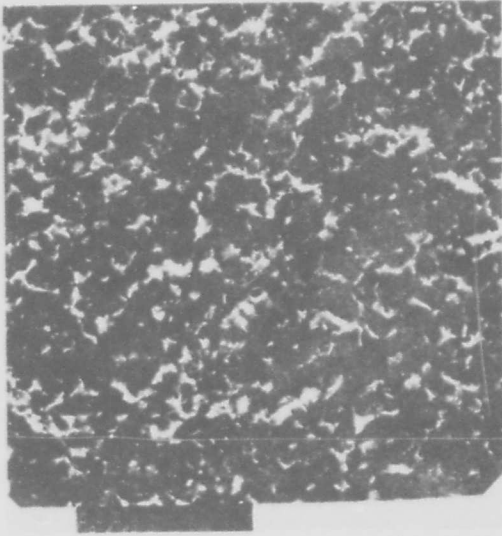


(a) 1000X



(b) 4000X

Figure 81 SEM pictures of vapor degreased Ti-6Al-4V.

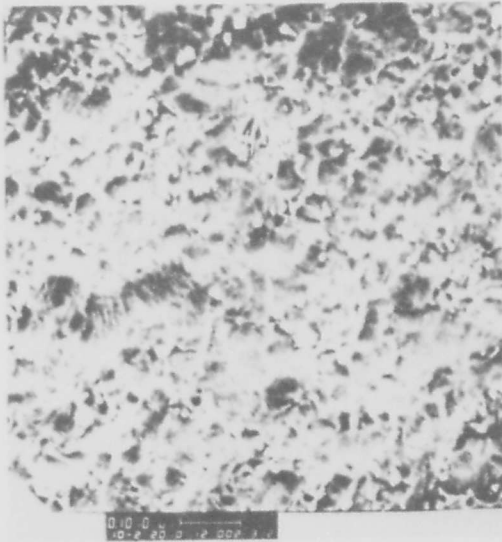


(a) 1000X

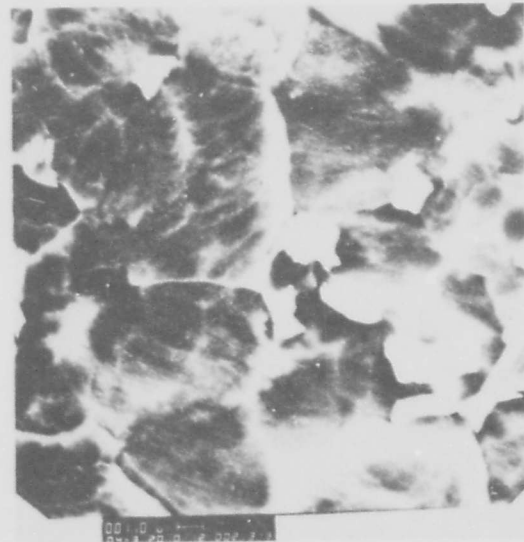


(b) 4000X

Phosphate-fluoride Ti-6Al-4V



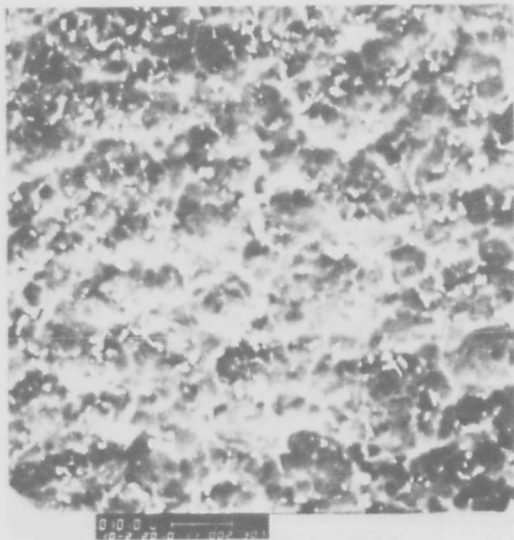
(c) 1000X



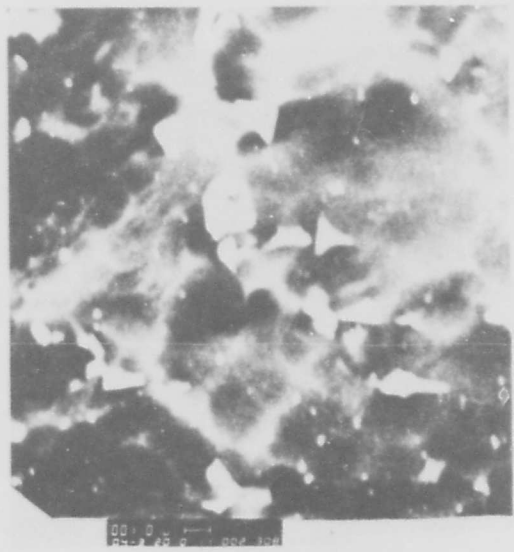
(d) 4000X

Turco Ti-6Al-4V

Figure 82 SEM pictures of Ti-6Al-4V, a+b) after phosphate-fluoride treatment, c+d) after the Turco treatment.

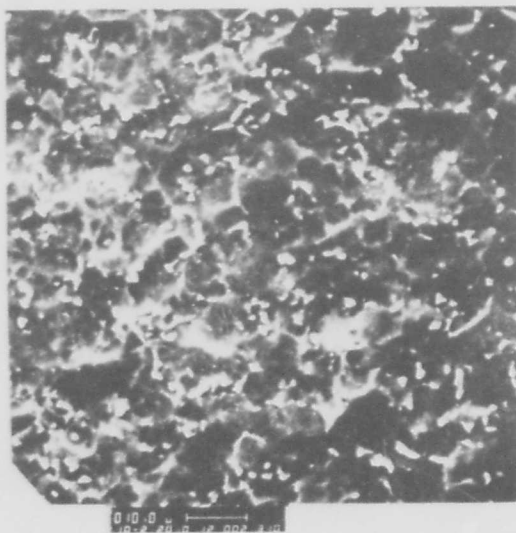


(a) 1000X

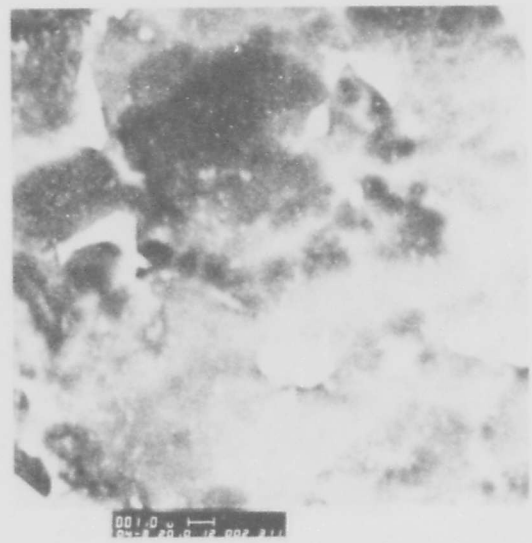


(b) 4000X

Nitric acid-fluoride Ti-6Al-4V



(c) 1000X



(d) 4000X

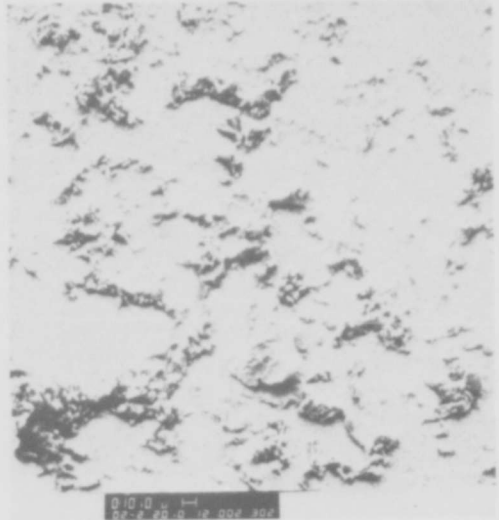
Pasa Jell Ti-6Al-4V

Figure 83 SEM pictures of Ti-6Al-4V, a+b) after Nitric acid-fluoride treatment, c+d) after Pasa Jell treatment.





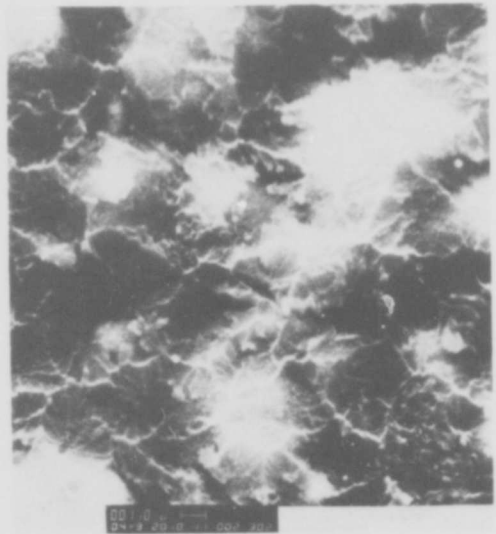
(a) 20X



(b) 200X



(c) 4000X

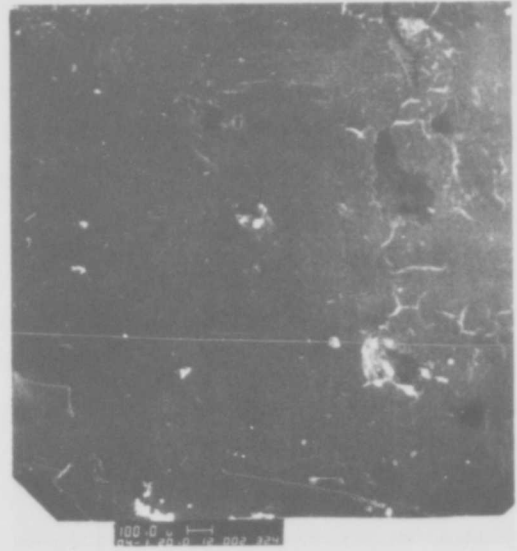


(d) 4000X

Figure 84 SEM pictures of Ti-6Al-4V - HT424 joint after fracture.



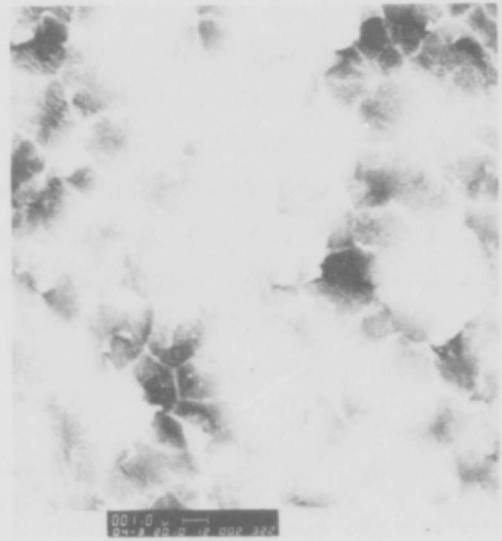
(a) 20X



(b) 40X



(c) 1100X



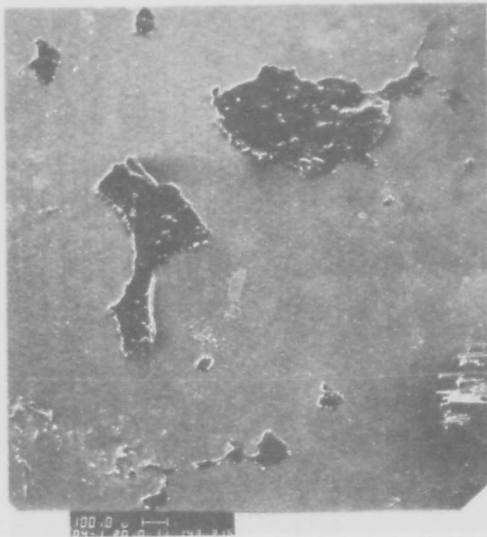
(d) 4000X

Figure 85 SEM pictures of Ti-6Al-4V - FM-34B-32 joint after fracture adhesive areas.

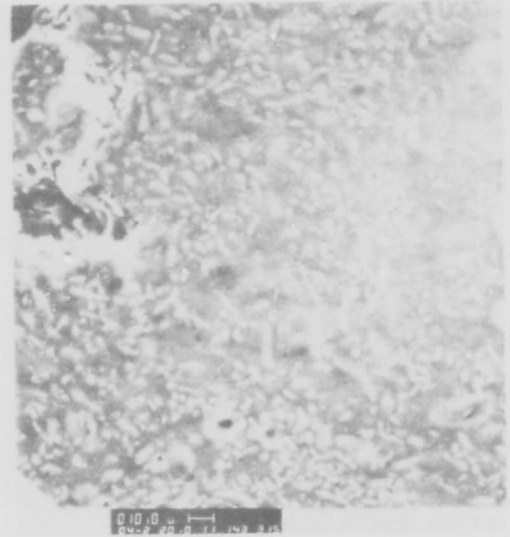
failure. Figure 85b is for the adhesive surface in an area that failure was interfacial. Figure 85c is a larger magnification of the adhesive surface, showing some glass fibers and Fig. 85d is a still larger magnification of the adhesive surface. Figure 85c is similar to Fig. 85d and is a replication of the phosphate-fluoride treated surface. Figure 86 shows SEM micrographs after fracture of Ti-6Al4V-HT424 for the nitric-acid-fluoride surface treatment. Figure 86a is for mostly interfacial failure at metal surface. Figure 86b is for the mating surface of the adhesive. Figure 86c is a larger magnification of a region of Fig. 86a near the edge of some adhesive and Fig. 86d is a larger magnification of the metal surface with some adhering adhesive particles. Figure 87 is a similar set of pictures for the PASA-JELL process. Figure 88 shows SEM pictures taken after fracture of Ti-6Al4V - HT424 bonds with the TURCC process. Figure 88a shows void areas, glass fiber areas and interfacial areas. Figure 88b is a larger magnification of the interfacial area in Fig. 88a. It is apparent that a considerable part of this area has failed cohesively. Much of the adhesive is left on the surface. Figure 88c shows the mating adhesive surface after fracture. In contrast to the rather smooth appearance of the adhesive surface after fracture, with the nitric acid-fluoride treatment or the replication of the substrate as for the phosphate fluoride, the adhesive surface is very rough with elongated particles that have failed cohesively.

### 1.1.2 Effect of Surface Roughness

The SEM pictures in Fig. 87 and 88 indicate that the nitric-acid-fluoride treatment yields a less rough surface than the phosphate fluoride or TURCO treatment. Light scattering measurements are shown in Fig. 89. For comparison the results for a vapor deposited aluminum mirror surface is also shown in Fig. 89. The roughness parameters, rms deviation from a mean



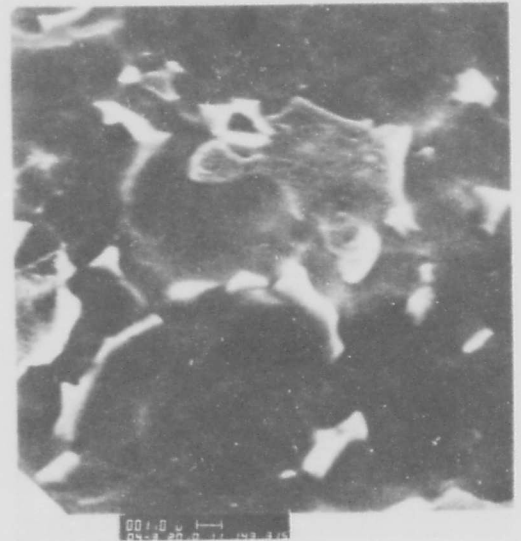
(a) 40X



(b) 400X

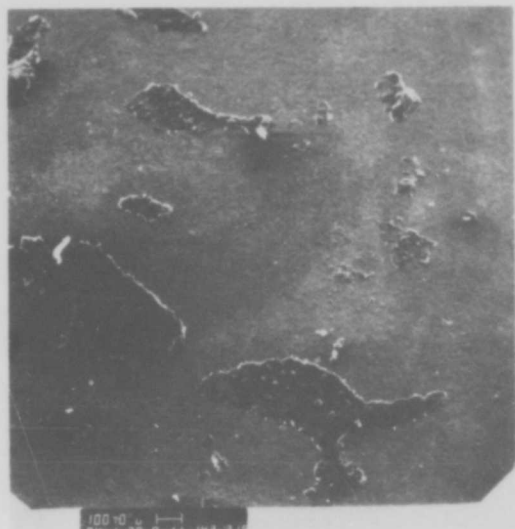


(c) 1000X

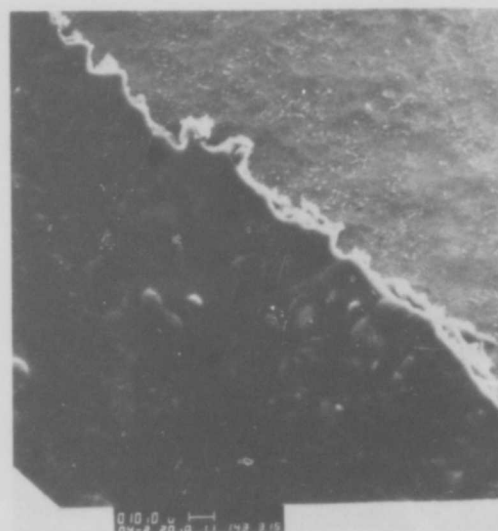


(d) 4000X

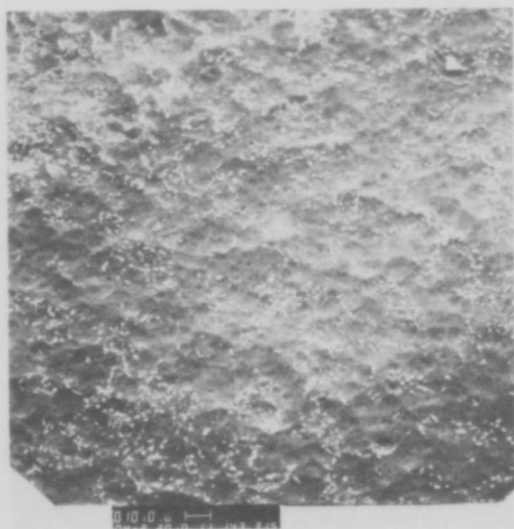
Figure 86 SEM pictures of Ti-6Al-4V - HT 424 joint after fracture  
Nitric acid-fluoride process.



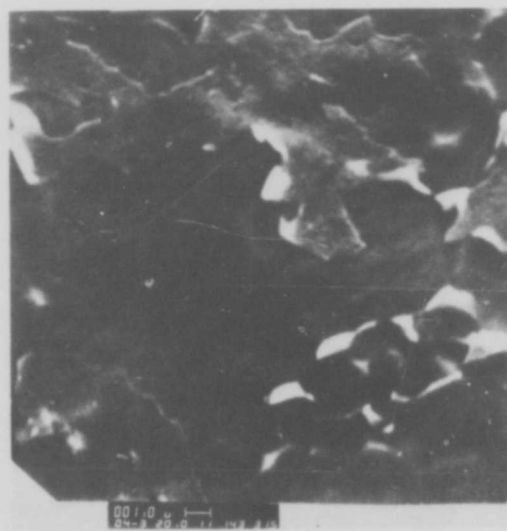
(a) 40X



(b) 400X



(c) 400X



(d) 4000X

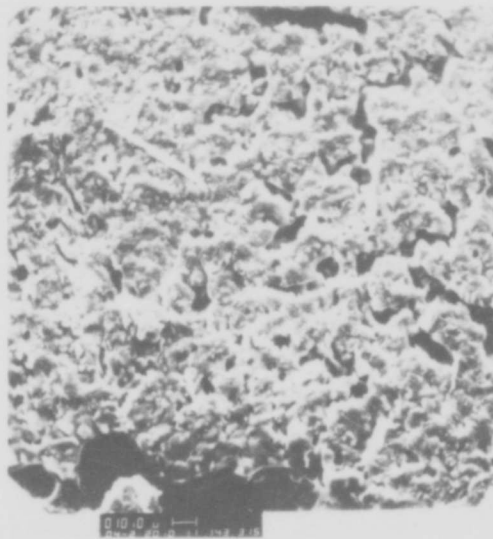
Figure 87 SEM pictures of Ti-6Al-4V - HT424 joint after fracture - Pasa Jell 107 process.



(a) 40X



(b) 400X



(c) 400X

Figure 88 SEM pictures of Ti-6Al-4V - HT424 joint after fracture-Turco process.

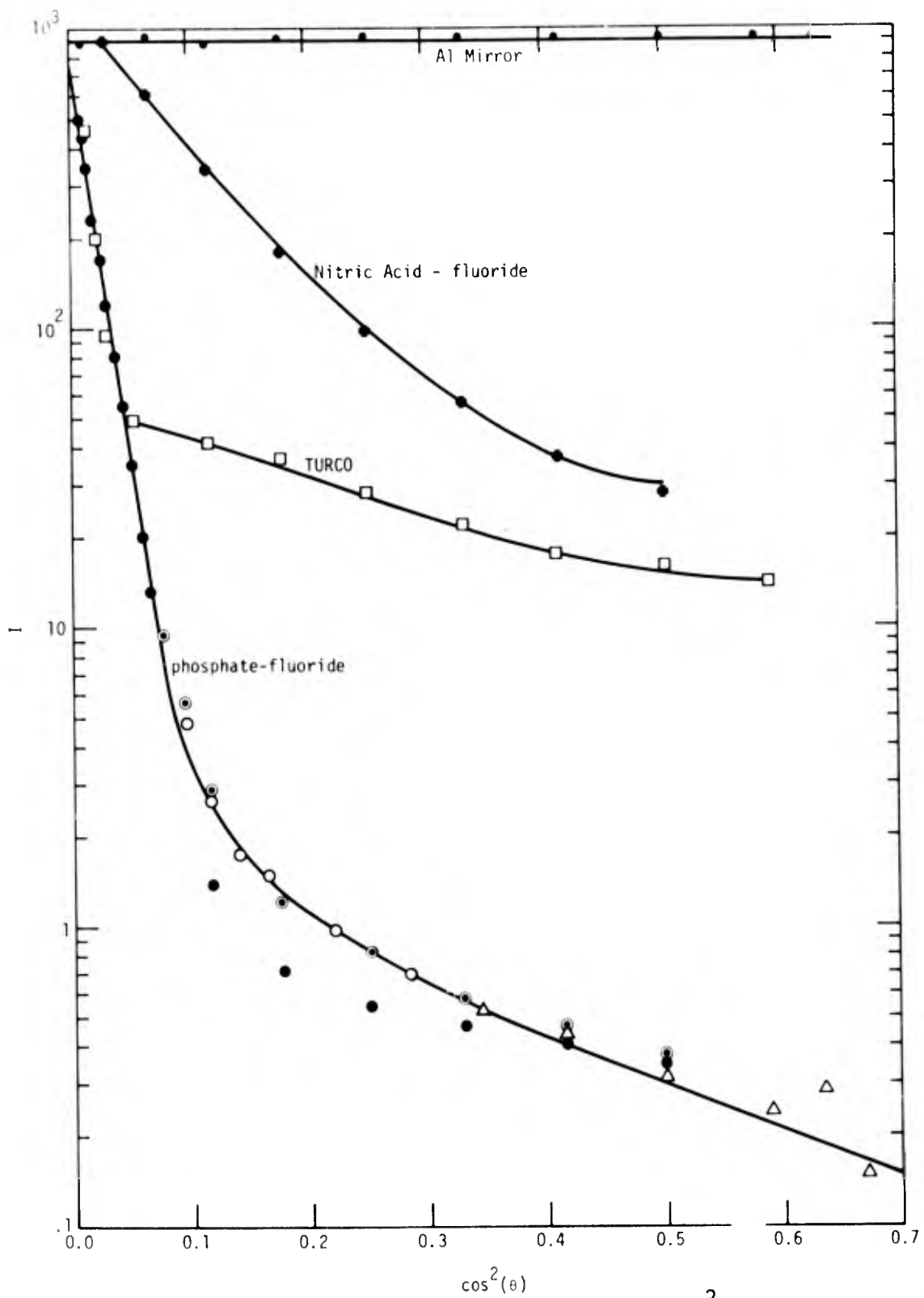


Figure 89. Plot of light intensity  $I$  vs  $\cos^2 \theta$  for an aluminum mirror and Ti-6Al-4V after the nitric acid-fluoride, TURCO and phosphate fluoride treatments.

plane  $\sigma$  and autocorrelation length  $T$  are given in Table 29. Although the slopes of the curves at small  $\cos^2\theta$  yield  $\sigma$  values that decrease in the order TURCO, phosphate-fluoride, and nitric acid-fluoride, the general shapes indicate decreasing roughness in the order of decreasing bond strength phosphate-fluoride, TURCO, nitric acid-fluoride.

### 1.1.3 Surface Properties and Bond Strength

To establish the effect of various surface treatments on surface properties and bond strength, Ti-6Al4V samples were surface treated and bonded with HT424. After each surface treatment ellipsometry, SPD and contact angle measurements were performed. Table 29 gives the surface property and bond strength results. All of the treatments yield wettable surfaces (contact angles  $\sim 0^\circ$ ). The surface potential difference values are the same, except for the TURCO process. The ellipsometric results are different for the TURCO and phosphate-fluoride than for the nitric-acid-fluoride and PASA-JELL. There does not appear to be any particular correlation between surface properties and average bond strength except the trend of stronger bonds with decreasing  $\Delta$  (i.e. increasing film thickness). The SEM pictures (Fig. 87) show the phosphate-fluoride and TURCO surfaces to be rougher than the nitric-acid fluoride or PASA-JELL surface (Fig. 88). If the increased bond strength of the phosphate-fluoride and TURCO processes are due to their roughness compared to the nitric-acid-fluoride surface then some other parameter has caused the PASA-JELL treatment to yield high bond strength. To check the low bond strength for nitric-acid fluoride, six more bonds were made; the average bond strength proved to be  $2292 \pm 272$  psi. in accordance with the previous results. Since the solid surface energy  $\gamma_{SV}$  is high and the same for each treatment (all surfaces with contact angles near zero) it is concluded that roughness is the important factor as to bond strength for Ti-6Al4V - HT424. There is a correlation in Table 29 between bond strength and



Table 29

SURFACE PROPERTY AND BOND STRENGTH RESULTS FOR  
VARIOUS SURFACE TREATMENTS OF T1-6Al4V - HT424

<u>Surface Treatment</u>	$\Delta$	$\psi$	$\underline{n_f}$	$\underline{k_f}$	Film Thickness ( $\text{\AA}$ )	SPD (Volts)	$\underline{\gamma_{SV}}$	<u>rms roughness</u>		$\underline{\sigma_b}$ (psi)
								T ( $\mu$ )	$\underline{\sigma}$ ( $\mu$ )	
HNO <sub>3</sub> /HF	107	30	2.8	0	100	0.34	66	19	0.17	2477±322
PASA-JELL	100	31	2.5	0	140	0.50	66			3233±118
TURCO	99	25	2.8	0.3	160	0.04	66	45	0.66	3083±318
Phosphate- fluoride	72	30	2.8	0.1	200	0.38	60	10	0.4	3430±233

oxide film thickness but, as will be shown next, the evidence indicates that interfacial failure does not occur in the oxide.

Table 30 is ellipsometric data for the surface of Ti-6Al4V in areas that failed interfacially after bonding with HT424. The values of  $\Delta$  and  $\psi$  for nitric acid-fluoride and PASA JELL correspond with the values before bonding, indicating interfacial failure is at the oxide-primer interface and not in the oxide as for Al 2024-T3 - HT424. According to Lively, the nitric-acid-fluoride and PASA JELL treatments are very similar. The large amount of adhesive remaining on the phosphate-fluoride and TURCO surfaces after fracture prohibited meaningful ellipsometric measurements. It is believed (from the SEM pictures) that interfacial failure is also between the oxide and primer for these preparations.

## 1.2 Various Phosphate - Fluoride Treatments

### 1.2.1 Comparison of SEM study

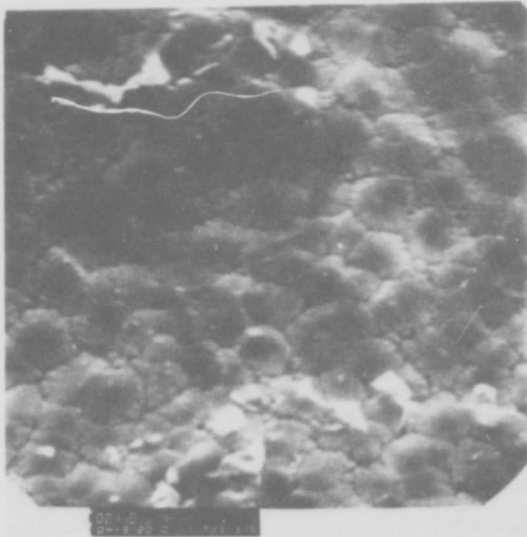
To check the effect slight differences of procedure in the phosphate-fluoride treatment might have on SEM micrographs, we followed each of the procedures in Appendix A and B as closely as possible and then took SEM pictures as shown in Fig. 90. All of the micrographs in Figure 90 have the same general features of grain boundary outline; however, each of the pictures a, b and c differ slightly in roughness and the amount of material that appears white. The increase in white material is in the order a, b, c and d. The SEM picture for the Science Center process is quite reproducible and shows much more crystalline character than the other pictures. Figures 90a, b and c look like those reported for the same procedures in Refs. 18 and 19 but not a great deal like that in Ref. 20. As noted by Alexander<sup>20</sup>, slight differences in procedure for the phosphate-fluoride treatment can result in quite different surface morphology.

### 1.2.2 Surface Properties and Bond Strengths

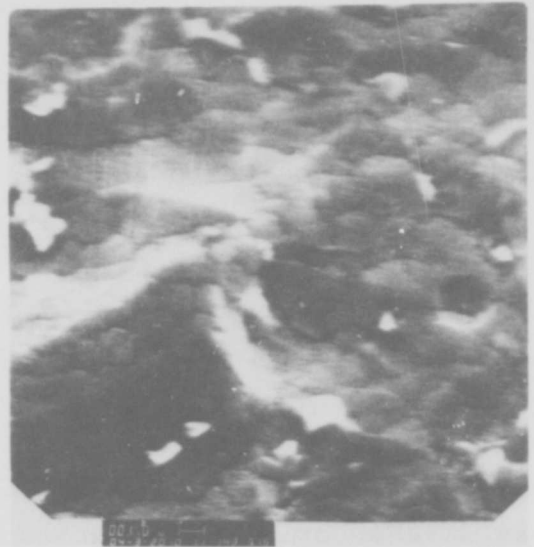
Table 30

ELLIPSOMETRIC RESULTS FOR Ti-6Al4V SURFACES  
 THAT HAD FAILED INTERFACIALLY AFTER VARIOUS  
 SURFACE TREATMENTS AND BONDING WITH HT424.

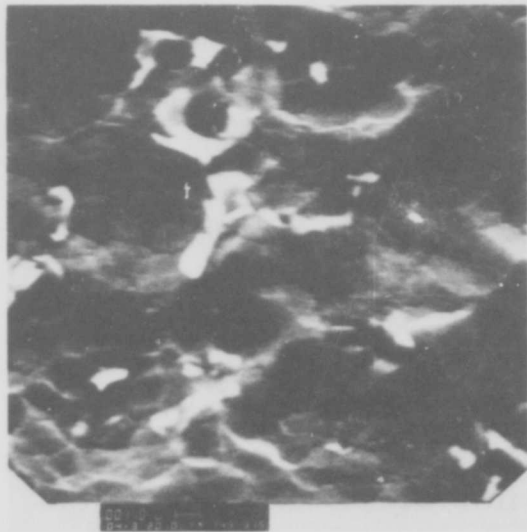
<u>Surface Treatment</u>	$\Delta$	$\psi$	$\underline{n_f}$	$\underline{\kappa_f}$	<u>Thickness (Å)</u>
HNO <sub>3</sub> /HF	107.6	30.5	2.8	0	100
PASA-JELL	107.1	30.3	2.8	0	100
TURCO	-40±10	18±3		-	
Phosphate-fluoride	138±10	22±3		-	



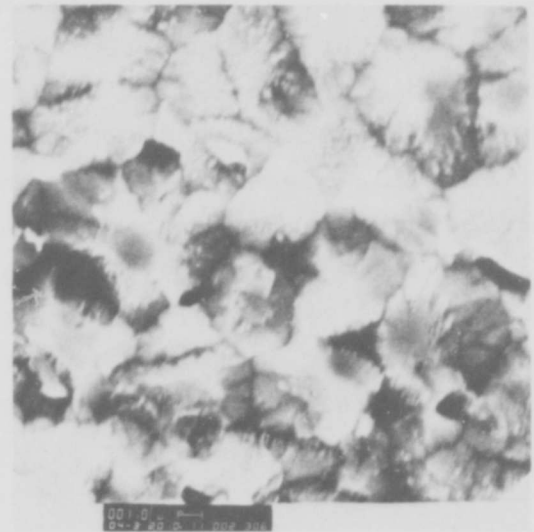
(a) Gillette



(b) Lively



(c) Battelle



(d) Science Center

Figure 90 SEM pictures of four phosphate-fluoride processes on Ti-6Al-4V: 4000X

Table 31 shows the ellipsometric and SPD surface characters, at the center of the sample area to be adhesively bonded, for the various phosphate - fluoride treatments. The corresponding double overlap bond strengths are also given in Table 31. Figure 91 shows that the main cause of scatter is the GLT. However, even with the same value of GLT there is large scatter. This result is opposite to that for Al 2024-T3 - HT424. The double overlap joints decreased the deviation from the mean to about 1% for aluminum. Values of  $\Delta$  and SPD differ considerably for the Science Center process as compared to the others. It was thought that a clue as to one of the causes of large deviations for bond strength for a given surface preparation might be due to non-uniform surface character after the preparation. The non-uniformity may be due to inadvertent surface contamination during preparation or to built in metallurgical nonuniformity. The non-uniformity is revealed in surface maps after surface preparation.

### 1.2.3 Surface Character Maps

Procedures for automatic surface mapping have been developed under a separate IR&D program. The samples of table 31 had been prepared and mapped with respect to surface potential difference (SPD), ellipsometry and photo-electron emission (PEE). Column 3 of Table 32 gives the bond strengths,  $\sigma_b$ , obtained for the various phosphate-fluoride treatments. Bond strengths vary from 2300 to 6000 psi for a particular triplicate set of tests. Only the central member of the three samples used to make one double-overlap joint, was mapped, and only for one joint of each triplicate set. This central member was mapped on both sides, referred to as side a and side b. Side a is the side that failed first, followed by failure at b as in a single overlap joint. Therefore, although the maps are given for sides a and b values of  $\sigma_b$  correspond only with side a.

Figures 92 and 93 show SPD maps of sides a and b, for the various treatments. No maps are shown for the American Cyanamid

Table 31

SURFACE CHARACTER AND BOND STRENGTH FOR Ti-6Al4V -  
HT424 WITH VARIOUS PHOSPHATE-FLUORIDE TREATMENTS

Laboratory Process	$\Delta$	$\psi$	SPD	Double Overlap Bond Strength (psi)	
					avg.
Science Center	67.5	28.9	0.38	2330	4340±1340
				4670	
				6020	
Gillette	83.5	27.4	0.12	4930	3867± 984
				2390	
				4280	
Battelle	88.4	29.5	- 0.02	3420	4397± 654
				4920	
				4850	
Am. Cyanamid	83.6	29.5	- 0.05	4520	4693± 500
				4120	
				5440	

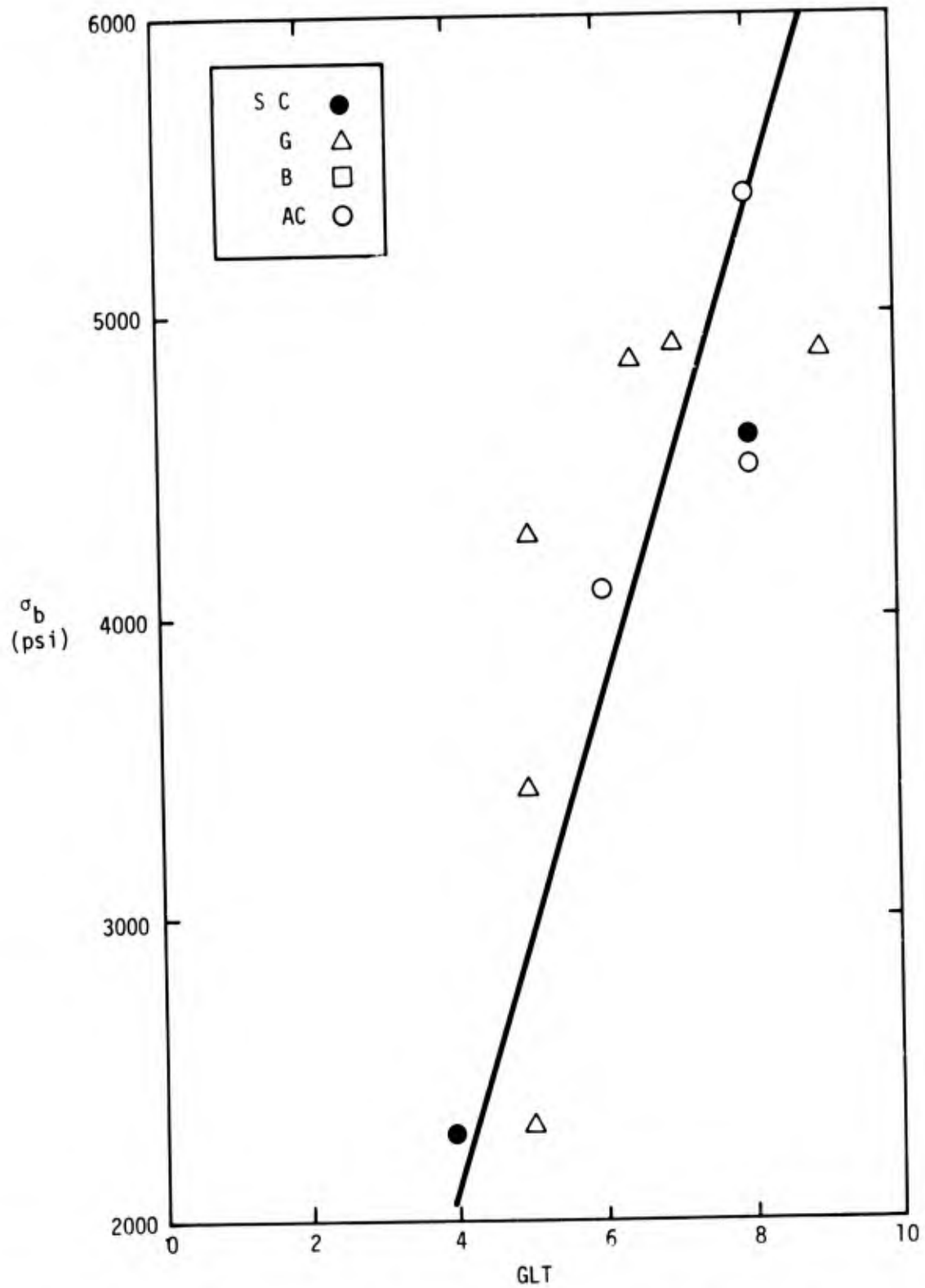


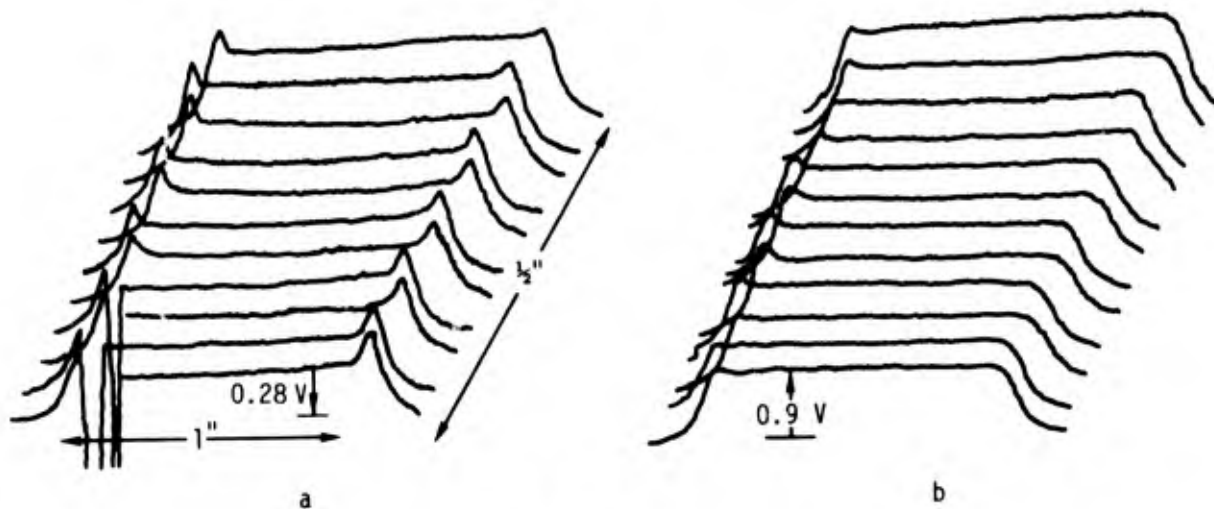
Figure 91. Plot of  $\sigma_b$  vs GLT for Ti-6Al-4V - HT424.

Table 32

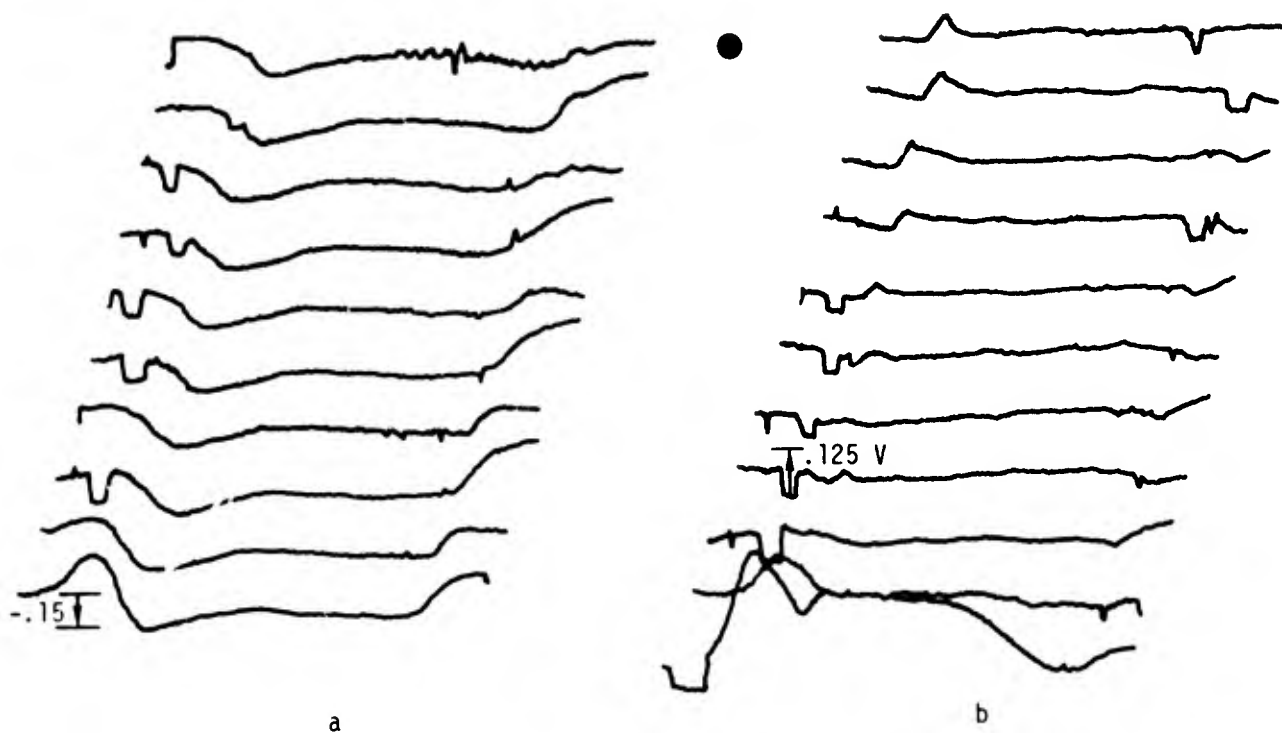
SURFACE CHARACTER AND BOND STRENGTHS  
FOR VARIOUS PHOSPHATE-FLUORIDE TREATMENTS

<u>Preparation</u>	<u>Side</u>	$\sigma_b$ <u>P<sub>Si</sub></u>	<u>SPD</u> <u>(Volts)</u>	<u>PEE</u> <u><math>\times 10^{-11}</math> (amps)</u>
Science Center	a	4670	0.28	8.4
	b		0.90	5.0
		6020		
		2330		
Battelle	a	4920	-0.03	0.0
	b		0.07	0.0
		4850		
		3420		
American Cyanamid	a	4120		0.0
	b			0.0
		4520		
		5440		
Gillette	a	2390	0.00	1.0
	b		0.30	0.5
		4280		
		4930		



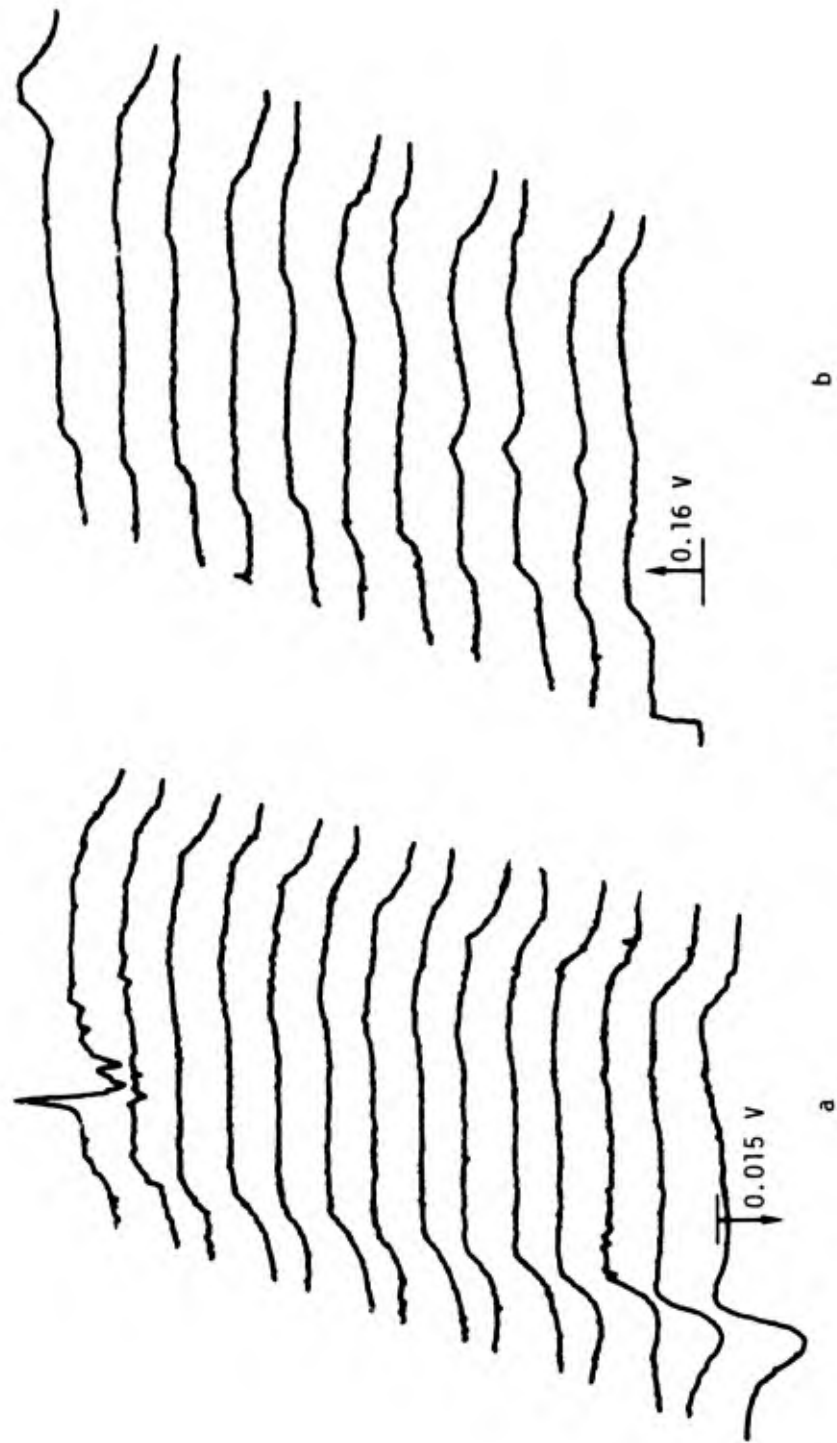


Science Center



Battelle

Figure 92. SPD maps for phosphate-fluoride treated Ti-6Al-4V.



GILLETTE

Figure 93. SPD maps for phosphate-fluoride treated Ti-6Al-4V.

treatment due to an electrical problem during mapping. The maps cover the bonding area, 1" x 1/2". The 1/2" dimension along the sample is expanded in each case to separate the scan curves. In each map the vertical axis is for a positive change in SPD, except for the Battalle map (a). In this case the recorder input cables were inadvertently reversed. The average changes in SPD are reported in Table 32. It is noted that the side that failed first (side a) had a lower value of SPD as compared to side b, in every instance, although each surface was fairly uniform with respect to SPD.

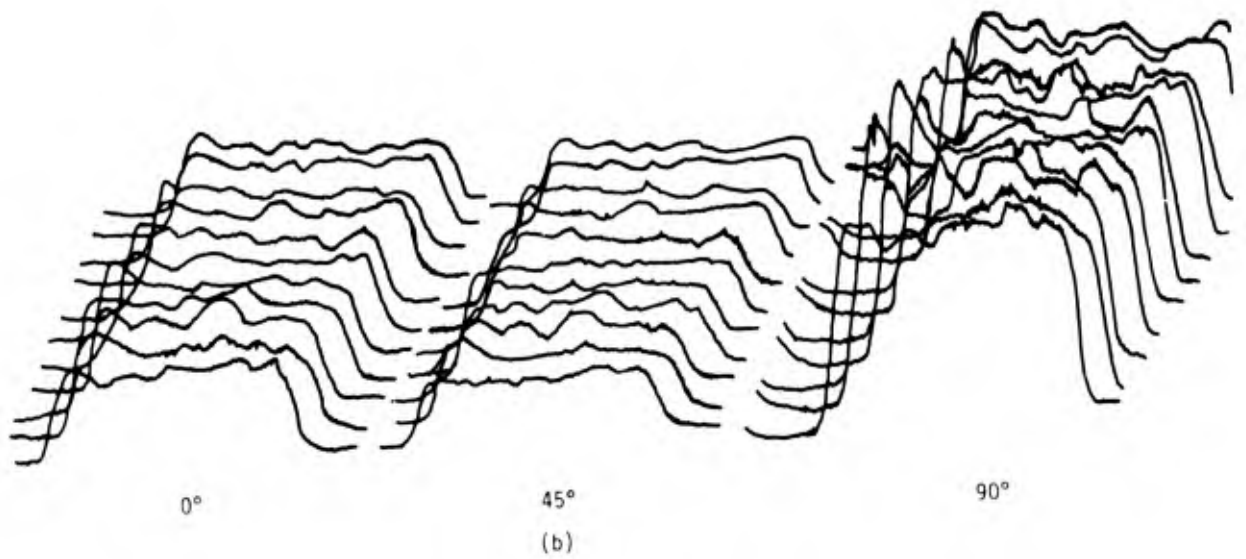
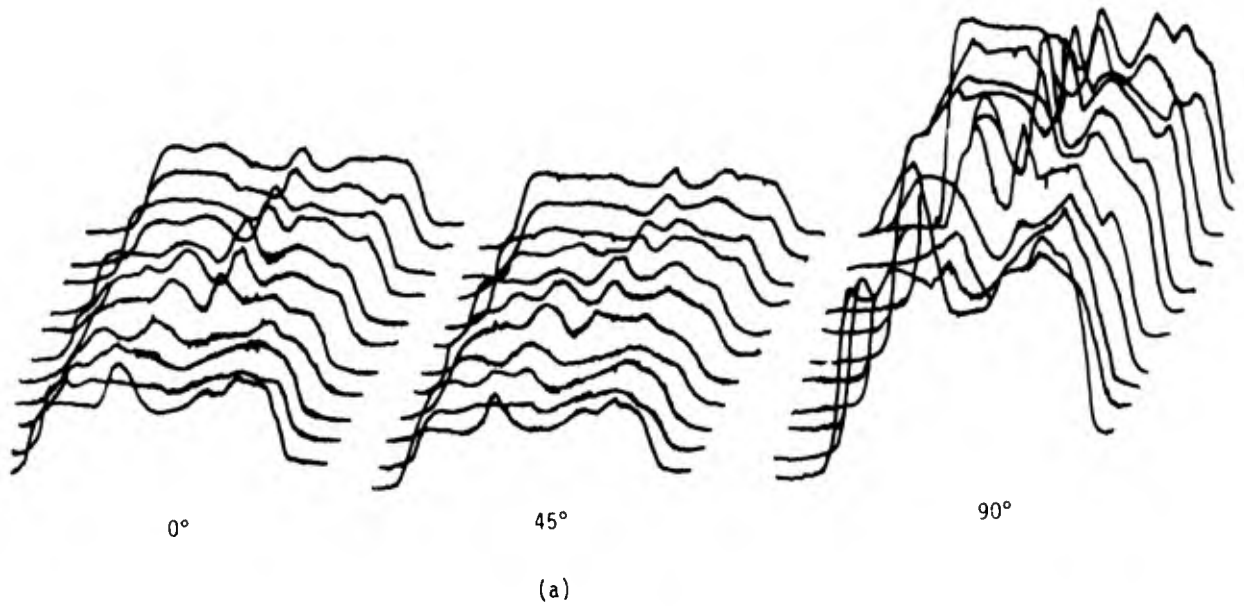
In the case of Ti-6Al4V (contrary to Al 2024-T3) the PEE was too low to give good maps. However, an estimate of the average emission currents are given in Table 32. For the Science Center and Gillette treatment, which gave measurable currents, side a gave higher currents than side b.

Figures 94 to 97 are reflectivity maps obtained with the automatic recording ellipsometer. Each scan gives the light intensity reflected from the surface. The map designated 0°, 45° and 90° are for light polarized parallel, at 45° and perpendicular to the plane of incidence respectively. Information of three types are obtained from these maps. First, the magnitude of the light intensity  $I_0$ ,  $I_{45}$  and  $I_{90}$  at any position on the sample is directly related to the reflectivity at that position. Second, the ratio of the intensity values are related to the ellipsometric parameters  $\Delta$  and  $\psi$  by the equations

$$\psi = (1/2) \arccos \left\{ \frac{I_{90} - I_0}{I_{90} + I_0} \right\}$$

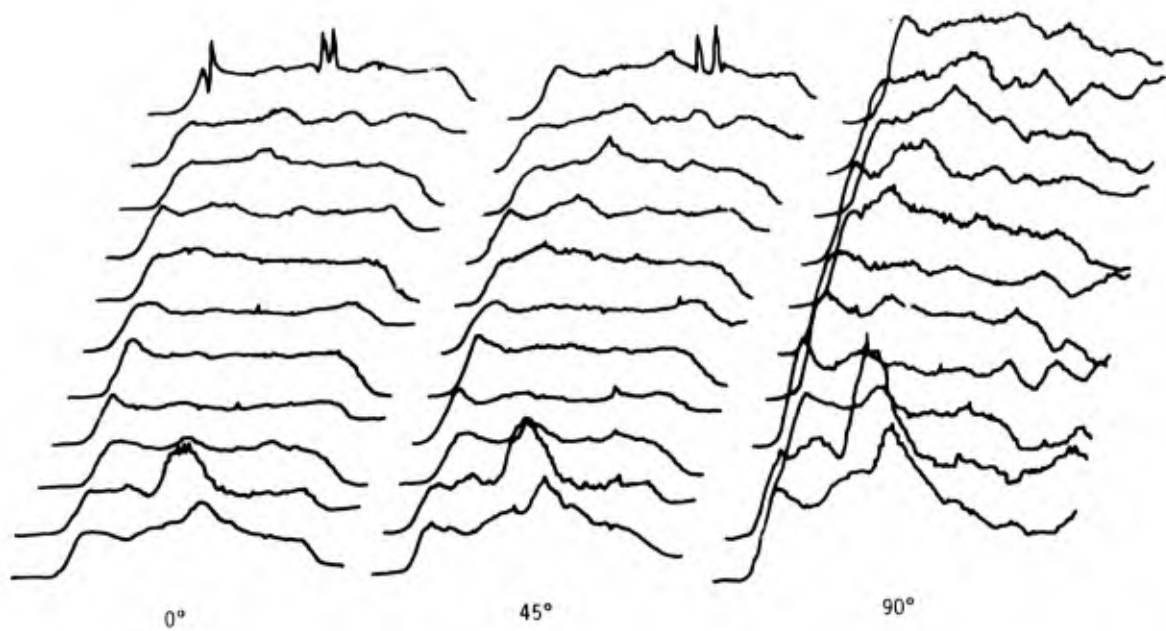
$$\Delta = \arccos \left\{ \frac{I_{45} - (1/2)(I_0 + I_{90})}{\sqrt{I_{90} I_0}} \right\}$$

Thirdly, the variations in I over the surface are related to the surface topography (surface roughness) due to light scattering away from the photo-detector. As observed for maps at 0, 45 and



ELLIPSOMETRIC MAPS (Science Center)

Figure 94. Reflectivity maps for phosphate-fluoride treated Ti-6Al-4V.



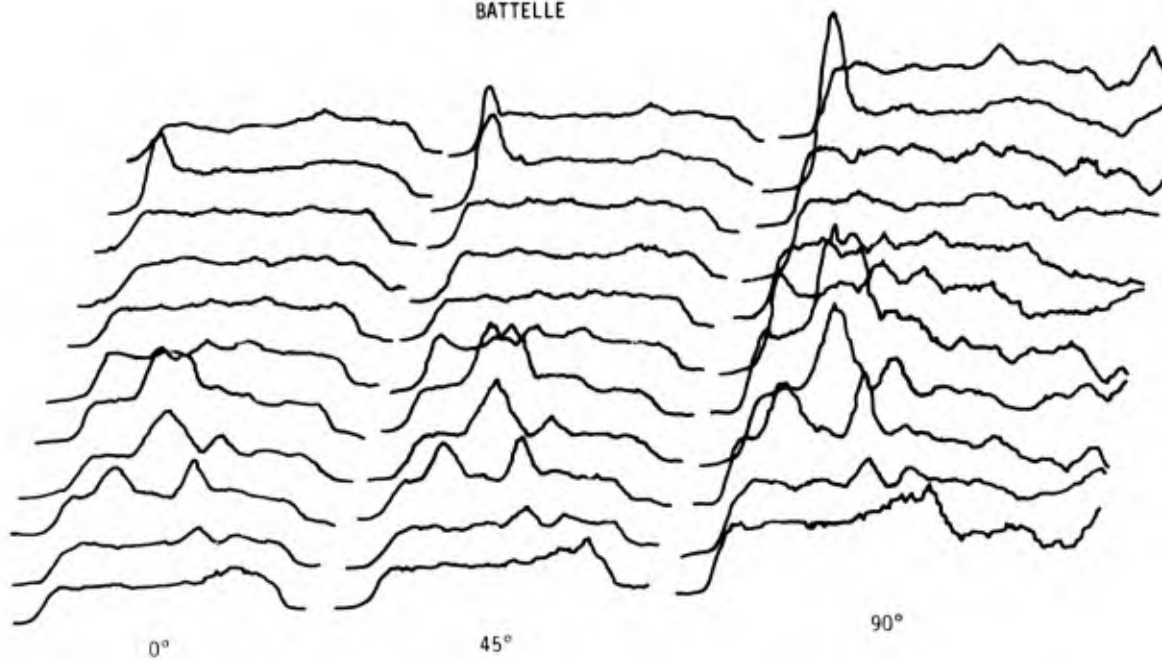
0°

45°

90°

(a)

BATTELLE



0°

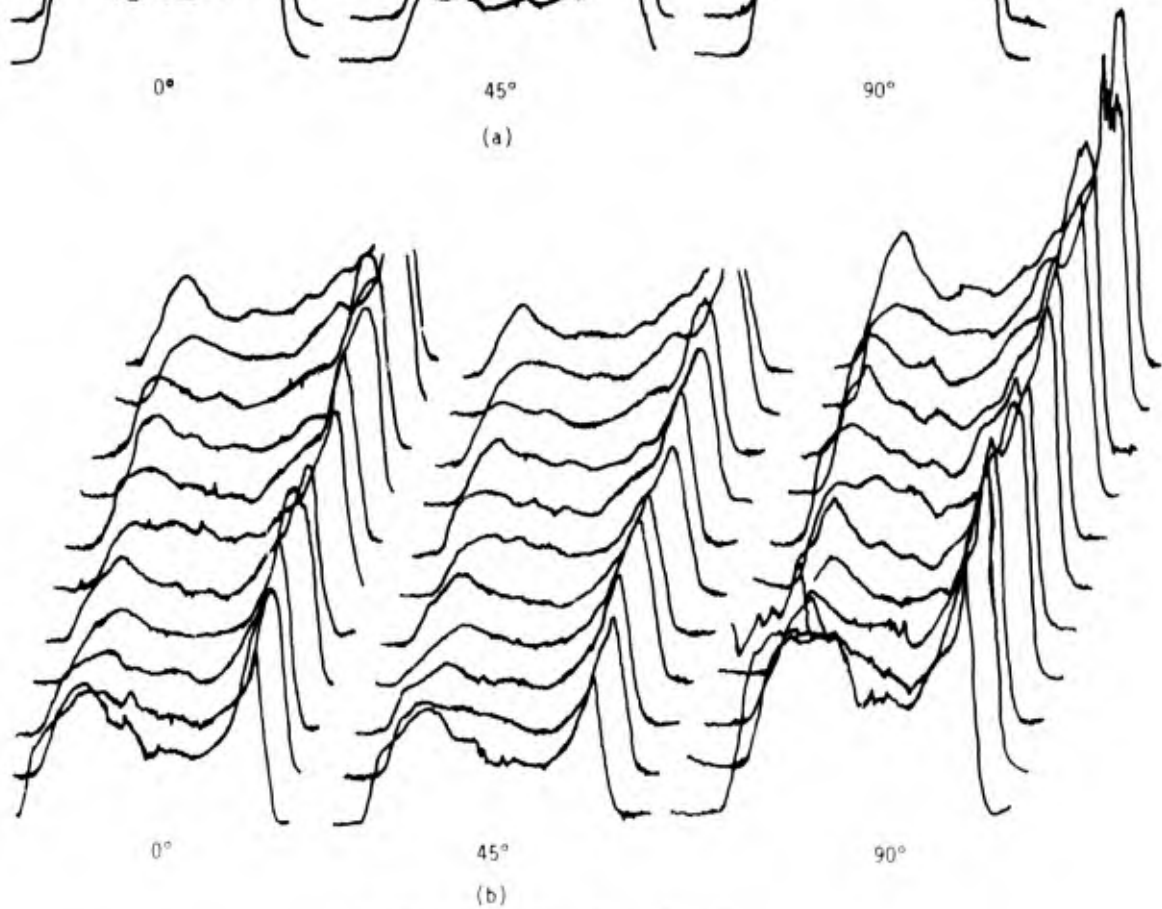
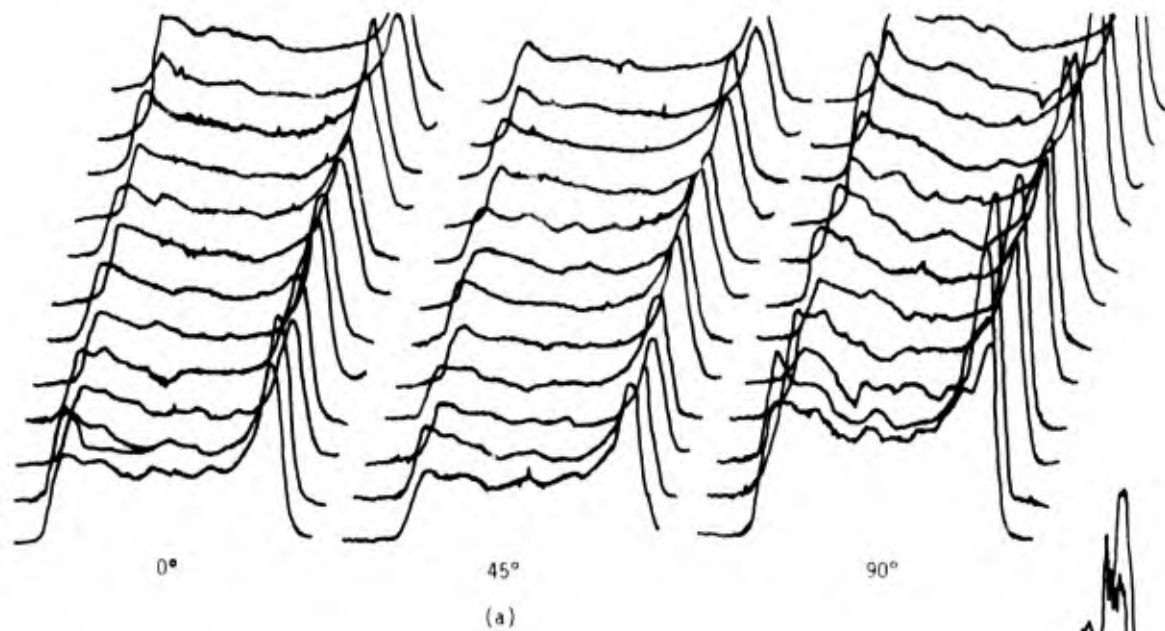
45°

90°

(b)

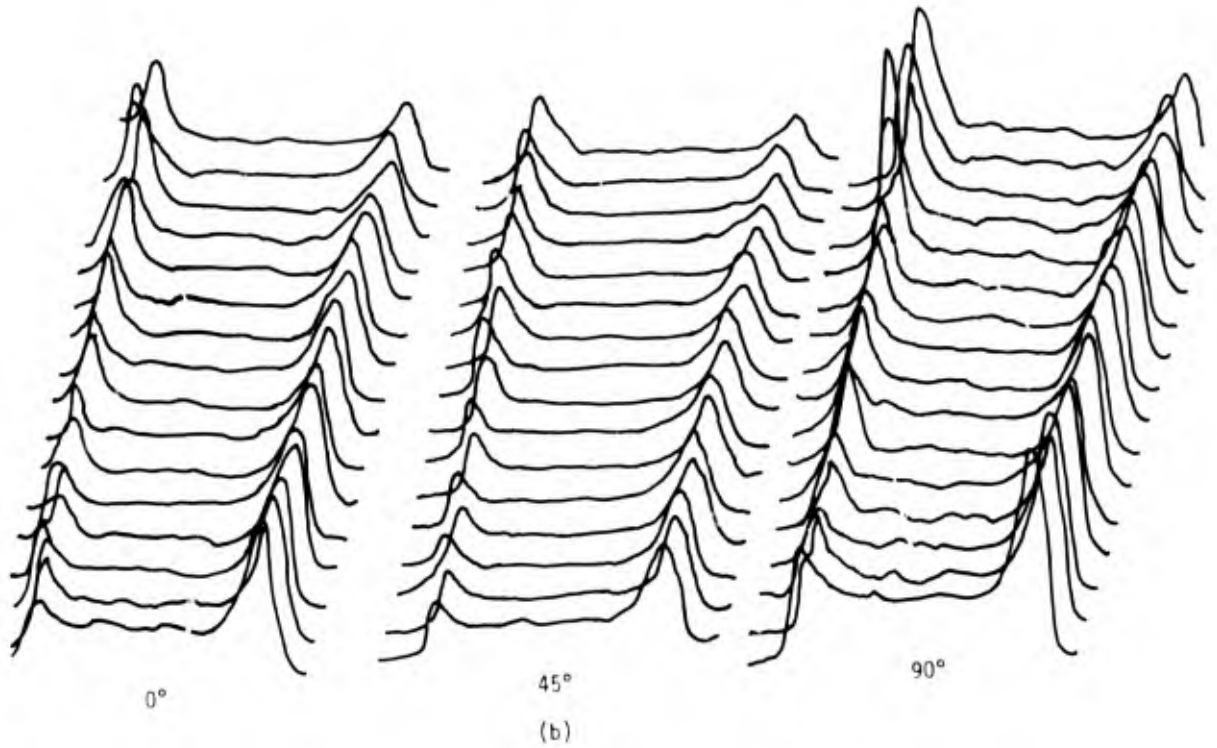
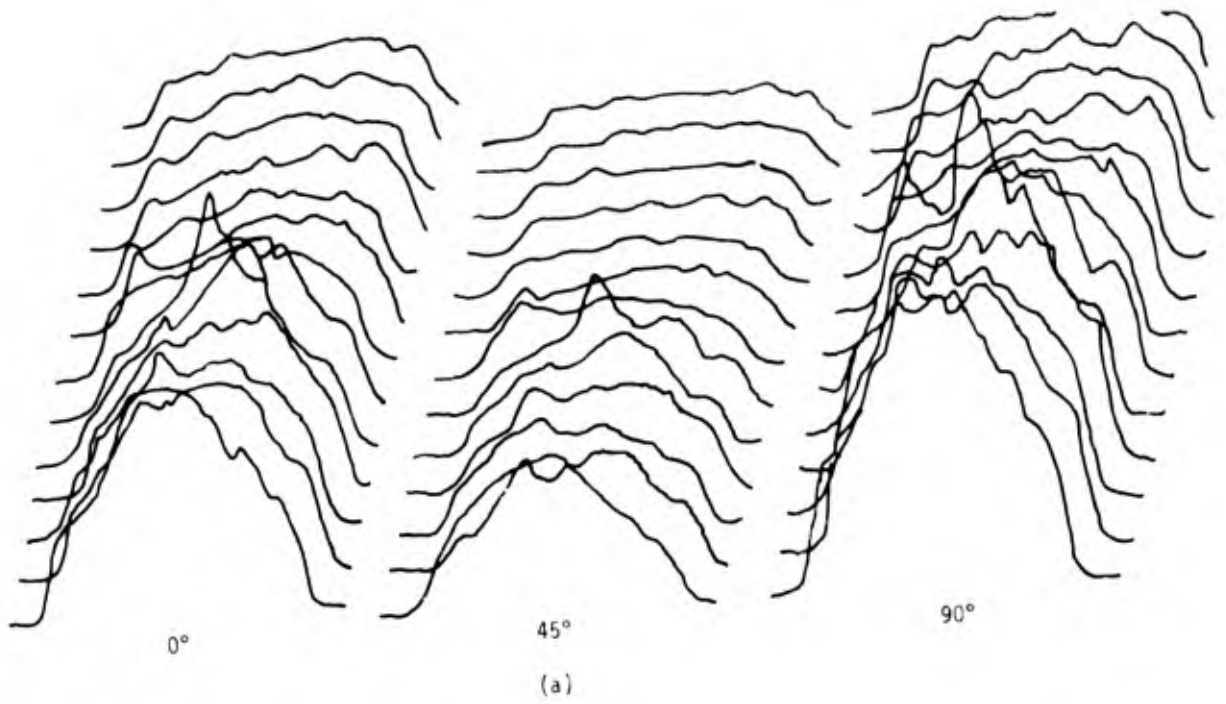
ELLIPSOMETRIC MAPS (Battelle)

Figure 95. Reflectivity maps for phosphate-fluoride treated Ti-6Al-4V.



ELLIPSOMETRIC MAPS (Amer. Cyan.)

Figure 96. Reflectivity maps for phosphate-fluoride treated Ti-6Al-4V.



ELLIPSOMETRIC MAPS (Gillette)

Figure 97. Reflectivity maps for phosphate-fluoride treated Ti-6Al-4V.

90° the roughness effect gives identical relative profiles for each scan. A number of repeat scans across the same path are shown in Fig. 98. Scans 1, 4 and 5 were made with the normal laser beam ( 2 mm diameter). Scans 4 and 5 were done twice each to show that identical traces are produced; however, scan 4 was made very slowly and scan 5 rapidly to show that the light detector is fast with respect to the scanning rates. Scans 2 and 3 are a slow and fast scan respectively, but with the beam focused to ~ 0.2 mm on the sample. The much greater structure of scans 2 and 3 is due to the greater resolution with the focused beam. Thus, the scanning ellipsometer can be used as a profilometer. We have yet to demonstrate the relationship between traces such as in Fig. 98 and actual profilometer traces made with a stylus. Figures 99 and 100 are computer plots of  $\Delta$  and  $\psi$  from Figs. 94a and 97a respectively, showing that roughness is cancelled.

Although the reflectivity maps for sides a and b are similar in Figures 94, 95 and 96, this is not the case in Figure 97a. It is believed that the maverick maps in Fig. 97a reveal differences that may be partly related to the low bond strength (2300 psi) for this surface.

Maps such as those in Figures 92 to 97 are obtained automatically and fairly rapidly. However, maps as shown in Figures 99 and 100 are time consuming due to the manual tabulation of the data for the computer. These maps are not accurate due to error in transferring data for the same sample position. We are in the process of developing, on another IR&D program, data acquisition on tape, of  $I_0$ ,  $I_{45}$  and  $I_{90}$ , during each revolution of the analyzer, which will minimize the error in calculating  $\Delta$  and  $\psi$  for a particular position along the scan. Further programming will allow reflectivity maps to be transformed to film thickness maps.

It is concluded that irreproducible bonding for Ti-6Al4V may be partly due to inadvertant differences in surface character



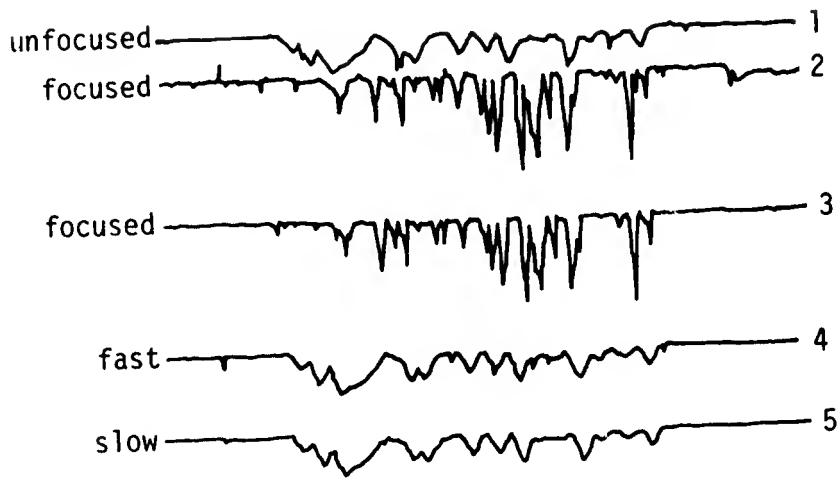


Figure 98. Reflectivity showing macroscopic roughness effect.

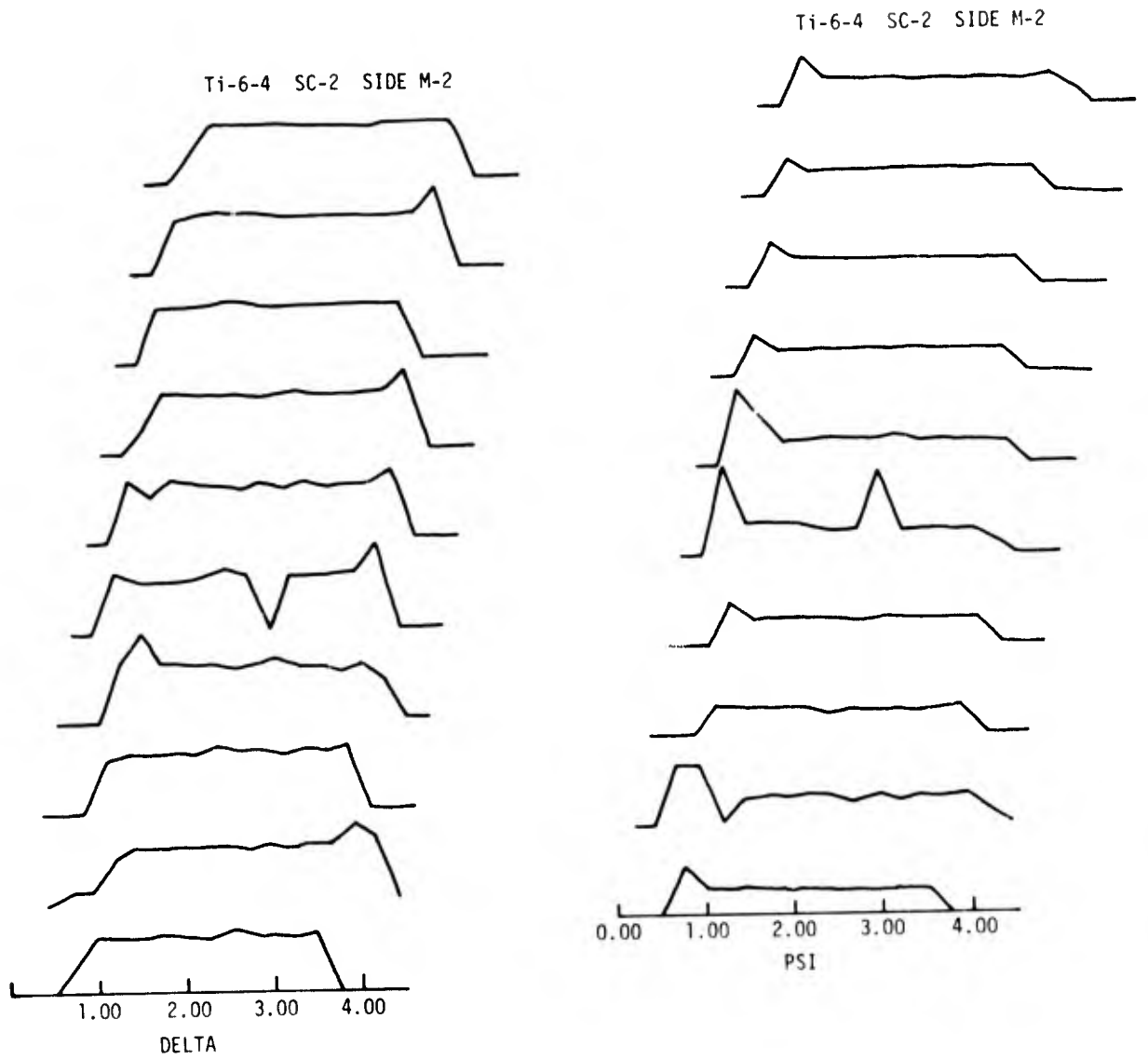


Figure 99. Computer plots of  $\Delta$  and  $\psi$  from reflectivity maps (94a).

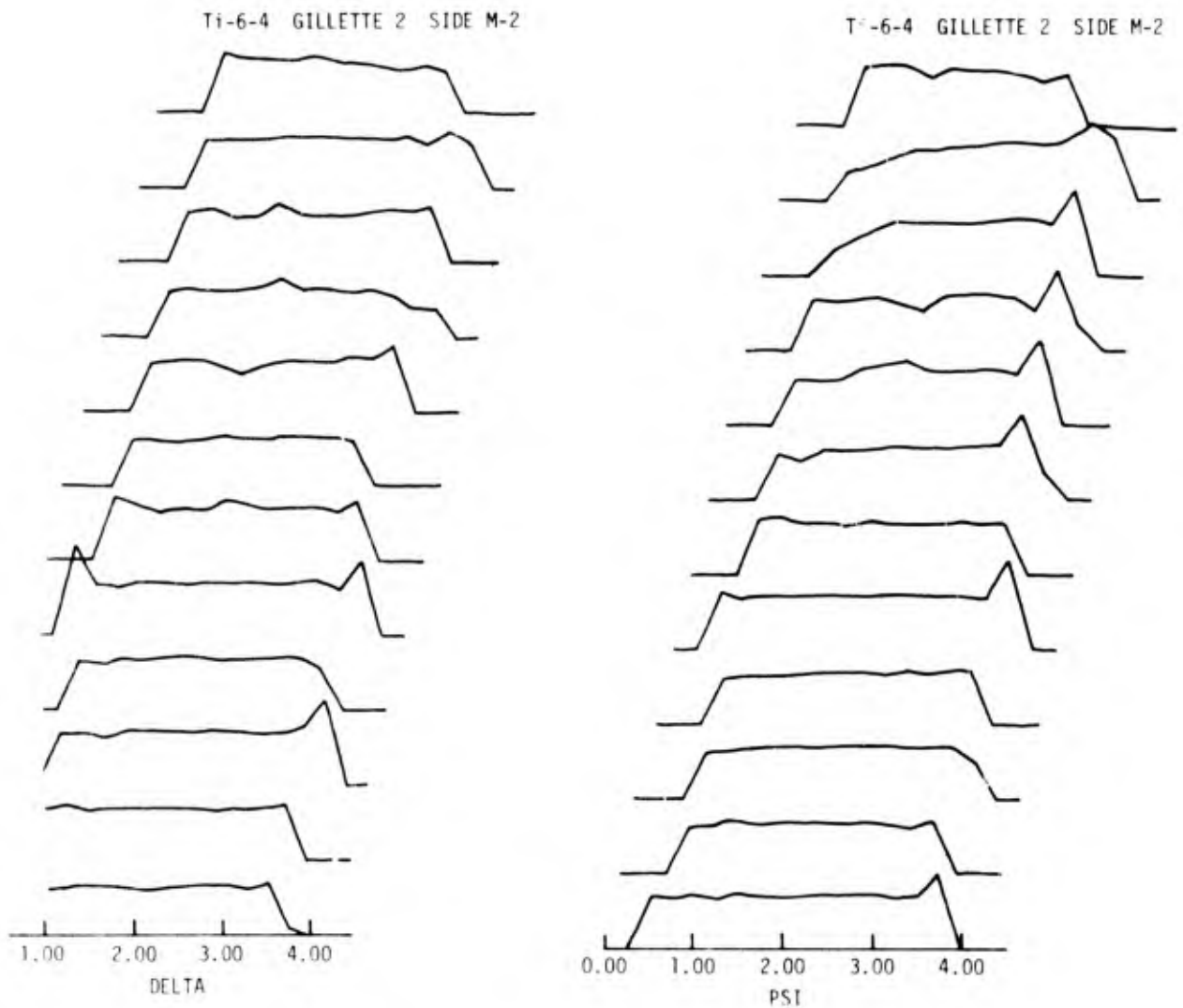


Figure 100. Computer plots of  $\Delta$  and  $\psi$  from reflectivity maps (97a).

after surface preparation, and the mapping of individual specimens may bring this to light. The possible cause of the differences in surface character is considered next.

Having discovered that different bond strengths for Ti-6Al4V - HT424 adhesive may be related to non-uniform surfaces, it is important to establish whether the non-uniformity results from our surface preparation or the previous metallurgical history of the Ti-6Al4V material. The answer to this has already been partially established since our AFML-TR-74-73 report (Table 48 and Fig. 99) indicates that a given sample is non-uniform with respect to ellipsometry and SPD and this non-uniformity is directly related to the fraction of the surface that failed interfacially ( $\phi_I$ ). The average values for  $\Delta$  and  $\psi$  in a given map region for the six control samples (1164A, 1164E, 1165A, 1165B, 1166A and 1166B) are given in Fig. 101, along with a plot of the average  $\Delta$  and  $\psi$  vs position. It is seen that a random non-uniformity of about  $2^\circ$  in  $\Delta$  and  $\psi$  exists for a given sample position. The random non-uniformity must be due to non-uniformity of the metallurgical specimens.

Measurements were made to establish experimental error as follows: Values of  $\Delta$  and  $\psi$  were measured for a given sample, only renulling the analyzer and polarizer to obtain the reproducibility of this part of the ellipsometric measurement. Table 33a shows that the instrument can be renulled with a precision of  $\pm 0.14^\circ$  in  $\Delta$  and  $\pm 0.08^\circ$  in  $\psi$  for one quadrant (zone 3) with compensator at  $-45^\circ$ . Table 33b shows that with a sample in position, measurement in 4 zones can be done with optical alignment errors of  $\pm 0.24^\circ$  in  $\Delta$  and  $\pm 0.4^\circ$  in  $\psi$ . Table 33c shows that removing the sample and replacing it in the instrument, then averaging with respect to 4 zones can be done with a precision of  $\pm 0.32^\circ$  in  $\Delta$  and  $\pm 0.16^\circ$  in  $\psi$ . None of these errors account for the  $2^\circ$  and  $1^\circ$  scatter in  $\Delta$  and  $\psi$ . It is concluded that the non-uniformity is a real property of the Ti surface.

Ti-6-4  
Avg. of 6 Samples

	8	7	6	5
$\Delta$	$72.0 \pm 1.6$	$71.5 \pm 2.7$	$70.2 \pm 1.4$	$69.2 \pm 1.8$
$\psi$	$28.7 \pm 0.6$	$29.1 \pm 1.3$	$29.1 \pm 1.2$	$27.1 \pm 1.0$
	1	2	3	4
$\Delta$	$72.0 \pm 2.6$	$71.4 \pm 3.6$	$71.6 \pm 1.7$	$69.0 \pm 1.9$
$\psi$	$28.4 \pm 0.9$	$28.4 \pm 0.9$	$28.0 \pm 1.1$	$27.0 \pm 2.5$

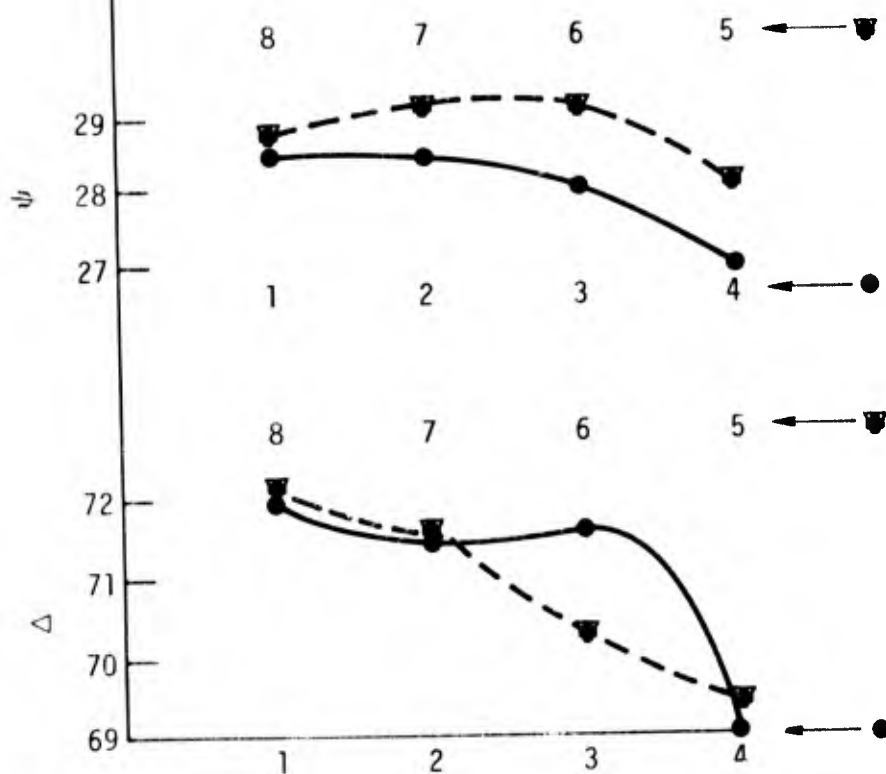


Figure 101. Average values of  $\Delta$  and  $\psi$  for various map positions of 6 Ti-6Al-4V phosphate-fluoride treated samples.

- corresponds to positions 1,2,3,4
- ▽ corresponds to positions 5,6,7,8.

Table 33

CHECK OF THE SENSITIVITY AND REPRODUCIBILITY  
OF THE ELLIPSOMETRIC MEASUREMENTS

Operation	C	P	A	$\Delta$	$\psi$
a) Null only in 1 zone	- 45	80.31	152.04		
		80.30	152.05		
		80.47	152.16		
		80.26	152.35		
		80.15	152.25		
		80.25	152.20		
		<u>80.18</u>	<u>152.22</u>		
	avg	80.27	152.18	70.54	27.82
		$\pm 0.07$	$\pm 0.08$	$\pm 0.14$	$\pm 0.08$
b) Null only in 4 zones	- 45	349.13	27.90	68.26	27.90
	- 45	79.93	153.10	69.86	26.90
	+ 45	100.37	27.46	69.26	27.46
	+ 45	10.23	153.13	<u>69.54</u>	<u>26.87</u>
		avg		69.23	27.28
			$\pm 0.24$	$\pm 0.40$	
c) Remove Sample re-align				69.14	27.65
				69.23	27.28
				68.63	27.68
				<u>69.83</u>	<u>27.81</u>
		avg		69.20	27.60
			$\pm 0.32$	$\pm 0.16$	

### 1.3 Aged Etch Solution

Since there seems to be a small decrease in the values of  $\Delta$  for measurements now with respect to those made a year ago, it was thought this may be due to aging of the phosphate fluoride solution. Five Ti-6Al4V samples were prepared in the old solution and five in a new solution. Table 34 shows that although the scatter of  $2^\circ$  in  $\Delta$  and  $1^\circ$  in  $\psi$  exists in either case due to non-uniformity, the average value of  $\Delta$  from the new solution is about  $2^\circ$  higher than from the old solution and  $\psi$  is about  $1.4^\circ$  lower for the new solution with respect to the old solution, indicating that solution age does have an effect. Since the average values of SPD and photo electron-emission (PEE) in Table 34 are about the same for either solution, it is thought that the differences in the ellipsometry data are due to surface roughening rather than film thickness.

### 2. Effect of Controlled Contamination on Surface Properties

Figure 102 shows the change in  $\Delta$ ,  $\psi$ , PEE and SPD vs the number of dips through a monolayer of erucic acid or water. Deposition of erucic acid on phosphate-fluoride treated Ti-6Al4V decreases SPD as for FPL etched Al 2024-T3. A plot of I vs film thickness is given on semi log paper in Fig. 103. The current can be expressed

$$I = 5 \times 10^{-11} e^{-d/(69 \text{ \AA})} \quad (\text{amps})$$

where  $d$  is the film thickness and the attenuation index is  $69 \text{ \AA}$ . The attenuation of electrons by erucic acid is much less than by myristic acid. This is attributed to the poor packing that results from the bent cis-molecule with effective packing diameter of  $\sim 6.3 \text{ \AA}$  as compared to  $4.2 \text{ \AA}$  for myristic acid. The change in  $\psi$  is larger for the rough surface compared to the theoretical change for a smooth surface as it was for aluminum.

Table 34

EFFECT OF SOLUTION AGE ON SURFACE CHARACTER FOR THE  
PHOSPHATE-FLUORIDE TREATMENT OF Ti-6Al4V

Sample	<u>Old Solution</u>			
	$\Delta$ (deg)	$\psi$ (deg)	SPD volts	PEE amps $\times 10^{-11}$
1	65.50	28.02	0.42	4.9
2	68.60	27.73	0.52	4.2
3	64.95	28.63	0.55	3.9
4	67.77	27.81	0.45	3.6
5	71.81	26.55	0.44	3.3
avg	$67.73 \pm 2.0$	$27.75 \pm 0.49$	$0.48 \pm 0.05$	$4.0 \pm 0.5$

Sample	<u>New Solution</u>			
	$\Delta$ (deg)	$\psi$ (deg)	SPD volts	PEE amps $\times 10^{-11}$
1	69.85	26.37	0.38	4.2
2	70.25	25.12	0.43	4.0
3	73.95	26.17	0.35	3.6
4	69.29	25.43	0.42	3.8
5	65.72	28.74	0.51	3.7
avg	$69.81 \pm 1.8$	$26.37 \pm 1$	$0.42 \pm 0.04$	$3.9 \pm 0.2$



Erucic acid / P.F. Ti 6-4

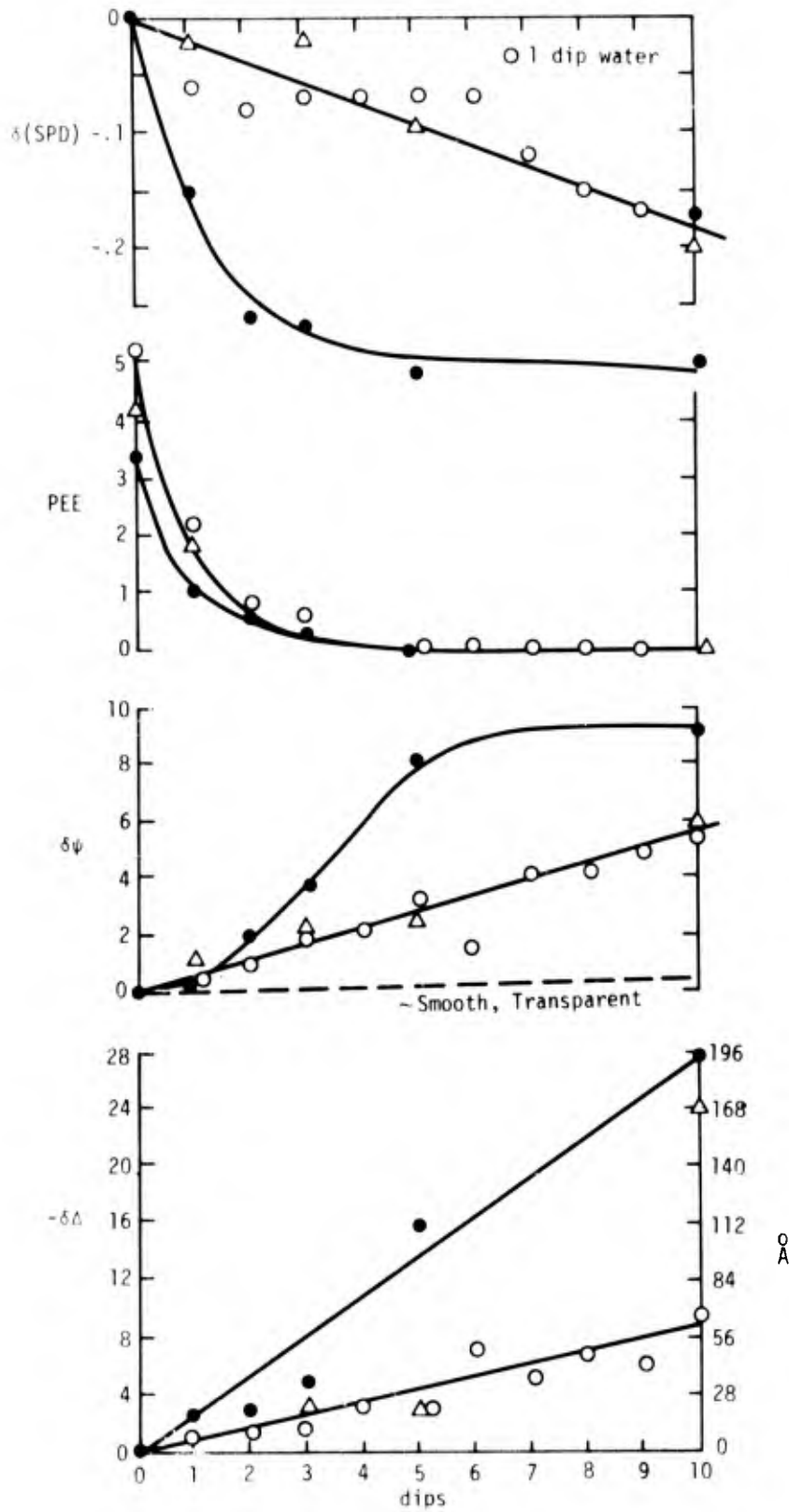


Figure 102. Plot of  $-\delta\Delta$ ,  $\delta\psi$ , PEE and  $\delta(\text{SPD})$  vs number of dips of Ti-6Al-4V through erucic acid on water.

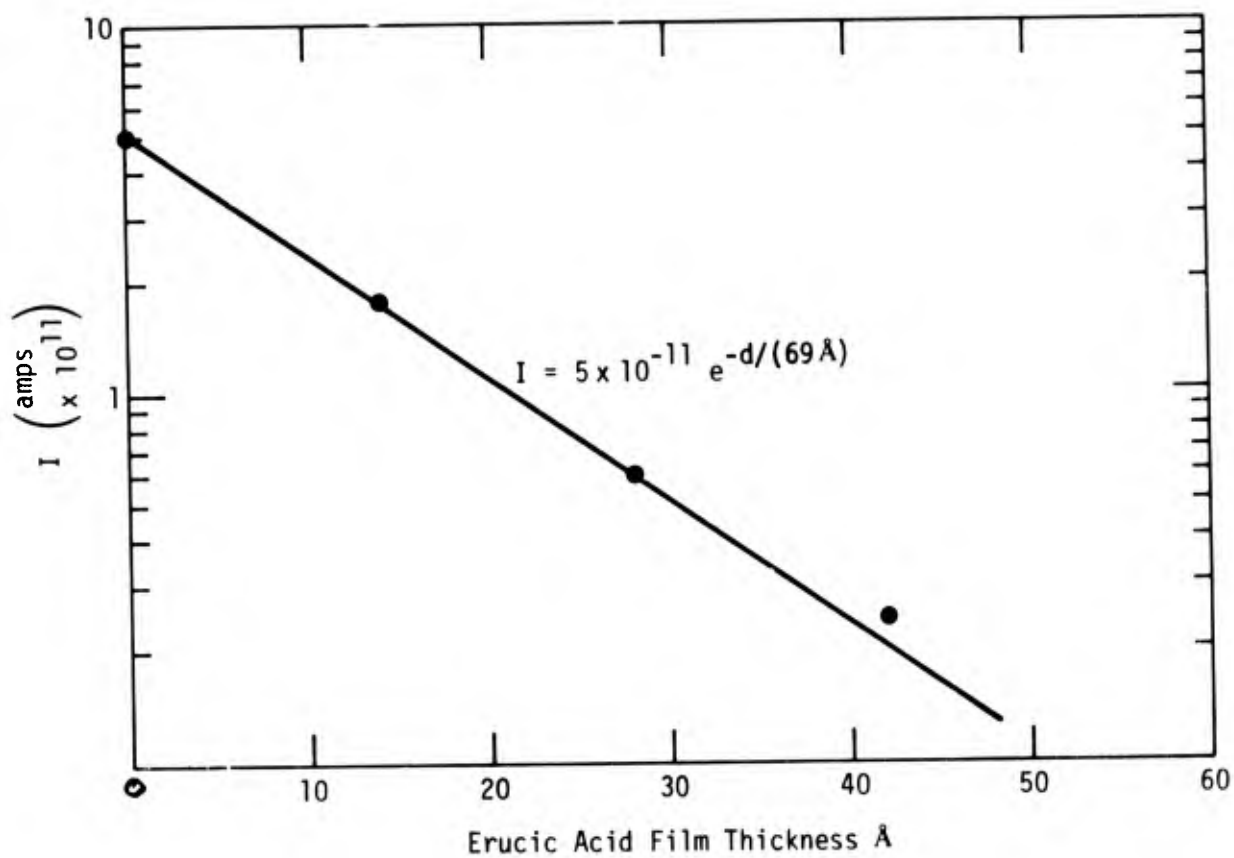


Figure 103. Plot of photo current  $I$  vs film thickness of erucic acid on Ti-6Al-4V.

The three sets of data in Fig. 102 are for three separate experiments. The change in  $\Delta$  indicates that the erucic acid molecules deposit in the erect orientation  $\sim 20\text{\AA}/\text{dip}$  (top curve solid points) or lying flat  $\sim 6\text{\AA}/\text{dip}$  (bottom curve open circles). The experiment represented by open triangles indicate that the molecules lay flat for the first 5 dips then in the erect orientation for the next 5. Experiments to test the effect of controlled contamination on bond strength have not as yet been performed.

### 3. Effect of Different Environments

#### 3.1 SET in the UHV Chamber

Table 35 gives the surface parameters for phosphate-fluoride etched Ti-6Al4V that was placed in the UHV chamber for 148 hours in dry nitrogen and then exposed to 97% RH for 140 hours.

After 148 hours in dry nitrogen in the UHV chamber the contact angle remained approximately zero. Exposure of the sample to air for a few minutes for the ellipsometer measurements caused the contact angle to increase to  $45^\circ$ . The ellipsometric and PEE data correspond to an increase of about  $20\text{\AA}$  of film thickness if it is assumed that the increase in contact angle was due to organic contamination. Continued exposure to 97% RH in the UHV chamber for 44 hours caused the contact angle to decrease to approximately zero again. Exposure to the air caused the contact angle to increase to  $10^\circ$ . The ellipsometric data corresponds to an increase of about  $80\text{\AA}$  in film thickness assuming the increase is due to oxide growth in the UHV chamber. It appears that the Ti-6Al4V phosphate-fluoride surface is much more active than FPL etched Al 2024-T3 as to adsorption of contamination upon exposure to air. However, contrary to aluminum the contamination is removed by exposure to 97% RH in the UHV chamber.

TABLE 35

EFFECT OF SET IN THE UHV CHAMBER ON SURFACE PROPERTIES  
OF Ti-6Al4V AFTER THE PHOSPHATE-FLUORIDE TREATMENT

SET (hrs)	$\Delta$ (deg)	$\psi$ (deg)	SPD (volts)	PEE amps $\times 10^{-11}$	$\phi_{H_2O}$ (deg)
0	82.7	25.7	-0.41	3.9	2
148 in N <sub>2</sub> Expose to air	79.8	26.0	0.16	2.1	45
44 in 97% RH					2
140 in 97% RH Expose to air	68.2	31.1	-0.13	5.4	10

### 3.2 SET of Ti-6Al4V in Water Vapor (glass jars) and in Water

Table 36 gives the surface parameters for Ti-6Al4V after exposure to 55°C, 95% RH water vapor and after exposure to 50°C distilled water and 100°C distilled water. The data are plotted in Figures 104, 105 and 106. Figure 104 shows that SET at 55°, 95% RH in glass jars causes a large increase in the water contact angle, presumably from organic contamination. After SET in water the contact angle remains low. Figure 105 shows that SPD changes very little for SET in 55°C, 95% RH inspite of the large change in  $\phi_{H_2O}$ . There is a dramatic decrease in SPD for SET in water. The PEE changes only slightly for SET in water vapor or water. Figure 106 shows that there is some differences in  $\Delta$  and  $\psi$  after the initial phosphate-fluoride treatment but little change with SET in water vapor or water. It is interesting to note that the sample with the thickest initial film ( $\sim 250\text{\AA}$ ) decreased in thickness, with exposure to 100°C water, to about 200 $\text{\AA}$  and became smoother. It was shown in AFML-TR-74-73 that inspite of the degradation in  $\phi_{H_2O}$  or surface energy with SET the bond strength did not degrade.

#### 4. BET of Ti-6Al4V in Water Vapor and Water

Table 37 gives the bond strengths for Ti-6Al4V - HT424 after the phosphate-fluoride surface preparation and exposure to 100°C, 95% RH, 100°C water and 50°C water. The average bond strengths are plotted in Fig. 107. The trends in bond degradation were the same as for Al 2024-T3 - HT424. The decrease in bond strength at 1000 hours in water is about the same, 1,200 to 1,300 psi but the rate of degradation is much faster (complete in 10 hours) in the 100°C water. The degradation in 100°C, 95% RH is about the same as for the aluminum ( $\sim 600$  psi). The initial bond strengths for the Ti-6Al4V are much larger than for the aluminum because HT424 from batch 3 was used rather than from batch 2 for the aluminum.

TABLE 36

EFFECT OF SET AT 55°C, 95% RH  
IN GLASS JARS ON SURFACE PROPERTIES

SAMPLE	SET (hrs)	$\Delta$ (deg)	$\psi$ (deg)	SPD (volts)	PEE (amps $\times 10^{-11}$ )	$\theta_{H_2O}$ (deg)
1	0	77.8	26.3	0.17	7.2	10
	1.5	77.6	27.1	0.11	5.4	109
	5	79.8	27.4	0.14	6.2	116
	22	77.6	27.0	0.11	5.5	117
50°C distilled water immersion						
2	(min)					
	0	75.6	25.7	0.20	3.0	11
	5	75.2	26.4	0.0	3.0	7
	10	75.4	26.4	-0.10	2.4	6
	15	76.2	26.6	-0.12	2.0	6
	30	76.0	26.5	-0.15	1.8	2
	70	75.0	26.7	-0.13	2.1	5
	130	75.4	26.7	-0.19	1.8	4
18 hrs.	74.0	26.6	-0.24	1.5	3	
100°C distilled water immersion						
3	(min)					
	0	70.6	26.2	0.28	4.0	9
	1	70.4	26.7	0.06	4.0	2
	2	72.4	27.8	-0.06	1.7	8
	3	72.4	27.3	-0.07	1.8	3
	10	72.4	27.3	-0.04	1.7	2
	30	76.8	27.5	-0.10	1.6	3
	60	79.6	26.9	-0.10	1.5	3
17 hrs.	77.8	29.2	-0.16	2.0	8	

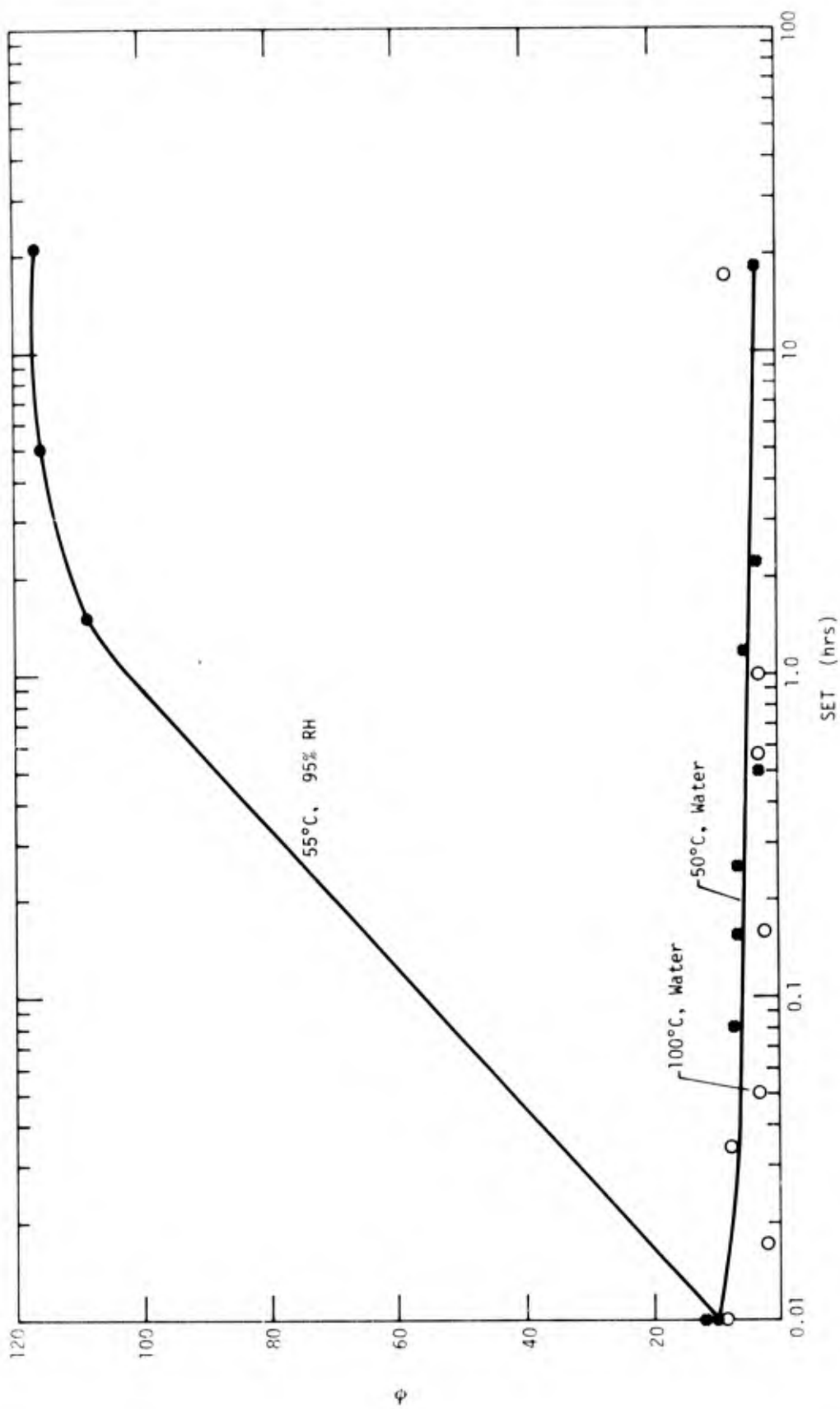


Figure 104. Plot of  $\phi_{H_2O}$  vs SET for Ti-6Al-4V in water and water vapor.

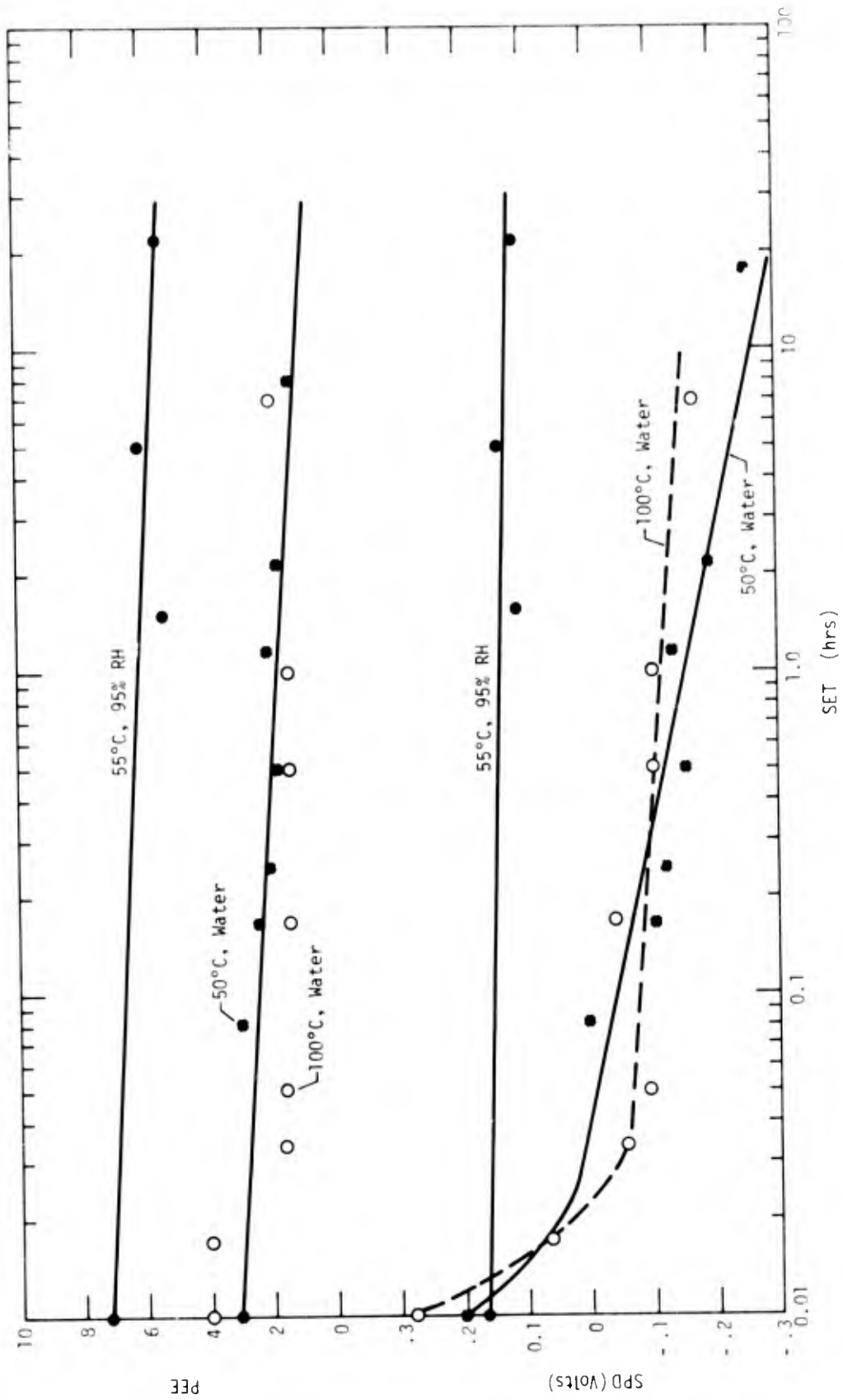


Figure 105. Plot of SPD and PEE vs SET for Ti-6Al-4V in water and water vapor.



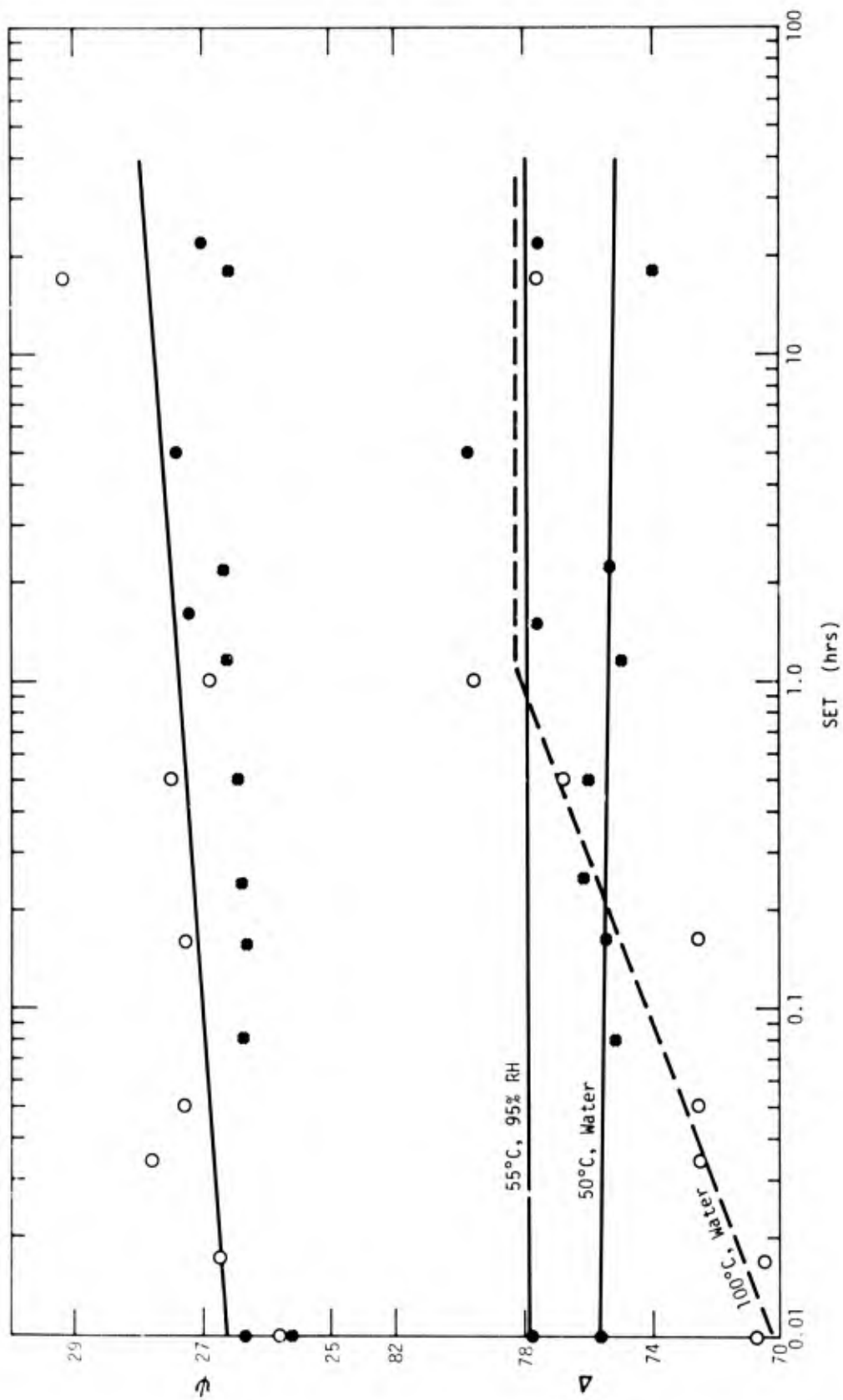


Figure 106. Plot of  $\Delta$  and  $\psi$  vs SET for Ti-6Al-4V in water and water vapor.

Table 37

EFFECT OF BET IN WATER VAPOR AND IN WATER FOR  
Ti-6Al4V - HT424 (PHOSPHATE-FLUORIDE TREATMENT, SINGLE OVERLAP)

BET hours	Environment	Bond Strength (psi)					Avg.	
0		2800	3520	3190	3000	2960	3840	3218±308
10	100°C, 95%RH		3200	3070	2880			3050±113
100	"		2600	2820	2980			2800±133
500	"		1420	2530	2830			2260±560
1000	"		2750	2660	2440			2617±118
10	100°C, water		1150	2540	2420			2037±531
100	"		1830	2230	2250			2103±182
500	"		2140	2320	1070			1843±576
1000	"		2270	2260	1450			1993±362
10	50°C, water		3430	3670	3090			3397±204
100			3010	2790	2420			2740±213
500			2440	1910	2350			2233±216
1000			2130	1350	2260			1913±376

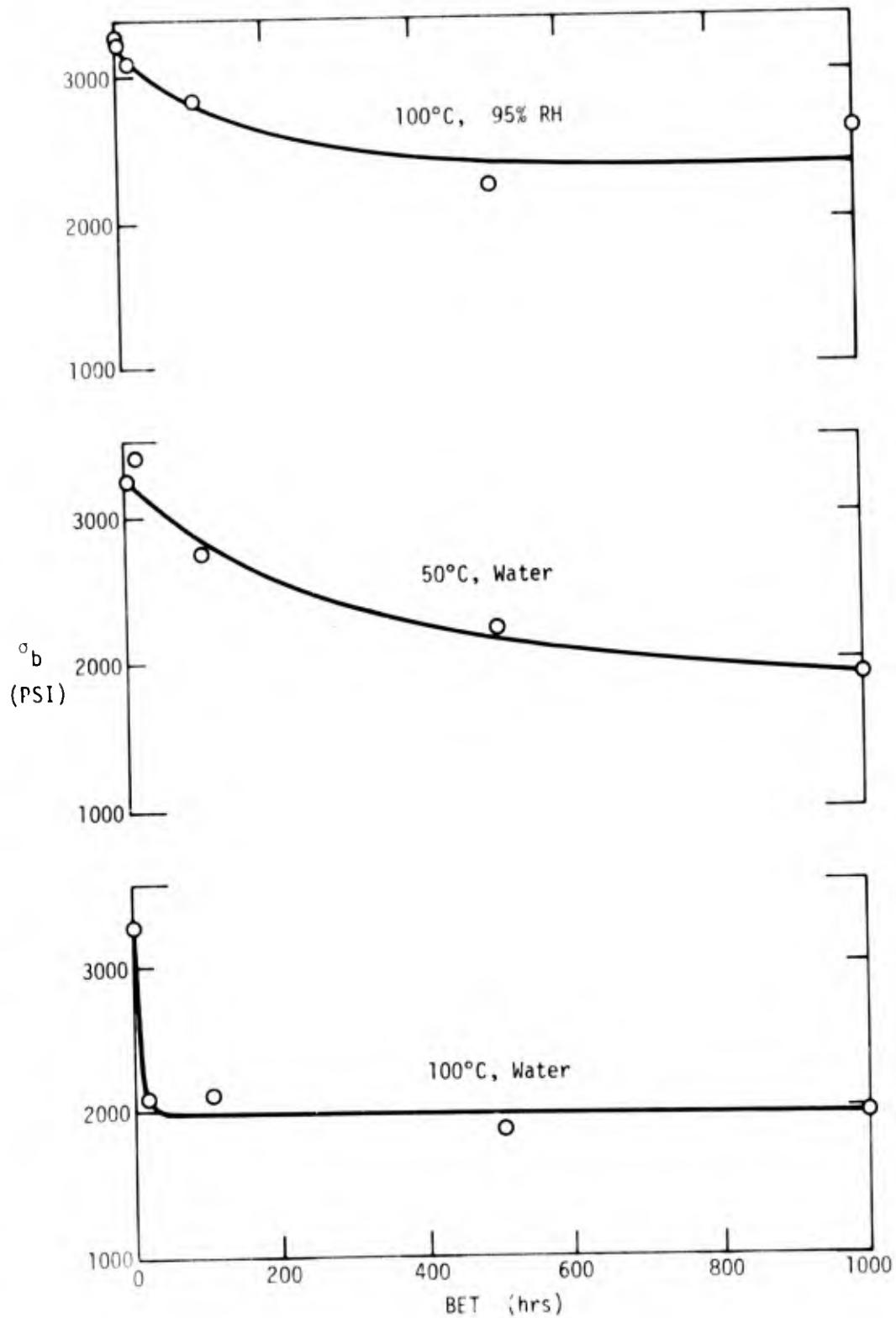


Figure 107. Plot of  $\sigma_b$  vs BET for Ti-6Al-4V - HT424 joints in water and water vapor.

## C. Discussion of Results

### 1. Aluminum

The results reported here provide the answers to most of the questions posed in the introduction. These questions will be considered in sequence.

#### 1.1 Answers to Questions

a) What relevance have laboratory bond tests to real adhesive joint performance?

Different standard laboratory joints relate to different aspects of real systems and the test chosen for study should be tailored to reveal the particular aspect of interest. The common lap shear joint (single overlap) has both shear and peel forces as to be expected in most real joints and therefore is useful for simulating real joints. Due to the small bond area, edge effects are emphasized. This is an advantage with respect to the time needed for studying bond degradation but complicates stress analysis.

The double overlap joint concentrates the stress along a particular surface and causes the forces to be mostly shear in nature. The second couple to fracture becomes a single overlap joint. Therefore, the double overlap joints provide information about the shear surface as well as the surfaces that bend to yield both shear and peel forces. For a given hydrostatic pressure during the cure the double overlap joints had a more reproducible glue line thickness for HT424 with glass carrier. Because the shear stress is focused along one surface, the double overlap joint is advantageous for studying the effect of surface properties after preparation and aging.

Butt joints provide essentially tensile stress. If small areas are bonded, as in our study, the edge effect is greatly emphasized and it is difficult to characterize the surfaces. On

the other hand, butt joints with large surfaces are difficult to control with respect to even stress distribution. The result is poor reproducibility in bond strength.

Other tests, such as cantilever beam, static or under stress, tension and peel tests are useful for revealing various aspects of real systems and should be chosen to meet the particular interest.

b) What effect has the adhesive film or bond strength?

The bond strength increases linearly with GLT (5 to 10 mils) for HT424 with glass but decreased linearly for HT424F without glass. The glass carrier provides a shim, limiting the GLT, and provides channels for water vapor escape during cure. This effect is probably of considerable importance even for large real joints. As the gas escapes at the bond edges it blows holes in the extruded adhesive. These holes then provide easy access for degrading environments.

The water vapor generated during cure cannot escape from the glass free adhesive (HT424F) and leaves large void volume throughout the bond. The bonds are considerably weakened by the void volume.

The lightweight, fine glass mesh, adhesive HT435 without aluminum filler produced small GLT and weak bonds. Therefore the effect of the aluminum filler was not determined. The void volume is greater within the glass net, than for the filled adhesive.

c) What effect does controlled surface roughness have on surface properties and bond strength?

FPI etched Al 2024-T3 surfaces with rms roughness in the range  $\sim 0.1$  to  $0.6\mu$  yield essentially the same bond strength. There may be a roughness effect for very smooth surfaces but, due to contamination of the smoothest surfaces, an effect could not be established.

d) Can specific types of hydroxide films and organic molecules be used to calibrate surface tools in order to

understand experimental results for unknown causes of surface degradation?

The use of ellipsometry for establishing the thickness of thin oxides and organic monolayers is excellent but it is of limited use for thick ( $>1000\text{\AA}$ ) oxides or hydroxides unless the film is tracked during growth. The photo-electron emission measurement is directly related to film thickness and type of film for thin films but is limited in use for thick films. Surface potential measurements are least reproducible but show definite trends depending on the film and its nature. It is primarily related to the outer dipole layer and changes as molecules reorient themselves as well as during growth. The SPD decreases and then increases whether aging takes place in a clean chamber (UHV) or a contaminated chamber. Experiments with controlled contamination shows that SPD will increase with myristic acid and decrease with erucic acid. Experiments for fatty acids, alkanes and alcohols on clean mercury<sup>21</sup> show that positive or negative changes depend on the packing and orientation of the molecules. SEM, ellipsometry and light scattering are extremely useful for measuring roughness and morphology. Auger spectroscopy is very useful for semi quantitative surface analysis but suffers most from the effect the electron beam imposes on the surface. The electron beam reduces  $\text{Al}_2\text{O}_3$  to Al and  $\text{TiO}_2$  to Ti as well as desorbing carbon compounds. ESCA is excellent inasmuch as the electron beam problem does not exist but suffers from the time it takes to make measurements. Contact angle measurements are extremely sensitive to surface degradation.

The answer to question d is that the tools can be calibrated with known systems but the degree of usefulness for identifying unknown systems will depend upon the extent of and number of systems calibrated. The more work done in this area, the more useful the tools will become.

e) What effect does exposure to ultraviolet light have on the surface contamination and cleaning?

It has been discovered that UV light can accelerate surface contamination or remove contamination. Exploration in this area is very promising since it may establish a single inexpensive means for surface preparation for adhesive bonding.

f) What effect does the gas environment have on the aging process? Specifically, will FPL etched Al2024-T3 degrade with respect to surface energy and bond strength if aged in the absence of organic contamination and/or the absence of water vapor?

We have discovered that in the absence of water vapor and contamination degradation is not detected in a period of weeks. In the absence of contamination but in the presence of water vapor, degradation does occur. It is believed that degradation is associated with the blunting of field emission type metal ridges that are formed during etching.

The extremely reactive FPL etched aluminum surface will adsorb most contaminating species that might be present in the environment and if this occurs more rapidly than oxidation (blunting) of the metal ridges, the ridges may be preserved by the contaminant.

g) Is the effect of aging in liquid water qualitatively similar to aging in humid atmospheres?

This question is difficult to answer since the type of reaction product that is formed in water or water vapor depends upon the metal history. The surface always becomes contaminated with carbonaceous matter when aged in water vapor (except in the UHV chamber) and does not when aged in distilled water. The reaction kinetics are much faster in water than in water vapor. In an experiment with HT424 from Batch 2 the bond strengths for Al2024-T3 were approximately the same (~2600 psi) whether aged in water, water vapor or unaged. On the other hand HT424 from Batch 3 produced high bond strength (~3300 psi) if aged in 100°C water

vapor or 100°C water to produce the same hydroxide film thickness (~2600 Å). Thicker films produced weaker bonds. Bonds with Al2024-T3 acetone degreased and 100°C water aged (~3000 Å) were very weak (~420 psi) inspite of the wettability of the surface.

h) What are the properties of anodic films formed in phosphoric acid and why do they not degrade as fast as other preparations?

The phosphoric acid anodic films on Al 2024-T3 are about 2200 Å thick, (for 10V, 20 min.) and have the unusual property that although they are high energy surfaces (completely wettable) they are extremely inactive and adsorb contamination very slowly. After 700 hours in laboratory air the water contact angle is only 5°. These anodic films have about the same properties regardless of the surface pretreatment even in the as-received condition. These features account for the excellent aging properties of phosphoric acid anodized samples.

### 1.2 Adhesive Joint Structure and Failure Mechanisms

Figure 108 shows the general characteristics of a fresh FPL etched Al 2024-T3 surface. The cross section a of Fig. 108 indicates that etch pits of the order of 10 μ diameter are formed during the standard 13 minute FPL treatment (see Fig. 34). Inside the large pits are smaller pits of the order of 2-3 μ represented by the cross section b. A rather uniform set of smallest pits of the order of 500 to 1000 Å are observed over the entire surface as represented in cross section c. The schematic representation c is the same as that presented by Bijlmer<sup>22</sup> except that black peaks representing metal in the anodic areas have been introduced by myself. It has been shown that if the metal beneath the oxide is smooth, with respect to dimension of the order of 100 Å, normal ellipsometric parameters Δ and ψ (for a smooth surface) are theoretically predicted and obtained regardless of the oxide roughness. The low values of ψ for the FPL etched surface is indicative of the rough metal surface on



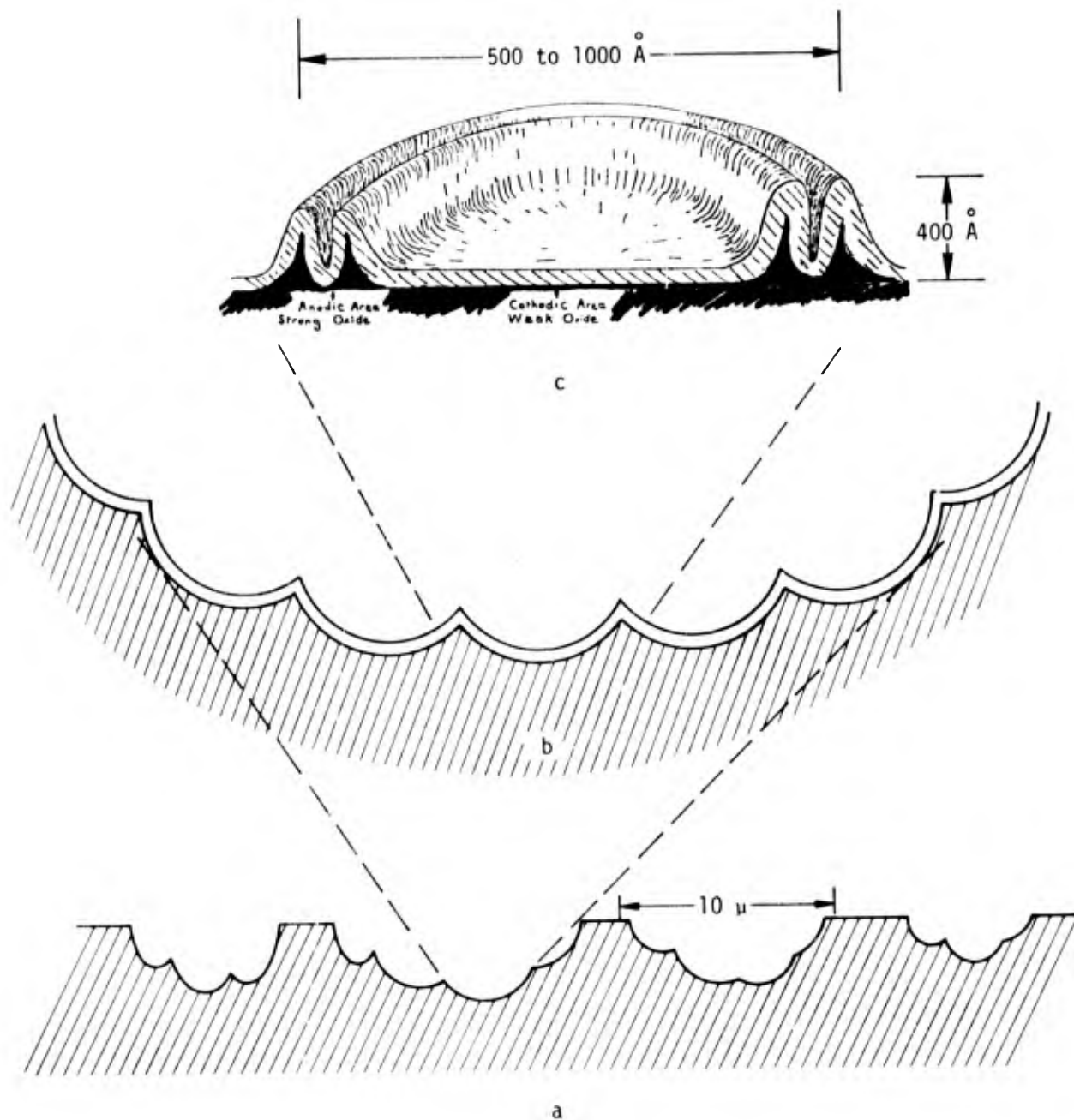


Figure 108. Schematic representation of FPL etched aluminum at three magnifications.

the microscopic level ( $\ll \lambda$ , where  $\lambda = 6328 \text{ \AA}$ ). When the effect of roughness is corrected for, the average oxide film thickness is of the order of  $100 \text{ \AA}$ . However, observation of the oxide thickness by SEM of bent samples by Bowen, reveals the oxide ridge height of about  $400 \text{ \AA}$ .

The presence of the sharp metal ridges left by the fresh FPL etch accounts for a number of observations. One of the most significant features of the fresh FPL etched surface is its extremely reactive nature. It will adsorb any contaminating gas that happens to be present even at extremely low partial pressures. This is believed due to the higher electric fields associated with the sharp metal ridges. The sharp ridges cause enhanced field emission of photo electrons and lowered work function (from SPD) and cause the surface to be very wettable.

The clean high energy (wetable) surface with very thin oxide film produced by the FPL etch, gives the process its utility for adhesive bonding. However, it is the reactive nature of the FPL etched surface that causes its poor stability, especially in humid atmosphere.

The active high energy FPL etched surface is wet entirely by the primer and fills etch pits with primer (see Fig. 24b AFML-TR-74-73). All clean aluminum surfaces were sufficiently rough on a microscopic scale to produce mostly cohesive failure, so that an increase in roughness had little if any effect.

Figure 109 is a schematic drawing of a bond before (top) and after (bottom) fracture for cohesive failure. The bundle of glass fibers have very little shear strength. The void volume caused by the water vapor collects primarily at the glass bundle where the vapor can escape along the channels between fibers to the outside of the bond. Near the outer edge much larger void volume is made and the extruded polymer has holes formed by the escaping gas.

The locus of failure depends upon the weakness of a particular area and the stress distribution. Thin glue line

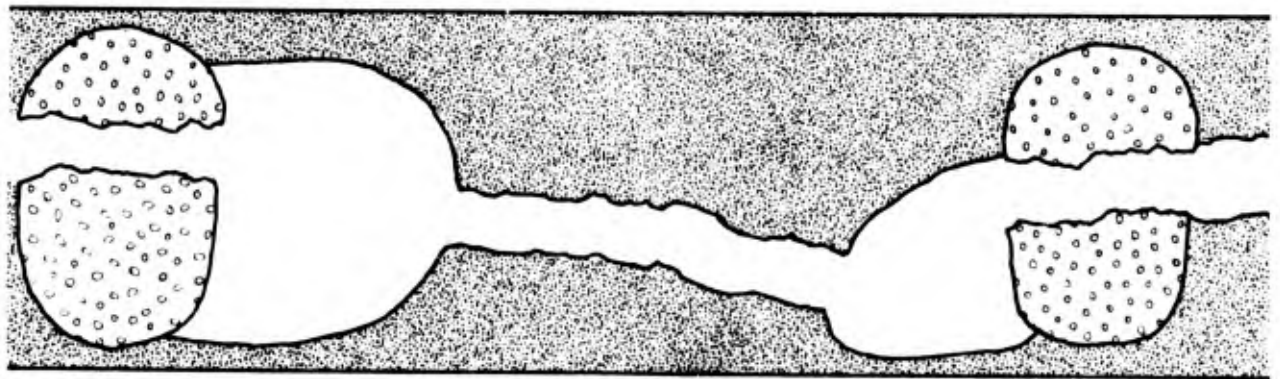
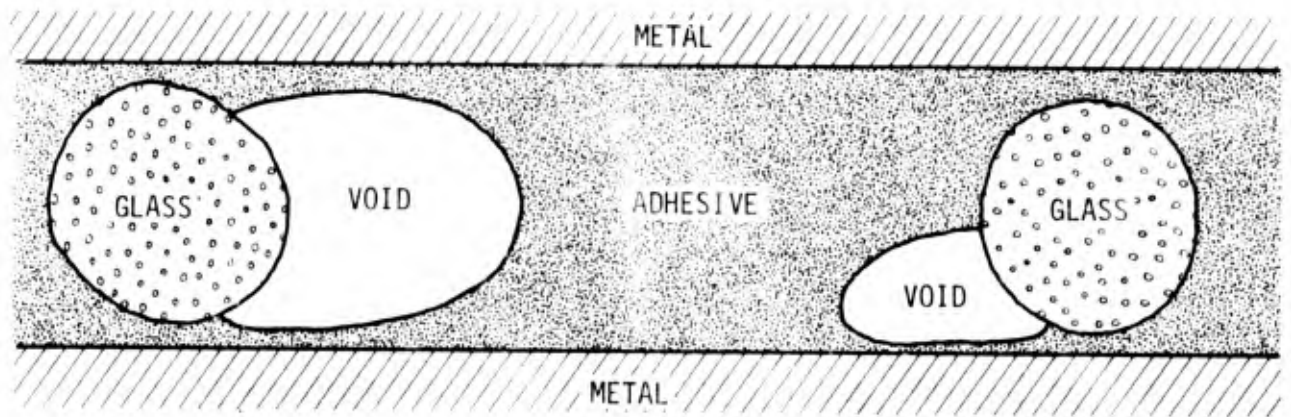


Figure 109. Schematic representation of an adhesive bond before (top) and after (bottom) cohesive fracture.

thickness tends to focus the stress at the surface as the single overlap adherends bend. The thicker GLT allows a more even stress distribution and failure becomes more cohesive for adhesive with glass carrier cloth. Adhesive without glass has much more void volume due to the lack of vapor escape channels and the bond strength decreases with increasing GLT due to the increase in void and defect probability. It is apparent that the glass has an effect upon the stress distribution as well as the water vapor entrapment.

Two degradation processes occur in gas environments both of which produce low energy (non wettable) surfaces. One process is degradation of the sharp metal ridges and the other is adsorption of contamination. In a perfectly clean dry atmosphere the active surface remains indefinitely. In a perfectly clean chamber, except for water vapor, degradation occurs by oxidation of the metal ridges leaving oxide or hydroxide ridges and a smoother metal substrate, on the microscopic level. The reason that a microscopically rough but clean oxide or hydroxide layer on a smoothed metal causes high contact angle is a mystery. At Boeing, Smith<sup>23</sup> found that if a negative potential was applied during etching, high contact angles and weak bonds resulted whereas zero or positive potential left the FPL etched surface completely wettable with high bond strength. He found the hydrous layer formed at negative potential to have high dielectric loss. I believe that cathodic conditions during etching causes oxidation such that the sharp ridges do not form.

If our hypothesis concerning the metal ridges is true, once the surface is degraded by reaction with water vapor, it will not be regenerated by heating unless the oxide is thickened. We found that if samples had been aged in the UHV chamber or in air, such that large water contact angles ( $\sim 100^\circ$ ) prevailed, heating the samples with argon did not lower the contact angle. However, if a water drop was placed on a hot surface the contact angle would decrease with time as the surface was oxidized in the

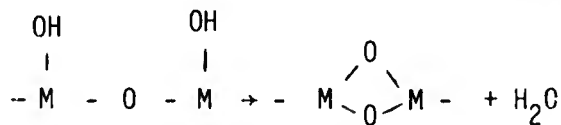
vicinity of the drop. These results are consistent with our hypothesis. Smith<sup>23</sup> reports that heating the hydrophobic surfaces formed at negative potentials to high temperature, changed the surface to hydrophilic, presumably by oxidation to thicker oxide.

It is known that some oxide-free metal surfaces are hydrophobic and it was thought that the hydrophobic nature of the aged FPL etched aluminum was associated with the hydrophobic nature of the clean metal if the oxide is thin enough and the substrate was smooth. To check the wettability of a thin oxide on smooth aluminum, aluminum was vapor deposited onto smooth glass and the contact angle measured within seconds of removal from the high vacuum system. The surface proved to be hydrophilic (contact angle  $\sim 0^\circ$ ). The oxide film thickness was measured within four minutes and found to be  $\sim 50 \text{ \AA}$ . It is therefore concluded that smooth aluminum with oxide film between zero and  $50 \text{ \AA}$  is hydrophilic and that the hydrophobic nature of the clean aged FPL etched surface is not attributed to smoothing of the substrate alone. The hydrophobic nature seems to be related to the roughness of the very thin oxide layer on the partially smoothed substrate, in spite of the fact that smooth or rough bulk oxides or hydroxides of aluminum are completely wettable if clean.

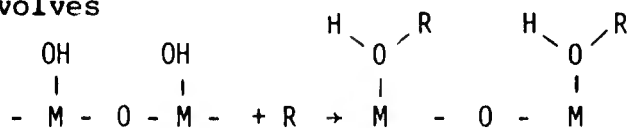
If the FPL etched aluminum surface is aged in glass jars or in the laboratory air, the surface soon becomes contaminated. Experiments with known organic molecules show that the wettability and bond strength is greatly reduced by one monolayer.

White<sup>24</sup> and DeLollis<sup>25</sup> interpret the degradation of the polar character to be due to specific adsorption of organic contamination. White shows that degradation occurs in every system he tested except a pre-baked ultrahigh vacuum system. Although White observed that the polar character of fused silica changes to non-polar character upon heating (speculates that  $\text{Si-O-Si} \rightarrow \text{Si} \begin{matrix} \text{OH} & \text{OH} & \text{O} \\ | & | & / \backslash \\ & & \text{Si} \end{matrix}$ ) he concluded that organic adsorption rather than this mechanism was involved in the usual SET experiments. We also conclude that specific adsorption is involved as well as the metal ridge smoothing.

We have found that some contaminated surfaces can be regenerated to polar character by heating in dry nitrogen. In this case, the adsorbed contamination must have protected the metal ridges from oxidation. If the degradation of



is involved, one would expect that exposing a degraded surface to hot-dry nitrogen would either leave the surface unchanged or degrade it even further. On the other hand if the degradation process involves



where R represents contamination, exposure to hot-dry nitrogen would tend to regenerate the polar surface, as long as the temperature is high enough to break O - R bonds but not  $\begin{matrix} \text{H} \\ | \\ \text{O} \\ | \\ \text{M} \end{matrix}$  bonds. Lewis et al<sup>26</sup> have shown that the hydroxyl groups are on the surface under all conditions (except perhaps high temperatures) whether the underlying oxide is a hydroxide or not. Also, if a monohydrate is formed during acid-etch and converted to alumina during SET one would expect the ratio of the Auger peak to peak height for oxygen to Al to decrease by 30% whereas in fact the ratio increases by 36% for the Al (55 eV) peak and by 5% for Al

(1390 eV) peak. These results indicate SET may increase hydration but not decrease it. Aging Al 2024-T3 in water always leaves the surface wettable if the temperature is high enough and the time long enough, even if the surface was only degraded. Thick hydroxides are formed in water. It has been shown by Altenpohl<sup>27</sup> and Vedder and Vermilyea<sup>10</sup> that although only boehmite (~76°C) and bayerite (~60°C) are observed by X-ray diffraction, the stoichiometry is not that of the bulk minerals. They report, as we have found in this report, the  $H_2O/Al_2O_3$  ratio ranges from 0.56 to 3.77. Altenpohl<sup>27</sup> reports that 1 hour in boiling distilled water produces a film between 3000 and 4000 Å, in good agreement with our result in Fig. 78. Bond exposure to humid atmospheres or water allows water to penetrate along glass fiber bundles and degrade the adhesive joint. The speed of degradation depends on the environment and temperature. More research is needed to establish the mechanism of adhesive or interface degradation during BET.

## 2. Titanium

### 2.1 Answer to Questions

a) What is the effect of the surface treatments phosphate-fluoride, Turco, PASA-JELL and nitric acid-fluoride, on surface properties and bond strength?

All of these treatments produce high energy (wetable) surfaces. The bond strength increases in order of surface roughness. Oxide films are very thin ~100 Å and strong. Failure does not appear to occur in the oxide.

b) What effect does slight variations in the phosphate-fluoride treatment at different laboratories have on surface properties and bond strength?

All of the treatments produce similar morphology but there are detectable differences in surface parameters. Within experimental error (mostly due to differences in GLT) bond strengths are the same ( 4000 psi) for double overlap joints.

c) What effect has aging of the phosphate-fluoride solution on surface properties?

Aging the solution for one year made a detectable difference to the surface parameters but they were so small as to be considered negligible.

d) What is the effect of controlled contamination on surface properties?

Deposition of erucic acid on phosphate-fluoride treated Ti-6Al4V decreased SPD as for aluminum. The changes in surface parameters correspond to deposition of one molecular layer per dip. The molecular layer can be deposited with the molecules erect or lying flat.

e) What is the effect of different SET environments on surface properties and bond strength?

Exposure of titanium to dry nitrogen in the clean UHV chamber maintains the surface in a wettable condition with very little change in surface parameters. Removal of the titanium from the UHV chamber into laboratory air caused the surface to immediately physically adsorb contamination which is removed when replaced in the vacuum system. Contrary to aluminum, titanium remains wettable when exposed to humid atmospheres in the clean UHV chamber. It was shown in AFML-TR-74-73 that SET did not degrade the bond strength for Ti-6Al4V - HT424. As for BET in humid atmospheres, BET in water degrades the bond strength in approximately the same manner as for Al 2024-T3 - HT424. This probably indicates that degradation is primarily in the HT424 adhesive which is common to both systems.



## 2.2 Adhesive Joint Structure and Failure Mechanisms

The structure of the bond is the same as observed in Fig. 109. The titanium bonds differ from the aluminum bonds in two ways. First, the surface is not pitted but has a rather uniform pyramidal structure with rms height of  $\sim 0.4\mu$  and base of  $\sim 10\mu$ . There is no evidence for the submicroscopic pits with sharp metal ridges as for the FPL etched aluminum. Consequently the titanium does not degrade with respect to wettability by sharp metal ridge blunting in the clean UHV chamber. The lack of sharp metal ridges and associated high fields, causes the titanium surface to be less strongly bonded to the adhesive so that if failure occurs at the interface it occurs between the metal-oxide and primer. The presence of a monolayer or less of contamination deposited during SET in humid atmospheres does not degrade the molecular bonding sufficient to cause lower bond strengths. Second, the titanium specimens are much more stiff than the aluminum so that the stress distribution with respect to GLT is quite different. The bond strength is considerably more sensitive to GLT.

## 3. Conclusions

### 3.1 Adhesion Mechanisms

The question of what constitutes a good metal surface preparation and why as-received, or minimal preparation is unsatisfactory has been greatly elucidated in this study. Aside from the obvious removal of weak boundary layers such as grease or loose particles the surface must meet certain requirements at the metal - oxide interface, in the oxide and at the oxide primer interface. The oxide must have a strong bond to the metal and must be strong internally. A degreased metal surface usually meets these requirements and yet will yield low bond strength as compared to an etching surface treatment.

We have demonstrated that a degreased aluminum or titanium surface has no more than a monolayer or so of organic contamination which we do not consider to be a weak boundary layer. We conclude that the surface must have strong enough adsorption power for the adhesive primer as to cause the adhesive material to first wet the surface for maximum contact and second adhere strongly under stress. The second requirement is usually met if the first is met. The adsorptive power is partially reflected in the polar and dispersive surface energy revealed by wettability or contact angle measurements. In this regard two observations are significant. First, although aluminum and titanium show similar surface degradation with aging in terms of surface energy (see Figs. 46 and 85 of AFML-TR-74-73), for the same adhesive, aluminum shows a corresponding bond degradation whereas titanium does not. The difference is attributed to the higher adsorptive power (stronger oxide - primer bonding) of the titanium as evidenced by the second observation that at  $\phi_c \approx 1$ ,  $\sigma_b$  is much higher for titanium, ~5000 to 6000 psi, as compared to aluminum ~3800 psi. That is, the property  $M_{o-p}$  (see Eq. 2a) is larger for Ti than for Al and due to the difference in stiffness of Ti and Al, the bending properties differ and therefore  $S_j$  also differs. The higher  $\sigma_{o-p}$  for Ti shifts the weakest region to the adhesive where failure initiates. As a consequence  $\sigma_b$  is insensitive to surface contamination during aging for titanium.

With respect to degradation of aluminum surfaces upon aging in humid atmospheres, the question as to whether degradation was caused by contamination, by formation of weak hydroxide films or both arose. By forming known hydroxide films on aluminum and performing wettability analysis, we show that the degradation of surface energy (wettability) during aging is not related to the formation of hydroxide films. Also by placing known organic molecules on FPL etched Al 2024-T3 we show that all of the trends in surface measurements ( $\Delta$ ,  $\psi$ , SPD, PEE and  $\phi_{H_2O}$ ) during aging can be explained in terms of organic contamination. It therefore

became necessary to perform ultra clean humidity aging experiments to see if degradation could occur in the absence of organic contamination.

Experiments were performed in an ultra high vacuum system used as a humidity chamber. We have demonstrated that degradation with respect to surface energy (wettability) as well as with respect to bond strength can occur in the absence of organic contamination but only if water vapor is present. Degradation does occur in the presence of most active gaseous contaminants such as silicones, hydrocarbons, fluorides etc., even at extremely low partial pressures.

The cause of the high adsorptive power (and high bond strengths) of freshly FPL etched aluminum is also the cause of its degradation properties. Freshly etched aluminum leaves a pitted surface represented in Fig. 108. A rather uniform set of microscopic pits form on the surface of much larger pits. The small pits have very sharp metal ridges. The entire surface is covered with a very thin oxide layer ( $\sim 100 \text{ \AA}$ ). The sharp metal ridges have very high electrical fields (similar to field emission tips) that give the surface its very highly reactive nature, and the surface is very wettable and forms strong bonds with adhesives. In the presence of active contamination gases, chemisorption occurs on the ridges and act as poisons with respect to attraction to liquids or adhesives thus degrading the surface during aging. Contaminated surfaces can be rejuvenated by sputter cleaning the contamination away. In the absence of contamination but in the presence of water vapor oxidation of the metal ridges occurs which blunts them and permanently degrades the surface with respect to wettability and bond strength.

Titanium forms rough surfaces by the usual surface preparation etching solutions but does not form sharp points or ridges as for aluminum and wettability degradation in the absence of organic contamination does not occur. In the presence of organic contamination, physical adsorption takes place which can

be removed by desorption in a vacuum system.

It is concluded from this analysis that degreased metal would probably yield strong bonds if the monolayer of organic contamination could be removed. It would be greatly advantageous if a simpler, less expensive means than the acid etch treatments could be found for this purpose. We have discovered that simple exposure to UV light in ambient temperature can remove contamination, but that it can also increase contamination. A careful study should be made to establish the utility of this technique for cleaning. It is of interest to note that exposure of contaminated aluminum to UV light can change a non wettable surface to a very wettable surface without increasing the bond strength, and that a non wettable titanium surface can form strong bonds indicating that wettability (water break test) is not always a criteria for good bonding.

Surface roughness will increase bond strength at the interface between the adhesive and the metal by increasing the area of actual contact per unit area of projected area and perhaps by a hook and latch effect if adhesive can penetrate into pit holes, crevices, etc. However, the effect on  $\sigma_b$  of roughness, as for the effect of contamination, will not be observed if bonding in the interfacial region is strong enough to shift initial failure into the adhesive as in the case of aging of phosphate - fluoride treated Ti-6Al4V. If the interfacial region is weakened by using a different surface treatment (e.g.,  $\text{HNO}_3$ -HF treatment) the effect of roughness might be expected and is observed. In the case of aluminum, if the undegraded adhesive (from batch 3) is used, initial failure is shifted to the adhesive, the bond strength is high and no effect of roughness is observed. The degraded adhesive (from batch 2) yields much lower bond strengths and either a contamination or roughness effect is observed. This indicates that degradation of the adhesive has affected its interaction

with the interface rather than its internal strength. This would occur if degradation is a result of surface contamination of the adhesive film. This should be checked by making a wettability analysis of the adhesive from batch 2.

Joints between metal adherends and glass - carrier - film - adhesives form bonds with the structure represented in Fig. 109. During the adhesive cure under pressure at temperature, water vapor is released as a reaction product. The water vapor collects at the glass fiber bundles and leaves some large cavities along the fiber bundle. However, most of the vapor is able to escape along channels, associated with the fiber bundles, to the bond edge and therefore to the atmosphere. Adhesive without glass carrier cannot release the water vapor to the atmosphere. For the glass-free adhesive, the resultant void volume is greatly increased and the bond strength greatly decreased. The glass carrier has the disadvantage of filling about a third of the bond area with low shear strength material but this disadvantage is outweighed by the removal of large void volume that has no shear strength at all. The glass carrier also has the advantage of providing a shim that produces a glue line thickness (GLT) of approximately the diameter of the glass fiber bundle. As a result, the compliance of the composite is increased and the stress is more uniformly distributed in the bond. This effect increases with GLT so that the bond strength of the lap shear joints tend to increase with GLT. Without the glass carrier the compliance should also increase with GLT but this effect is over-shadowed by the large void volume and the increased probability of defects in the adhesive with increasing GLT. Although the glass carrier has the advantage of providing channels for water vapor escape during cure, it has the disadvantage that these channels provide easy access to degrading environments after the cure process. It is estimated by taking into account the void volume and the glass carrier that the shear strength of the epoxy adhesive is of the order of 9000 psi. This is close to the tensile strength

measured by the butt joint tests. It follows that if the void volume and glass carrier were not present the bond strength may nearly be tripled in metal - epoxy - metal joints.

### 3.2 Suggestions for Improvements

The weak regions in the Al 2024-T3 - HT424 joints are the void volume created by the natural production of water vapor during the cure, and the weak glass carrier. The glass carrier is needed because it provides escape channels for the water vapor and therefore greatly decreases the void volume. It also has an effect with respect to the stress distribution. It is suggested that a carrier be found that acts as a hygroscopic water sink. Even better would be a hygroscopic powder filler to replace the aluminum filler, to reduce void volume and the weak carrier. It is suggested that edges where the glass carrier and extruded adhesive with gas blown channels, be sealed with additional adhesive to prevent access to degrading environments.

## APPENDIX A

### DETAILS OF SURFACE PREPARATIONS FOR Ti-6Al4V

#### 1) Phosphate-Fluoride Surface Treatment

- a. Wipe metal with acetone soaked cloth, followed by a 10 minute ultrasonic cleaning in acetone.
- b. Emulsion clean in TURCO 3878 for 15 min. at 54-60°C.
- c. Water rinse-spray and overflowing dip.
- d. Water-break test.
- e. Pickle 1 min at 23°C in the following solution:
  - 70% HNO<sub>3</sub>
  - 10 oz/gal NH<sub>4</sub>HF<sub>2</sub>
- f. Deionized water rinse for 2 min at 23°C.
- g. Dip in the following stirred solution for 1/2 minute at 27°C:
  - 7.3 oz/gal Na<sub>3</sub>PO<sub>4</sub> · 12 H<sub>2</sub>O
  - 1.5 oz/gal NaF
  - 7.3% by volume HF (60% solution).
- h. Deionized water rinse - 15 min.
- i. Deionized water blast to remove film.
- j. Dry samples under ambient air conditions.

#### 2) Nitric Acid-Fluoride Treatment

- a. Solvent trichlorethylene (TCE) wipe metal with cloth.
- b. 10 minute TCE - ultrasonic cleaning.
- c. 10 minute cleaning in TURCO 4215 alkaline cleaner at 66°C.
- d. Rinse in distilled water.
- e. Pickle in the following distilled water solution at room temperature for 5 minutes.
  - Nitric acid 15% by weight

Hydrofluoric acid 3% by weight

f. Rinse in distilled water at room temperature.

3) PASA-JELL Treatment

a. thru e. same as No. 2 but add:

f. Apply PASA-JELL 107 liquid to the titanium surface by dip or with an acid resistant brush. Cover the entire surface by cross brushing.

g. Allow to dry for 20 min.

h. Rinse thoroughly with water.

i. Dry 15 min. at 40°C in dry N<sub>2</sub>.

4) TURCO Treatment (LAD Modification)

a. Wipe metal with acetone-soaked cloth, followed by a 10 min. ultrasonic cleaning in acetone.

b. Emulsion-clean in TURCO 3878 for 15 min. at 54-60°C.

c. Deionized water rinse.

d. Etch in TURCO 5578 for 10 min. at 66°C.

e. Deionized water rinse.

f. Dry in air.



## APPENDIX B

### Gillette

Bell process FW-4352, Rev. E, Phosphate-Fluoride Treatment

- 1) Degrease
- 2) Alk. clean 5-15 min. 140-180°F.
- 3) Rinse.
- 4) Pickle - 2.0-3 oz/gal HF  
40-50 oz/gal. HNO<sub>3</sub>
- 5) Rinse.
- 6) Phosphate-Fluoride 2 min. max, RT  
6.5 - 7.0 oz/gal Na<sub>3</sub>PC<sub>4</sub>  
  
2.5 - 3 oz/gal KF  
  
2.2 - 2.5 fluid oz/gal (70%) HF
- 7) Rinse RT
- 8) Hot water soak 145-155°F 15 min.
- 9) Final rinse (quick spray) RT - 160°F .3 to 1 min.
- 10) Dry air RT - 160°F.

### General Dynamics (Battelle formulation)

- 1) Methyl ethyl ketone wipe.
- 2) Trichlorethylene-vapor degrease.
- 3) Pickle in the following water solution at room temperature for 30 sec:  
Nitric acid - 15 percent by volume of 70 percent HNO<sub>3</sub> solution  
Hydrofluoric acid - 3 percent by volume of 50 percent HF solution.
- 4) Rinse in tap water at room temperature.

- 5) Immerse in the following water solution\* at room temperature for 2 min:  
Trisodium phosphate - 50 grams/liter of solution  
Potassium fluoride - 20 grams/liter of solution  
Hydrofluoric acid (50 percent solution) - 26 milliliters/liter of solution
- 6) Rinse in tap water at room temperature.
- 7) Soak in 150°F tap water for 15 min.
- 8) Spray with distilled water and air-dry.

-----  
\*This bath composition was developed at the Battelle Memorial Institute and is protected by U.S. Patent 2,864,732. Licensing arrangements can be obtained from the Battelle Development Corporation, Columbus, Ohio.

## REFERENCES

1. T. Smith, *J. Appl. Phys.*, 46, 1553 (1975).
2. D. H. Hensler, *Applied Optics*, 11, 2522 (1972).
3. B. B. Bowen, "Symposium on Adhesion and Adhesive State of the Art" University of Pittsburgh, May, 1974.
4. K. E. Weber and G. R. Johnston, *SAMPE, Quarterly*, Oct. 1974.
5. W. T. McCarvill and J. P. Bell, *J. Adhesion*, 6, 185 (1974); *J. Appl. Polymer Sci.* 18, 2243 (1974); 18, 335 (1974); 18, 343 (1974).
6. A. Pattnaik and J. D. Meakin, Tech. Rep. 4699, Picatinny Arsenal, Dover, New Jersey, July 1974.
7. A. W. Bethune, *SAMPE*, April, 1974.
8. M. C. Ross, R. F. Wegman, M. J. Bodnar and W. C. Tanner, *SAMPE*, Jan. to April, 1974.
9. J. D. Minford, *Adhesive Age*, July, 1974.
10. W. Vedder and D. A. Vermilyea, *Trans. Faraday Soc.*, 65, 561 (1969) and 2644 (1969).
11. W. J. Bernard and J. J. Randal, Jr., *J. Electrochem. Soc.*, 108, 822 (1961).
12. M. S. Hunter, P. F. Towner and D. L. Robinson, *Proc. Amer. Electroplaters Soc.*, 220 (1959).

13. S. Tajima, *Adv. Corr. Sci and Tech.*, 1, 234 (1970).
14. R. D. Paul and J. D. McGivern Jr., *Soc. Adv. of Materials and Process*, 581 (1973).
15. K. Wefers and B. M. Bell, *Tech. Paper No. 9, "Oxides and Hydroxides of Aluminum"* Alcoa Research Laboratories, 1972.
16. P. Beckman, "The Scattering of Electro-magnetic Waves from Rough Surfaces" (MacMillan, New York, 1963). Part 1.
17. I. Ohlidal and F. Lukes, *Optica Optica*, 19, 817 (1972).
18. G. W. Lively, AFML-TR-73-270, Jan. 1974.
19. W. C. Hamilton and G. A. Lyerly, *Picatinny Arsenal Report 4185*, March, 1971.
20. E. L. Alexander, NA-71-545, July 1971, IR&D Report at Los Angeles Division (LAD) of North American Rockwell (now Rockwell International Corp.)
21. T. Smith, *Advances in Colloid and Interface Science*, 3 161 (1972).
22. P.F.A. Bijlmer, *J. Adhesion*, 5, 319 (1973).
23. A. W. Smith *Electrochem Soc.: Solid State Science and Technology* 1151 (Nov. 1973).
24. M. W. White, "The Detection and Control of Organic Contamination on Surfaces" Marcel Dekker Inc. (1968), p. 361.

25. N. J. DeLollis, "Adhesives for Metals" Industrial Press Inc., N.Y. (1970), p. 11
26. B. F. Lewis, M. Mosesmangund, W. H. Weinberg, Surf. Sci. 41 142 (1974).
27. D. G. Altenpohl, Corrosion, 18, 143f (1962).